

The Influence of Jointed Fabric and Stress Ratio on Deformation and Fluid Flow

by

Atena Pirayehgar

A thesis
presented to the University of Waterloo
in fulfillment of the
thesis requirement for the degree of
Doctor of Philosophy
in
Civil Engineering

Waterloo, Ontario, Canada, 2017

© Atena Pirayehgar 2017

AUTHOR'S DECLARATION

This thesis consists of material all of which I authored or co-authored: see Statement of Contributions included in the thesis. This is a true copy of the thesis, including any required final revisions, as accepted by my examiners.

I understand that my thesis may be made electronically available to the public.

STATEMENT OF CONTRIBUTIONS

I hereby declare that I am the sole author of this thesis. Materials in Chapters 4 and 6 have already been published. Materials in Chapter 5 have been accepted to the Journal of Natural Gas Science and Engineering - Elsevier. Mike Yetisir as the co-author provided some figures and a section within this chapter. Materials in Chapter 7 have been submitted to the Journal of Natural Gas Science and Engineering - Elsevier. Professor Maurice Dusseault as the supervisor of the research co-authored all publications.

The above mentioned publications do not constitute the entirety of the publications created by the research done throughout this doctorate. These publications were not included as their topics strayed too far from the central focus of the dissertation.

ABSTRACT

There are remarkable volumes of hydrocarbon resources in low-permeability naturally fractured rock masses (NFRs) characterized by naturally occurring discontinuities. Natural fractures are one of the most important factors controlling the hydraulic behavior of the rock masses and most low-permeability rocks are very strong, stiff, and fractured. Hydraulic fracturing in low-permeability hard NFRs has recently gained popularity both in the petroleum and mining industries, with different goals.

A strong understanding of the behavior of natural fractures provides engineers with better insight into the hydraulic fracturing technology and development strategies. To gain this knowledge, different methodologies and mathematical codes have been introduced to numerically model jointed systems. The first step for every model would be generating geometries that realistically represent the naturally fractured rock mass. Consequently, generating fabrics with different geometric attributes and assessing fabric effects on fluid flow and deformation are points of interest in this research. In addition, stress fields play a prominent role in hydraulic and mechanical responses of natural fractures, and this forms another core direction of the current project.

This research presents some attempts to simulate and emulate hydraulic fracturing in hard low-permeability naturally fractured rock masses. In a rock with a hard matrix, only pre-existing fractures may re-activate during the process of pressurization and no new fractures are created. Analysis may lead to a better physical and empirical explanation for how different fabric patterns and deviatoric stress conditions affect the hydro-mechanical behavior of NFRs during injection and after shut-in.

A commercial software, Universal Distinct Element Code (UDECTM), is used to generate NFRs in the study. Various geometries have been generated in a two-dimensional framework and subjected to biaxial stresses. Among all generated fabrics, three of the primary contributors to the study include: Voronoi tessellation, Cross-joints and Cross-cuts. Given stipulated differences in in-situ stresses, pore pressure distribution during injection is monitored and shear and normal displacements of joints are investigated. Some important concepts such as size of the stimulated zone and induced shear events were studied in conjunction with this data collection.

In order to calibrate numerical emulations with field data, two case studies of waste disposal were modeled. The first attempt was to find the closest geometry and subsequently match the bottom-hole pressure with the fluid pressure at the injection point. Some success in gaining a reasonable and good correspondence indicates that the studies can contribute to greater understanding of such complicated subjects and are of essential importance in qualitative and semi-quantitative evaluations.

ACKNOWLEDGMENTS

I would like to express my most sincere gratitude and appreciation to my supervisor Prof. Maurice B. Dusseault for his mentorship, guidance, encouragement and exceptional support throughout my PhD studies at the University of Waterloo. I am also appreciative to have the support of Prof. Robert Gracie as a co-supervisor for my PhD dissertation and I am grateful for all of the suggestions I received from the members of my PhD committee. These inspiring members were Prof. Peter Kaiser, Prof. Andre Unger and Prof. Giovanni Cascante. I would also like to thank Prof. Erik Eberhardt for agreeing to be the external examiner for my PhD defence.

Furthermore, I would like to recognize the support and collaborative efforts of Mr. Roman Bilak and the engineering team of Terralog Technologies Inc. for providing me with an opportunity to gain valuable industrial experience. The helpful advice of Dr. Branko Damjanac and Dr. Azadeh Riahi as mentors, from whom I have learned such valuable lessons, is also due a grateful acknowledgement and my sincere appreciation.

The support from NSERC-IPS for funding this research is also greatly appreciated in addition to the partial financial support I received from the Center of Excellence in Mining Innovation (CEMI) Thank you also to the ITASCA Consulting Group for your technical support and for allowing me research access to UDEC™.

It was also a great pleasure to work with Mike Yetisir on a number of aspects of this research and likewise, I am grateful for the invaluable assistance of Matin Parchei Esfahani.

I would like to thank my officemates, Roya Cody, Erfan Amiri Abedian, Anlui Rodrigues and Shayan Sepiani for being my school family and made this journey so much more memorable for me. Thanks to my old friends Leila Ahmadi and Mohammad Amin Jafari for always having been such a support system for me.

Finally, I am particularly grateful to my family for their unwavering encouragement and unconditional love throughout my life. This includes my cousin, Amirali Gorgan, for his continuous support and most importantly, for being the family I very much needed in Canada.

DEDICATION

This thesis is dedicated to my beloved parents, sister and brother whose love and support sustained me through.

TABLE OF CONTENTS

Author's Declaration	ii
Statement of Contributions.....	iii
Abstract.....	iv
Acknowledgments	v
Dedication	vi
Table of Contents	vii
List of Figures.....	x
List of Abbreviations	xvi
List of Symbols	xvii
Chapter 1 Introduction.....	1
1.1 Problem Definition	1
1.2 Research Objectives	4
1.3 Significance of the Study.....	5
1.4 Components and Outline of the Thesis.....	6
Chapter 2 Background	7
2.1 Basic Definitions and Concepts	7
2.2 Review of Numerical Modeling of Hydraulic Fracturing.....	13
2.3 Summary	17
Chapter 3 Numrical Modeling of Hydraulic Fracturing.....	18
Overview.....	18
3.1 Notation	18
3.2 Definition.....	19
3.3 Continuum Solid Mechanics.....	21
3.3.1 Force.....	21
3.3.2 Stress	21
3.3.3 Strain	23
3.3.4 Plane State of Strain	24
3.3.5 Equilibrium	25
3.3.6 Conservation Laws.....	26
3.3.7 Constitutive Equation (Stress-Strain Laws)	28
3.3.8 Governing Equations for Solid Linear Elastic Material.....	29
3.4 Numerical Solutions	30
3.4.1 Implicit and Explicit Algorithms.....	30
3.4.2 Finite Difference Schemes	31
3.4.3 Discretization of the Domain	32
3.4.4 Mathematical Modeling	35
3.5 Fluid Mechanics.....	37
3.6 Initial and Boundary Conditions.....	38
3.7 Discrete Element Methods	38
3.7.1 Contact Between Two Bodies.....	41
3.7.2 The Universal Distinct Element Code (UDECTM)	45
3.8 Summary	57

Chapter 4	Importance of the Study and Parametric Analyses	61
Overview		61
4.1	Naturally Fractured Rock	62
4.2	Simulations of Basic Geometries	64
4.2.1	Model Geometries	64
4.2.2	Model Initial Conditions	65
4.2.3	Basic Simulations	66
4.3	Simulations of Representative Geometries of a Naturally Fractured Rock Mass	73
4.3.1	Flow From an Injection Point in a Biaxial Stress Field in a Voronoi Tessellation Rock Fabric	73
4.3.2	Flow From an Injection Point in a Biaxial Stress Field in a Rock Mass with Oriented Joint Sets	87
4.3.3	Flow From an Injection Point in a Biaxial Stress Field in a Rock Mass with Complex Fabric	88
4.4	Summary	91
Chapter 5	Stimulated Zone Associated with Hydraulic Fracturing in Low-Permeability Naturally Fractured Rocks	94
Overview		94
5.1	Introduction	94
5.1.1	Naturally Fractured Rock	95
5.1.2	Parameters Affecting the Stimulated Zone	97
5.2	Hydraulic Fracture Simulations	97
5.3	Assessing the Stimulated Zone	100
5.4	Parametric Study	104
5.4.1	Effect of Rock Fabric	105
5.4.2	Effect of In-situ Stress	108
5.4.3	Effect of Injection Rate	112
5.5	Summary	116
Chapter 6	Numerical Investigation of Shear/Slip Events Associated with Hydraulic Fracturing	118
Overview		118
6.1	Introduction	119
6.2	Methodology	122
6.2.1	Moment Magnitude Scale, Seismic Moment	122
6.2.2	Moment Magnitude Scale, Seismic Energy	123
6.2.3	Intensity	124
6.3	Hydro-Mechanical Simulations using UDEC™	125
6.3.1	Model Options	125
6.3.2	Effects of Stress Ratio on Energy Release Magnitude in the Voronoi Tessellated Rock Fabric	127
6.3.3	Effects of Stress Ratio on Slip in Cross-Joint Rock Fabric	129
6.3.4	Effects of Fault Inclination on Slip in the Voronoi Tessellated Rock Fabric	131
6.3.5	Effects of Joint Inclination on Slip in a Cross-Joint Rock Fabric	131
6.4	Injection Energy	132
6.5	Summary	134
Chapter 7	A Discrete Element Method Approach to Model Waste Injection Operations	136
Overview		136
7.1	Introduction	136

7.2	Case Study A: Middle East Field	138
7.2.1	Model Generation – Case A	138
7.2.2	Injection Strategy – Case A.....	143
7.2.3	Joint Model Pressure Matching – Case A	144
7.2.4	Physical Understandings of The CRI Operation # 1	145
7.3	Case Study B: North Sea Field	151
7.3.1	Model Generation – Case B	151
7.3.2	Injection Strategy – Case B.....	153
7.3.3	Joint Model Pressure Matching – Case B	154
7.3.4	Interpretation of CRI Operation # 2 Results	155
7.4	Upgraded Modeling Approach – Case A.....	159
7.5	Discussion	163
7.6	Summary	165
Chapter 8	Discussion and Conclusions	168
8.1	Chapter Summaries.....	169
8.1.1	Parametric Studies.....	169
8.1.2	Stimulated Zone Associated with Hydraulic Fracturing in Low-Permeability Rocks	170
8.1.3	Numerical Investigation of Shear/Slip Events Associated with Hydraulic Fracturing	171
8.1.4	A Discrete Element Method Approach to Model Waste Injection Operations	171
8.2	Further Research.....	172
8.2.1	Three-Dimensional Modeling	172
8.2.2	Thermo-Hydro-Mechanical Coupling.....	172
8.2.3	Evaluating the Rock Stiffness (Bulk Elastic Properties).....	172
8.2.4	Joint Conductivity	173
Bibliography		174

LIST OF FIGURES

Figure 1.1. Bedding surface of the Brown Shale, Central Sumatra Basin, Indonesia (Dusseault 2015).	1
Figure 1.2. Columnar jointed basalts, hexagonal, Giant's Causeway, Ireland (Gillian Finnie 2016).	1
Figure 1.3. HF in a NFR generates stress and permeability changes (Dusseault 2011).	2
Figure 1.4. The stimulated zone from HF in a NFR (Dusseault and Jackson 2013).	3
Figure 1.5. Hydro-mechanical coupling concept (Zangeneh et al. 2015).	4
Figure 2.1. A schematic diagram of systematic and non-systematic fractures (Sorkhabi 2014).	7
Figure 2.2. A schematic diagram of a tensile fracture and a shear fracture.	7
Figure 2.3. Three modes of fracture deformation (Hudson and Harrison 1997).	8
Figure 2.4. In-situ stresses on a block of rock for a hypothetical stress state.	9
Figure 2.5. Three types of interaction between a hydraulic fracture and a natural fracture (Thiercelin and Makkhyu 2007).	10
Figure 2.6. a) Properly oriented joints will slip before opening during injection. b) Coulomb slip model.	12
Figure 2.7. Schematics of shear dilation of a joint (Rahman et al. 2002).	12
Figure 2.8. Wedging and block rotation contribute to joint conductivity (Dusseault 2015).	13
Figure 2.9. Deformation mechanisms affect conductivity enhancement during hydraulic fracturing (Dusseault 2015).	13
Figure 3.1. Undeformed (initial) and deformed (current) configurations of a body. Ω is the domain of the initial configuration; Ω' is the domain of the current configuration; μ is the boundary of the initial configuration; μ' is the boundary of the current configuration; P is a material point in the initial configuration; P' is a material point in the current configuration; X is the position vector of a particle in the initial configuration and in the alternative notation is given by.	19
Figure 3.2. Schematic of a) Displacements; b) Strains.	20
Figure 3.3. Decomposition of forces.	22
Figure 3.4. Mohr's circle representing stresses at a point (Fjaer et al. 2008).	23
Figure 3.5. Plane state of strain; a) strain components, b) stress components.	25
Figure 3.6. Geometric interpretation of finite difference approximations.	32
Figure 3.7. a) Discretized domain; b) Three-node linear-displacement triangular element.	33
Figure 3.8. Physical categories of contact in a two-dimensional framework (Riahi et al. 2010).	33
Figure 3.9. a) Three-node triangular element showing nodal displacements, nodal forces and the equivalent element body force; b) tractions.	34
Figure 3.10. Constitutive law for each contact. kn and ks are joint normal and shear stiffness. C and ϕ are joint cohesion and friction angle. (Fn, un) and (Fs, us) are components of the force-displacement law in normal and shear directions (n, s) . Fc is the total contact force and i is the time step at which calculation starts (Asgian 1989).	41

Figure 3.11. Normal and tangential forces applied on contacts.....	42
Figure 3.12. a) Favorably oriented joint; b) Mohr-Coulomb shear mechanism (Dusseault 2015).	43
Figure 3.13. Joint mechanical deformation in rock. a) Normal and shear stiffness between rocks. b) Constitutive behavior in shear and tension (Lisjak and Grasselli 2014). All springs may be non-linear.	44
Figure 3.14 Coulomb friction law for computing contact tangential force (Favier et al. 2009)...	45
Figure 3.15. Schematic of block, contact, zone and domain in UDEC TM (ITASCA Consulting Group Inc. 2010).....	46
Figure 3.16. Solution algorithm for each timestep in UDEC TM (ITASCA Consulting Group Inc. 2010).	47
Figure 3.17. Relation between hydraulic aperture and joint normal stress (ITASCA Consulting Group Inc. 2010).....	51
Figure 3.18. Concept of damping.	53
Figure 3.19. Basic joint behavior model used in UDEC TM (ITASCA Consulting Group Inc. 2010).	56
Figure 4.1. Well-developed joint sets on flagstones at St. Mary’s Chapel, Caithness, Scotland. Not counting bedding planes, two orthogonal joint sets are visible (Sorkhabi 2014).	62
Figure 4.2. Hydro-mechanical coupling: a) Fluid pressure effect; b) Mechanical effect on aperture; c) Fluid flow; d) Fluid pressure gradient (ITASCA Consulting Group Inc. 2010).	63
Figure 4.3. Simplified geometrical components of a natural fracture network a) single through- going joint; b) T-junction joints; c) cross- joints; d) stepped joints.....	65
Figure 4.4. Effects of geometry on displacement distribution under anisotropic stress (30,20 MPa), a) single joint; b) T-junction joints; c) cross-joints; d) stepped joints.	67
Figure 4.5. Effects of geometry on block rotation under anisotropic stress (30,20 MPa) and hydrostatic pressure, a) single joint; b) T-junction joints; c) cross-joints; d) stepped joints.....	68
Figure 4.6. Effects of geometry on flow direction with gradients in the y, then the x direction. a) single joint; b) T-junction joints; c) cross joints; d) stepped joints.....	69
Figure 4.7. UDEC TM model of the stepped geometry with five observation points.....	70
Figure 4.8. Effects of joint stiffness on normal displacement under anisotropic stress (30, 20 MPa) and hydrostatic pressure for the stepped fracture.....	71
Figure 4.9. Effects of joint stiffness on shear displacement under anisotropic stress (30, 20 MPa) and hydrostatic pressure for the stepped fracture.	71
Figure 4.10. Effects of joint stiffness on flow-rates under anisotropic stress (30, 20 MPa) and hydrostatic pressure for the stepped fracture.	71
Figure 4.11. Effects of stress ratio on normal displacement under anisotropic stress and hydrostatic pressure for the stepped joint.	72
Figure 4.12. Effects of stress ratio on shear displacement under anisotropic stress and hydrostatic pressure for the stepped joint.	73

Figure 4.13. Effects of stress ratio on flow-rate under anisotropic stress and hydrostatic pressure for the stepped joint.	73
Figure 4.14. UDEC TM model of a Voronoi tessellated rock fabric.....	74
Figure 4.15. Ratio of maximum unbalanced force in an anisotropic stress field (15, 30 MPa) in the Voronoi tessellated rock fabric.	75
Figure 4.16. Pore pressure propagation around an injection point in the Voronoi tessellated rock fabric during HF injection.....	76
Figure 4.17. Local stress effects on fracture propagation in a naturally fractured rock (Dusseault 2013).	76
Figure 4.18. Global orientation of fracture propagation in the Voronoi tessellated rock fabric...	77
Figure 4.19. a) Block rotation and b) displacement vectors around the pressurized injection point in the Voronoi tessellated rock fabric during HF injection.....	77
Figure 4.20. Flow direction in joints during fluid injection from the injection point in various anisotropic stress fields in the Voronoi tessellated rock fabric.....	79
Figure 4.21. Fluid pressure histories versus number of cycles in the Voronoi tessellated rock fabric.	79
Figure 4.22. a) Normal and b) shear displacements on joints around a pressurized injection point in the Voronoi tessellated rock fabric in an anisotropic stress field (30, 15 MPa).	80
Figure 4.23. Maximum value of shear and normal displacements for different stress ratios in the Voronoi tessellated rock fabric.	81
Figure 4.24. UDEC TM model of an injection point in a rock mass containing a Voronoi tessellation with a) persistent and b) non-persistent discontinuities.....	81
Figure 4.25. a) Shear and b) normal displacements on joints around a pressurized injection point in the Voronoi tessellated rock fabric with a nearby fault plane.	82
Figure 4.26. Maximum value of joint shearing and opening vs stress ratio for different Voronoi tessellated rock fabric with a nearby fault plane.....	83
Figure 4.27. a) Shear and b) normal displacements on joints around a pressurized injection point in the Voronoi tessellated rock fabric with non-persistent discontinuities.	83
Figure 4.28. Maximum value of joint shearing and opening vs stress ratio for different Voronoi tessellated rock fabric with non-persistent discontinuities.	84
Figure 4.29. Pore pressure progression around a pressurized injection point in the Voronoi tessellated rock fabric with a) persistent and b) non-persistent discontinuities.....	84
Figure 4.30. Maximum pore pressure values around a pressurized injection point in the Voronoi tessellated rock fabric with a) persistent and b) non-persistent discontinuities.....	85
Figure 4.31. Values of pore pressure for a monitoring plot close to the pressurized injection point in the Voronoi tessellated rock fabric with a) persistent and b) non-persistent discontinuities. ..	85
Figure 4.32. Values of pore pressure for a monitoring plot far from the pressurized injection point in the Voronoi tessellated rock fabric with a) persistent and b) non-persistent discontinuities.	85

Figure 4.33. Maximum value of normal displacements vs stress ratio for different Voronoi tessellated rock fabrics.....	86
Figure 4.34. Maximum value of shear displacements vs stress ratio for different Voronoi tessellated rock fabrics.....	86
Figure 4.35. Maximum value of pore pressure vs stress ratio for different Voronoi tessellated rock fabrics.....	87
Figure 4.36. Maximum values of shear and normal displacements for different oriented joint sets in an anisotropic stress field (30, 23 MPa).	87
Figure 4.37. a) Normal and b) shear displacements around a pressurized injection point in orthogonal joint sets.....	88
Figure 4.38. Shear displacement around a pressurized injection point for different orientations of joint sets.	88
Figure 4.39. UDEC TM models for different geometries representing various levels of a) high, b) medium and c) low joint density.....	89
Figure 4.40. Pore pressure distribution in a fully connected geometry with various levels of a) high, b) medium and c) low joint density.	89
Figure 4.41. Joint shear displacement around a pressurized injection point in a fully connected geometry with various levels of a) high, b) medium and c) low joint density.	90
Figure 4.42. Joint normal displacement around a pressurized injection point in a fully connected geometry with various levels of a) high, b) medium and c) low joint density.	90
Figure 4.43. Maximum values of joint normal and shear displacements vs number of contacts in joint networks with different joint density.....	91
Figure 5.1. Representative geometries of natural fracture (joint) networks: a) Voronoi tessellation, b) Cross-joints; c) Cross-cuts.....	99
Figure 5.2. Gridpoint force vectors for different geometries: a) Voronoi tessellation, b) Cross-joints; c) Cross-cuts.....	99
Figure 5.3. Schematic of the stimulated zone outlining the difference between an idealized circular shape and the actual polygonal shape. (Fomin et al. 2006).....	100
Figure 5.4. Polygonal stimulated zone based on normal displacement for various model simulations and flow rates and a stress ratio of 2 with Voronoi tessellated rock fabric. SB = Small Block size, LB = Large Block size, SM = Small Mesh size.	102
Figure 5.5. Polygonal stimulated zone based on shear displacement for various model simulations and flow rates and a stress ratio of 2. SB = Small Block size, LB = Large Block size, SM = Small Mesh size.	103
Figure 5.6. Comparison of the different stimulated zone geometries for the case of the Voronoi tessellated rock fabric. The stimulated zone based on an ellipse is approximately 44% larger than that based on the convex polygon hull.....	104
Figure 5.7. Opening under different stress states for: a) Voronoi tessellation, b) Cross-joints; c) Cross-cuts.....	106

Figure 5.8. Shearing under different stress states: a) Voronoi tessellation, b) Cross-joints; c) Cross-cuts.....	107
Figure 5.9. Pore pressure under different stress states for the representative geometries of natural fracture networks: a) Voronoi tessellation, b) Cross-joints; c) Cross-cuts.	108
Figure 5.10. Flow direction in joints during fluid injection from the borehole in various anisotropic stress fields in the Voronoi tessellated rock fabric.....	109
Figure 5.11. Fluid pressure profiles along the horizontal axis under different stress ratios and flow rate #3: a) Voronoi tessellation, b) Cross-joints; c) Cross-cuts.....	110
Figure 5.12. Associated stimulated zones with a determined threshold of 2.5mm for the Voronoi tessellated rock fabric, injection rate #1, and various stress ratios. Stimulated zones calculated based on both ellipse and convex hull geometries.....	112
Figure 5.13. Effects of injection rate on normal displacement for the Voronoi tessellated rock fabric and various stress ratios: a) rate#1, b) rate#2 and c) rate#3.	113
Figure 5.14. Effects of injection rate on shear displacement for the Voronoi tessellated rock fabric and various stress ratios: a) rate#1, b) rate#2 and c) rate#3.	114
Figure 5.15. Effects of injection rates on shear displacement for the Voronoi tessellated rock fabric and various stress ratios: a) rate#1 (5 L/s), b) rate#2 (10 L/s) and c) rate#3 (15 L/s).	114
Figure 5.16. Effects of injection rates on shear displacement for the Cross-joints rock fabric and various stress ratios: a) rate#1 (5 L/s), b) rate#3(15 L/s).....	115
Figure 5.17. Effects of injection rate on normal displacement for the Cross-joints rock fabric and various stress ratios: a) rate#1 (5 L/s), b) rate#3 (15 L/s).....	116
Figure 6.1. Frequency vs magnitude for 198 published examples of induced seismicity (Davies et al, 2013).	119
Figure 6.2. Comparison of different magnitude scales (Kanamori 1983).	122
Figure 6.3. UDEC™ model in a rock mass containing a) Voronoi tessellation and b) cross-joint sets.....	126
Figure 6.4. Magnitude of events vs stress ratio in the Voronoi tessellated rock fabric.	127
Figure 6.5. Values of shear and normal displacements vs stress ratio in the Voronoi tessellated rock fabric.	128
Figure 6.6. Relations among earthquake scaling parameters (Maxwell 2013).....	129
Figure 6.7. Magnitude of a) M_w and b) M_e vs stress ratio for different rock fabrics.	130
Figure 6.8. Average a) normal and b) shear displacements vs stress ratio for different rock fabrics.....	130
Figure 6.9. Magnitude of shear events vs fault inclinations in the Voronoi tessellated rock fabric.	131
Figure 6.10. Magnitude of shear events vs angle of cross-joint sets to the orientation of the σ_{MAX}	132
Figure 6.11. The amount of energy associated with fracturing and shear events in the Voronoi tessellated rock fabric.	133

Figure 6.12. The amount of energy associated with a) fracturing and b) slip events in the Voronoi tessellated and cross-joint rock fabrics.	134
Figure 7.1. CRI operation #1; a) well schematic and b) geology information.	139
Figure 7.2. Geometry of a hydraulic fracture.	140
Figure 7.3. Generated geometries, case A.	142
Figure 7.4. Injection actual data of the first case study, case A.....	143
Figure 7.5. Matching numerical and real pressure curves, case A.	145
Figure 7.6. Effective zones around the injection point, case A.	145
Figure 7.7. Cumulative a) normal and b) shear displacements vs edge of the effective zones for three cycles of injection and Shut-in, case A.....	147
Figure 7.8. Right and left lateral shear displacements during a) injection and b) shut-in, case A.	148
Figure 7.9. Cumulative a) closure and b) opening vs edge of effective zones for three cycles of injection and shut-in, case A.....	149
Figure 7.10. X-displacement contour during a) injection and b) shut-in, case A.	150
Figure 7.11. Pore pressure profile along x-axis during a) injection and b) shut-in, case A.....	151
Figure 7.12. CRI operation #2; a) well schematic and b) geology information, case B.....	152
Figure 7.13. Geometries generated by UDEC TM , case B.....	153
Figure 7.14. Injection actual data of the second case study, case B.	154
Figure 7.15. Matching numerical and real pressure curves, case B.....	154
Figure 7.16. Fluid pressure trends over one cycle operation for five monitoring points, case B.	155
Figure 7.17. Displacement vectors after one cycle of injection.....	156
Figure 7.18. Normal displacement for five monitoring points during a) injection and b) shut-in, case B.	157
Figure 7.19. Joints undergo shear displacement during a) injection and b) shut-in, case B.....	158
Figure 7.20. Effective zones around the injection point, case B.....	158
Figure 7.21. Cumulative a) closure and b) opening vs edge of effective zones for three cycles of injection and shut-in, case B.	159
Figure 7.22. Schematic of the model and injection points.....	159
Figure 7.23. Joints undergo opening during a) injection and b) shut-in, case A.	161
Figure 7.24. Joints undergo shearing during a) injection and b) shut-in, case A.....	162
Figure 7.25. Pore pressure distribution around the injection point, case A.	162
Figure 7.26. Matching numerical and real pressure curves using the upgraded approach, case A.	163
Figure 7.27. PAN pressure match during injection and shut-in for Middle East field.	165
Figure 7.28. PAN pressure match during injection and shut-in for North Sea field.....	165

LIST OF ABBREVIATIONS

3DEC TM	3D – Discrete Element Code
DEM	Discrete/Distinct Element Method
DFN	Discrete Fracture Network
FEM	Finite Element Method
HF	Hydraulic Fracture/Fracturing
NF	Natural Fracture
NFR	Naturally Fractured Rock
UDEC TM	Universal Discrete Element Code
XFEM	Extended Finite Element Method

LIST OF SYMBOLS

a	Aperture
a_0	Joint aperture at zero normal stress
a_i or \mathbf{a}	Acceleration components, acceleration vector
b_i or \mathbf{b}	Body force
C	Cohesion
E	Young's modulus
$\mathbf{e}_1, \mathbf{e}_2, \mathbf{e}_3$ or e_i	Unit vectors along coordinate axes
f_i or \mathbf{f}	Surface force
F_n	Normal force
F_s	Shear force
G	Shear modulus
K	Bulk modulus
k_c	Contact conductivity factor
k_j	Joint conductivity factor
k_s	Joint shear stiffness
k_n	Joint normal stiffness
k_w	Fluid bulk modulus
m	Mass
\mathbf{n}	Unit normal in the current configuration
p	Pressure
q	Flow rate
t	Time
t_i or \mathbf{t}	Traction vector

\mathbf{u}_n	Normal displacement
\mathbf{u}_s	Shear displacement
u_i or \mathbf{u}	Displacement components, or displacement vector
v_i or \mathbf{v}	Velocity vector
x_1, x_2, x_3 or x_i or \mathbf{x}	Cartesian coordinates
X_i or \mathbf{X}	Material coordinates
ρ	Density
μ	Friction coefficient
ϕ	Friction angle
ν	Poisson's ratio
ψ	Dilation angle
Ω	Domain
σ_n	Normal stress
σ_s	Shears stress
σ_i	Principal stress
σ_{ij}	Cauchy stress tensor's components
ε_{ij} or $\boldsymbol{\varepsilon}$	Infinitesimal strain tensor
δ_{ij}	Kronecker delta
$\nabla\phi = \mathbf{grad}\ \phi = \phi_{,j}$	Gradient of scalar ϕ
$\nabla\mathbf{v} = \partial_j\partial_i\mathbf{v} = v_{i,j}$	Gradient of vector \mathbf{v}
$\nabla\cdot\mathbf{v} = \partial_j\partial_j\mathbf{v} = v_{j,j}$	Divergence of vector \mathbf{v}

CHAPTER 1 INTRODUCTION

1.1 PROBLEM DEFINITION

A **Naturally Fractured Rock (NFR)** is a rock mass containing natural fractures. A joint is a type of natural fracture formed predominantly by Mode I fracture (Nelson 2001). In this study, the term joint is defined as a plane of discontinuity and it is interchangeably used for “natural fracture”. NFR is also called a jointed rock mass in this study. Figure 1.1 shows an example of NFRs with two orthogonal sets of natural fractures. Figure 1.2 shows a polygonal configuration of natural fractures, which is called a Voronoi tessellation in this study. Natural fractures show substantial variations due to their origin, geometry and rock properties. The configuration of natural fractures is referred to as geometry or fabric in this work. Different authors use the term fabric in slightly different ways. A broad definition of the term is adopted in this research, based on the definition introduced by (Twiss and Moores 1992): “The fabric of the rock is defined by the geometric organizations of the structures in the rock.”



Figure 1.1. Bedding surface of the Brown Shale, Central Sumatra Basin, Indonesia (Dusseault 2015).



Figure 1.2. Columnar jointed basalts, hexagonal, Giant's Causeway, Ireland (Gillian Finnie 2016).

Large volumes of oil and gas resources are located in low-permeability rock masses which are naturally fractured in many cases. A worldwide increase in energy consumption has led to attempts to produce energy through unconventional methods and has therefore resulted in the introduction of new technologies (Gil et al. 2011). In this way, hydraulic fracturing (HF) has been introduced. This covers a wide variety of applications: productivity enhancement (Rahman et al. 2002), gas drainage (Wu et al. 2013), heat extraction in geothermal systems (Legarth et al. 2005), slurried waste injection (Veil and Dusseault 2003) and rock mass property and stress management (Economides and Nolte 2013). Hydraulic fracturing leads to changes in the volume of the natural fractures and in turn changes in stresses and fluid pressures (Figure 1.3).

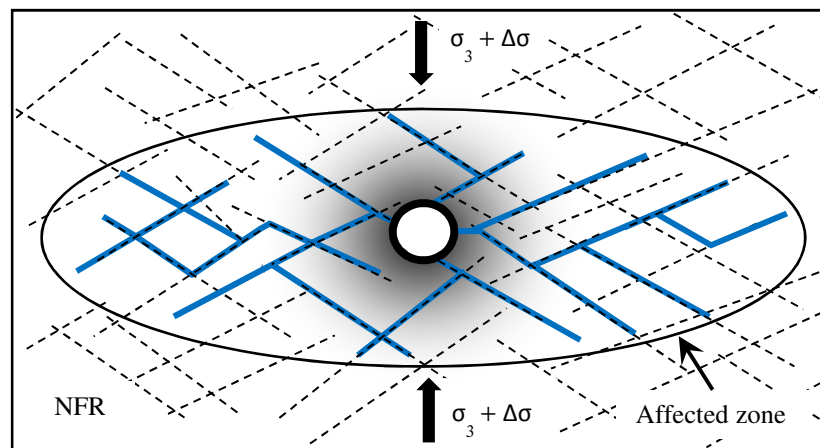


Figure 1.3. HF in a NFR generates stress and permeability changes (Dusseault 2011).

HF is usually performed to create new fractures or open existing natural fractures (joints) by tensile or opening mode deformation processes. The term fracture is used for hydraulically driven fractures in this study; and the term pre-existing fracture describes a natural fracture. Natural fractures have a potential to become hydraulic fractures if they are opened under hydraulic pressure. Pre-existing fractures are also referred to as joints, as mentioned above.

Hydraulic fracturing in naturally fractured rock (NFR) masses has been performed with different intentions including jointed igneous rock fracturing at depth to help the extraction of geothermal energy; deep slurried solid waste injection; and, development of oil and gas trapped in stiff jointed rock masses (Curtis 2002; Dusseault 2015). Historically, the implications of natural fractures on hydraulic fracture stimulation of reservoirs have been mostly ignored by the petroleum industry, but in recent years, with the advent of shale gas and shale oil development, the industry knowledge of naturally fractured reservoirs has increased, and there has been a growing interest in better understanding the effects of natural fractures in order to use them to the advantage of a hydraulic fracture operation (Nelson 2001).

An increase in the flow capacity or productivity enhancement is called “**stimulation**” in the oil and gas industry and leads to the concept of “**stimulated zone**” (Dusseault 2015). The size of the

stimulated zone around the injection point shows the lateral distance that the fluid flows. The deformation pattern also follows the fluid flow patterns. Thus, the patterns of induced flow and deformation are valuable pieces of information for well design or for assessing the degree of flow interconnectivity of multiple wells. Figure 1.4 shows a stimulated zone consisting of a pressurized zone in the center of a model in which opening is the major deformation mechanism. This central area is surrounded by a region in which small-scale shear and dilation occurs and causes local (scale no larger than a few meters) stick/slip events.

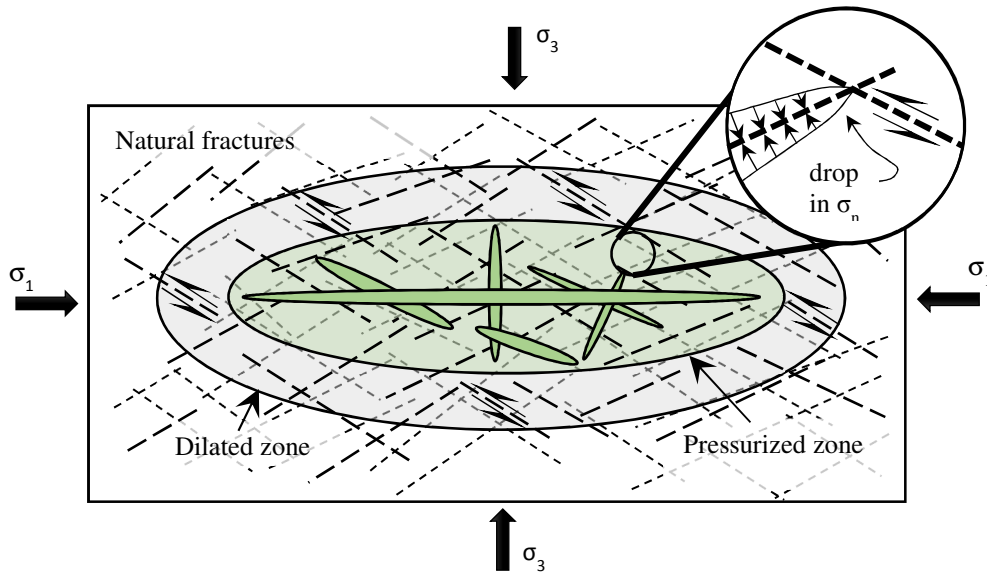


Figure 1.4. The stimulated zone from HF in a NFR (Dusseault and Jackson 2013).

It is known that hydraulic fracturing may induce seismicity (Warpinski 2014). Better modeling of hydraulically induced seismicity can help predictions about the magnitude and occurrence of seismic events. This should aid in design and management of stimulation projects (Rutqvist et al. 2013a). Consequentially, another focus of this research is about the energy release and potential shear events associated with hydraulic fracturing.

Calibration of numerical models to field data should provide insight into the changes taking place in a rock mass. This will allow better project management. In particular, when an anomalous event takes place during or after an injection, numerical modeling may help provide an explanation for it. Numerical modelling could potentially aid in the design of subsequent phases.

In the context of these applications and potential benefits to design, this thesis presents an attempt to answer some interesting and relevant geomechanical questions:

- How closely can a two-dimensional discrete element scheme represent the real behavior of hydraulically induced fractures in jointed rocks?

- How do different rock mass fabrics affect the hydraulic fracture treatment?
- Can shear stresses be relieved in a deviatoric stress field through the process of injection?

Hydraulic fracturing in naturally fractured rocks is a fully coupled **hydro-mechanical**¹ process. This means that the mechanical behavior of natural and hydraulic fractures cannot be evaluated separately from fluid flow effects (Figure 1.5) (Nagel 2013).

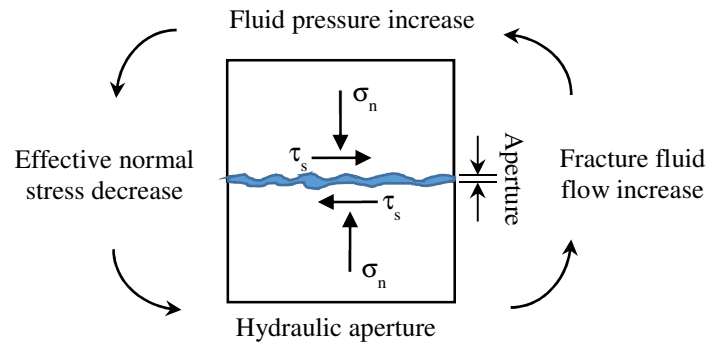


Figure 1.5. Hydro-mechanical coupling concept (Zangeneh et al. 2015).

In order to answer these questions, coupled hydro-mechanical simulations are performed with the Universal Distinct Element Code (UDECTM), a two-dimensional Discrete Element Method (DEM) numerical code (ITASCA Consulting Group Inc. 2010). The purpose of DEM is to treat a naturally fractured rock in a more realistic manner than most continuum models (Jing and Stephansson 2007).

1.2 RESEARCH OBJECTIVES

This project aims to enhance the understanding of the process of hydraulic fracturing in low-permeability naturally fractured competent rocks, and in particular to identify effects of different fabric patterns on re-initiation (opening and shearing) of pre-existing fractures and the development of induced fracture complexity. Particular emphasis is placed on the relationship between the fluid flow and mechanical deformation due to different magnitudes and directions of earth stresses as well as the variations in fracture network geometry. The objectives of this thesis as well as the potential value of the results are defined as follows:

- To evaluate the effects of rock mass fabric on fluid flow and deformation of two-dimensional jointed rock mass models using a discontinuum framework. An understanding of the effects of fabric may aid in deciding which HF strategy leads to better results.
- To evaluate the size of the stimulated zone associated with hydraulic fracturing. This will

¹ More correctly, it is a thermo-hydro-mechanical-chemical process, which is more complicated to analyze.

help set the optimum well spacing, help assess the possible need for an additional upper row of wells in a thick reservoir, help evaluate the best spacing of hydraulic fracture sites along the wellbore, and help decide on the optimum size and rate of the HF treatment and the depth within the reservoir in which the wells be drilled.

- To evaluate energy release from deviatorically stressed rock masses, considering issues of well design optimization and productivity enhancement. This may provide some insight into the magnitude and distribution of induced seismicity during HF and potentially help to develop strategies to manage the seismicity.
- To investigate how in-situ stresses affect the behavior of re-initiated natural fractures. This can be used to develop a stress management program to reduce risks and planning more effective hydraulic fracturing processes, especially in terms of HF interaction with pre-existing faults.
- To calibrate numerical results with real data. Matching numerical results with field data may allow the empirical calibration of a DEM model to a particular set of injection conditions.

1.3 SIGNIFICANCE OF THE STUDY

Hydraulic fracturing may lead to practical stress management possibilities by creating opportunities to induce and control stress redistribution, or by protecting locations where high stresses pose a threat to operations. These possibilities have applications in petroleum engineering as well as mining. Understanding NFRs behavior using a modeling approach can help to interpret data and optimize processes in the field, even if the simulations remain semi-quantitative in nature. A deeper understanding of NFRs behavior should lead to better predictions of rock mass response to hydraulic fracturing treatment and induced fracture behavior.

The interaction of hydraulic fractures with natural fractures remains poorly understood, which can hinder attempts to optimize hydraulic fracture treatments in different rock mass conditions. Natural fractures have the potential to either benefit or negatively affect hydraulic fracture stimulation efforts. For example, too many open joints can lead to severe limits in fracture propagation, as might be the case in intensely fractured carbonates (Nicol 2013). On the other hand, an array of natural fractures that can be opened somewhat by the hydraulic fracturing process will almost certainly improve the stimulation results (Johri and Zoback 2013). As such, there exists a need for further understanding of hydraulically induced fracture propagation in naturally fractured media in order to use the existence of natural fractures in an advantageous manner to achieve the goals of the hydraulic fracture operation.

It is necessary to generate a geometry that is representative of the jointed rock mass for analysis. Difficulties arise in quantifying and then mathematically representing a complex natural fracture

system. Representing and determining the complex mechanical deformation mechanisms that are greatly influenced by the interaction between individual fractures is also difficult.

1.4 COMPONENTS AND OUTLINE OF THE THESIS

This dissertation is prepared as a manuscript based thesis and it is organized as follows:

- After the general introduction and the description of objectives for this research, chapter 2 begins with basic definitions and concepts that are used in this study.
- Chapter 3 introduces basic definitions in continuum solid and fluid mechanics to mathematically formulate engineering problems and solve such problems using numerical methods. The use of two-dimensional Distinct Element Methods is explained in this chapter and is suggested as an appropriate approach to perform analysis according to the defined objectives.
- Chapter 4 is focused on studying the effects of fabric on deformability and permeability of naturally fractured hard rocks under different stress states. To this end, this chapter is focused on the explanation of basic definitions and preliminary simulations demonstrating the importance of this study.
- Chapter 5 describes the effects of fabric patterns and stress ratio on the stimulated zone. The size of the opened area may be quite different from the size of the sheared area under different stress ratios because the numbers of joints that undergo shear displacement and the magnitude of such displacements change with stress and stress ratio.
- Chapter 6 introduces the concepts of seismic moment, seismic energy and moment magnitude to measure the size of shear events associated with hydraulic fracturing in a naturally fractured rock mass. Comparing the energy released by fracturing or seismic events indicates their contribution to the total amount of released energy.
- Chapter 7 describes part of a feasibility study to numerically model hydraulic fracture injection associated with granular waste disposal processes as an attempt to achieve a better empirical understanding of this procedure. Two case studies with different locations, geologies and injection strategies are studied. This chapter outlines the understandings, challenges and lessons learned from numerical modeling of slurried solid waste disposal and provides suggestions for future studies.
- Chapter 8 gathers all conclusions and understandings developed in the current study.

CHAPTER 2 BACKGROUND

2.1 BASIC DEFINITIONS AND CONCEPTS

The term **fracture** is a collective and general name for any type of discontinuity in rocks. Fractures are planes of weakness where shear and tensile strength of discontinuities are substantially lower than in the adjacent rock mass (Singhal and Gupta 2010). Fractures are categorized into systematic and non-systematic fracture systems: systematic fractures are planar with approximately regularly spaced distributions; in contrast, non-systematic fractures are more likely to be relatively curved with irregular distributions (Figure 2.1).

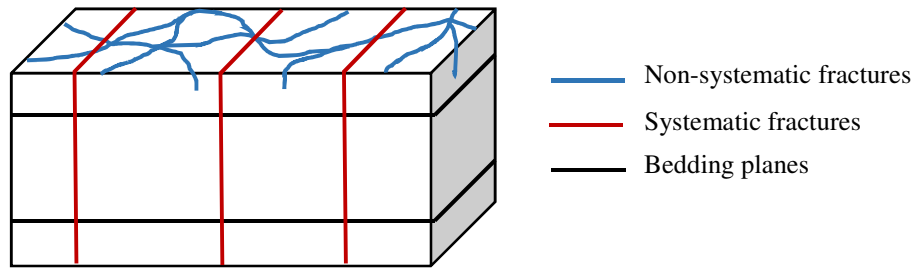


Figure 2.1. A schematic diagram of systematic and non-systematic fractures (Sorkhabi 2014).

Systematic fractures can be divided into three categories: **shear fractures**, **tensile fractures** and hybrid fractures (Singhal and Gupta 2010). Tensile fractures occur when two fracture surfaces are pulled apart under tensile stress. Alternatively, shear fractures occur when the surfaces of a fracture slide past each other (Figure 2.2).

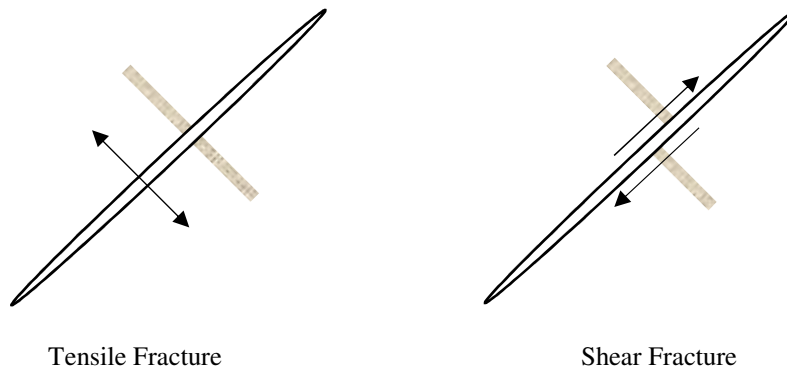


Figure 2.2. A schematic diagram of a tensile fracture and a shear fracture.

To be more exact, three modes of deformation including opening, sliding, and tearing modes, can be recognized near a fracture front. These are responsible for fracture propagation, direction and segmentation, respectively (Figure 2.3). Mode I or opening mode fracture occurs when the displacements of the fracture surface are perpendicular to the fracture plane and therefore the pressure in the fracture must exceed the normal stress for the fracture to open. In Mode II fracture, the displacements of the fracture surface are in the plane of the fracture and

perpendicular to the fracture front. This is also called the in-plane shear mode. The pressure in the fracture must reduce the frictional resistance enough so that shear slip can take place. In Mode III fracture, the shear displacements of the fracture surfaces are parallel to the fracture front, which is also called the out-of-plane mode. This is also governed by a slip criterion, usually taken to be the same as for Mode II fracture. There also exists mixed-mode fractures, which commonly have out-of-plane propagation components (Wu et al. 2009).

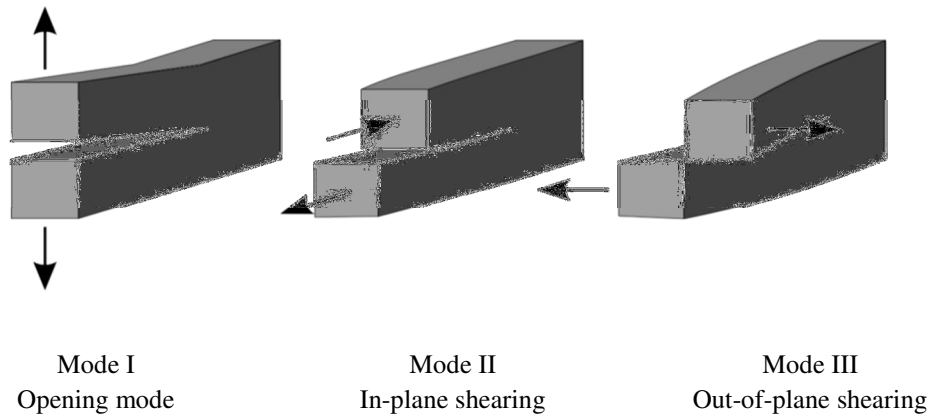


Figure 2.3. Three modes of fracture deformation (Hudson and Harrison 1997).

Fractures are perceived as essentially important in rock engineering from scientific, technological and economic perspectives. Rock fractures are important features to study in various fields of science and engineering because they significantly control the behavior of rock masses. For example, in petroleum engineering, fractures represent pathways along which fluids - water, oil and gas - can flow through and therefore affect deformation and permeability of the rock mass. The literature on fractures is extensive, although much remains to be understood.

In petroleum engineering, it is important to distinguished between **natural fractures** (naturally occurring) and **hydraulic fractures** (induced by hydraulic fracturing). Natural fractures are discontinuities with low cohesion and tensile strength values. Natural fractures may be format a microscale to a macroscale and are found in all types of rocks (igneous, sedimentary and metamorphic). **Bedding planes** and **joints** are the most noticeable natural rock fractures. Bedding planes are surfaces that separate layers of rock. The term joint was initially introduced by miners who thought that rocks are “joined” along bedding planes like building bricks (Sorkhabi 2014).

Joints may undergo normal and shear displacement. Although normal and shear displacements usually occur together, they are basically different features of mechanical deformation. Normal displacement can affect a joint in both its opening and closure mechanisms. Shear displacement varies from submillimetric to centimeters in scale, while faults may have larger magnitudes of displacement (Sorkhabi 2014). Faults are a type of natural fracture that is predominantly formed by Mode II and/or Mode III (Twiss and Moores 1992).

A **Naturally Fractured Rock (NFR)** is a rock mass containing natural fractures or joints. Naturally fractured rock masses are generated through tectonic deformations of igneous or sedimentary rock, or physical diagenesis of sedimentary rocks. Natural fractures or joints are macroscopic planar discontinuities in a rock that are capable of having either positive or negative effects on hydraulic fracturing operations (Nelson 2001).

Forces apply on a deeply buried rock from all sides. These are field stresses or in-situ stresses¹. There are three types of stresses: compression (σ), tension (σ) and shear stress (τ). Compression is considered positive in rock mechanics while tension is signed negative.

A state of stress at a point in a solid body (rock) can be expressed by the orientations and the magnitudes of the principal stresses. The principal stresses are related to three orthogonal planes related to x-, y- and z-axes (Cartesian coordinate system or xyz-space) and therefore are perpendicular to each other. The principal stresses are always compressive in the earth and are defined such that $\sigma_1 \geq \sigma_2 \geq \sigma_3$. As mentioned before, joints are extensional fractures and they need tensile stress to form, which seems contrary to the fact that principal stresses are generally all compressive. The tensile stresses that existed at the time of formation of the fractures likely have resulted from high pressures in the fluids in rock flaws causing tension and creating joints. In-situ stresses on a block of rock for a hypothetical stress state are shown in Figure 2.4.

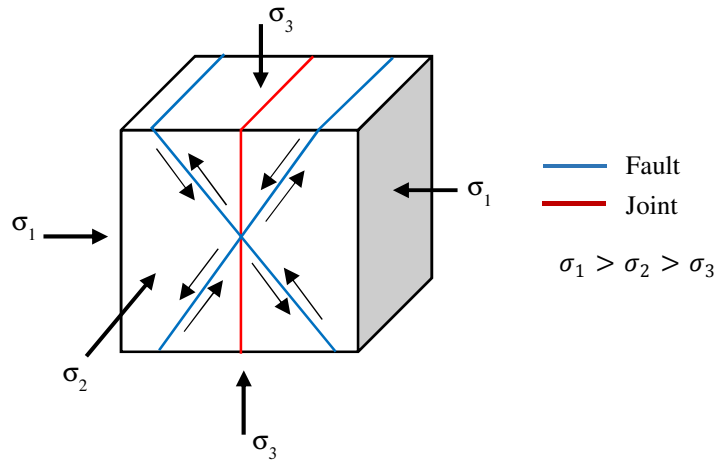


Figure 2.4. In-situ stresses on a block of rock for a hypothetical stress state.

When a hydraulic fracture induced by high fluid pressure intersects a natural fracture, it may initially arrest, but with continued pumping, it either crosses or opens it. As shown in Figure 2.5, the hydraulic fracture may cross the natural fracture (Figure 2.5-c) or be captured by it (Figure 2.5-b). It may directly leave the natural fracture without opening it (Figure 2.5-e), or it may branch into the natural fracture before leaving it (Figure 2.5-f). Additionally, the hydraulic

¹ Stress is a measure of the force applied over unit area of a plane.

fracture may leave the natural fracture with an offset in the same or in a different orientation (Figure 2.5-g) (Thiercelin and Makkhyu 2007).

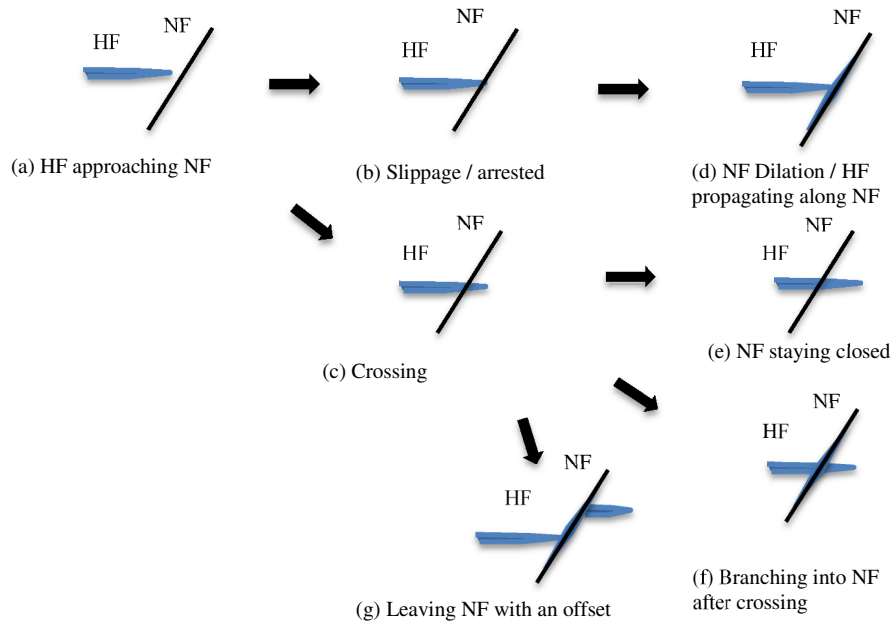


Figure 2.5. Three types of interaction between a hydraulic fracture and a natural fracture (Thiercelin and Makkhyu 2007).

According to the research of Blanton (Blanton 1982) and Warpinski and Teufel (Warpinski and Teufel 1987), pressures, stress gradient and the angle of penetration significantly control local fracture behavior, whether during the formation of natural fractures or during active hydraulic fracturing. High stress gradients and high angles of approach lead to the crossing of the natural fracture pattern, whereas intermediate to low stress gradients and angles of approach can either result in an arrest or in offset fracture patterns. It is worth mentioning that their results were obtained from analysis of the interaction of a single wing of a hydraulic fracture with a single natural fracture (Zhou et al. 2010), but their observations seem valid for natural fracture growth as well. In a complex natural fracture system containing bedding planes, several joint sets, and a strongly deviatoric stress field, prediction of induced fracture propagation behavior is both conceptually and mathematically difficult.

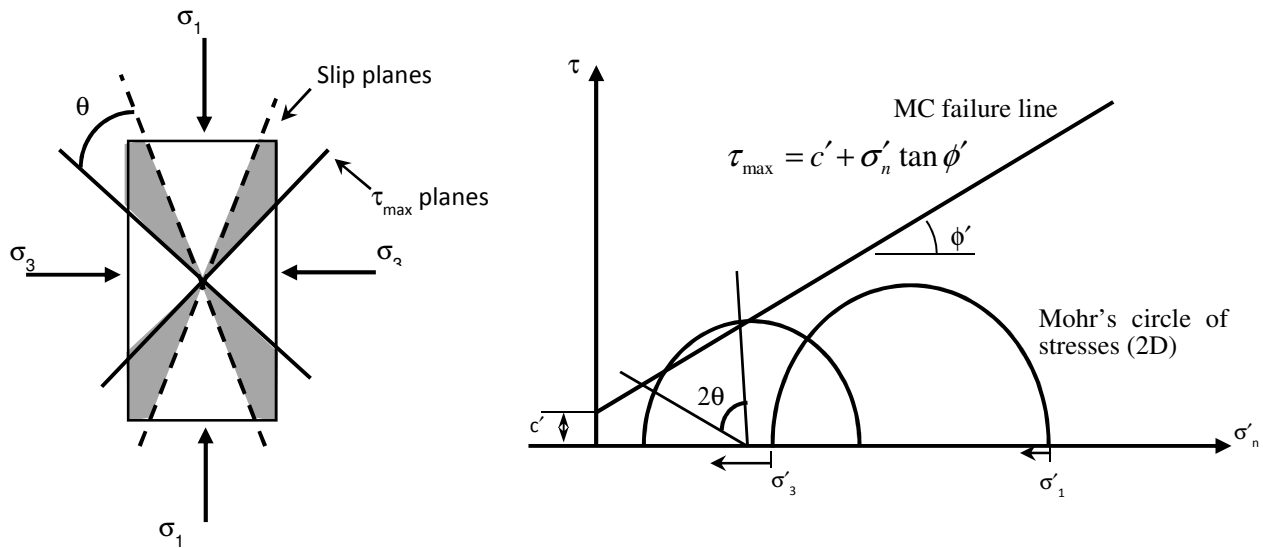
Zangeneh et al. (2015) used a discrete element method (DEM) to investigate the effects of natural fractures on hydraulic fractures. A Voronoi tessellated rock fabric was generated for her study to represent a naturally fractured shale gas reservoir. The effect of the angle at which a natural fracture intersects a hydraulic fracture was studied. According to her study, at low differential stresses and angle of approach, hydraulic fractures will leave natural fractures with some offset; under higher differential stresses, hydraulic fractures tend to cross natural fractures (Zangeneh et al. 2015).

Warpinski (Warpinski 1991) indicated that conventional HF is relatively inefficient for regions with high deviatoric stresses and natural fractures and recommended investigation of other stimulation techniques. It was found that the presence of natural fractures in an inappropriate direction of fracture propagation causes fracture tortuosity which ultimately may cause the treatment to fail in its goals. Although adjusting well trajectory and perforation direction can minimize the failure probability, the random nature of NFRs is a natural peril that stands as a challenge to the treatment efficiency (Hossain et al. 2000).

An alternative technology is presented by Hossain et al. (2002) for hydraulic stimulation, which is known as self-propping. Recently this has been called “shear dilation” treatment. The concept of shear dilation of discontinuities was first introduced in the 1970s and this has led to a great deal of research concerning the hydraulic behaviour of natural fractures over the years (Rahman et al. 2002). This strategy relies upon the reopening of pre-existing natural fractures instead of creating new fractures (East et al. 2011). The mechanism of shear dilation is based on natural mismatches and the creation of asperities resulted from shear displacement (Hossain et al. 2002).

Joint slip and dilation is a major deformation mechanism in NFRs. Injecting pressurized fluid in NFRs may first lead to shearing along pre-existing fractures or bedding planes, even at a pressure that is below the HF breakdown and propagation pressure. This may take place because as high pressure fluid flows into pre-existing fractures during injection, it increases the pore pressure and decreases the effective normal stress (Jeffrey et al. 2010a) (Figure 2.6a).

Shearing of pre-existing fractures before tensile opening (Mode I) is far more likely if there is a large difference between the minimum and maximum principal stresses in the ground (the deviatoric stresses), such that the rock mass is relatively close to a critical stress state for shear slip along preferentially oriented surfaces (Dusseault 2015). This can be explained by the Coulomb-slip model (Figure 2.6b).



(a)

(b)

Figure 2.6. a) Properly oriented joints will slip before opening during injection. b) Coulomb slip model.

When the slip criterion is satisfied for the joint, a small shear displacement occurs to relieve the shear stresses. It is believed that part of the dilation of natural fractures remains after injection because the joint surface is rough at the small scale (Dusseault 2015). This residual displacement creates remnant flow channels and changes in the bulk permeability of the rock mass (Min et al. 2004). Shearing (Mode II) of a joint causes stick/slip events in the stiff rock mass (Mcgarr 2002). Joint dilation can also lead to self-propping because of joint surface roughness (Rutledge and Phillips 2001). Figure 2.7 shows the joint dilation mechanism.

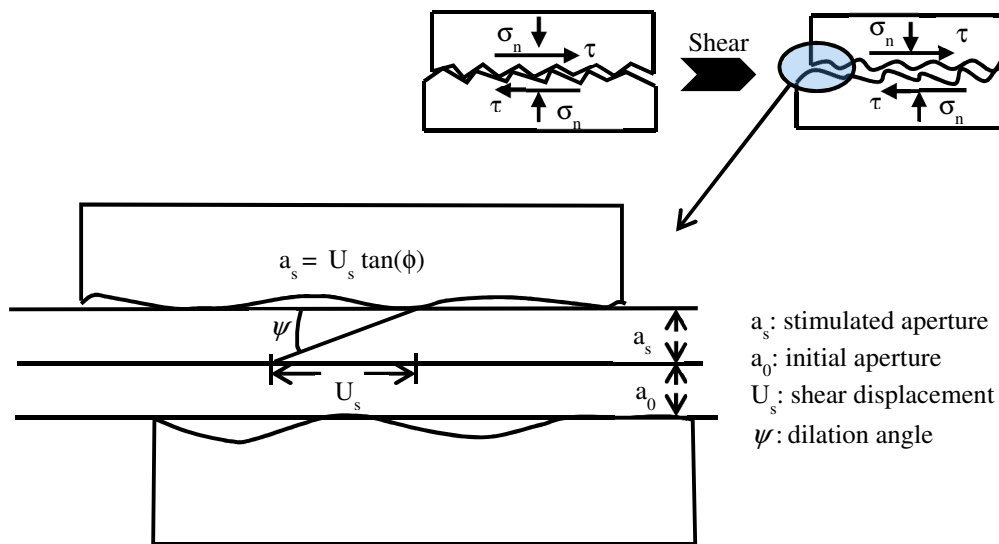


Figure 2.7. Schematics of shear dilation of a joint (Rahman et al. 2002).

Hydraulic fractures tend to propagate perpendicular to the minimum principle stress – σ_3 ; this is the path of least resistance so the fracture pressure required to open the fracture is the least in that direction. However, in the presence of natural fractures, the path of least resistance is often the natural fractures which are inevitably not in the same direction as the preference of the hydraulic fracture. Somewhat higher pressures are necessary to open a Mode I fracture in a direction that is not normal to σ_3 . The higher pressures may also cause other joints to open and shear so that the overall stimulated fracture network becomes more widespread and complex.

In a NFR with strong joints, wedging also contributes to joint opening because of the rigidity of the blocks, and self-propping can occur, leaving residual aperture, as when the pressure is relieved, the blocks do not fit perfectly back together because of surface roughness or the introduction of a granular proppant. Wedging involves block rotation which more easily opens surrounding joints as shown in

Figure 2.8. Block rotation redistributes both shear and normal stresses at different locations along block interfaces (Dusseault 2015).

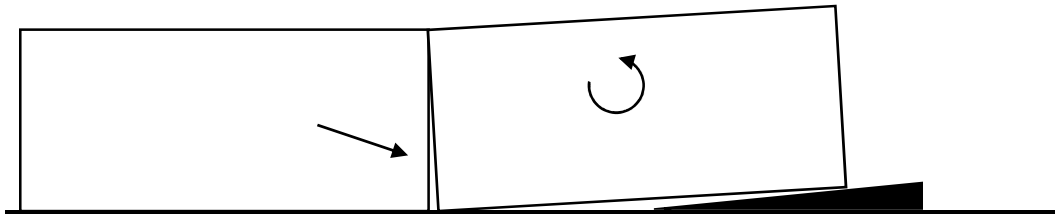


Figure 2.8. Wedging and block rotation contribute to joint conductivity (Dusseault 2015).

All mechanisms (Mode I and II, shear dilation, block rotation and wedging) are involved in hydraulic fracturing and contribute to mechanical deformation of joints, thus resulting in changes in joint conductivity, as shown in Figure 2.9.

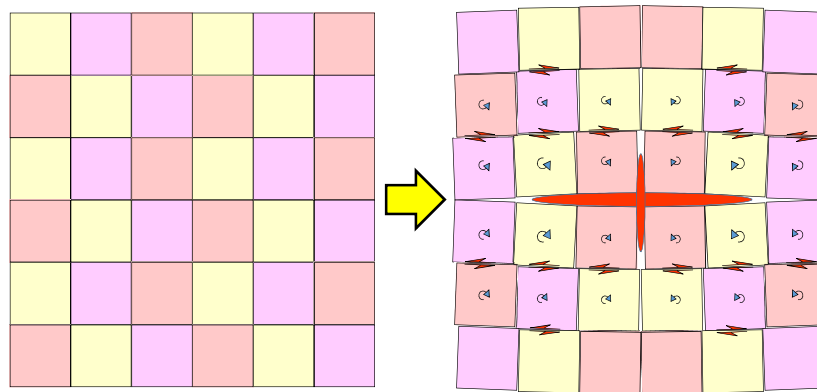


Figure 2.9. Deformation mechanisms affect conductivity enhancement during hydraulic fracturing (Dusseault 2015).

2.2 REVIEW OF NUMERICAL MODELING OF HYDRAULIC FRACTURING

Modeling of hydraulic fractures started with semi-analytical calculations that assume a planar, vertically constrained bi-wing fracture propagating symmetrically away from the injection point (Khristianovic and Zheltov 1955)(Geertsma and De Klerk 1969)(Perkins and Kern 1961)(Nordgren 1972). More recently, interaction of hydraulic fractures with natural fractures has been studied theoretically (Potluri et al. 2005), experimentally (Zhou and Xue 2013) and analytically (Rahman et al. 2000). Yet, most of these attempts for the most part did not consider the mechanical interactions of hydraulic fractures with natural fractures; in other words, it was assumed that hydraulic fractures have no effect on in-situ stresses along the natural fractures (Sesetty and Ghassemi 2012), and merely have an effect of increasing the leak-off.

Over time, it has been concluded that conventional modeling with inappropriate physical

assumptions cannot reliably represent fluid-driven fracture behavior in a complex natural fracture network. Thus, the subject of appropriate numerical modeling has been raised and has led to many attempts using finite element methods (Vandamme et al. 1988) or discrete element simulations (Vandamme et al. 1988). While conventional modeling methodologies are appropriate to find a solution for propagation of a simple bi-wing symmetrical fracture geometry in a homogeneous continuum (Perkins and Kern 1961)(Geertsma and De Klerk 1969), more sophisticated numerical modeling must be developed to simulate behavior of hydraulic fractures in more complicated natural fracture networks (Jeffrey et al. 2010b)(Adachi et al. 2007).

Numerous mathematical codes have been introduced to the industry to help with fracture modeling according to the nature of the problems and available data. Most of these are not appropriate to model hydraulic fracturing in naturally fractured rocks because they do not genuinely address fracture propagation in a mathematical representation of a naturally fractured system. In other words, these programs really only treat the rock mass as a continuum (almost invariably linear elastic) and therefore cannot address non-planar propagation, branching, sudden direction changes, or shear slip of pre-existing natural fractures (Hofmann et al. 2014). Much effort is currently being devoted to progress in this area with methods based on the Discrete Fracture Network (DFN) approach (Williams-Stroud et al. 2012), the Extended Finite Element Method (XFEM) (Ladubec et al. 2015) and the Discrete Element Method (Nagel et al. 2013).

Based on the research carried out by Hofmann et al. (2014), the main parameters influencing hydraulic fracture network growth are in-situ stresses, natural fracture network characteristics and fluid type. It is also mentioned in this work that the number (spacing) of pre-existing joints, joint fabric, deviatoric stresses, rock mechanical moduli and fluid viscosity are affecting the complexity of the jointed rock mass (Hofmann et al. 2014). Some challenges of modeling NFRs are introduced by Dusseault (2015) and listed as follows (Dusseault 2015)

- The joint fabric at depth is not clear.
- The initial spatial distribution of open and closed joints, their connectivity and aperture are unclear.
- The shear behaviour of joints is important in generating interconnected flow paths but rigorously identifying parameters affecting this behavior is difficult.

It is not yet clear what methods will be optimum for the modeling of naturally fractured rocks subjected to HF. However, DEM has flexibility in its ability to handle large numbers of natural fractures in a mathematical formulation based on contact laws. This method is judged to be the most suitable one currently available for the modelling of hydraulic fractures as it can accommodate natural fractures in various configurations, allowing them to dilate and slide within the simulation. The other methods investigated, including all continuum approaches and discrete fracture network models, cannot easily handle these aspects. Extensive reviews of numerical

methods in geomechanics is provided by (Jing and Hudson 2002). Also, details in fundamentals and applications of DEMs is given by (Jing and Stephansson 2007).

Jing (2003) provided an overview and enhanced understanding about the numerical methods used for modeling continuous and discontinuous rock masses that are generally implemented in rock mechanics. According to his paper, choosing between the continuum and discrete methods depends on many problem-specific factors and mainly on the problem scale and fracture system geometry. The discrete approach is most appropriate for moderately jointed rock masses where the behavior is governed by the discontinuities or where large scale displacements of individual blocks are expected (Jing 2003). Lisjak and Grasselli (2014) reviewed selected discrete element and hybrid finite-discrete element modeling techniques for fracturing processes in discontinuous rock masses. Their study is complemented with a brief review of applications on laboratory-scale models of rock failure processes and on the simulation of damage development around underground excavation (Lisjak and Grasselli 2014).

Hofmann et al. (2015) introduced a new hybrid simulation approach to evaluate the efficiency of hydraulic stimulation treatments (Hofmann et al. 2015). PFC2D as a discrete element method was used to perform a hydro-mechanical coupling and OpenGeoSys (OGS) as a finite element method was used to model thermo-hydraulic coupling. It was concluded in this work that DEM is capable of simulating complex tensile and shear fracture development in a naturally fractured network, and hybrid finite-discrete element modeling makes it possible to model hydraulic fracturing process in extensively jointed (>100,000 joints) rock fabrics and to evaluate the efficiency of the process (Hofmann et al. 2015).

Early studies (Koshelev and Ghassemi 2003) of mechanical interactions of natural and hydraulic fractures did not consider fluid flow. Zhang et al. (2010) considered fluid flow in the hydraulic fracture intersecting a single natural fracture, but without details of fracture interactions (Jeffrey et al. 2010b). Weng et al. (2011) considered multiple natural fractures and their mechanical fracture interactions were modeled via the displacement discontinuity method (Weng et al. 2011). Ghassemi and Sesetty (2012) used a fully hydro-mechanical coupled approach based on the boundary element method for modeling an interaction of a hydraulic fracture with natural fractures in both equilibrium and non-equilibrium states (Sesetty and Ghassemi 2012). Zangeneh et al. (2013) studied transient, hydro-mechanical coupling in a naturally fractured rock mass using the DEM approach. Results show that the interactions between hydraulic and natural fractures can potentially negatively affect the efficiency of the hydraulic fracturing treatment by excessive fluid diversion to natural fractures, impaired proppant transport and restricting the extent of the hydraulic fracture stimulated network size (Zangeneh 2013).

Kezarani and Zhao (2010) established a calibration procedure to find a single set of mechanical properties of blocks and contacts. They used UDEC™ for this purpose and they concluded that each material/block mechanical property (i.e. block Young's modulus, Poisson's ratio, internal

friction angle, internal cohesion, and tensile strength) is directly originated from and distinctly related to the contact properties (i.e. normal and shear stiffness, friction angle, cohesion, and tensile strength) (Kazerani and Zhao 2010).

McLennan et al. (2010) described a three-dimensional approach to model a hydraulic fracture evolution using a DEM commercial program (3DECTM - three-Dimensional Distinct Element Code). This research was intended to study the influence of operational parameters (such as injection rate) on the volumetric extent of a domain, the extent of fluid penetration into the natural fractures and the change of conductivity in the fracture system. They also used DFN (Discrete Fracture Network) models for fluid flow aspects (McLennan et al. 2010).

Gil et al. (2011) focused their attention on optimizing HF operations via 3DECTM. They carried out hydro-mechanical coupled modeling of a naturally fractured rock to investigate the failure type and operational parameters that affect the tensile/shear failure ratio. They found that injection rate and fluid viscosity affect the amount and type of failure created during fluid injection (Gil et al. 2011).

Damjanac et al. (2010) used UDECTM to present the influence of fluid compressibility on hydraulic fracture patterns in a naturally fractured rock. They came to the conclusion that a very compressible fluid created a more complex fracture geometry (Damjanac et al. 2010).

Zhang et al. (2002) studied the deformation and permeability of a naturally fractured rock using a Voronoi tessellated rock fabric under loading and unloading. They studied the evolution of microcrack growth and the stress condition at which connected fracture networks form (Zhang and Sanderson 2002). Riahi et al. (2013) performed a series of sensitivity analysis using a discrete element method to evaluate conductivity enhancement of tight hard rocks. Fully coupled hydro-mechanical modeling was carried out to study the influence of fracture density, fracture length and injection rate on fracture propagation in the naturally fractured rock. This study focused on analyzing the geometrical parameters on one specific geometry (Riahi and Damjanac 2013).

Ghazvinian (2016) implemented a three-dimensional Voronoi tessellated rock fabric via 3DECTM to study the hydro-mechanical response of the generated geometry to single- and multiple-stage fluid injection. A series of verification tests were performed to check the suitability of the proposed approach. It was observed in this study that the model is able to capture the correct mechanics of hydraulic fracture and natural fracture interactions (Ghazvinian and Kalenchuk 2016).

Preisig et al. (2015) performed a discrete element model to study joint conductivity enhancement in a jointed rock mass. Based on the results presented in this work, "...the opening of a hydraulic fracture is accompanied by millimeter-scale shear displacements associated with slip and wedging between adjacent blocks" (Preisig et al. 2015). Because of the joint asperities, this may

lead to permanent flow channels; however, if the asperities are not rough or strong enough, then the millimetre-scale shear displacements are too small to prevent a fully-elastic closure when injection stops (Preisig et al. 2015).

Although numerous types of NFR models have been generated, fabric effects remain poorly understood in the research of this discipline. Therefore, this thesis is focused on studying the effect of geometry on mechanical and hydraulic behavior of joints subjected to injection. Comparing different geometries under identical conditions is the core part of simulations.

More detailed discussions of the literature are undertaken in subsequent chapters.

2.3 SUMMARY

When hydraulic fractures propagate through a formation, interaction with natural fractures in the rock mass can affect the local direction in which the fracture will continue to travel. In addition to affecting the direction of hydraulic fracture propagation, natural fractures have the potential to reactivate (open or shear) during hydraulic fracturing (Hossain et al. 2002). Oftentimes, if properly engineered, this initiation of shearing of natural fractures can be highly beneficial to a hydraulic fracturing operation as it can widen the zone of stimulation, increasing the efficiency of the hydraulic fracture treatment (Gale et al. 2007).

As fluid is injected into a naturally fractured rock mass, the pressure in the rock mass is increased while the effective normal stress acting across the natural fractures in the rock is decreased, promoting shear slippage along some of the natural fractures. This process increases individual joint conductivity, which is beneficial in enhancing the reservoir permeability (Jeffrey et al. 2010b). Shear dilation occurs when fracture fluids have sufficient pressure to penetrate into the natural fracture in a rock mass (Warpinski et al. 2009) to lead to shear and a small amount of permanent displacement. When the fluid pressure is high enough to overcome the minimum in-situ stress, the fracture fluid begins to open natural fractures and causes them to propagate, as long as fluid pressure remains sufficiently elevated. This physical opening of the fractures is known as normal displacement and it also greatly affects the bulk permeability of the rock mass.

The interaction of natural and hydraulic fractures plays a prominent role in the efficiency of the hydraulic fracturing process; therefore, it is of importance to have a quantitative or semi-quantitative understanding of this phenomenon. The question remains as to which method and what software program fits the requirements of the given problem. In this study, the main objective is defined as generating jointed rock fabrics and evaluating the coupled hydro-mechanical process of injection and hydraulic fracture. The determination of an appropriate methodology and software program is crucial for ensuring that the main thesis problem is analyzed effectively.

CHAPTER 3 NUMRICAL MODELING OF HYDRAULIC FRACTURING

In order to address the question of how numerical models can represent the real behavior of NFRs, it is important to select an appropriate modeling method and a suitable software application to perform analyses. This chapter explains some basic definitions in continuum solid and fluid mechanics, governing equations and numerical methods to solve these equations.

OVERVIEW

Equilibrium problems are one of the main categories of engineering problems. Engineering problems can be explained as physical processes and they can be mathematically formulated using differential equations and boundary conditions. Thus, for any given problem, it is important to define a framework and find boundary conditions and governing equations that are valid within the framework. After having developed an appropriate set of differential equations of a problem, it is then necessary to solve them. Different methods have been introduced and numerical techniques are being developed to reach this goal. Finite Element, Finite Difference, Boundary Element and Discrete Element are at the top of the list of widely used approaches to solve governing equations of a system. Discrete Element Method (DEM) is explained in this chapter as the means of addressing goals of achieving a better understanding of the role of natural discontinuity fabric in HF. UDECTM is introduced as a qualified DEM code to implement the requirements of this study.

3.1 NOTATION

There are different standards of notations in mathematics, continuum mechanics and numerical methods. Indicial notation, tensor notation and matrix notation are the three common standards. Equations in continuum mechanics are mostly expressed by tensor and indicial notation; however in numerical methods, equations are given in matrix and indicial notation (Belytschko et al. 2000).

Indicial notation is a method to write scalars, vectors and tensors without having to write the entire representation. An important application of indicial notation is to compactly represent sets of equations in coordinate systems. A three-dimensional coordinate system using x , y and z is represented by x_1 , x_2 and x_3 , respectively. Using indicial notation x as a coordinate system, a vector can be written as x_i . Quantities in this study refer to the Cartesian coordinate system and a range of three (i.e., 1, 2, 3) is picked for all indices (Mase and Mase 2009). Therefore,

x_i has 3 components (x_1 , x_2 and x_3)

T_{ij} has $3^2=9$ components (T_{11} , T_{12}, \dots, T_{33})

A_{ijk} has $3^3=27$ components

C_{ijkl} has $3^4=81$ components

Consider the Cartesian coordinate system with unit vectors $(\hat{e}_1, \hat{e}_2, \hat{e}_3)$. Any vector \hat{u} in the coordinate system x_i has three components and can be written in the form of a linear combination of unit vectors:

$$\hat{u} = u_k e_k = u_1 e_1 + u_2 e_2 + u_3 e_3$$

No indices are used in **tensor notation** (Belytschko et al. 2000). Tensors are conventionally denoted with boldface letters. Lower case and upper case boldface letters respectively indicate tensors of first and higher orders. The Cauchy stress tensor, $\boldsymbol{\sigma}$, is shown by a lower case Greek symbol which is an exception for a second-order tensor (Belytschko et al. 2000).

Matrix notation is usually used for computational purposes to facilitate components manipulations. Components of a vector are shown by a 3×1 columnar matrix and components of a second-order tensor are represented by a 3×3 matrix (Belytschko et al. 2000).

3.2 DEFINITION

Bodies subjected to forces are generally described by geometry and appropriate variables (displacements, strains and stresses), relationships between variables (constitutive relationships), governing equations and boundary conditions. For a two-dimensional linear elastic body, the following descriptions are valid, and are graphically represented in Figure 3.1.

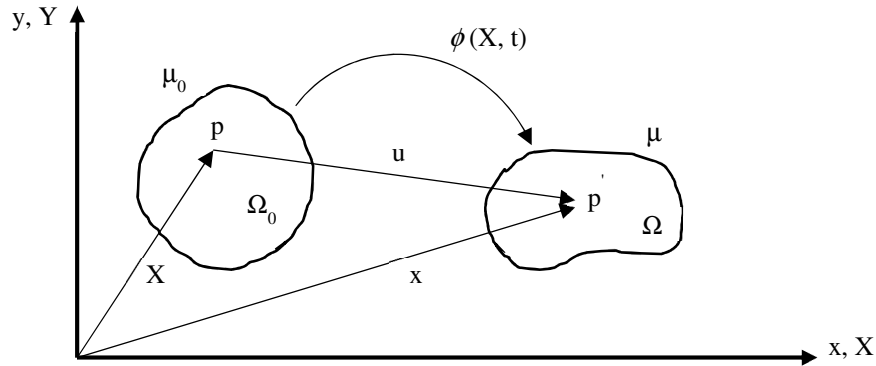


Figure 3.1. Undeformed (initial) and deformed (current) configurations of a body. Ω is the domain of the initial configuration; Ω' is the domain of the current configuration; μ is the boundary of the initial configuration; μ' is the boundary of the current configuration; P is a material point in the initial configuration; P' is a material point in the current configuration; \mathbf{X} is the position vector of a particle in the initial configuration and in the alternative notation is given by

$$\mathbf{X} = X_i e_i = \sum_{i=1}^{n_{SD}} X_i e_i \quad (n_{SD} \text{ is the number of space dimensions})$$

$$\text{for a two - dimensional space } n_{SD} = 2 \text{ and } \mathbf{X} = X_i e_i = \sum_{i=1}^2 X_i e_i$$

$$x \text{ is the position vector of a particle in the current configuration; } \mathbf{x} = x_i e_i = \sum_{i=1}^{n_{SD}} x_i e_i$$

$$\text{and } u \text{ is the displacement vector of a particle in the initial configuration; } \mathbf{u}(\mathbf{X}, t) = u_i e_i = \sum_{i=1}^{n_{SD}} u_i e_i$$

Belytschko defines these terms as follows:(Belytschko et al. 2000):

- **Displacement** (\mathbf{u}) is a change in a configuration of a body.
- A **configuration** is a finite set of coordinates of all particles of a body.
- **Deformation** is the transformation of a body from an initial or undeformed configuration to a current or deformed configuration, which can be initiated by external forces, body forces, etc.
- The **Motion** of a body is a function of the initial positions and time.

$$\mathbf{x} = \boldsymbol{\phi}(\mathbf{X}, t) \quad \text{or in an alternative notation} \quad x_i = \phi_i(X, t) \quad (3-1)$$

where $\phi(X, t)$ is a map between the initial and current configurations and \mathbf{X} is the position vector of a particle in the initial configuration. The subscript i may be any of the numbers 1, 2 and 3, representing the x-, y- and z-axis, respectively, in a Cartesian coordinate system.

- **Displacement Vector** is a vector connecting a particle of a body in the undeformed and deformed configurations. The difference between the current and initial positions gives displacement

$$\mathbf{u}(\mathbf{X}, t) = \boldsymbol{\phi}(\mathbf{X}, t) - \boldsymbol{\phi}(\mathbf{X}, 0) = \boldsymbol{\phi}(\mathbf{X}, t) - \mathbf{X} \quad \text{or} \quad \mathbf{u} = \mathbf{x} - \mathbf{X} \quad (3-2)$$

$$\text{or in an alternative notation} \quad u_i = x_i - X_i = \phi_i(X, t) - X_i$$

- **Strain** is a relative displacement of particles in a body and is defined as

$$\boldsymbol{\varepsilon}(\mathbf{X}, t) = \frac{\partial \mathbf{x}}{\partial \mathbf{X}} - \mathbf{1} = \frac{\partial \mathbf{u}}{\partial \mathbf{X}} \quad (3-3)$$

Figure 3.2 shows displacement and strain for a single body.

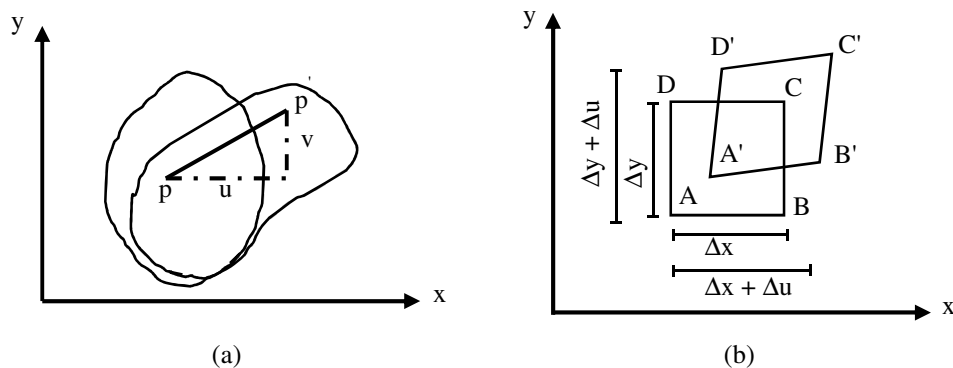


Figure 3.2. Schematic of a) Displacements; b) Strains.

- **Velocity** is the rate of motion of a material point or the time derivative of a displacement.

$$\mathbf{v}(\mathbf{X}, t) = \partial \boldsymbol{\phi}(\mathbf{X}, t) / \partial t = \partial \mathbf{u}(\mathbf{X}, t) / \partial t = \dot{\mathbf{u}} \quad (3-4)$$

- **Acceleration** is the rate of change of velocity of a material point or the time derivative of a velocity.

$$\mathbf{a}(\mathbf{X}, t) = \partial \mathbf{v}(\mathbf{X}, t) / \partial t = \partial^2 \mathbf{u}(\mathbf{X}, t) / \partial t^2 = \dot{\mathbf{v}} \quad (3-5)$$

3.3 CONTINUUM SOLID MECHANICS

In the sections that follow, the following assumptions are considered:

- Two-dimensional space;
- Linear elastic material;
- Lagrangian system;
- Constant mass;
- Initially undeformed system;
- Static system;
- Isothermal system.

3.3.1 FORCE

Forces are generally categorized as external and internal forces. External forces are applied externally and are divided into body forces and traction forces. Traction forces acting on a surface may be the consequence of bodies in contact, and these contact forces are a fundamental aspect of the mathematical study of particulate media such as jointed rock masses. Body forces are applied to all particles over the volume of the body and are a consequence of being in a force field such as gravity (Mase and Mase 2009).

3.3.2 STRESS

The **physical stress** is also known as the **Cauchy stress** and is given by:

$$\boldsymbol{\sigma} = \mathbf{F} / A \quad (3-6)$$

where A is the current area of a given section and F is the force acting on it (Mase and Mase 2009).

Force may be decomposed into two components, normal and parallel to a specified surface. The two components, when divided by the area of application, respectively represent the shear and normal stresses (Figure 3.3) (Mase and Mase 2009).

$$\sigma_n = F_n/A \text{ and } \tau = F_p/A \quad (3-7)$$

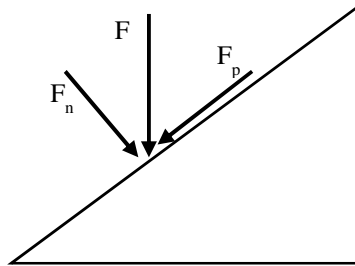


Figure 3.3. Decomposition of forces.

Stress values at a material point change from one orientation to another due to the fact that:

- there are infinitely many planes that can pass through a point
- the intensity of the internal forces is a function of the orientation of these planes; or in other words, a body would strain in response to applied forces

Three perpendicular (orthogonal) planes are introduced to find three values of stress vectors (t_i) at a material point. In a two-dimensional framework, each stress vector can be resolved into two components. In a complete description, a given point P in a body has nine components of stress related to these orthogonal planes (Mase and Mase 2009). This expression of stress is called the stress tensor (σ_{ij}) and is defined for a two-dimensional case by:

$$t_i = \sigma_{ij}e_j \quad (3-8)$$

$$\sigma = \begin{bmatrix} \sigma_{11} & \sigma_{12} & 0 \\ \sigma_{21} & \sigma_{22} & 0 \\ 0 & 0 & 0 \end{bmatrix}$$

The first subscript of stress components refers to the plane they belong to and the second subscript refers to the direction of that component (Mase and Mase 2009).

In a two-dimensional Cartesian framework, consider a normal and shear stress acting on a surface as shown on Figure 3.4a. Principal stresses can be defined as $\sigma_1 \geq \sigma_2$.

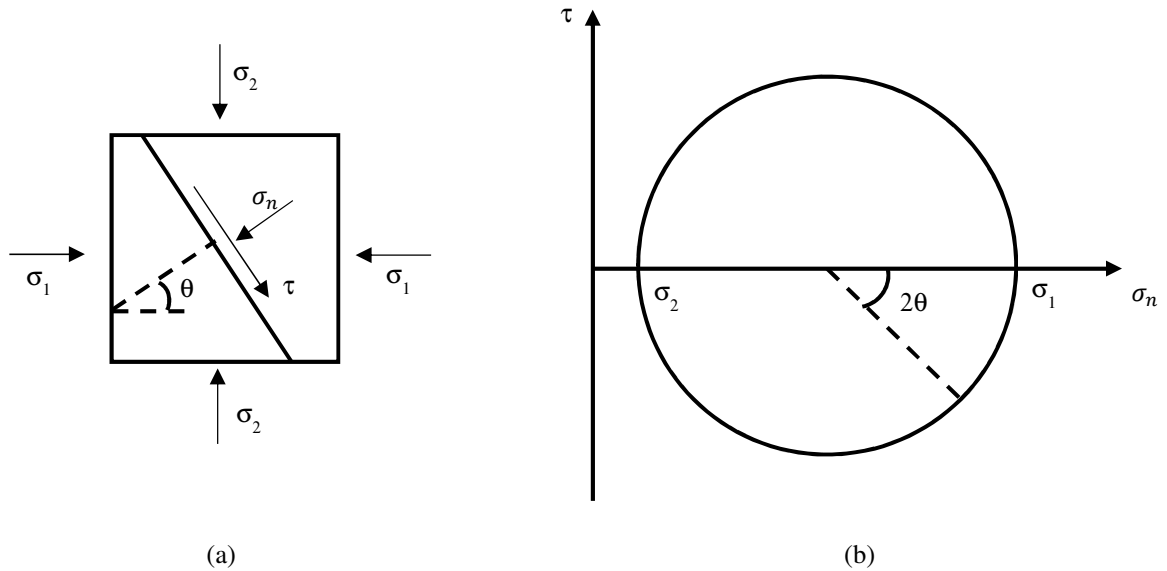


Figure 3.4. Mohr's circle representing stresses at a point (Fjaer et al. 2008).

The angle θ between the principal stress directions and the defined plane can be given by

$$\tan 2\theta = \frac{2\tau}{\sigma_1 - \sigma_2} \quad (3-9)$$

Equation (3-9) has two solutions corresponding to two principal axes of stress for which the shear stress on the plane is zero. Plotting the corresponding values of shear and normal stresses for all angles of planes passing through the point in an equivalued σ_n - τ axis diagram generates the Mohr's circle (Figure 3.4b). The Mohr's circle is a helpful tool in the analysis of conditions of rock failure (Fjaer et al. 2008) because the shear and normal stresses across any plane through a point can be graphically compared to the σ_n - τ slip condition for a discontinuity (joint or bedding plane) at that orientation with respect to the principal stresses.

3.3.3 STRAIN

Motion can be described with either Lagrangian or Eulerian coordinates. The Lagrangian description of motion is based on tracking a material point from fixed position \mathbf{X} through the ambient space, while the Eulerian description is based on following physical particles through ambient material at a fixed spatial position \mathbf{x} . From another aspect, Lagrangian description is focused on what is happening to the particles when they move and the Eulerian description is focused on the events taking place at specific positions in space. Lagrangian and Eulerian descriptions of motion are respectively referred to as direct and reverse motion problems (Mase and Mase 2009).

As motion occurs, two neighboring material points must be tracked to measure the local deformation in a material. There are Lagrangian and Eulerian measures of deformation respectively known as the **right Cauchy-Green deformation tensor** and the **left Cauchy-Green deformation tensor**. Having these definitions of deformation, two measures of strain can be given (Mase and Mase 2009).

The Lagrangian and Eulerian measure of strain are respectively called the **Green-Lagrange strain tensor** and the **Almasi-Euler strain tensor**. The Green-Lagrange strain tensor is a complete definition of strain. The engineering (infinitesimal) definition of strain is an approximation of the Green-Lagrange strain tensor if deformations and rotations are small. Most problems (e.g., linear elasticity) only address small deformations, hence infinitesimal strain is a reasonable measure of strain. On the other hand, the linearized form of the Eulerian measure of strain is also equal to engineering strain. This shows that the linear theory of elasticity is an approximation (Mase and Mase 2009). The engineering strain is defined as:

$$\varepsilon_{ij} = \frac{1}{2}(\partial u_{i,j} + \partial u_{j,i}) \quad (3-10)$$

$$\text{or in an alternative notation } \boldsymbol{\varepsilon} = \frac{1}{2}(\nabla \mathbf{u} + (\nabla \mathbf{u})^T) \quad (3-11)$$

3.3.4 PLANE STATE OF STRAIN

A plane state of strain refers to the strain state at a point where the all components of strain in one direction are zero; i.e., there is a direction at which no change of length or angle occurs (Mase and Mase 2009). With the assumption that the negligible strain is oriented in the z-direction, the strain and stress tensors for a plane strain case are expressed as:

$$\boldsymbol{\varepsilon} = \begin{bmatrix} \varepsilon_{11} & \varepsilon_{12} & 0 \\ \varepsilon_{21} & \varepsilon_{22} & 0 \\ 0 & 0 & 0 \end{bmatrix} \text{ and } \boldsymbol{\sigma} = \begin{bmatrix} \sigma_{11} & \sigma_{12} & 0 \\ \sigma_{21} & \sigma_{22} & 0 \\ 0 & 0 & \vartheta(\sigma_{11} + \sigma_{22}) \end{bmatrix}$$

Figure 3.5 shows strain and stress components for a plane strain case. Plane strain or plane stress states are the basic assumptions behind two-dimensional engineering mechanics analysis.

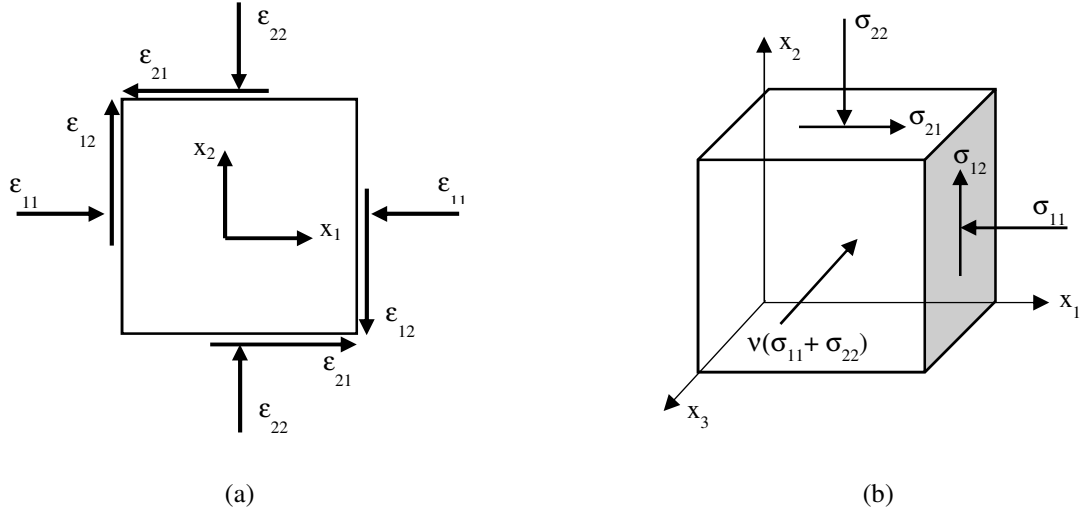


Figure 3.5. Plane state of strain; a) strain components, b) stress components.

3.3.5 EQUILIBRIUM

Consider a continuum of volume V with density ρ surrounded by a surface S under surface traction t and volume body force b . If the body is in static equilibrium, the sum of forces and moments must equal zero. Mathematically, the balance of forces and moments are given by (Belytschko et al. 2000):

$$\iint_S \mathbf{t}^n ds + \iiint_V \rho \mathbf{b} dV = 0 \quad (3-12)$$

$$\iint_S \mathbf{x} \times \mathbf{t}^n ds + \iiint_V \rho \mathbf{x} \times \mathbf{b} dV = 0 \text{ (here } \mathbf{x} \text{ is position vector)} \quad (3-13)$$

Substituting the Cauchy Rule¹ ($t_i^n = \sigma_{ji}n_j$) and using the Gauss theorem² ($\iint_S A_{ij}n_j dS = \iiint_V \frac{\partial A_{ij}}{\partial x_j} dV$) in the equation for force balance will give:

$$\iiint_V \left(\frac{\partial \sigma_{ij}}{\partial x_j} + \rho b_i \right) dV = 0 \quad (3-14)$$

This has to be true for all volume elements, thus:

$$\sigma_{ij,j} + \rho b_i = 0 \quad (3-15)$$

¹ Stress on any arbitrary plane n can be expressed in terms of nine components using the Cauchy Rule.

² Gauss theorem is used to convert surface integrals to volume integrals and vice versa.

These three equations are called the stress equilibrium equations.

The balance of moments will show that Cauchy stress tensor is symmetric:

$$\sigma_{ij} = \sigma_{ji} \quad (3-16)$$

3.3.6 CONSERVATION LAWS

Satisfying conservation laws is a prerequisite for a closed system in continuum mechanics. These laws dictate that the three quantities of mass, momentum and energy will not change over time (Belytschko et al. 2000).

- Conservation of mass

The conservation of mass states that the mass of a closed system remains constant over time. The mass $m(\Omega)$ of a material domain Ω is given by:

$$m(\Omega) = \int_{\Omega} \rho(\mathbf{X}, t) d\Omega \quad (3-17)$$

where $\rho(X, t)$ is the density. The Lagrangian description of the mass conservation law is expressed as:

$$\int_{\Omega} \rho d\Omega = \int_{\Omega_0} \rho_0 d\Omega_0 \quad (3-18)$$

$$\rho(\mathbf{X}, t) J(\mathbf{X}, t) = \rho_0(\mathbf{X}) \quad (3-19)$$

Here, $J(X, t)$ is the Jacobian that relates integrals between the current and initial configurations.

- Conservation of momentum: Linear and angular

Momentum takes two forms: linear and angular¹. Conservation of linear momentum is equivalent to Newton's second law of motion, which relates forces acting on a moving body to its motion. Let a domain Ω with boundary Γ be subjected to surface tractions \mathbf{t} and body forces $\rho\mathbf{b}$ (\mathbf{b} is a force per unit mass and \mathbf{t} is a force per unit area). The total external force acting on this continuum is given by:

¹ Angular momentum (\mathbf{L}) is a product of body's moment of inertia¹ (\mathbf{I}) and its angular velocity ($\boldsymbol{\omega}$) such that $\mathbf{L} = \mathbf{I} \cdot \boldsymbol{\omega}$

$$f(t) = \int_{\Gamma} \mathbf{t}(\mathbf{X}, t) d\Gamma + \int_{\Omega} \rho \mathbf{b}(\mathbf{X}, t) d\Omega \quad (3-20)$$

The linear momentum (\mathbf{p}) is a vector quantity and is given by a product of mass and velocity:

$$\mathbf{p}(t) = \int_{\Omega} \rho \mathbf{v}(\mathbf{X}, t) d\Omega \quad (3-21)$$

Using the Cauchy Rule, the divergence or Gauss theorem, and the fact that the material time derivative of linear momentum equals the net force, the moment equation is defined by:

$$\frac{D}{Dt} \int_{\Omega} \rho \mathbf{v} d\Omega = \int_{\Gamma} \mathbf{t} d\Gamma + \int_{\Omega} \rho \mathbf{b} d\Omega \quad (3-22)$$

$$\int_{\Omega} \rho \frac{D\mathbf{v}}{Dt} d\Omega = \int_{\Omega} (\nabla \cdot \boldsymbol{\sigma} + \rho \mathbf{b}) d\Omega \quad (3-23)$$

$$\rho \frac{D\mathbf{v}(\mathbf{X}, t)}{Dt} = \nabla \cdot \boldsymbol{\sigma} + \rho \mathbf{b} \quad (3-24)$$

In problems with no inertial effects (loads are applied slowly and inertial forces are negligible), the acceleration term in the momentum equation can be dropped. In such cases, the momentum equation will be the same as the stress equilibrium equation ($\sigma_{ij,j} + \rho b_i = 0$).

- Conservation of energy

The conservation of energy relates the external and internal energies of the system to the work of surface and body forces plus all energies that enter or leave the system. The total amount of energy in a closed system remains constant. Energy exists in different forms, which are all convertible. The law of conservation of energy states that the rate of change (material time derivative) of the total energy in the body equals the rate of work done by applied forces (surface and body forces) and heat (energy) sources. According to the conservation of energy, Reynold's transport theorem¹, Gauss theorem and the Cauchy Rule, the energy equation is expressed as:

¹ Reynold's transport theorem is used to bring the total derivative inside the integral and convert all surface integrals to domain integrals.

$$\rho \frac{Dw^{int}}{Dt} = \mathbf{D} : \boldsymbol{\sigma} - \nabla \cdot \mathbf{q} \quad (3-25)$$

where ρw^{int} is the internal energy per unit volume and \mathbf{q} is the heat flux vector. The symbol “:” denotes the contraction¹ of a pair of repeated indices which appear in the same order. In an alternative notation:

$$\rho \frac{Dw^{int}}{Dt} = \sigma_{ij} D_{ij} - q_{j,j} \quad (3-26)$$

where D_{ij} is the rate of deformation or a symmetric component of a velocity gradient ($v_{i,j}$) and σ_{ij} is the Cauchy stress.

In purely mechanical cases where there is no heat source, the energy equation reduces to

$$\rho \frac{Dw^{int}}{Dt} = \sigma_{ij} D_{ij} \quad (3-27)$$

This equation is called the internal energy rate and describes the rate of energy communicated to a unit volume of the body in terms of stress and strain.

3.3.7 CONSTITUTIVE EQUATION (STRESS-STRAIN LAWS)

Constitutive equations are the equations that describe material behavior under the effects of changes in stress, temperature, and other extrinsic factors. **Linear Elasticity** is one of the classic sets of constitutive equations. All linear elastic materials undergo very small deformation changes under loading: these have a linear relationship in terms of the stresses and deformations², and the body returns to the original shape after load removal (reversible strains). Linear elasticity is an appropriate approach to model this type of behavior (Belytschko et al. 2000).

Stress and strain are the two fundamental concepts of the theory of linear elasticity. The generalized Hooke’s law describes the most general linear relation among all components of the stress and strain tensors (Mase and Mase 2009):

¹ Contraction is the operation of replacing two free indices with dummy index and reduces the rank of a tensor by two.

² Infinitesimal strain is a good measure of strain in linear elasticity where strains are small.

$$\sigma_{ij} = C_{ijkl}\varepsilon_{kl} \quad \text{or} \quad \boldsymbol{\sigma} = \mathbf{C}:\boldsymbol{\varepsilon} \quad (3-28)$$

where C_{ijkl} is the elasticity tensor representing the material properties (elastic constants). Elasticity tensor is a fourth order tensor and has 81 components. However for the simplest elastic case (linear, isotropic), there are only two independent components to the tensor. In this case, the elasticity tensor can be defined as:

$$\lambda\delta_{ij}\delta_{kl} + \mu\delta_{ik}\delta_{jl} + \nu\delta_{il}\delta_{jk} \quad (3-29)$$

where λ, μ and ν are arbitrary scalars and δ is Kronecker Delta

$$\delta_{ij} = \begin{cases} 1 & \text{for } i = j \\ 0 & \text{for } i \neq j \end{cases} \quad (3-30)$$

Substituting this equation in Generalized Hooke's law yields:

$$\sigma_{ij} = (\lambda\delta_{ij}\delta_{kl} + \mu\delta_{ik}\delta_{jl} + \nu\delta_{il}\delta_{jk})\varepsilon_{kl} \quad (3-31)$$

$$\sigma_{ij} = \lambda\varepsilon_{kk}\delta_{ij} + 2\mu\varepsilon_{ij} \quad (3-32)$$

λ and μ are independent material properties known as Lamé's constants. These constants are related to Young's modulus (E), Poisson's ratio (ν) and shear modulus (G) as:

$$E = \frac{\mu(2\mu + 3\lambda)}{\mu + \lambda}; \quad \nu = \frac{\lambda}{2(\mu + \lambda)} \quad \text{and} \quad G = \mu \quad (3-33)$$

3.3.8 GOVERNING EQUATIONS FOR SOLID LINEAR ELASTIC MATERIAL

Governing equations are defined as partial differential equations (strong form) or integral equations (weak form) coupled with boundary conditions. The following are conditions governing the behavior of linear elastic isotropic material (Belytschko et al. 2000)

- Conservation of mass
- Conservation of momentum
- Conservation of energy
- A measure of deformation (strain-deformation equation)
- A constitutive equation, which describes material behavior (stress-strain law)

Having these conditions, field equations for linear isotropic elasticity can be obtained as (Mase and Mase 2009):

- Three equilibrium equations obtained by force (stress) consideration of motion

$$\sigma_{ij,j} + \rho b_i = 0 \quad (3-34)$$

- Six compatibility equations obtained by kinematics considerations of motion

$$2\varepsilon_{ij} = u_{i,j} + u_{j,i} \quad (3-35)$$

- Six linear elasticity equations in the form of Hooke's law

$$\sigma_{ij} = \lambda e_{kk} \delta_{ij} + 2\mu \varepsilon_{ij} \quad (3-36)$$

These 15 equations have 6 unknown strains, 6 unknown stresses and 3 unknown displacements. These may be combined in three equations with three unknown displacements known as Navier-Cauchy equations:

$$(\lambda + \mu)u_{k,ki} + \mu u_{i,jj} + \rho b_i = 0 \quad (3-37)$$

3.4 NUMERICAL SOLUTIONS

3.4.1 IMPLICIT AND EXPLICIT ALGORITHMS

All numerical methods involve transforming governing differential equations into a system of algebraic equations. To this end, the problem domains (time and space) are discretized into a finite number of sub-domains. Subdivision of a given time interval into a number of smaller subintervals (timesteps) is called time discretization. Space discretization is defined as creating a numerical mesh consisting of a finite number of computational points (Demirdzic et al. 2005).

Numerical approximations for differential equations are usually referred to as being explicit or implicit algorithms. An explicit algorithm is an updating scheme that updates the system based on its current state. Explicit methods use known parameters to find dependent variables while implicit methods are needed to solve algebraic equations (Bui 2010).

Explicit: $u_{i+1} = u_i + f(t_i, u_i)\Delta t$

Implicit: $u_{i+1} = u_i + f(t_i, u_{i+1})\Delta t$

The size of Δt or step size controls the accuracy of the approximate solutions as well as the number of calculations. Implicit algorithms are unconditionally stable and can have large Δt ,

while explicit schemes tend to be unstable and require a small Δt that is chosen to be smaller than a critical value that is estimated from characteristics of the numerical scheme. Explicit algorithms have simple calculations per time step, which are easy to program. Implicit schemes on the other hand are difficult, which makes them computationally intensive (Chapra and Canale 2015).

3.4.2 FINITE DIFFERENCE SCHEMES

Finite difference methods (FDMs) are discretization methods for solving differential equations using difference equations. Difference equations are derived from Taylor series and are categorized as forward, backward and central equations. Difference equations approximate the derivatives of functions in the differential equation. Derivatives are approximated by differences between the values of the function for a given small increment of the independent variable. Therefore, finite difference approximations can be used on a discretized domain¹ to numerically solve differential equations by replacing derivatives. This gives a large algebraic system of equations that can be solved one at a time (explicit) or simultaneously (implicit). Forward and central finite difference approximations are explicit algorithms, while backward finite difference equations is an implicit method (Chapra and Canale 2015).

Considering a Taylor series expansion of $u(x)$ about the point $x = x_i$

$$u(x) = \sum_{n=0}^{\infty} \frac{(x - x_i)^n}{n!} \left(\frac{\partial^n u}{\partial x^n} \right) \Big|_{x_i} \quad (3-38)$$

Finite difference approximations of first-order derivatives are as follows:

$$\text{Forward difference: } \left(\frac{\partial u}{\partial x} \right)_i \approx \frac{u_{i+1} - u_i}{\Delta x}$$

$$\text{Backward difference: } \left(\frac{\partial u}{\partial x} \right)_i \approx \frac{u_i - u_{i-1}}{\Delta x}$$

$$\text{Central difference: } \left(\frac{\partial u}{\partial x} \right)_i \approx \frac{u_{i+1} - u_{i-1}}{2\Delta x}$$

Figure 3.6 shows a geometric interpretation of finite difference approximations.

¹ Domain is partitioned in space and in time

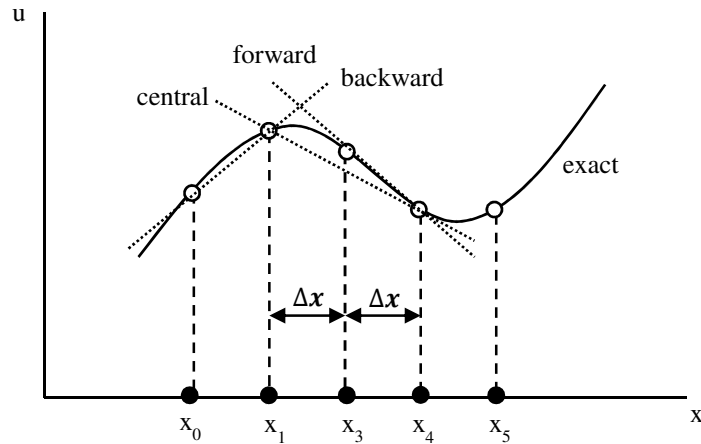


Figure 3.6. Geometric interpretation of finite difference approximations.

Central finite difference approximations of second-order derivatives are expressed as:

$$\left(\frac{\partial^2 u}{\partial x^2}\right)_i \approx \frac{u_{i+1} - 2u_i + u_{i-1}}{(\Delta x)^2} \quad (3-39)$$

3.4.3 DISCRETIZATION OF THE DOMAIN

The process of discretizing a body into a finite number of subdivisions is called meshing. The mesh can be generated in different shapes. A triangular mesh is one of the most prevalent types of mesh in numerical analysis as triangles can efficiently cover domains with complicated geometry. A triangular mesh consists of triangles (elements) connected with their edges and corners (nodes). Linear algebraic equations are developed to calculate displacements of each node (Fish and Belytschko 2007).

3.4.3.1 PLANE LINEAR TRIANGULAR ELEMENT

In a two-dimensional framework, each node has two degrees of freedom (displacements in x- and y- directions), while in a three-node linear triangular element, there would be six degrees of freedom. Figure 3.7 shows a body discretized into triangle elements and displacement vectors for a single three-node linear-displacement triangular element. Triangular elements are widely used because the approximation equations are easy to formulate (Fish and Belytschko 2007).

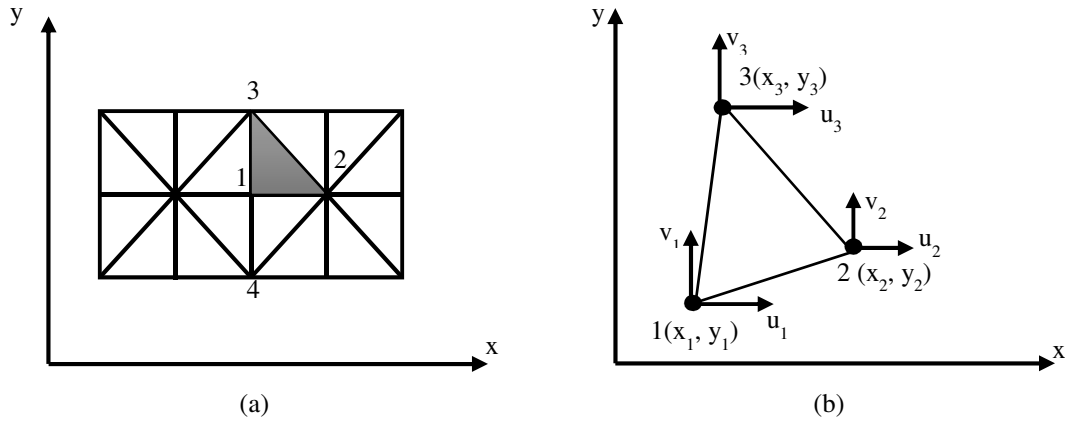


Figure 3.7. a) Discretized domain; b) Three-node linear-displacement triangular element.

3.4.3.2 GOVERNING EQUATIONS OF CONTACTS

The body is discretized into many elements. Points or edges at which elements meet are known as contacts. In a two-dimensional framework, contacts are physically categorized into three types: node-to-node contact, node-to-edge contact and edge-to-edge contact (Figure 3.8) (Munjiza et al. 2011).

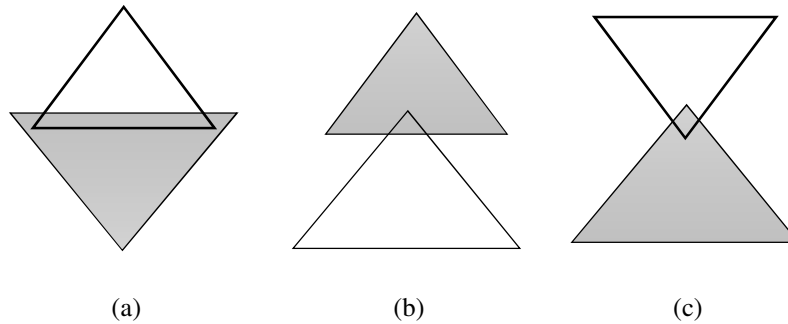


Figure 3.8. Physical categories of contact in a two-dimensional framework (Riahi et al. 2010).

Contact forces have two components of normal (f_N) and tangential (f_T) forces. Contact forces control the interpretation of objects while tangential forces control sliding or slipping of the contact (Munjiza et al. 2011). The total contact force is given by:

$$f_c = f_T + f_N \quad (3-40)$$

Consider the three-node triangular element in Figure 3.9. External forces (body forces in the domain and tractions on the surface) were applied on the nodes of the element. Here, the traction is applied to the edge connecting nodes 2 to 3, but the results can be applied to all nodes.

$$F_i^b = \int_{\Omega} \rho b_i d\Omega \quad (3-41)$$

$$F_i^T = \int_{\Omega} \nabla \cdot \sigma d\Omega = \int_{\Gamma} \sigma_{ij} n_j d\Gamma \approx \sum_{edge} (\sigma_f \cdot n_f) L_f \quad (3-42)$$

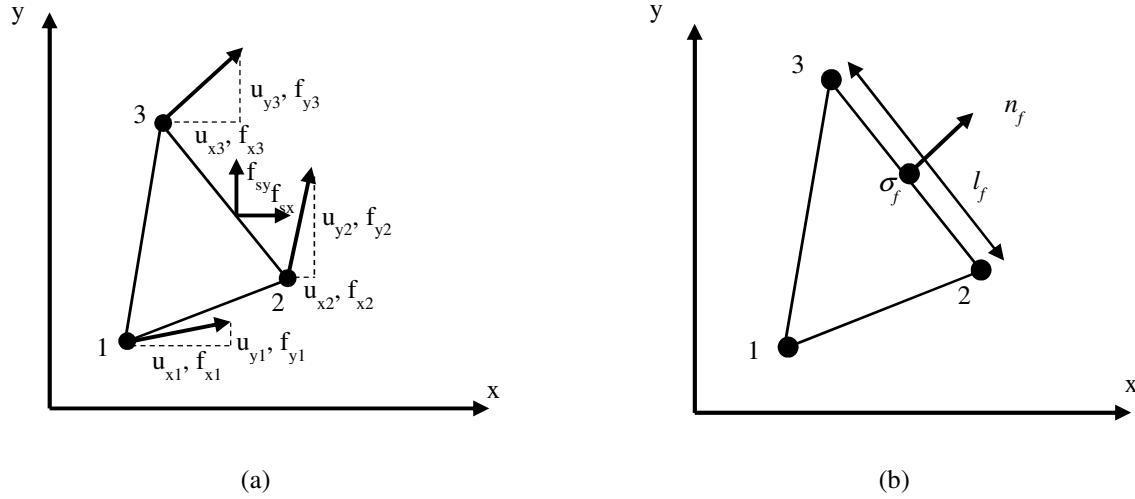


Figure 3.9. a) Three-node triangular element showing nodal displacements, nodal forces and the equivalent element body force; b) tractions.

The total force acting on the nodes of the element is the result of all internal and external forces. The result of all external forces applied to the nodes, f_i^{ext} , is given as:

$$f_i^{ext} = \sum_{elem} f_i^{elem} = F_i^b + F_i^T + F_i^c \quad (3-43)$$

The strain-displacement and stress-strain equations of a plane triangular element are given as:

$$\sigma^T = \{\sigma_{xx} \sigma_{yy} \sigma_{xy}\} \text{ and } \varepsilon^T = \{\varepsilon_{xx} \varepsilon_{yy} \varepsilon_{xy}\} \quad (3-44)$$

$$\varepsilon_{xx} = \frac{\partial u}{\partial x}, \varepsilon_{yy} = \frac{\partial v}{\partial y}, \varepsilon_{xy} = \frac{\partial u}{\partial y} + \frac{\partial v}{\partial x} \quad (3-45)$$

Strain can be defined by nodal displacements of the element. Strain within a linear triangular element is constant, and thus so is the stress. Therefore, the linear triangular elements are also

known as constant strain elements or constant stress elements. A strain matrix is required to compute element matrices such as a stiffness matrix and then the element external force (Fish and Belytschko 2007).

3.4.4 MATHEMATICAL MODELING

In continuum mechanics, the motion and deformation of a single body are governed by the principle of conservation of linear momentum:

$$\rho \dot{v}_i = \sigma_{ij,j} + \rho b_i \quad (3-46)$$

Substituting equation (3-32) in (3-46)

$$\rho \dot{v}_i = (\lambda \varepsilon_{kk} \delta_{ij} + 2\mu \varepsilon_{ij}),j + \rho b_i \quad (3-47)$$

$$\frac{\partial}{\partial t} \left(\rho \frac{\partial u_i}{\partial t} \right) = \frac{\partial}{\partial x_i} \left(\lambda \frac{\partial u_k}{\partial x_k} \right) + \frac{\partial}{\partial x_j} \left[\mu \left(\frac{\partial u_i}{\partial x_j} + \frac{\partial u_j}{\partial x_i} \right) \right] + \rho b_i \quad (3-48)$$

or in tensor notation:

$$\frac{\partial}{\partial t} \left(\rho \frac{\partial \mathbf{u}}{\partial t} \right) = \nabla (\lambda \nabla \cdot \mathbf{u}) + \nabla \cdot [\mu (\nabla \mathbf{u} + (\nabla \mathbf{u})^T)] + \rho \mathbf{b} \quad (3-49)$$

This basic system of equations of linear elasticity can be written in integral form as:

$$\int_{\Omega} \frac{\partial}{\partial t} \left(\rho \frac{\partial u_i}{\partial t} \right) d\Omega = \int_S \left\{ \frac{\partial}{\partial x_i} \left(\lambda \frac{\partial u_k}{\partial x_k} \right) + \frac{\partial}{\partial x_j} \left[\mu \left(\frac{\partial u_i}{\partial x_j} + \frac{\partial u_j}{\partial x_i} \right) \right] \right\} \cdot n dS + \int_{\Omega} \rho b_i d\Omega \quad (3-50)$$

This is known as the strong form of the differential equation.

For a two-dimensional problem, by neglecting the out-of-plane motion, equation (3-32) can be rewritten as:

$$\frac{(\lambda + 2\mu)}{\rho} \frac{\partial^2 u_x}{\partial x^2} + \frac{\mu}{\rho} \frac{\partial^2 u_x}{\partial y^2} + \frac{(\lambda + \mu)}{\rho} \frac{\partial^2 u_y}{\partial x \partial y} + b_x = \frac{\partial^2 u_x}{\partial t^2} \quad (3-51)$$

$$\frac{(\lambda + 2\mu)}{\rho} \frac{\partial^2 u_y}{\partial y^2} + \frac{\mu}{\rho} \frac{\partial^2 u_y}{\partial x^2} + \frac{(\lambda + \mu)}{\rho} \frac{\partial^2 u_x}{\partial x \partial y} + b_y = \frac{\partial^2 u_y}{\partial t^2} \quad (3-52)$$

Employing the central difference approximation for both time and space yields the difference equations that follow:

$$\begin{aligned}
& \frac{u_x(x_i, y_j, t_{n+1}) - 2u_x(x_i, y_j, t_n) + u_x(x_i, y_j, t_{n-1}))}{\Delta t^2} \\
&= b_x + \frac{(\lambda + 2\mu) u_x(x_{i+1}, y_j, t_n) - 2u_x(x_i, y_j, t_n) + u_x(x_{i-1}, y_j, t_n)}{\rho \Delta x^2} \\
&+ \frac{\mu u_x(x_i, y_{j+1}, t_n) - 2u_x(x_i, y_j, t_n) + u_x(x_i, y_{j-1}, t_n)}{\rho \Delta y^2} \\
&+ \frac{(\lambda + \mu) u_y(x_i, y_j, t_n) - u_y(x_{i-1}, y_j, t_n) - u_y(x_i, y_{j-1}, t_n) + u_y(x_{i-1}, y_{j-1}, t_n)}{\rho \Delta x \Delta y}
\end{aligned} \tag{3-53}$$

$$\begin{aligned}
& \frac{u_y(x_i, y_j, t_{n+1}) - 2u_y(x_i, y_j, t_n) + u_y(x_i, y_j, t_{n-1}))}{\Delta t^2} \\
&= b_y + \frac{(\lambda + 2\mu) u_y(x_i, y_{j+1}, t_n) - 2u_y(x_i, y_j, t_n) + u_y(x_i, y_{j-1}, t_n)}{\rho \Delta y^2} \\
&+ \frac{\mu u_y(x_{i+1}, y_j, t_n) - 2u_y(x_i, y_j, t_n) + u_y(x_{i-1}, y_j, t_n)}{\rho \Delta x^2} \\
&+ \frac{(\lambda + \mu) u_x(x_i, y_j, t_n) - u_x(x_{i-1}, y_j, t_n) - u_x(x_i, y_{j-1}, t_n) + u_x(x_{i-1}, y_{j-1}, t_n)}{\rho \Delta x \Delta y}
\end{aligned} \tag{3-54}$$

Consequently, the components of displacement in x- and y-directions can be explicitly updated in a timestepping scheme as:

$$\begin{aligned}
& u_x(x_i, y_j, t_{n+1}) \\
& = 2u_x(x_i, y_j, t_n) - u_x(x_i, y_j, t_{n-1}) + b_x \Delta t^2 \\
& + \frac{(\lambda + 2\mu)\Delta t^2}{\rho} \frac{u_x(x_{i+1}, y_j, t_n) - 2u_x(x_i, y_j, t_n) + u_x(x_{i-1}, y_j, t_n)}{\Delta x^2} \\
& + \frac{\mu\Delta t^2}{\rho} \frac{u_x(x_i, y_{j+1}, t_n) - 2u_x(x_i, y_j, t_n) + u_x(x_i, y_{j-1}, t_n)}{\Delta y^2} \\
& + \frac{(\lambda + \mu)\Delta t^2}{\rho} \frac{u_y(x_i, y_j, t_n) - u_y(x_{i-1}, y_j, t_n) - u_y(x_i, y_{j-1}, t_n) + u_y(x_{i-1}, y_{j-1}, t_n)}{\Delta x \Delta y}
\end{aligned} \tag{3-55}$$

$$\begin{aligned}
& u_y(x_i, y_j, t_{n+1}) \\
& = 2u_y(x_i, y_j, t_n) - u_y(x_i, y_j, t_{n-1}) + b_y \Delta t^2 \\
& + \frac{(\lambda + 2\mu)\Delta t^2}{\rho} \frac{u_y(x_i, y_{j+1}, t_n) - 2u_y(x_i, y_j, t_n) + u_y(x_i, y_{j-1}, t_n)}{\Delta y^2} \\
& + \frac{\mu\Delta t^2}{\rho} \frac{u_y(x_{i+1}, y_j, t_n) - 2u_y(x_i, y_j, t_n) + u_y(x_{i-1}, y_j, t_n)}{\Delta x^2} \\
& + \frac{(\lambda + \mu)\Delta t^2}{\rho} \frac{u_x(x_i, y_j, t_n) - u_x(x_{i-1}, y_j, t_n) - u_x(x_i, y_{j-1}, t_n) + u_x(x_{i-1}, y_{j-1}, t_n)}{\Delta x \Delta y}
\end{aligned} \tag{3-56}$$

Note that, the solving process in DEM involves application of Newton's second law for blocks and a force-displacement law at contacts in a time-marching algorithm that is mostly explicit. Therefore, calculation process in DEM follows same type of mathematical procedure.

3.5 FLUID MECHANICS

Mathematically, a Newtonian fluid is the simplest fluid in continuum mechanics models (Cengel and Cimbala 2006). The basic equations for incompressible Newtonian viscous fluids ($\nabla \cdot \mathbf{v} = 0$) are:

- Balance equations

$$\text{Conservation of mass: } \frac{D\rho}{Dt} + \rho \nabla \cdot \mathbf{v} = 0 \tag{3-57}$$

$$\text{Conservation of momentum: } \rho \frac{D\mathbf{v}}{Dt} = \nabla \cdot \boldsymbol{\sigma} + \rho \mathbf{b} \quad (3-58)$$

$$\text{Conservation of energy: } \rho \frac{D\mathbf{u}}{Dt} = \mathbf{D} : \boldsymbol{\sigma} - \nabla \cdot \mathbf{q} \quad (3-59)$$

- Constitutive equations

$$\sigma_{ij} = C_{ijkl}\varepsilon_{kl} - p\delta_{ij} \quad (3-60)$$

- Governing equations

$$\rho \left(\frac{\partial v_i}{\partial t} \right) + \rho \left(\frac{\partial (v_i v_j)}{\partial x_j} \right) = -\frac{\partial p}{\partial x_i} + \frac{\partial}{\partial x_j} \left[\mu \left(\frac{\partial v_i}{\partial x_j} + \frac{\partial v_j}{\partial x_i} \right) \right] + \rho b_i \quad (3-61)$$

In the case of assuming constant values of viscosity (μ) and mass density (ρ) for the fluid, the system of equation reduces to the Navier-Stokes equation:

$$\rho \frac{D\mathbf{v}}{Dt} = -\nabla p + \mu \nabla^2 \mathbf{v} + \rho \mathbf{b} \quad (3-62)$$

3.6 INITIAL AND BOUNDARY CONDITIONS

Governing equations are defined as partial differential equations or integral equations coupled with boundary conditions. There are different types of initial and boundary conditions that should be selected based on the specific problem. For example, one might specify the stresses along a distant boundary to be constant throughout the calculations, or define one of the boundaries as a zero displacement boundary.

3.7 DISCRETE ELEMENT METHODS

Whether it is in the class of continuum or discontinuum problems, a range of numerical methods are available (Munjiza et al. 2011). **Discrete Element Methods (DEM)** have become a widely used numerical method for discontinuous media. DEM permits finite displacement and rotations of discrete bodies including complete detachment, which are prerequisites for modeling issues such as aperture opening and shear slip during hydraulic fracturing in a discontinuous system. For this approach to modeling, the strain and displacement algorithms must be written to be able to detect new contacts or loss of contacts during the computations. DEM generally have the following features (Wang 1992):

- Discrete bodies are defined by explicit geometrical boundaries that may interact with other discrete bodies in the simulation only through their contacts;
- Large rotations and large displacements of blocks are allowed, although the contacts between bodies may have a strong cohesion that must be overcome before displacements or rotations can take place;
- New contacts may be formed and existing contacts lost during deformations, and these changes are explicitly recognized and tracked as the calculations continue;
- The solution algorithm is explicit in time, which allows the possibility of large deformations and non-linear constitutive behavior for both blocks and joints with little extra computational cost (although large simulations are extremely lengthy).

With the first two features, DEM can describe some important mechanisms like shear slippage, and therefore behavior laws such as a cohesion-friction model for shear slip must be specified for each contact. The last two attributes in the list above make the model generally applicable for discontinuous masses undergoing relative block movements.

DEM is a Lagrangian numerical method (i.e., discretization follows deformation), which was first introduced by Cundall in 1971 (Cundall 1971) and then further developed by others including Williams, Hocking and Mustoe (Williams et al. 1985). DEM uses a time-marching scheme to solve the equations of motion directly for an assemblage of shapes defined through their contacts. In DEM, the equilibrium equations do not need to be assembled into a large global matrix to solve the equations of the whole domain for each time step, and thus the problem can be solved through a step-by-step procedure using the discretized equations of motion. Thus, DEM has two advantages compared to continuum modeling methods: (i) complex problems can be run on a PC due to small computer storage memory requirements of this method; (ii) displacements of contacts and rotations of blocks can be directly taken into account for each timestep with appropriate contact detection algorithms. The global matrix representing complete block interconnectivity is never assembled, which makes the calculations computationally economic (Zhang and Sanderson 2002). However, the time steps must be small for stability and for problems involving large numbers of discrete elements (blocks or shapes), that is, a large number of contacts, the number of calculations is large, and execution time for large problems may be days to weeks on a PC.

The fundamental concepts incorporated into DEM models are Newton's laws of motion, constitutive models for contacts in normal and shear displacement, and the timestepping scheme that is explained below (Wang 1992):

- The unbalanced forces on a block at any instant in time will lead to accelerations that transfer the block to new coordinates in a small time stem, based on Newton's laws of motion. When these forces are fully balanced for all blocks in the model, the system is at rest (equilibrium) or experiencing a constant velocity (no inertial forces).

- Interaction forces between blocks result from block movements at contacts according to a force-displacement constitutive law stipulated for each contact.
- Block overlaps are usually negligible relative to block dimensions because of the high stiffness of an interpenetrating contact stimulated in the contact laws.
- Block deformation under applied forces is calculated by discretizing the blocks into constant-strain finite elements during the meshing process, and the interior strains can thus be calculated for each new state (for each timestep or after a specified number of timesteps).

Each physical process has a domain and a boundary, which in a mathematical formulation are implied as differential equations and boundary conditions. The main concept in DEM is that the domain of a physical process is represented by the specified assemblage of rigid or deformable blocks/bodies/particles interacting at their boundaries (Cundall 1971). The term block may stand for individual rock grains or any intact area (or volume in 3D) surrounded by natural fractures or specified planes of weakness within the domain. For example, the deformation of a brick wall, even its toppling, can be analyzed in the DEM formulation as a family of blocks defined by their contacts. In this case, as in a naturally fractured rock mass, the interface between the bricks is called a “contact” and is considered as a joint, which, before it is opened, may be viewed as a planar contact (a surface-to-surface contact in Figure 3.8). Therefore, in the context of a DEM model, the terms contact and joint are to some degree used interchangeably, although when a joint is fully opened by a high-pressure fluid during injection, it no longer makes contact with the adjacent block.

Blocks can be generated in different shapes, giving different types of rock fabric, and this may be varied to study different cases considered to be reasonable representations of the actual rock mass. Thus, it is possible to specify the fabric with any number of explicit patterns that have somewhat different characteristics. In the current study, polygonal block models or Voronoi tessellated rock fabrics were first considered because they provide a reasonably realistic representation of rock macro-structure (Lemos 2012), and are similar to the joint patterns seen in some igneous rock bodies such as granites and columnar basalts. However, to fulfill the main objective of the research, blocks are generated in other fabrics as well to represent rock masses with strong directional structures, such as dominant sets of joints of substantial length.

On loading of a DEM model, the jointed rock mass is treated as a series of blocks (Figure 3.10) with displacement possible only along and across joints. The deformation behavior of the rock block system is mainly controlled by relative movements between blocks (Zhang and Sanderson 2002), but in this work, no provision is made for the generation of a new fracture across any block.

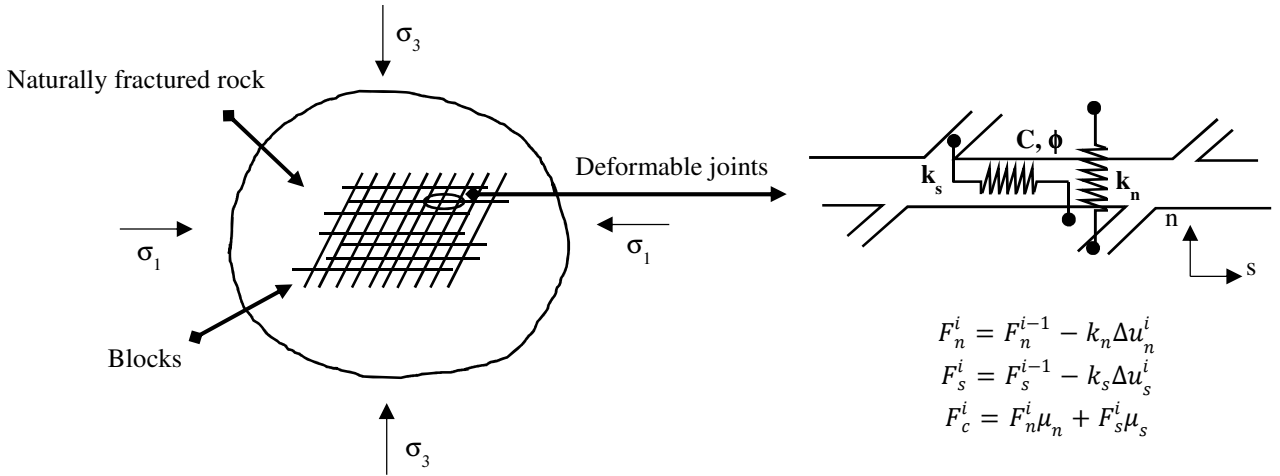


Figure 3.10. Constitutive law for each contact. k_n and k_s are joint normal and shear stiffness. C and ϕ are joint cohesion and friction angle. (F_n, u_n) and (F_s, u_s) are components of the force-displacement law in normal and shear directions (n, s) . F_c is the total contact force and i is the time step at which calculation starts (Asgian 1989).

3.7.1 CONTACT BETWEEN TWO BODIES

Based on the theory of simple impacts in physics, when two bodies with a certain mass and velocity interact, the post-interaction behavior can be explained in terms of initial mass and velocity of the bodies and the energy loss during the impact. The energy loss may occur in different forms of energy such as mechanical energy and in terms of deformation. Based on the material behavior, the deformations can be temporary (elastic state) or permanent (plastic state), or some component of each. The force resulting from the contact interaction is used to calculate the stresses and strains of the system (Carles 2014). Contact detection and contact interaction are the most important aspects of DEM, and there are several algorithms introduced for contact detection. Details on this subject can be found in a book by Munjiza (Munjiza 2004).

3.7.1.1 CONTACT CONSTITUTIVE LAWS

As previously mentioned, the information about the contacts is essential to compute the stresses and strains of a system. Contact constitutive laws govern the mechanical behavior (normal and tangential displacements) of two contacting blocks and as a result the mechanical behavior of a DEM model (Kazerani and Zhao 2010). Regardless of whether blocks are rigid or deformable in themselves, a contact law must be stipulated to define the interaction between them. Several contact laws have been introduced so far in the context of particle modeling.

Soft contact model is the starting point of the DEM. Blocks are considered as rigid bodies. Small overlaps are allowed in this model. The interaction force can be computed by a contact law and block motions can be defined by dynamic equations (Newton's second law) (Carles 2014).

For a finite element discretization, each block is deformable and would be discretized into many elements. Therefore, contact interaction is studied in a smaller area of impact and gives more realistic results (especially under high stress changes, the deformation of real rock blocks is not negligible). However, the computational cost increases dramatically with a fine discretization because of the large number of bodies and elements involved (Carles 2014).

The solution process in the DEM involves application of Newton’s second law for blocks and a force-displacement law at contacts. A force-displacement law is used to find contact forces from known displacements. Newton’s second law gives the motion of the blocks resulting from the known forces acting on them (Kazerani and Zhao 2010).

Force-displacement law

The law of force-displacement gives a relation between the relative displacement and the local contact force exerted on contacts. The contact force is broken down into normal and tangential components (Figure 3.11).

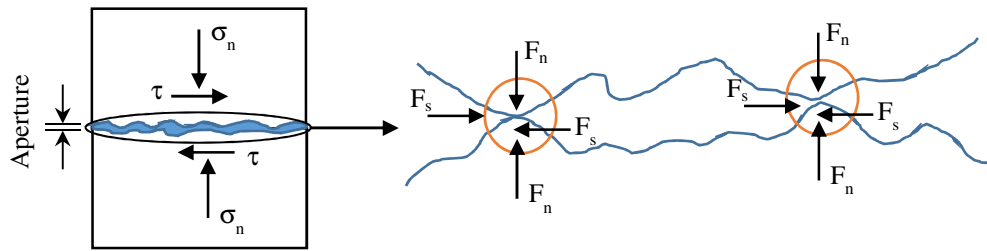


Figure 3.11. Normal and tangential forces applied on contacts.

The Coulomb-slip model is the conventional model used to describe joint slip based on the concepts of joint cohesion and friction, effective stress and stress orientation. Figure 3.12a shows the concept of a joint that is oriented favorably with respect to the possibility of experiencing shear slip in a specified principal stress field value and orientation. The joint is pressurized by fluid at pressure p . According to the Coulomb criterion, the conditions for slip are met when $\tau = \mu(\sigma_n - p)$, in the absence of any bonding (cohesive) resistance. The term $(\sigma_n - p)$ is called the effective stress. The Coulomb criterion specifies that slip may occur under some combination of three processes: a decrease of the total normal stress, an increase of the pore pressure in the discontinuity, and an increase of the shear stress. In DEM simulations of hydraulic fracturing, for example, before fluid injection the initial stress state is specified so that the model is static and stable; thereafter, pressurization associated with injection of a fluid could cause changes in the stress such that the slip condition is met for the specified joint (contact) (Figure 3.12b). The effective stress acting over an area gives the effective normal force, F_n .

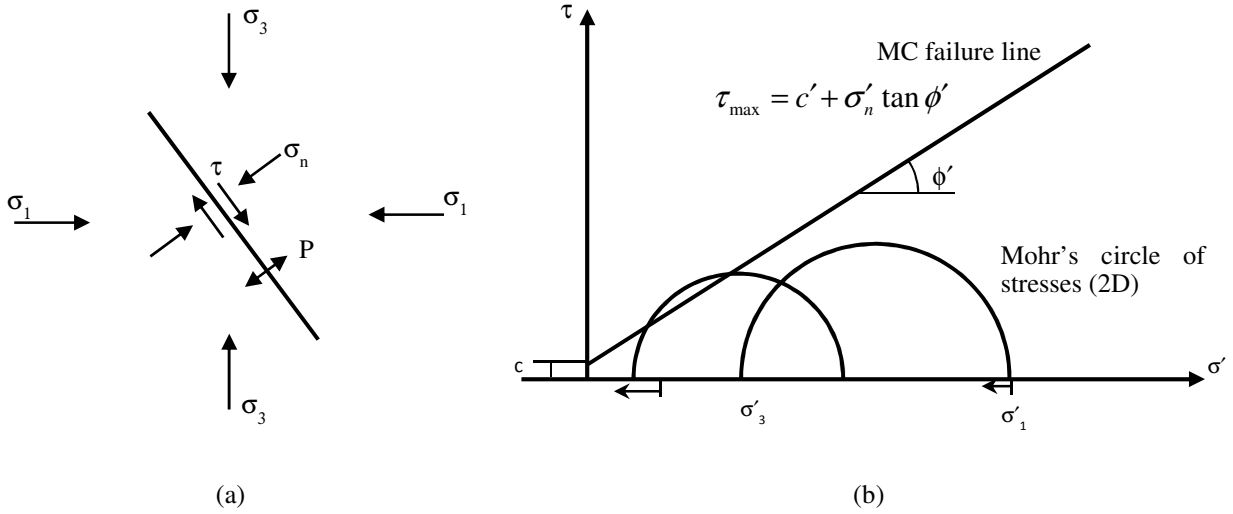


Figure 3.12. a) Favorably oriented joint; b) Mohr-Coulomb shear mechanism (Dusseault 2015).

Normal displacement can be taken as a first approximation to be linearly related to the effective normal force such that:

$$\Delta F_n = -k_n \Delta u_n \quad (3-63)$$

where ΔF_n is the effective normal force increment, Δu_n is the displacement increment and k_n is the joint normal stiffness. There is also a threshold value for tensile strength, F_n^{max} , for any contact. If the tension exceeds this value, i.e. $F_n \leq -F_n^{max}$, then $F_n = 0$. In the case that contacts undergo compression, blocks may overlap, which is controlled by contact normal stiffness, k_n (Kazerani and Zhao 2010). Note that in reality, k_n can be strongly non-linear, and generally an extremely high k_n is used to minimize overlap during compression.

The shear force, F_s , is constrained by a combination of contact cohesion (C) and friction angle (ϕ) such that:

If,

$$|F_s| \leq C + F_n \tan \phi = F_s^{max} \quad (3-64)$$

then,

$$\Delta F_s = -k_s \Delta u_s^e \quad (3-65)$$

If,

$$|F_s| \geq F_s^{max} \quad (3-66)$$

then,

$$F_s = \text{sign}(\Delta u_s) F_s^{\max} \quad (3-67)$$

where Δu_s is the total incremental shear displacement and Δu_s^e is the elastic component of the incremental shear displacement (Kazerani and Zhao 2010). Figure 3.13 shows schematics of joint mechanical deformation mechanisms.

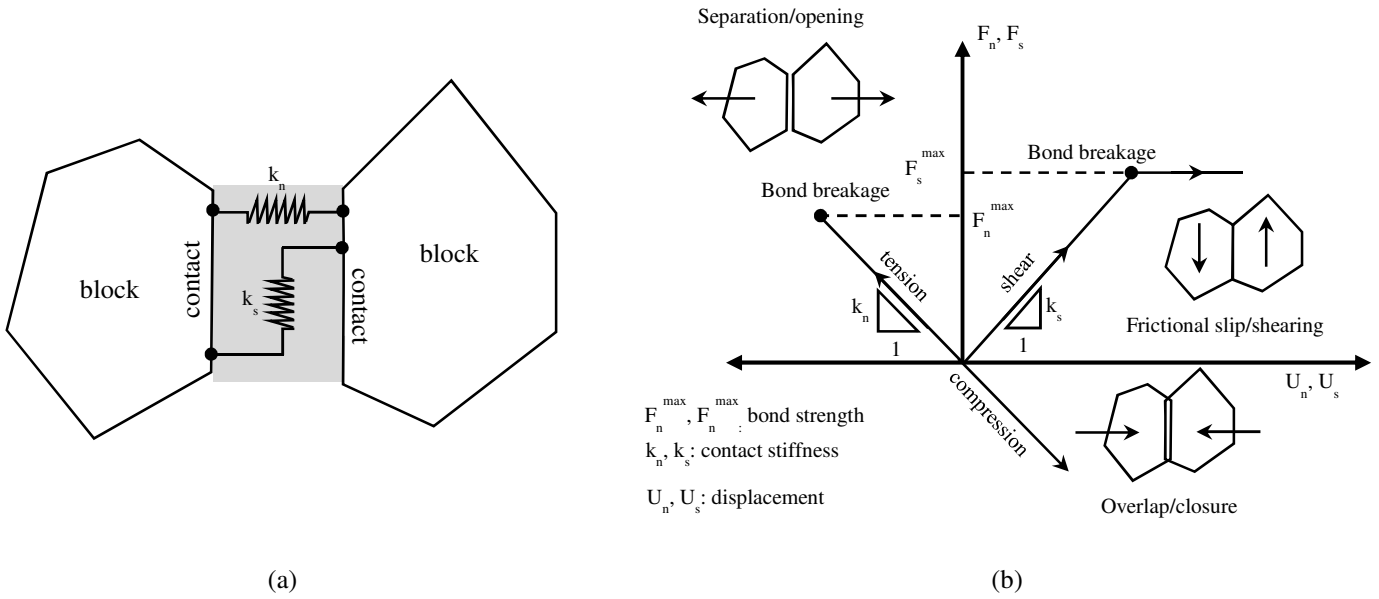


Figure 3.13. Joint mechanical deformation in rock. a) Normal and shear stiffness between rocks. b) Constitutive behavior in shear and tension (Lisjak and Grasselli 2014). All springs may be non-linear.

Frictional forces result from the adhesion of sliding/sticking contacts and they are applied in the opposite direction of displacements (Luding 2008). The Coulomb friction model is the most common model for implementation of friction in the DEM (Carles 2014). The tangential force is coupled to the normal force by a Coulomb friction law. Based on the Coulomb friction law, the frictional portion of the tangential force is given by (Favier et al. 2009):

$$F_s^{fric} = \mu F_n \quad (3-68)$$

where μ is the friction coefficient (Figure 3.14). Following the Coulomb friction law, the tangential contact force is the minimum value between the F_s^{fric} and F_s .

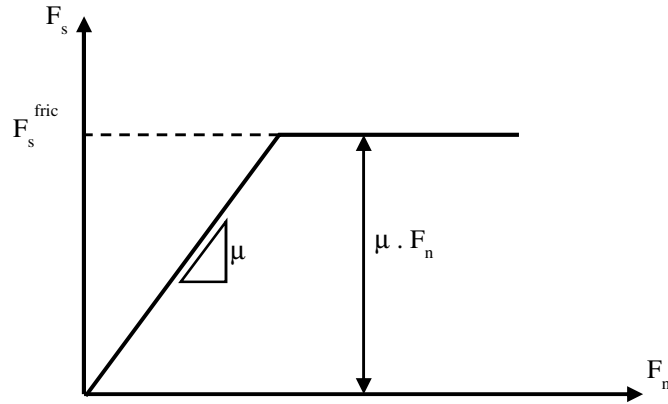


Figure 3.14 Coulomb friction law for computing contact tangential force (Favier et al. 2009).

3.7.2 THE UNIVERSAL DISTINCT ELEMENT CODE (UDECTM)

According to the solution algorithm used, DEMs can be divided into two groups, explicit and implicit formulations. Many of the numerical representations of the explicit DEM are implemented with **The Universal Distinct Element Code (UDECTM)** (Kazerani and Zhao 2010). UDECTM, developed by the ITASCA Consulting Group, is an implementation of the Discrete Element Method for blocks in a two-dimensional framework. UDECTM has the ability to perform analysis of fluid flow through the discontinuities of a system of impermeable blocks. Flow in discontinuities is modeled as flow between domains. Domains are the regions of space between blocks, which are separated by contacts.

3.7.2.1 Basic definitions in UDECTM

In the standard configuration of a UDECTM model, a rock mass is represented as a series of distinct **blocks** that can be rigid or deformable. Commonly, rigidity is assumed for solid materials in which deformation is negligible. All blocks are rigid by default; they are made deformable by discretizing specified blocks into constant-strain finite-difference triangular elements (**zones**) during the meshing process. Joints are represented numerically as **contacts** or interfaces between blocks. Adjacent blocks can touch along an edge segment (edge-edge contacts) or at discrete points (corner-corner or corner-edge contacts). Domains are the regions of space between blocks, which are separated by contact points. Flow in joints is modeled as flow between domains (Batchelor 1967). Figure 3.15 depicts these definitions.

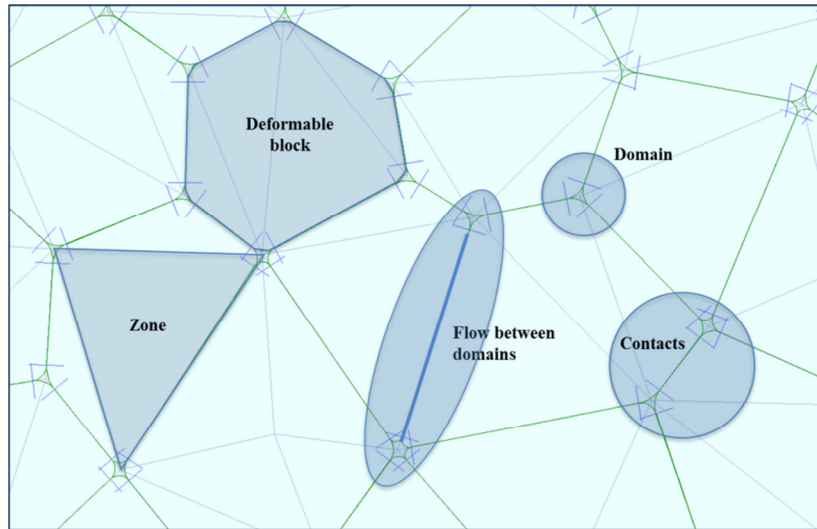


Figure 3.15. Schematic of block, contact, zone and domain in UDECTM (ITASCA Consulting Group Inc. 2010).

3.7.2.2 Mechanical interactions between blocks

In deformable blocks, point contacts are created at all gridpoints located on the block edge in contact with another block. Contact points are updated automatically as block motion occurs. UDECTM identifies blocks and their locations through time by tracking the contact coordinates. Forces of mechanical interaction between blocks are only applied at contacts (Batchelor 1967).

The law of motion for each block, a force-displacement law for each contact and a continual updating of gridpoints' coordinates in a time-marching algorithm defines the calculation cycle in UDECTM. Each timestep starts with updating contact coordinates with known displacements. A force-displacement law is used to find contact forces from these known displacements. The contact constitutive model chosen for each contact affects the contact's response to the force. Newton's second law gives the motion of the blocks resulting from the known forces acting on them. Velocities and positions of gridpoints are updated. For the deformable blocks, motion is calculated at the gridpoints of the triangular constant-strain elements within the blocks. Then, the application of the block material constitutive relations gives new stresses within the elements (Jing and Stephansson 2007). Figure 3.16 shows the calculation algorithm for one timestep in UDECTM.

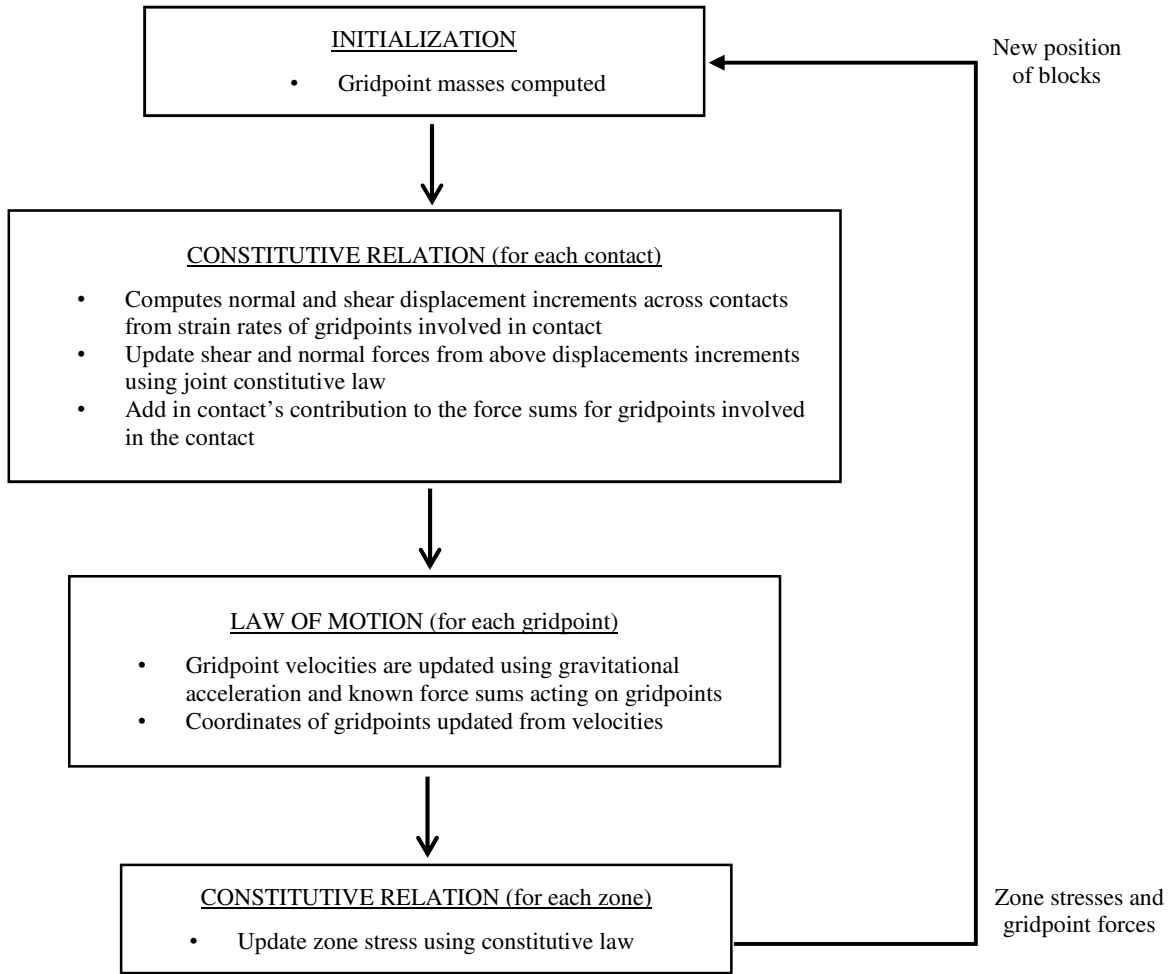


Figure 3.16. Solution algorithm for each timestep in UDEC™ (ITASCA Consulting Group Inc. 2010).

Newton's second law can be written for the one-dimensional motion of a single mass acted on by force \mathbf{F} , as:

$$\frac{\mathbf{F}^{(t)}}{m} = \frac{d\dot{\mathbf{u}}}{dt} \quad (3-69)$$

where $\dot{\mathbf{u}}$ is the velocity, t is time and m denotes mass.

The equations of motion for gridpoints of zones within the deformable blocks are identical to those for the centroids of rigid blocks, except that rotational terms are neglected for gridpoints. An explicit central finite difference scheme is used to solve the left-hand side of Newton's second law through time (more details are provided in section 3.4.4). Block velocities and displacements are determined by integration over increments in time. In the central difference scheme, the equilibrium of the system at time t is considered to calculate the displacement at time $t + \Delta t/2$ (Kazerani and Zhao 2010).

$$\frac{d\dot{\mathbf{u}}}{dt} = \frac{\dot{\mathbf{u}}^{(t+\Delta t/2)} - \dot{\mathbf{u}}^{(t-\Delta t/2)}}{\Delta t} \quad (3-70)$$

re-arranging

$$\dot{\mathbf{u}}^{(t+\Delta t/2)} = \dot{\mathbf{u}}^{(t-\Delta t/2)} + \frac{\mathbf{F}^{(t)}}{m} \Delta t \quad (3-71)$$

The solution for the nodal point displacements at time $t + \Delta t/2$ is obtained using the central difference approximation for the accelerations with velocities stored at the half-timestep point:

$$\dot{\mathbf{u}}^{(t+\Delta t)} = \mathbf{u}^{(t)} + \dot{\mathbf{u}}^{(t+\Delta t/2)} \Delta t \quad (3-72)$$

Since the force depends on displacement, the force-displacement calculation is done at one time instant. For blocks in two dimensions acted on by several forces as well as gravity, the velocity equation is (Kazerani and Zhao 2010):

$$\dot{\mathbf{u}}_i^{(t+\Delta t/2)} = \dot{\mathbf{u}}_i^{(t+\Delta t/2)} + \left(\frac{\sum \mathbf{F}_i^{(t)}}{m} + \mathbf{g}_i \right) \Delta t \quad (3-73)$$

where $\dot{\mathbf{u}}_i$ is the velocity component of the block centroid;

\mathbf{g}_i is the component of gravitational acceleration (body forces);

the subscript i denotes the component in a Cartesian coordinate system; and,

the superscripts denote time at which the corresponding variable is evaluated.

The new block location is identified using the updated velocities (Kazerani and Zhao 2010):

$$\mathbf{x}_i^{(t+\Delta t)} = \mathbf{x}_i^{(t)} + \dot{\mathbf{u}}_i^{(t+\Delta t/2)} \Delta t \quad (3-74)$$

where x is the coordinate of the block centroid.

The deformability of deformable blocks is governed by the assigned constitutive (i.e., stress-strain) relation. During each timestep, zone strain increments are calculated as:

$$\Delta \varepsilon_{ij} = \frac{1}{2} (u_{i,j} + u_{j,i}) \Delta t \quad (3-75)$$

The application of the constitutive relation for deformable blocks (equation (3-32)) gives the new zone stresses.

$$\Delta\sigma_{ij} = \lambda\varepsilon_{kk}\delta_{ij} + 2\mu\varepsilon_{ij} \quad (3-76)$$

In summary, each time step produces new block positions that generate new contact forces. In determining the forces acting on a gridpoint, the stresses in surrounding zones are accounted for by integrating over a surface, S , enclosing the gridpoint:

$$\mathbf{F}^Z = \int_{S_e} \sigma_{ij}n_j ds_e \quad (3-77)$$

where S_e is the surface enclosing the mass of surrounding elements at the gridpoint and n_j is the unit normal to S_e . The total force acting on a gridpoint is the result of all external forces applied to the gridpoint, plus the contribution from surrounding zones, F^Z . The resultant of all external forces applied to the gridpoint, \mathbf{F} , is given as:

$$\mathbf{F} = \mathbf{F}^Z + \mathbf{F}^c + \mathbf{F}^l \quad (3-78)$$

where F^Z is calculated from the contribution of the internal stresses in the zones adjacent to the gridpoints; F^c results from the contact forces; and F^l is the external load.

The procedure is repeated until either a satisfactory state of equilibrium or one of continuing failure results (Kazerani and Zhao 2010).

3.7.2.3 Momentum balance

Consider two bodies, denoted by subscripts a and b, that are in contact for a period of time (Zhang and Sanderson 2002); based on Newton's law, the force \mathbf{F} acts in opposite directions on the two bodies:

$$m_a\ddot{\mathbf{u}}_a = \mathbf{F} \quad \text{and} \quad m_b\ddot{\mathbf{u}}_b = -\mathbf{F} \quad (3-79)$$

combining the equations and integrating:

$$\int_0^T m_a\ddot{\mathbf{u}}_a dt = -\int_0^T m_b\ddot{\mathbf{u}}_b dt \quad (3-80)$$

$$m_a \dot{\mathbf{u}}_a^{(T)} + m_b \dot{\mathbf{u}}_b^{(T)} = m_a \dot{\mathbf{u}}_a^{(0)} + m_b \dot{\mathbf{u}}_b^{(0)} \quad (3-81)$$

According to this equation, the total momentum at the end of the time period is identical to that at the beginning (conservation of momentum).

3.7.2.4 Energy balance

Assume that a body with initial velocity of $\dot{\mathbf{u}}_0$ is brought to a final velocity of $\dot{\mathbf{u}}$ in a distance, S , by a constant force, \mathbf{F} , such that (Zhang and Sanderson 2002):

$$m\ddot{\mathbf{u}} = \mathbf{F} \quad (3-82)$$

Using the definition of acceleration and assuming that m is constant:

$$\frac{1}{2}m(\dot{\mathbf{u}}^2 - \dot{\mathbf{u}}_0^2) = \mathbf{F} \cdot \mathbf{S} \quad (3-83)$$

This equation indicates that the work done by the constant force, \mathbf{F} , is equal to the change in kinetic energy of the body.

3.7.2.5 Fluid flow

UDECTM has the ability to perform analysis of fluid flow through the fractures of a system of impermeable blocks, which is numerically implemented by a network of domains. Flow in joints is modeled as flow between domains. Each domain is assumed to be filled with fluid at a uniform pressure in the absence of gravity. Fluid flow is governed by the pressure differential between neighboring domains and flow rate can be calculated on the basis of contact type (ITASCA Consulting Group Inc. 2010). For a point contact, the flow rate is given by:

$$q = -k_c \Delta p \quad (3-84)$$

where k_c is a point contact conductivity factor and Δp is the pressure change over a fracture length.

In the case of an edge contact, the cubic law is used for flow in a planar fracture:

$$q = -k_j a^3 \frac{\Delta p}{l} \quad (3-85)$$

where a is the contact hydraulic aperture; l is the contact length defined as the sum of half the distance to the nearest contacts to the left and right; k_j is the joint conductivity factor; and $\frac{\Delta p}{l}$ is the pressure gradient. Joint conductivity factor is given by:

$$k_j = \frac{1}{12\mu} \quad (3-86)$$

where μ is fluid dynamic viscosity; and Δp is the pressure drop

$$\Delta p = p_2 - p_1 + \rho_w g (y_2 - y_1) \quad (3-87)$$

where p_1 and p_2 are domain pressures, ρ_w is the fluid density, g is the acceleration of gravity and y_1 and y_2 are domain y-coordinates. For problems with gravity, the fluid pressure is assumed to be linearly changing according to the hydrostatic gradient. This indicates that fluid flow may take place even when both domain pressures are zero (Hart 1991).

Hydraulic aperture is usually given by:

$$a = a_0 + u_n \quad (3-88)$$

where a_0 is the joint aperture at zero normal stress and u_n is the joint normal displacement (ITASCA Consulting Group Inc. 2010). Figure 3.17 shows the relation between hydraulic aperture and joint normal stress.

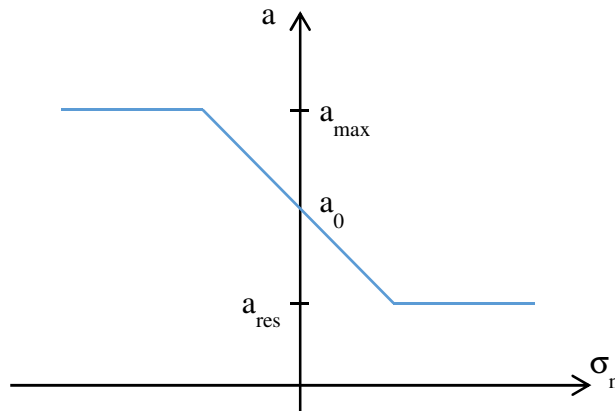


Figure 3.17. Relation between hydraulic aperture and joint normal stress (ITASCA Consulting Group Inc. 2010).

New values of aperture for all contacts and volumes of all domains are computed by updating the geometry of the system after each time step in the mechanical calculations. Also, flow rates and domain pressures should be updated. The new domain pressure after a timestep Δt is given by:

$$p = p_0 + K_w Q \frac{\Delta t}{V} - K_w \frac{\Delta V}{V_m} \quad (3-89)$$

where p_0 is the domain pressure in the preceding timestep;

Q is the sum of flow rates into the domain from all surrounding contacts;

K_w is the fluid bulk modulus;

$\Delta V = V - V_0$, V and V_0 are the new and old domain volumes, respectively; and

$V_m = (V + V_0)/2$.

Possible changes in domain pressure come partly from domain volume variations, which result from the incremental motion of adjacent blocks.

Using the new domain pressures, the forces exerted by the fluid on the edges of the adjacent blocks can be obtained and then can be added to the other forces applied on the block gridpoints (i.e., mechanical contact forces and external loads). Consequently, total stresses are obtained for inside the blocks and effective normal stress for the contacts (ITASCA Consulting Group Inc. 2010). This achieves a level of hydro-mechanical coupling that is adequate for modeling jointed rock masses where the fluid flux within blocks is negligible.

3.7.2.6 Numerical damping

Dynamic systems subjected to driving forces would oscillate forever without damping. Natural dynamic systems have some degree of damping in the form of gradual (or very sudden) suppression of vibrational energy in the system (Figure 3.18). Damping is used for both static and dynamic problems in order to reach a steady-state solution. Damping may occur either in contacts or blocks or in both. Part of the rationale for using strong damping in contacts is because of energy loss due to slip along contacts and because of internal friction loss in the intact material (Hart 1991).

Static problems need more damping than dynamic ones. Mass-proportional damping or viscous damping applies a force to gridpoints of deformable blocks. This force is proportional to the (mass) velocity but in the opposite direction. Another damping method is the stiffness-proportional method, which applies a force to contacts or a stress in zones. This force/stress is proportional to the incremental force or stress (Hart 1991). A damping matrix, C , is defined as:

$$C = \alpha M + \beta K \quad (3-90)$$

where M is the mass matrix, k is the stiffness matrix, α and β are the mass and stiffness proportional damping constants.

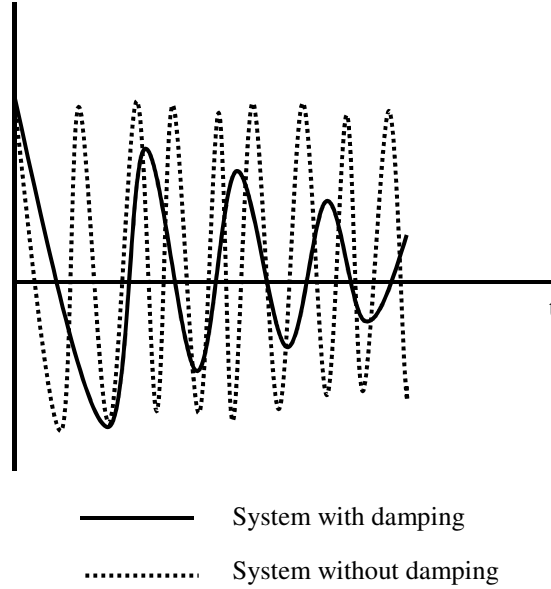


Figure 3.18. Concept of damping.

For quasi-static problems, only mass-proportional damping is generally used in UDECTM. UDECTM provides an automated or adaptive damping scheme which does not require user specification of damping constants. This scheme adjusts the mass damping constant, α , to the conditions which occur during solution. The scheme tracks the rate of energy change in the body during solution.

3.7.2.7 Numerical Stability in UDECTM

Mechanical time step and numerical stability

The explicit finite difference solution procedure used for the deformable blocks is only conditionally stable, therefore the critical timestep should satisfy both of the stability criteria for zone deformation and contact displacement. The timestep required for the stability of the zone computations is estimated as (Board 1989):

$$\Delta t^z = 2 \min \left[\frac{M_i}{K_i} \right]^{1/2} \quad (3-91)$$

where M_i is the mass of node i and K_i is a measure of stiffness of the elements around the node i .

The timestep required for the stability of the contact displacement is estimated as (Board 1989):

$$\Delta t^b = FRAC 2 \left[\frac{M_{min}}{2K_{max}} \right]^{1/2} \quad (3-92)$$

where M_{min} is the smallest block mass in the problem and K_{max} is the largest contact stiffness. FRAC stands for the fact that a block is in contact with several blocks. This constant is supplied by a user and is typically 0.1 (Wang 1992).

The critical mechanical time step is finally chosen as:

$$\Delta t^m = \min(\Delta t^z, \Delta t^b) \quad (3-93)$$

Hydraulic time step and numerical stability

The numerical stability of the fluid flow algorithm, for slowly varying domain areas, requires that the time step be limited to (Board 1989):

$$\Delta t^f = \min \left[\frac{A_i}{K_w \sum K_i} \right] \quad (3-94)$$

where the $\sum K_i$ is extended to all contacts surrounding the domain with area, A_i , and

$$K_i = \max(k_c, k_j a^3 / l) \quad (3-95)$$

where k_c is a contact conductivity factor;

k_j is joint conductivity factor;

K_w is fluid bulk modulus;

l is contact length;

and a is contact aperture;

For joint contacts (edge-edge), the domain area is the product of joint length and aperture. Because the minimum joint aperture is a_{res} , the domain area is always positive, even if the blocks are overlapping.

The minimum value of Δt^f is compared to the critical time step determined from the mechanical part of the model, Δt^m . The minimum defines the critical time step for the coupled hydro-mechanical analysis. A minimum domain area can be set for computational efficiency.

Finally, the time step is selected as:

$$\Delta t = \min(\Delta t^m, \Delta t^f) \quad (3-96)$$

3.7.2.8 *Material properties*

There are many choices of constitutive models available in UDECTM for representing material behavior of both joints and blocks. However, a problem analysis should always start with simple block and joint material models. Two aspects should be considered in choosing an appropriate constitutive model (Hudson and Harrison 1997):

- Known properties of the corresponding material
- Purpose of the analysis

The elastic block model and Mohr-Coulomb model are two of the most well-known block material models. The elastic, isotropic model is effective for homogenous, isotropic, continuous materials that show approximately linear stress-strain behavior. This model is usually applied in cases in which slip along discontinuities is the principal mechanism for failure. The Mohr-Coulomb failure criterion is commonly used for materials that yield under shear loading. The yield stress in this model only depends on major and minor principal stresses and the intermediate principal stress is assumed to have no influence. This constitutive model is widely used in underground mine analysis (Hudson and Harrison 1997). Using a Mohr-Coulomb block model, the following material properties are required (Keilich 2009):

- Density (kg/m^3);
- Young's Modulus (GPa);
- Poisson's Ratio;
- Bulk Modulus (GPa);
- Shear Modulus (GPa);
- Friction angle ($^\circ$);
- Dilation angle ($^\circ$);
- Cohesion (MPa); and
- Tensile Strength (MPa).

Typically, rock material properties are obtained either from tests or literature. One reference for these parameters could be (Fjaer et al. 2008).

The types of models available to characterize the physical response of rock discontinuities are limited and the Coulomb slip and Barton-Bandis joint models are generally used in rock mechanics. The Barton-Bandis failure criterion is a nonlinear empirical equation used to model shear strength of rock discontinuities and requires more detailed knowledge of joint behavior. Due to the complexity of this criterion, it is always recommended to first perform modeling based on the Coulomb-slip joint model to gain better understanding of joint behavior (Hudson and Harrison 1997). In the Coulomb-slip model, dilation is governed by a dilation angle, ψ . The Coulomb slip joint model is illustrated in Figure 3.19.

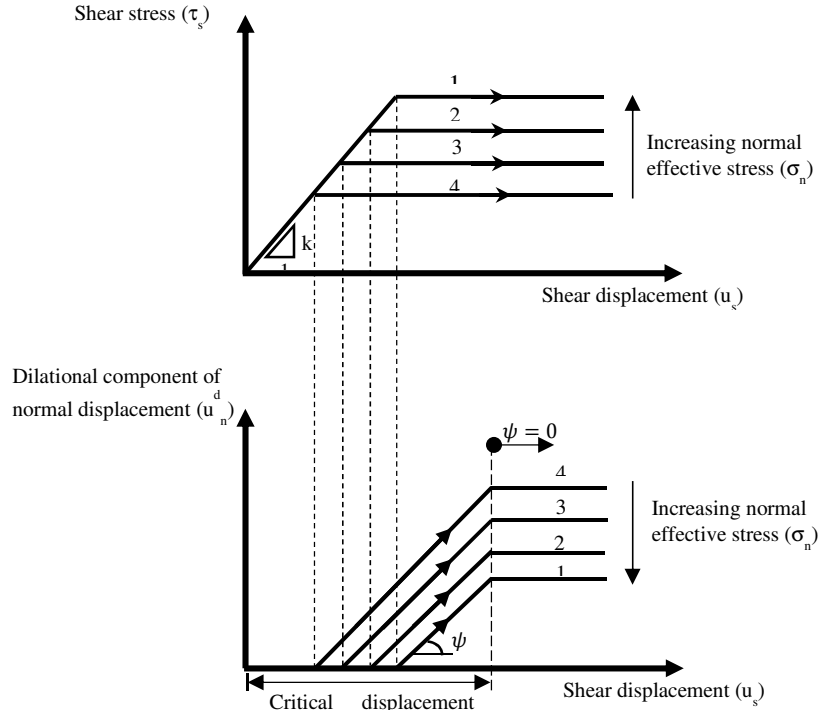


Figure 3.19. Basic joint behavior model used in UDEC™ (ITASCA Consulting Group Inc. 2010).

3.7.2.9 Joint material properties

The material properties assigned to joints in a DEM model must represent both the stiffness and strength of the real joints. These properties consist of joint friction angle, cohesion, dilation angle and tensile strength, as well as joint normal and shear stiffnesses. Joint properties are conventionally derived from tests on real joints (e.g., triaxial and direct shear tests) or from published data on materials similar to those being modeled. Stiffness properties (i.e., normal stiffness, k_n , and shear stiffness, k_s) are of essential importance. Joint stiffness can play an important role in the mechanical response and values must be selected carefully. A good rule of thumb is that k_n and k_s should be kept smaller than ten times the equivalent stiffness of the stiffest neighboring zone in blocks adjoining the joint (Hart 1991):

$$k_n \text{ and } k_s \leq 10 \left[\max \left[\frac{K + 4/3 G}{\Delta z_{\min}} \right] \right] \quad (3-97)$$

where K and G are bulk and shear moduli respectively to the block material, and Δz_{\min} is the smallest width of the zone neighboring the joint in the normal direction. If the joint stiffnesses are greater than 10 times the equivalent stiffness, the solution time of the distinct element model

will be significantly longer than for the case in which the ratio is limited to ten, without a significant change in the behavior of the system (Hart 1991).

In order to improve solution efficiency, small values of shear and normal stiffness should be selected. Joint normal stiffness can be estimated from:

$$u_n = \sigma_n / k_n \quad (3-98)$$

This displacement should be small compared to a typical zone size. If it is greater than 10% of an adjacent zone size for example, then either there is an error in one of the numbers, or the stiffness should be increased (Hart 1991). Values for normal and shear stiffnesses for rock joints can typically range from roughly 10 to 100 MPa/m for joints with soft clay in-filling to over 100 GPa/m for tight joints in granite and basalt. Published data on stiffness properties for rock joints are limited. Summaries of data can be found in (Kulhawy 1975), (Rosso 1976), and (Bandis et al. 1983).

Published strength properties for joints are more readily available than stiffness properties. Summaries can be found, for example, in (Jaeger et al. 2007), (Kulhawy 1975), and (Bandis et al. 1983). Friction angles can vary from less than 10° for smooth joints in weak or clayey rock, such as tuff, to over 50° for rough joints in hard rock, such as granite. Joint cohesion can range from zero cohesion to values approaching the compressive strength of the surrounding rock. Dilation angles for rock are typically low and less than the friction angle and most values are between 0° and 20° (Hart 1991).

Scale dependence of joint properties is a major question in rock mechanics. Often, the only way to guide the choice of appropriate parameters is through comparison to similar joint properties derived from field tests. However, field test observations are extremely limited (Hart 1991). Some results are reported by (Kulhawy 1975).

3.8 SUMMARY

Rock is a heterogeneous material with natural fractures and other features that make it unfeasible to attempt to simulate the exact behavior of the rock and its natural fracture fabric. Some level of simplification or homogenization is needed. This study tries to make reasonable simulations that still allow the emulation of the behavior of rock masses with natural fractures. An “emulation” in this sense is an attempt to capture and model important behavior with less of a physical link to the rock mass than in the case of a “simulation”. Results from emulations are considered to be more an aspect of “history matching” than a physically correct representation of a particular case. To this end, UDECTM was used in carrying out coupled hydro-mechanical analyses of models of naturally fractured rock masses being subjected to hydraulic fracture injection.

There are some advantages and disadvantages in using UDECTM for hydraulic fracture modeling. One advantage is that coupled hydro-mechanical analysis can be performed under different loadings (fluid pressure or in-situ stresses) via UDECTM. Another merit of using UDECTM is that pre-existing natural fractures can be incorporated and undergo large mechanical deformations. Furthermore, fracture modes, i.e. shearing and opening, are allowed. While most of the models oversimplify the rock mass as an equivalent continuum, UDECTM treats it as a discontinuum. From another aspect, UDECTM is a two-dimensional interface, which means that simulations may not be ideally close to reality especially in some particular cases. In such problems, three-dimensional codes may offer a better means of studying the interconnectivity between natural and hydraulically-driven fractures and can more closely represent the three-dimensional nature of the process. However, generating three-dimensional geometries is computationally demanding and requires much more execution time than two-dimensional models, even for modest problems. Because generating different fabrics was chosen to be one of the main parts of the current study, it was decided to continue with UDECTM.

UDECTM is not capable of creating new fractures, but can only assist with the opening and shearing of pre-existing fractures. However, because the current research is focused on hard low-permeability naturally fractured rocks such as jointed igneous rock masses or dense shale gas rock masses, where there is little tendency to fracture intact rock and generate a new fracture, UDECTM should be adequate to study the effect of different rock fabrics. Hence, that limitation would not be an issue for this particular research or for similar studies.

For the current study, DEM is deemed to be an appropriate approach to modeling the hydraulic fracturing process in a naturally fractured rock mass. Despite the fact the models are two-dimensional, UDECTM sufficiently represents a real medium with the inherent fabric of discontinuities, and is computationally efficient. Simulations for the research carried out in this thesis have exclusively used UDECTM to study the behavior of a fractured system during hydraulic fracturing under different conditions.

Finally, although it is possible to specify the constitutive behavior of each joint in these DEM analyses, or to use a statistical generator to achieve more realistic probabilistic distributions of joint properties, or to assign very different properties to different joint sets, it was decided to choose one constitutive relationship for all joints so that any probabilistic or uncertainty effects would not mask the behavior of the system. It also appears that there is little quantitative material in the literature that would allow a rational choice of statistical dispersion coefficients for various properties such as joint cohesion and roughness (dilation angle).

The following simplifying assumptions are made in the formulation of the numerical model.

- The intact rock blocks are linearly elastic.
- The dimension of the model perpendicular to the plane of analysis is large enough so that a plane strain condition is valid for the two-dimensional model.

- Fracture growth and rock deformations occur under equilibrium conditions; hence, quasi-static analysis is a valid approach.
- Quasi-static equilibrium is achieved through imposition of large mass and damping ratios to the accelerations and velocities calculated in the dynamic model.
- A large but finite number of joints exist.
- Joint displacements are small relative to joint dimensions.
- Jointed rock located at large distances from the perturbed area behaves as an intact rock due to presence of confining stresses.
- The shearing behavior of a joint is governed by Coulomb's friction law.
- The opening behavior of a joint is assumed to be elastic and nonlinearly proportional to the total normal stress. Shear displacement and shear dilation are assumed to be irreversible.
- A "closed" rock joint remains somewhat conductive; by imposing a minimum fracture aperture, fluid flow may take place through a "closed" joint.
- Flow in the rock joints can be described by the cubic law, in which flow rate is proportional to pressure gradient and cube of the joint aperture.
- There is no fluid leak-off from the joints into the rock matrix.
- Steady-state fluid flow is considered in the hydro-mechanically coupled model.
- Fluid boundary condition is applied such that boundaries are impermeable and fluid flow is zero at boundaries of the domain.
- Fracture propagation is not based on the linear elastic fracture mechanics (LEFM) and does not consider fracture toughness.
- Hydro-mechanical coupling is sequential. The fluid equation is solved first and then the solid equations are updated.

Advantages of the current study are listed below.

- While most of the models oversimplify the rock mass as an equivalent continuum, UDECTM treats it as a discontinuum.
- UDECTM sufficiently represents a real medium with the inherent fabric of discontinuities, and is computationally efficient.
- Pre-existing natural fractures can be incorporated and undergo large mechanical deformations.
- Fluid injection can be applied either as pressure (Essential) or flux (Natural) boundary condition in UDECTM, contrary to many other commercial codes which are deficient in applying flux boundary conditions for the fluid model.
- UDECTM is capable of applying different constitutive models for solid matrix and joints.
- Joint deformations are allowed in both Mode I (opening) and Mode II (shearing).
- The model is capable of simulating dilation of the rock mass (as in damage mechanics formulations) when shearing deformations along the rock joints are dominant.

Limitations of the present research are expressed as follows.

- UDECTM is a two-dimensional interface, which means that simulations may not be ideally close to reality. In such a case, three-dimensional codes may offer a better means of studying the interconnectivity between natural and hydraulically-driven fractures and can more closely represent the three-dimensional nature of the process. However, generating three-dimensional geometries is computationally demanding and requires much more execution time than two-dimensional models, even for modest problems.
- UDECTM is not capable of creating new fractures through intact rock; hydraulic fracture propagation is modeled through opening and shearing of pre-existing fractures. However, because the current research is focused on hard low-permeability naturally fractured rocks such as jointed igneous rock masses or dense shale gas rock masses, where the dominant hydraulic fracture propagation mechanism is assumed to be natural fracture reactivation, UDECTM should be adequate to study the effect of different rock fabrics.
- UDECTM is not capable of simulating permeable rock blocks, therefore no fluid leak-off can be simulated from the fracture network into the rock matrix.
- UDECTM only considers cubic law for the fluid model and other fluid constitutive models cannot be applied.
- Voronoi tessellation is picked as one of the main representatives of naturally fractured rock mass in this study. However, it may poorly represent local fracture growth because it does not necessarily offer preferred directions for the fracture to grow.
- Based on the constitutive model and model configuration chosen in chapter 6, there is not a strong stress drop (frictional stress) during slippage. Thus, seismic moment and seismic energy dissipation have almost equal values, which in turn gives small magnitudes of shear events.
- Due to computational limitations, injection time and injection rate are scaled in chapter 7. Although it may not be the most rigorous approach, it is still reasonable and sufficient to meet the determined objectives.

It is worth mentioning that the aforementioned limitations do not significantly affect the accomplishments of this study and the final results are considered valid within the context of a preliminary study with modest goals.

CHAPTER 4 IMPORTANCE OF THE STUDY AND PARAMETRIC ANALYSES

This thesis is focused on studying the effects of rock mass discontinuity fabric on deformability and permeability of naturally fractured strong rocks under different stress states when subjected to hydraulic injection. Chapter 4 presents a number of basic definitions and primary simulations to support the importance of this study in understanding rock mass behavior. An assessment is carried out to explore some additional parameter effects in rock masses subjected to hydraulic injection.

OVERVIEW

In reality, discontinuities act as channels for fluid transmission and therefore must be included in the modeling of fluid flow in naturally fractured rock masses. To geometrically characterize a NFR, parameters such as orientation, spacing distribution, spatial anisotropy and persistency of these natural discontinuities must be specified. All of these considered, and perhaps including bedding planes in the case of sedimentary rocks or schistosity in hard rocks, these comprise the dominant “fabric” of a rock mass that will govern its behavior (Zhang and Sanderson 1995). Fabric is perhaps the most important feature for quantifying mechanical (deformation mechanisms) and hydraulic (permeability) responses of NFR to applied changes in stress and pressure associated with injection.

In this work, the effects of joint geometries and properties on deformation and fluid flow are investigated. Coupled hydro-mechanical modeling is performed using the Universal Distinct Element Code (UDECTM), a Distinct Element Method (DEM) software. Fluid injection with steady-state flow through the naturally fractured rock mass has been modeled using simple common geometries of NFR. Given different basic components of a natural fracture fabric subjected to a hydraulic gradient, flow rates are examined and shear and normal displacements at different stress field anisotropy values are investigated.

Potential applications of these results are in stress management (relief of shear stress) by hydraulic fracturing in igneous rock mines and in improving hydraulic fracture treatments in arrays of wellbores in oil and gas development in stiff jointed rock masses. In practice, to better understand the efficacy of a HF operation, many fabric patterns and fluid parameters should be investigated. Results of simulations carried out in a jointed medium represented by a Voronoi tessellation are presented, and the effects on HF propagation of joint density and fabric variations are studied by adding persistent and non-persistent discontinuities to the initially isotropic Voronoi tessellated rock fabric. For some simulations, a through-going fault has been added to the DEM model at an angle to the principal stress directions to examine the role of a large persistent planar feature but with the same cohesive and frictional properties as the other joints. The intensity of fracturing was investigated and it is seen that the number of discontinuities inversely affects the area of the injection zone. In other words, the area in which injection fluid

flows through joints decreases by increasing the number of discontinuities that can accept flow. Better understanding of these factors may have positive economic benefits by helping to interpret the consequences of HF operations in practice.

4.1 NATURALLY FRACTURED ROCK

Most rocks possess mechanical discontinuities including joints, fractures, faults, shear zones, bedding planes, foliation, schistosity, gneissosity, cleavage and other geological structures. Natural fractures, interchangeably called joints, are the most common and important discontinuities and are usually found in sets, i.e., in groups or families of parallel or sub-parallel joints (Figure 4.1).



Figure 4.1. Well-developed joint sets on flagstones at St. Mary's Chapel, Caithness, Scotland. Not counting bedding planes, two orthogonal joint sets are visible (Sorkhabi 2014).

Discontinuities provide potential flow channels in a naturally fractured rock mass as well as potential slip planes (Singhal and Gupta 2010). Deformation is controlled by the geometrical characteristics of the NFR, the mechanical and hydraulic properties of joints, the stiffness of the rock matrix blocks and the in-situ stress conditions (Zhang and Sanderson 2002).

The interface between mechanical deformation, fluid pressure and fluid flow is demonstrated in Figure 4.2. Fluid pressure applies a force, F_i , at contacts, which contributes to the deformation of the block. At the same time, the aperture, a , at the interface is controlled by the normal displacements, u_n , of the joint. This, together with the fluid pressure gradients, determines the flow of fluid in the joint, which, in turn controls the redistribution of fluid pressure in the rock mass (ITASCA Consulting Group Inc. 2010). Modest changes in aperture may have large effects on flow because of the high order relationship between aperture and flow capacity in a joint.

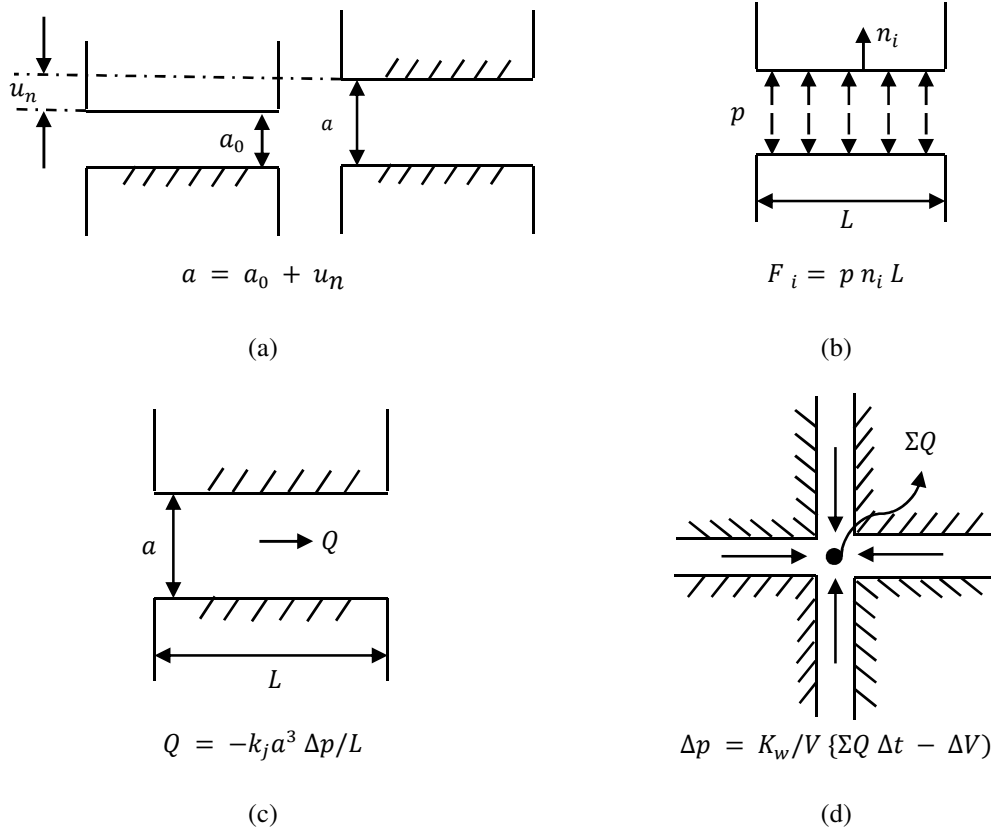


Figure 4.2. Hydro-mechanical coupling: a) Fluid pressure effect; b) Mechanical effect on aperture; c) Fluid flow; d) Fluid pressure gradient (ITASCA Consulting Group Inc. 2010).

Natural fractures are planes of weakness; the shear and tensile strength of these natural fractured are generally far lower than for the adjacent rock mass. Fractures are also compliant features with normal deformability values far greater than the intact rock, and under suitable pressures, natural fractures can also become fully open (non-contacting walls – Mode I fracture) as stresses and pressures change. Natural fractures are usually divided into two types: tectonic and non-tectonic fractures. Tectonic natural fractures are created by processes of deformation (folding, faulting), while non-tectonic natural fractures are related to physical diagenesis (loss of porosity, organic matter degradation, clay mineral dehydration, mineral changes, pressure and stress changes). In the context of the problems to be addressed in this study, the origin of the natural fractures is more non-tectonic than tectonic (Nelson 2001), and it is assumed that the natural fractures have not undergone previous shear displacement, they are purely Mode I natural fractures before any hydraulic injection. However, it is worthwhile to address this in more detail.

Natural fractures are viewed as closed or nearly-closed planes of weakness with low tensile strength that can be opened (Mode I) or sheared (Mode II or III) by stress changes (Wu et al. 2009). Because of different resultant properties of the joints, it is of importance to differentiate shear fractures from purely tensile ones. The following elements may help in such discrimination:

- Shear joints (Mode II and III) may exhibit displacement parallel to the plane of the joints, which is absent in the case of pure extension (Mode I) joints.
- Shear joints commonly occur in conjugate sets which may be indicated by a statistical analysis showing clustering in two directions separated by 50-60°. This also indicated that they developed in a differential stress field ($\sigma_1 \neq \sigma_2 \neq \sigma_3$), without which condition shear cannot generally occur.
- Generally, extension joints formed by diagenesis or cooling are more likely to be open or partially open, whereas pure shear joints are usually tightly sealed (dilatant shear of natural joints may leave some remnant aperture).
- The current orientation of extensional fractures and the slip direction of shear fractures may also provide information on the stress fields at the time of fracture formation and therefore help to understand the likely trends of shear and extension fractures. At the time of natural fracture formation, the maximum principal compressive stress - σ_1 - bisects the dihedral angle of conjugate Mode II shear fractures and is thus likely to be parallel to the orientation of the major set of extensional natural fractures (Mode I).

Caution must be exercised in assuming that the natural fracture fabric is truly indicative of the current stress state. Since the natural fractures were created, changes in the principal stress field magnitudes and orientations may have occurred, and pressures changed as well.

4.2 SIMULATIONS OF BASIC GEOMETRIES

4.2.1 MODEL GEOMETRIES

Generating a geometry that is somehow representative of the naturally fractured rock mass is important. Difficulties arise as to how to measure and then mathematically represent the complex joint system and how to interpret the complex mechanical deformation mechanisms that are significantly influenced by the interaction between joints and blocks. The geometry of a naturally fractured system is identified by joint orientation, spacing, length, persistency and connectivity, as well as the presence of bedding or foliation planes that are weak, as in the case of intensely bedded rocks, strongly fissile shale or mica schists.

In order to understand the behavior of the NFR system and quantify the deformation and permeability of the naturally fractured rock mass, it is worthwhile to understand the nature of joint plane intersections, using sub-areas that contain only two or three joints. These sub-areas may be viewed as the basic components of the NFR that reveal the local mechanisms of deformation and fluid flow. Four basic elements of a NFR are identified as follows (Zhang and Sanderson 2002) (Figure 4.3)

- Single through-going joint (Figure 4.3a): in this geometry, the angle with respect to the reference axes (often the principal stress directions) can be changed to study how

orientation may affect mechanical deformation and therefore how it affects flow-rate under given pressure conditions.

- T-junction joints (Figure 4.3b): this geometry is most usually seen in randomly oriented fracture networks. The angle of intersection does not have to be 90° between the joints.
- Cross-joints (Figure 4.3c): this geometry is often associated with tectonic joints, and the intersection angle in that case is usually about $50\text{-}60^\circ$. (The angle between sets and the stochastic variation of sets' directions, spacings, etc. allows study of hydro-mechanical impacts of system geometry, although this is a complex exercise.)
- Stepped joints (Figure 4.3d): a geometry most common in non-tectonic natural fracture patterns where there is one strongly dominant set.

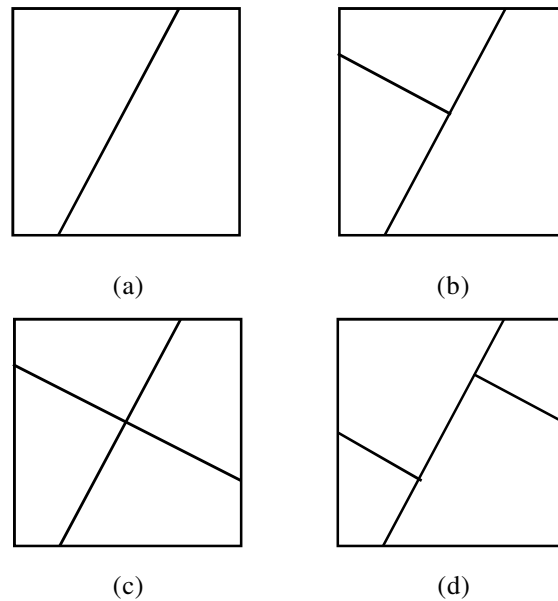


Figure 4.3. Simplified geometrical components of a natural fracture network a) single through-going joint; b) T-junction joints; c) cross-joints; d) stepped joints.

4.2.2 MODEL INITIAL CONDITIONS

Numerical simulations carried out with UDECTM were used to model pressurized joints with uniform fluid pressure gradients through the joints in x and y directions. Since mechanical deformation and fluid flow are interdependent, the hydro-mechanical coupling in UDECTM is implemented to aid in predictions of the rock mass mechanical and hydraulic response to hydraulic pressure changes. It is also possible to study the effects of various fabric patterns on the distribution of slip and opening of fractures at different stress field anisotropies. A two-dimensional plane-strain section is generated in UDECTM to represent a NFR $1\text{m} \times 1\text{m}$ in size, subjected to a biaxial in-situ stress state (two principal in-plane compressive stresses). The medium is initially dry and then hydraulic gradients of 1 kPa/m are applied in the x and y directions. The properties of the rock, the joints and the fluid are listed in

Table 4.1.

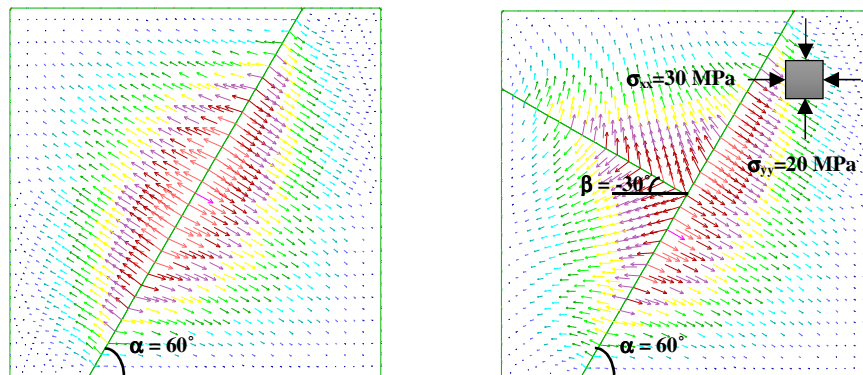
Table 4.1. Rock, joint and fluid properties.

Rock properties			Joint mechanical properties		
Density	2600	kg/m ³	Normal stiffness	100	GPa/m
Bulk modulus	40	GPa	Shear stiffness	40	GPa/m
Shear modulus	24	GPa	Friction angle	30	Degree
Friction angle	27	Degree	Cohesion	0.1	MPa
Cohesion	27	MPa	Dilation angle	5	Degree
Tensile strength	1	MPa			
Joint hydraulic properties			Fluid properties		
Permeability factor	0.83×10^8	MPa ⁻¹ s ⁻¹	Density	1000	kg/m ³
Residual hydraulic aperture	1×10^{-4}	m	Dynamic viscosity	10^{-3}	Pa·s
Aperture at zero normal stress	5×10^{-4}	m			

At an early stage in this work, it was decided to keep the properties of all joints the same, and to deal only with one set of mechanical properties for the intact rock blocks. In nature, one will expect variations in joint properties, especially between one set and another. However, this adds another level of complexity to the simulations, making interpretation and understanding of results more challenging. In future studies, once more insight is generated from these and additional simulations, issues of variability of natural properties can be addressed.

4.2.3 BASIC SIMULATIONS

In order to assess the importance of geometry, each geometrical component introduced in Figure 4.3 was subjected to similar simulations. Figure 4.4 illustrates the displacement vectors for each geometry. Pressurization of fluid tended to open pre-existing fractures in Mode I (extensional) deformation, but the direction and magnitude of the normal displacement are intimately related to the geometry and stress condition.



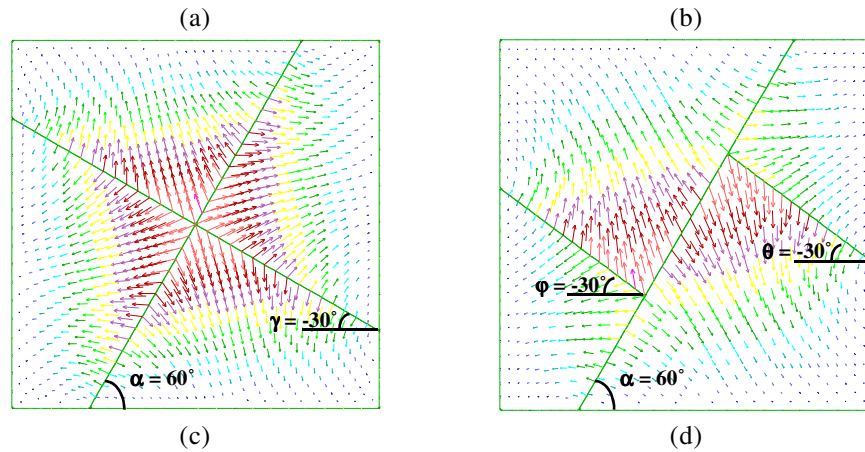
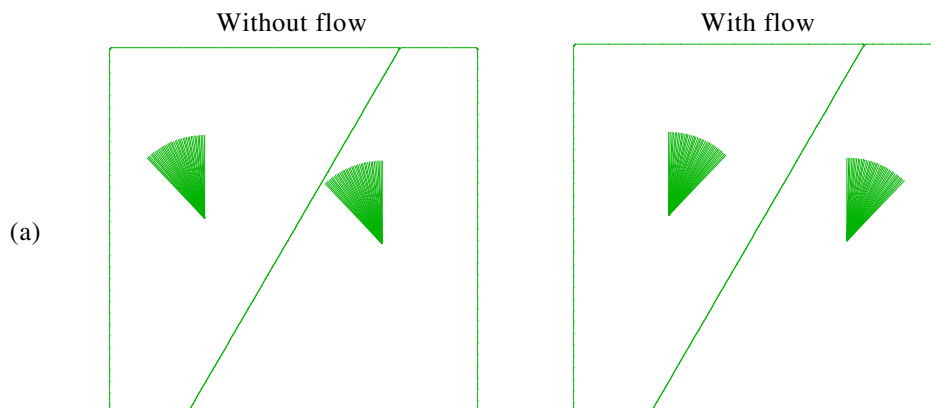


Figure 4.4. Effects of geometry on displacement distribution under anisotropic stress (30,20 MPa), a) single joint; b) T-junction joints; c) cross-joints; d) stepped joints.

Figure 4.5 shows block rotations for all geometries for an initially dry model as well as the model after it was subjected to 1 kPa/m fluid pressure gradient. Green fans indicate the direction and relative magnitude of block rotation. Comparing block rotations for each geometry indicates that each block in these simple models rotates independently as a function of fluid pressure and local stress conditions. Similarly oriented joints in different geometries undergo different amounts of opening or closure, indicating that geometry highly controls block deformation and aperture changes during induced fracturing. Of course, in more complex models with many joints, the contacts with adjacent blocks will alter and constrain the directions of block movement.



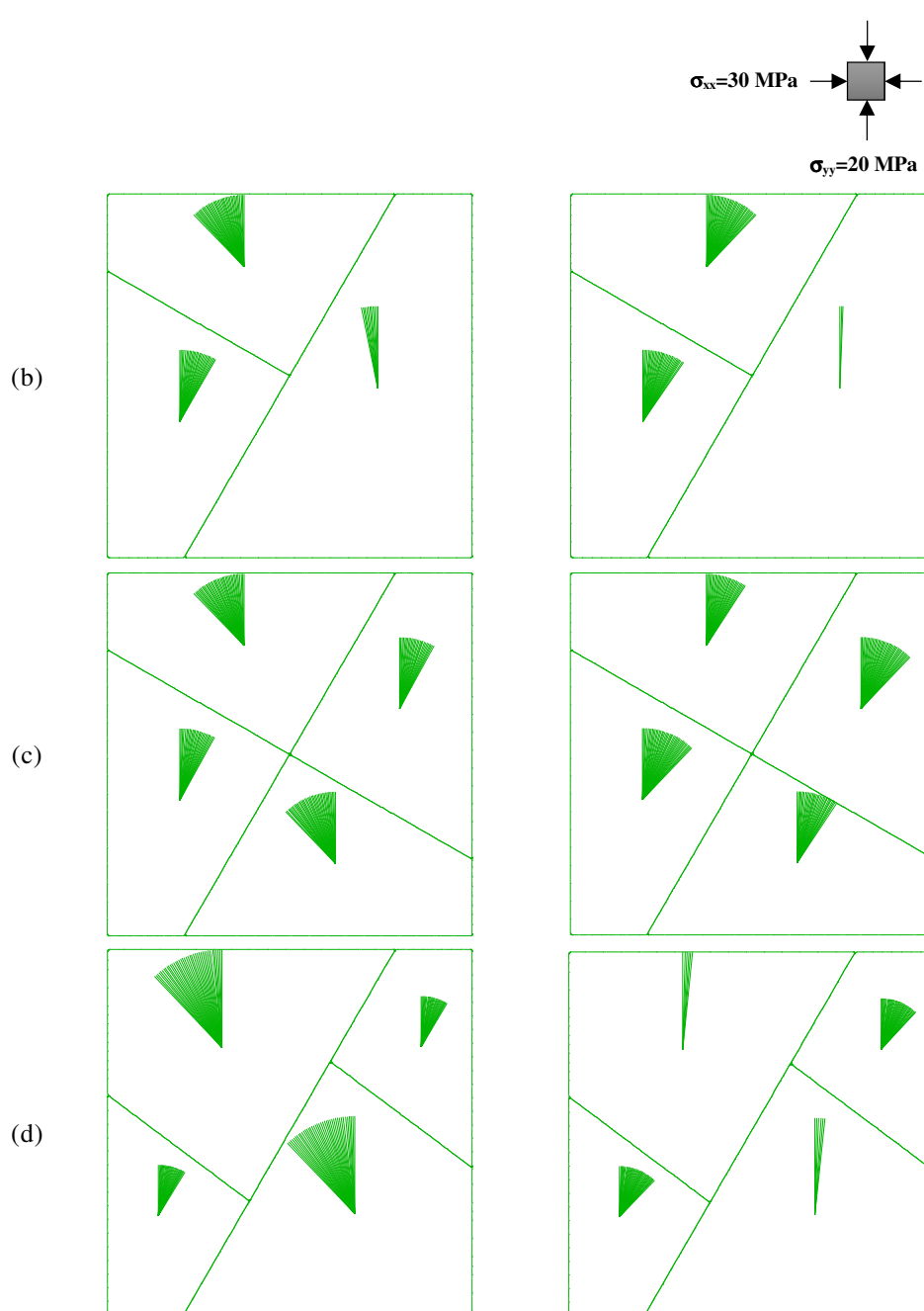


Figure 4.5. Effects of geometry on block rotation under anisotropic stress (30,20 MPa) and hydrostatic pressure, a) single joint; b) T-junction joints; c) cross-joints; d) stepped joints.

Figure 4.6 illustrates the flow directions for all geometries under a pressure gradient in the x and y directions, respectively shown as P_x and P_y . Flow direction in a joint oriented at a small angle to σ_{MAX} remains constant but in those joints inclined at larger angles, opposite flow directions under x and y gradients can develop. The situation is even more complicated in terms of flow-rate magnitude. In the case of the single through-going joint, flow-rate is directly related to the angle between the plane of the joint and the direction of σ_{MAX} ; that is, joints inclined at larger angles show more closure and hence sharply lower flow-rates. As stated above, in geometries with complex networks, flow-rate response will show more complex behaviour because of the complex interacting mechanical deformation mechanisms at work.

P_x

P_y

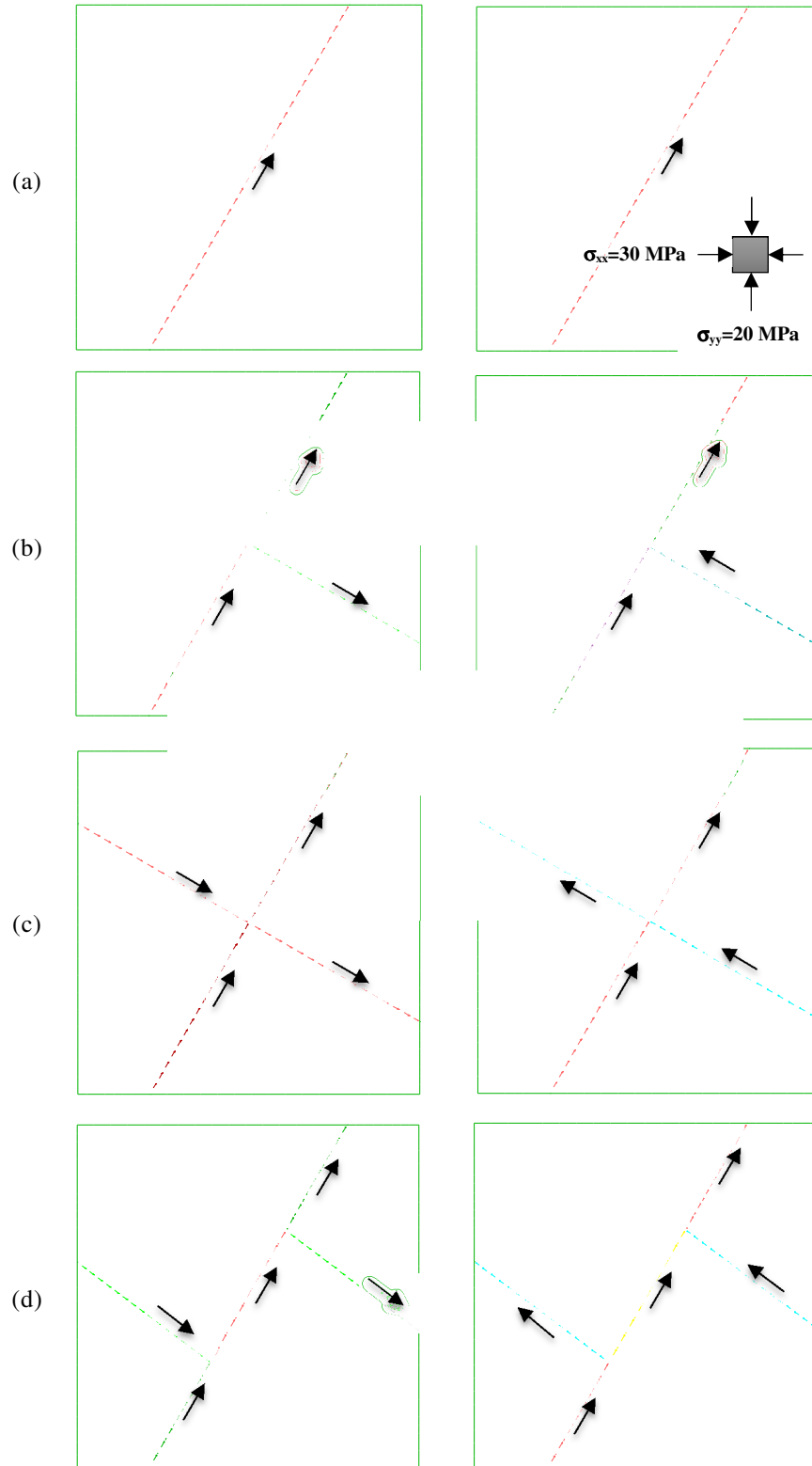


Figure 4.6. Effects of geometry on flow direction with gradients in the y, then the x direction. a) single joint; b) T-junction joints; c) cross joints; d) stepped joints.

Strong hydro-mechanical coupling exists in these systems such that fluid pressure affects the mechanical response of the rock mass, which in turn controls the redistribution of the fluid pressure through joint conductivity changes arising from joint aperture alterations. As this is a very strong response associated with a high order of non-linearity in the relationship between joint aperture and conductivity, the need for hydro-mechanical coupling is paramount in modelling any system where pressure changes are large enough to generate even modest changes in joint aperture (e.g. $\pm 10\text{-}15\%$).

4.2.3.1 EFFECTS OF JOINT PROPERTIES

Observation points are selected physical points in a model at which parameters of particular interest are being tracked during modelling. Five observation points indicated in Figure 4.7 are chosen for the stepped geometry. All following simulations are carried out on the same geometry but with different properties. Note that Figure 4.7 also shows the finite element discretization of the rock mass, which allows the deformability of the matrix to be included in the simulations.

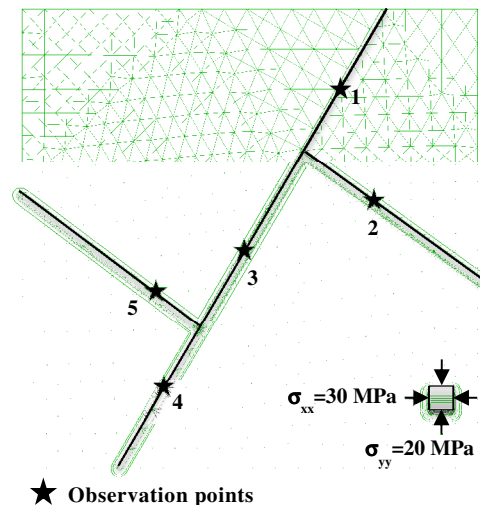


Figure 4.7. UDEC™ model of the stepped geometry with five observation points.

4.2.3.2 EFFECTS OF JOINT STIFFNESS

On loading, a naturally fractured rock mass is treated as a series of elastic blocks with displacement possible along and across natural fractures. The deformation behaviour of the rock block system is mainly controlled by relative movements between blocks.

Different values of fracture stiffness are selected to represent less and more stiff joints. As expected, increasing normal and shear stiffness will decrease normal and shear displacement; however, keeping the ratio of normal stiffness to shear stiffness constant and equal to 2.5 will allow normal displacement to take place substantially more than shear displacement. In this case, by increasing the shear and normal stiffness by four times at a constant ratio, opening and

shearing displacements change with factors of $\times 5$ and $\times 2$ respectively. Figure 4.8 and Figure 4.9 show values of normal and shear displacement at the observation points for the stepped joint. Observation points 2 and 5 are located on the joints that are orientated similarly; as is the case for observation points 1 and 4. These points show similar results under the same stiffness ratio and this is true for different values of stiffness. As an example, the middle observation point experiences different values of normal stress comparing to other observation points and this results in different magnitudes of normal and shear displacements.

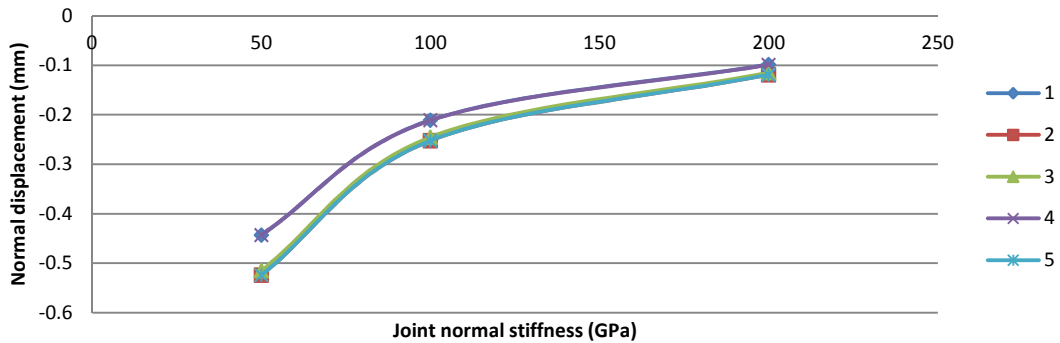


Figure 4.8. Effects of joint stiffness on normal displacement under anisotropic stress (30, 20 MPa) and hydrostatic pressure for the stepped fracture.

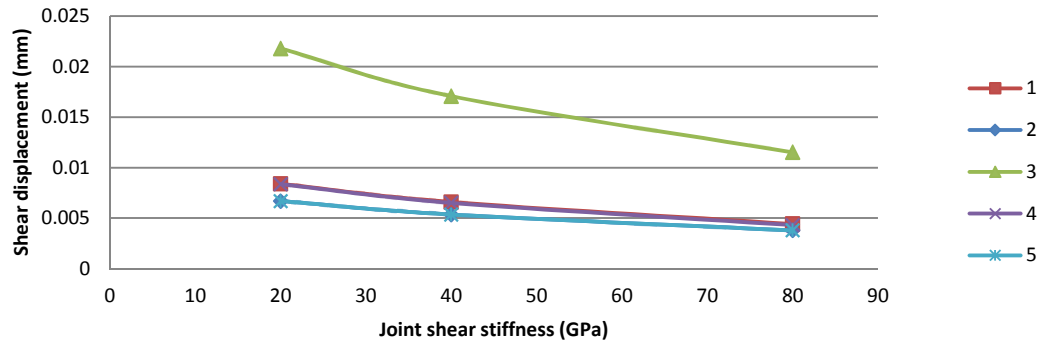


Figure 4.9. Effects of joint stiffness on shear displacement under anisotropic stress (30, 20 MPa) and hydrostatic pressure for the stepped fracture.

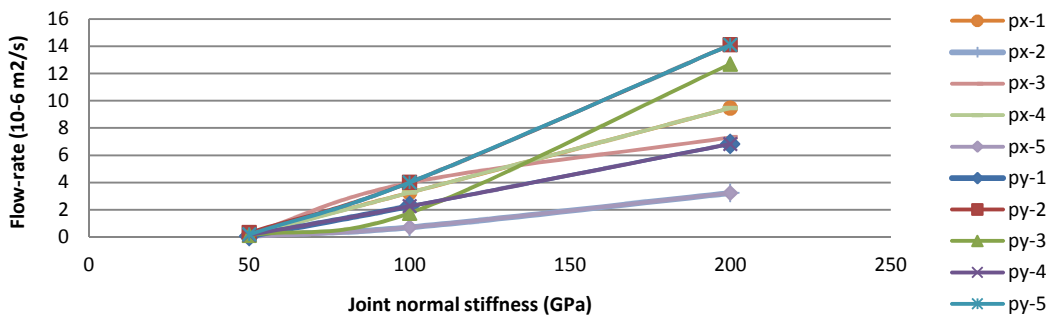


Figure 4.10. Effects of joint stiffness on flow-rates under anisotropic stress (30, 20 MPa) and hydrostatic pressure for the stepped fracture.

Flow rates show significant changes with increasing joint stiffness (Figure 4.10). In other words, closure of aperture in less stiff fractures leads to a large reduction of fluid flow. In general, flow rates developing from a pressure gradient in the y-direction show more dependency on stiffness and higher values of flow rate, especially in the stiffer cases. This may be explained as the effect of stress state. Since joints tend to reopen more easily if they are oriented parallel to the σ_{MAX} direction, less closure takes place in the x-direction and this will result in higher flow rates in that direction.

4.2.3.3 EFFECTS OF STRESS RATIO

In this section, some results related to the effect of stress ratio on deformation and fluid flow through the joints are discussed. To alter the differential principal compressive stresses, σ_{MAX} ($\sigma_{xx} = 30$ MPa) is kept constant and different values have been selected for σ_{min} . Figure 4.11 and Figure 4.12 illustrate joints that have experienced normal and shear displacements under differential stress states. As shown in these figures, the aperture increase from the normal stress effect is larger than the aperture increase from the shear dilation effect. In other words, normal displacements are much larger than shear displacements for the observation points studied. Under stronger differential stress, both shearing and opening show an increasing trend; however, the changes in aperture are essentially negligible for shear displacement. Those observation points located in lateral sections (points # 1, 2, 4, 5) have similar behaviour before fluid flow. It can be seen from these figures that the curves related to points 2 and 5 have an overlap (same as for points 1 and 4). This may result from the effect of the angle between the maximum principal stress and the plane of discontinuity.

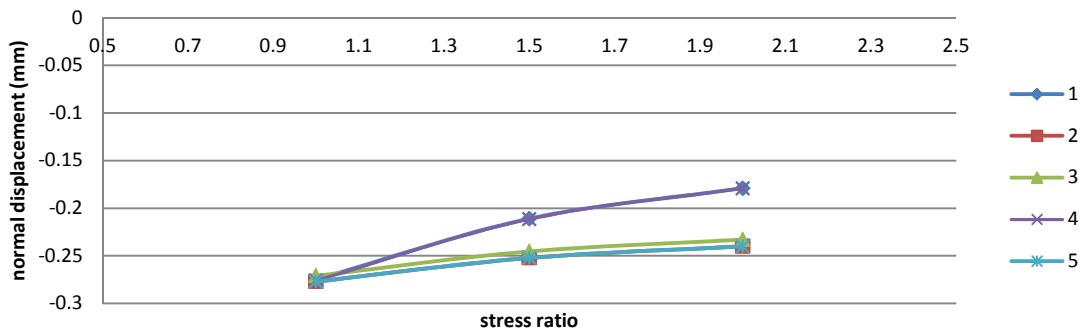


Figure 4.11. Effects of stress ratio on normal displacement under anisotropic stress and hydrostatic pressure for the stepped joint.

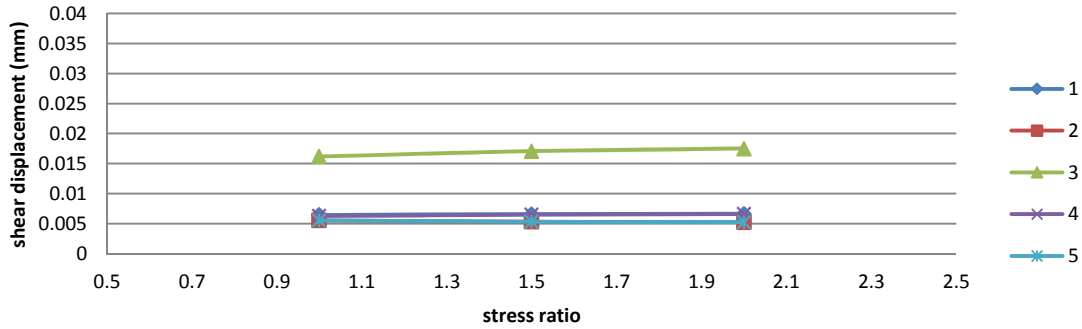


Figure 4.12. Effects of stress ratio on shear displacement under anisotropic stress and hydrostatic pressure for the stepped joint.

Figure 4.13 shows flow rates for different stress conditions and indicates that variation of flow rate is sensitive to changes in stress state. Flow rate has an increasing trend under higher differential stresses. Although changing the initial stress state affects displacements only slightly, such changes have very strong impacts on flow rate.

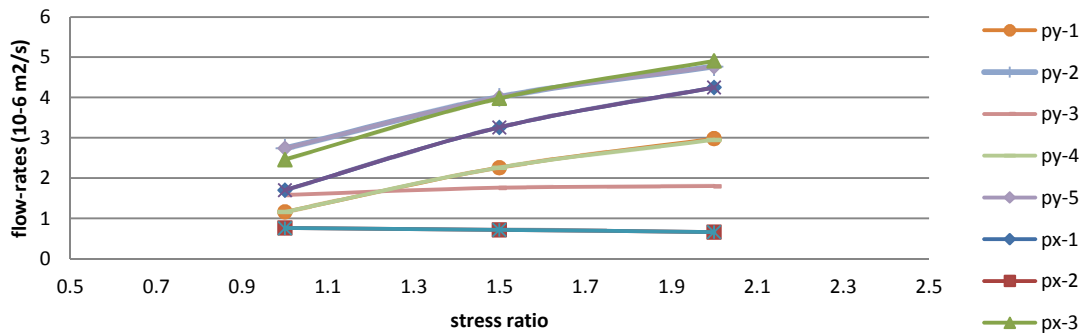


Figure 4.13. Effects of stress ratio on flow-rate under anisotropic stress and hydrostatic pressure for the stepped joint.

4.3 SIMULATIONS OF REPRESENTATIVE GEOMETRIES OF A NATURALLY FRACTURED ROCK MASS

4.3.1 FLOW FROM AN INJECTION POINT IN A BIAXIAL STRESS FIELD IN A VORONOI TESSELLATION ROCK FABRIC

As a first step in the process of model development, the Voronoi tessellation generator which is part of the UDECTM software has been used to simulate an isotropic polygonal natural fracture fabric. The generated model for this problem is shown in Figure 4.14.

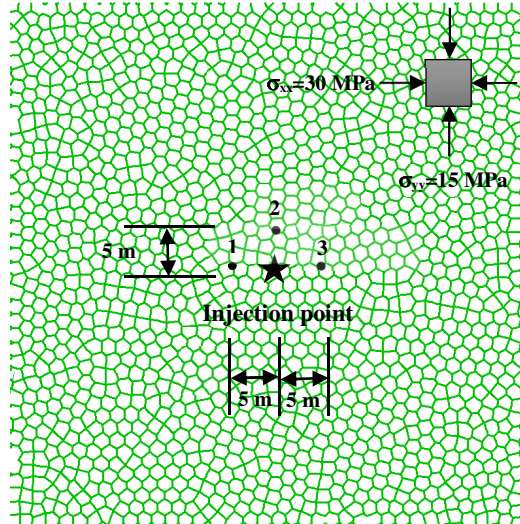


Figure 4.14. UDEC™ model of a Voronoi tessellated rock fabric.

The rock mass was subjected to a biaxial in-situ stress state. The UDEC™ model is 40m × 40m. The medium is initially dry. Fluid was injected at a constant flow rate of $10^{-4} \text{ m}^3/\text{s}/\text{m}$. In order to study the effect of stress ratio, the maximum principal stress ($\sigma_{xx}=30 \text{ MPa}$) is kept constant and different values have been selected for the minimum principal stress. Properties of rock, joint and fluid are listed in Table 4.2.

Table 4.2. Rock, joint and fluid properties.

Rock properties			Joint mechanical properties		
Density	2700	kg/m ³	Normal stiffness	100	GPa/m
Bulk modulus	40	GPa	Shear stiffness	40	GPa/m
Shear modulus	24	GPa	Friction angle	30	Degree
Friction angle	27	Degree	Cohesion	0.1	MPa
Cohesion	27	MPa	Dilation angle	5	Degree
Tensile strength	1	MPa			
Joint hydraulic properties			Fluid properties		
Permeability factor	0.83×10^8	MPa ⁻¹ s ⁻¹	Density	1000	kg/m ³
Residual hydraulic aperture	1×10^{-4}	m	Dynamic viscosity	10^{-3}	Pa·s
Aperture at zero normal stress	5×10^{-4}	m			

The unbalanced force is calculated continuously during timestepping and the maximum unbalanced force can be plotted for any model run. When the maximum unbalanced force or the maximum nodal force vector is zero, a steady-state solution is achieved; which never quite achieved in numerical analysis. Therefore, the model is considered to be at equilibrium when the maximum unbalanced force is small compared to the total applied forces in the problem. The

ratio of the maximum unbalanced force to the total applied forces is used as an asset to check the equilibrium. Low values of this ratio shows that forces balance at all gridpoints. The equilibrium ratio was set to 10^{-5} for the current simulations and the convergence condition of the model was monitored. As previously stated, equilibrium is obtained when both the unbalanced force ratio and the zero displacement conditions are satisfied. Figure 4.15 shows the maximum unbalanced force and displacement monitoring plot for one of the observation points indicated in Figure 4.14 for an anisotropic stress field (15, 30 MPa) in a two-dimensional Voronoi tessellated rock fabric. In this research, monitoring plots are available for representative points located to the left, right and above the injection point.

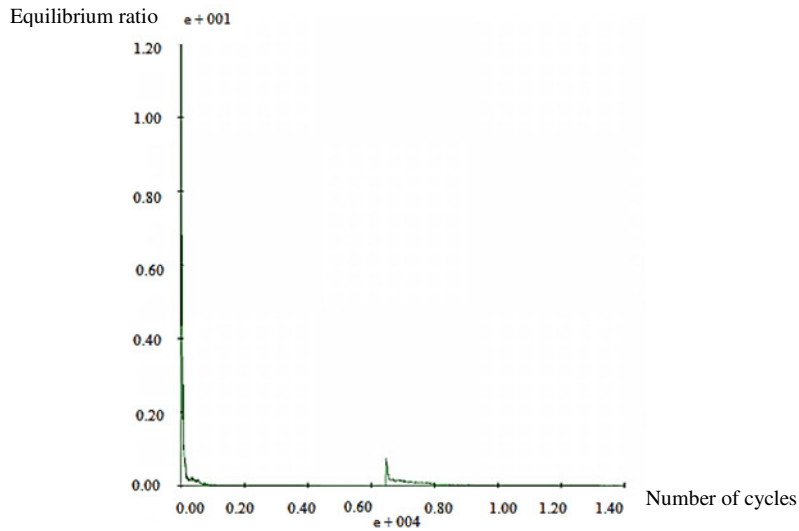
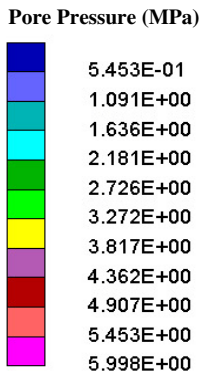


Figure 4.15. Ratio of maximum unbalanced force in an anisotropic stress field (15, 30 MPa) in the Voronoi tessellated rock fabric.

Figure 4.16 shows that pore pressure has a maximum value at the injection point (as it should) and is mostly horizontally distributed around the injection point. Anisotropy of the pressure is the consequence of the differential stress field favoring joint aperture increases in the direction normal to σ_3 . The sequence of parallel lines is an expression of magnitude, such that triple lines are larger in magnitude than double lines and so on. Fractures that have been hydraulically opened are in red. However, fluid distributes far away from the injection point through the model because even when closed, the natural fractures have some conductivity.



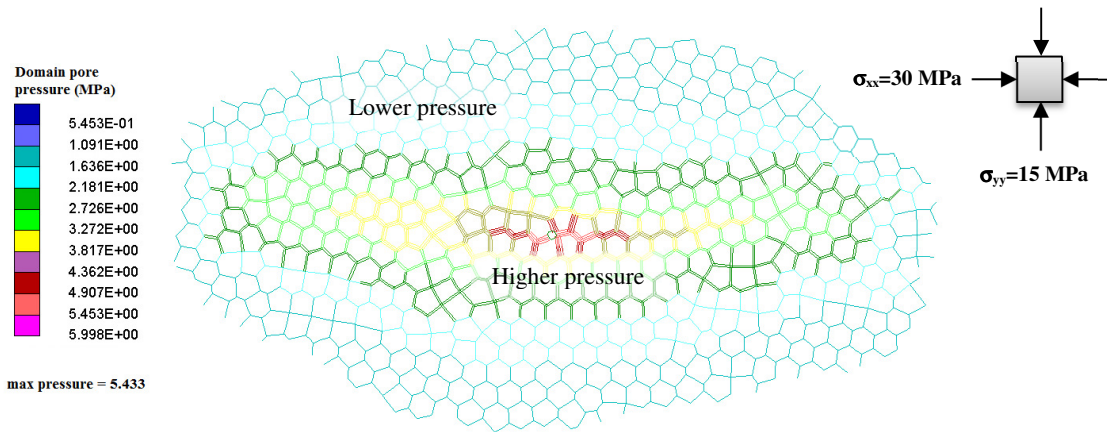


Figure 4.16. Pore pressure propagation around an injection point in the Voronoi tessellated rock fabric during HF injection.

Natural fractures have initial aperture and are not initially fully hydraulically closed. Therefore, fluid flows through the joint and fluid pressure exerts force on the surfaces of the joint. The effective normal stress acting across the natural fractures decreases and promotes shear slippage, which increases joint hydraulic conductivity. When fluid pressure exceeds the value of the stress normal to the joint, then it begins to open. This is the hydraulic fracturing condition. As long as fluid pressure remains sufficiently elevated, joints get connected one after another and build a larger hydraulically connected fracture network.

On the basis of the principle of minimum work, a fracture plane follows the local fabric in the strong rock containing natural fractures because it requires a great deal more energy (work) to break the rock block. However, when a natural fracture that is inclined to the orthogonal stress field is opened, it also undergoes shear displacement. Figure 4.17 shows the stress condition around the intersection of a slipped joint with a cross joint. Such a stress condition makes it easier for the fracture to change the propagation path than to continue propagating in the same direction. The inset in the figure shows the normal stress distribution across the offset joint due to the shear movement of the first opened natural fracture (Dusseault 2013).

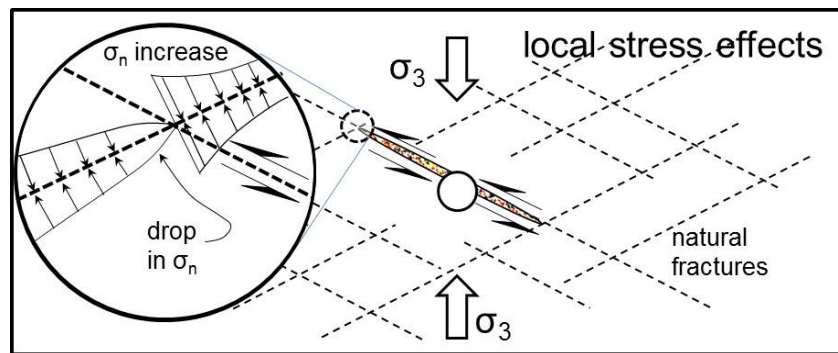


Figure 4.17. Local stress effects on fracture propagation in a naturally fractured rock (Dusseault 2013).

Figure 4.18 shows that although a hydraulic fracture follows the natural fractures, the global orientation of fracture growth remains normal to the minimum principal stress direction. This effect can be attributed to the minimization of the global work rather than the local work.



Figure 4.18. Global orientation of fracture propagation in the Voronoi tessellated rock fabric.

Furthermore, blocks located around the injection point rotate slightly and develop aperture that increases joint conductivity. Figure 4.19 shows a schematic diagram of block rotation and displacement vectors around the injection point.

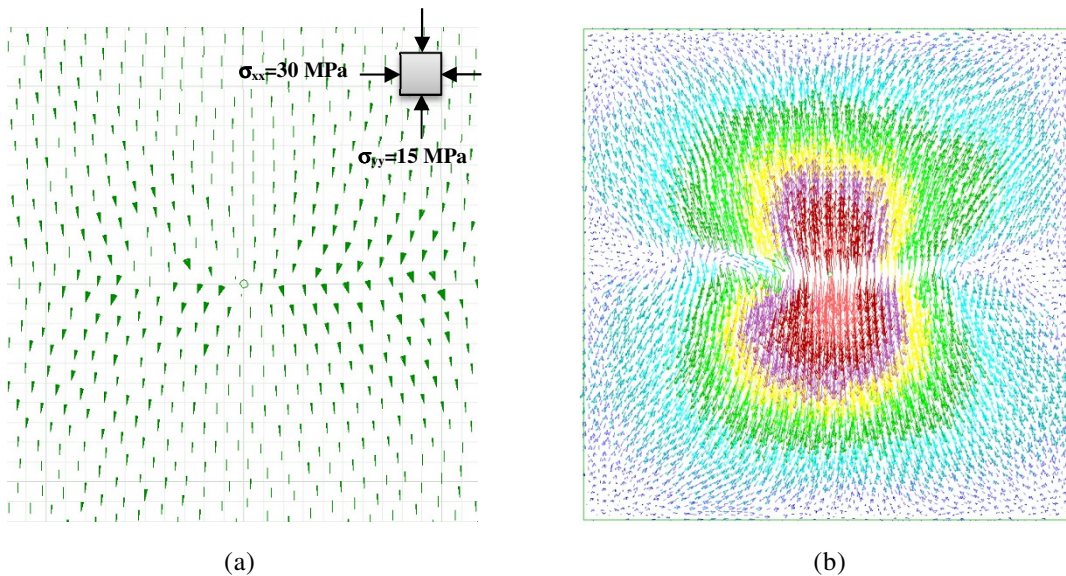


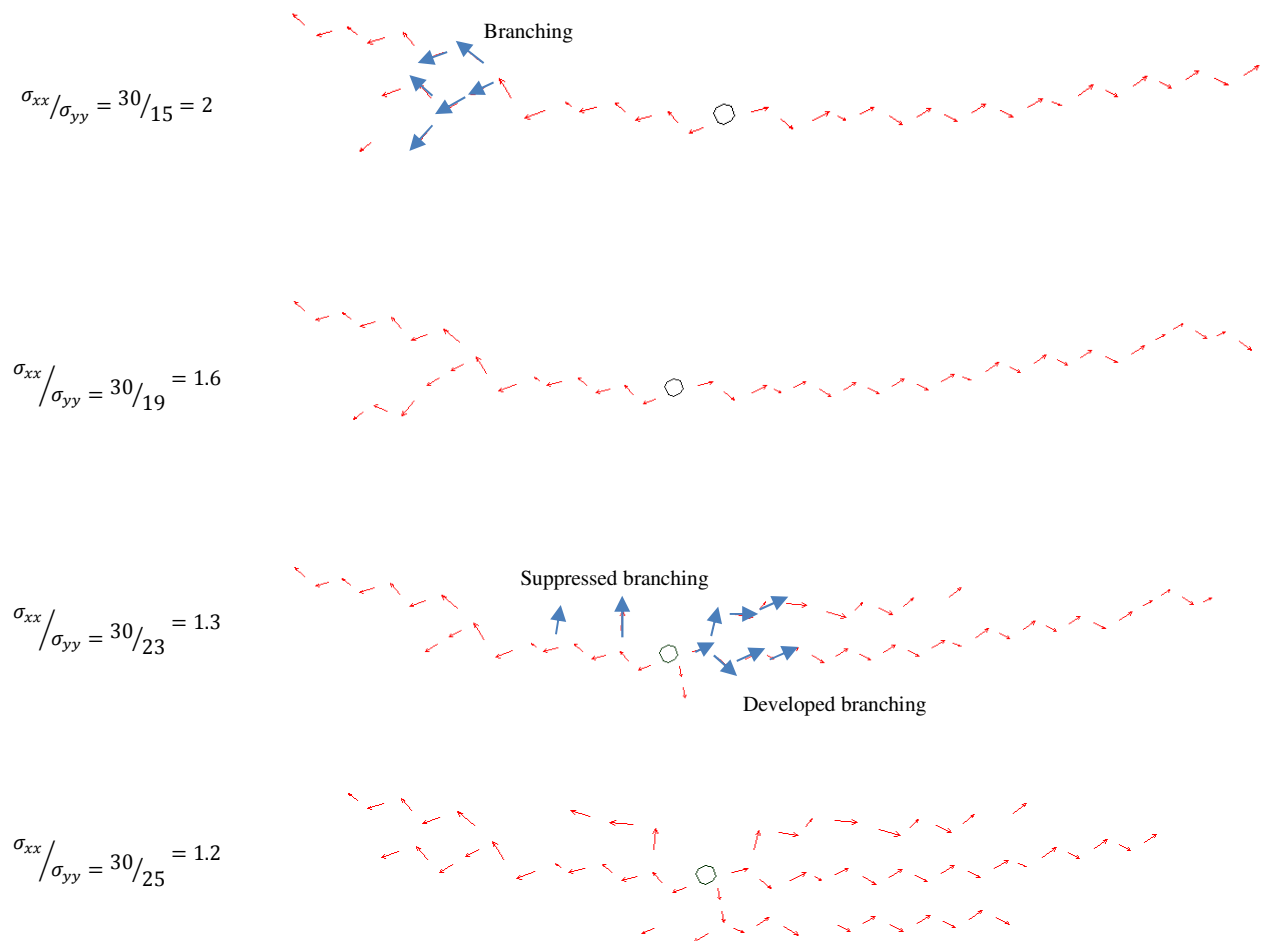
Figure 4.19. a) Block rotation and b) displacement vectors around the pressurized injection point in the Voronoi tessellated rock fabric during HF injection.

4.3.1.1 EFFECT OF STRESS RATIO

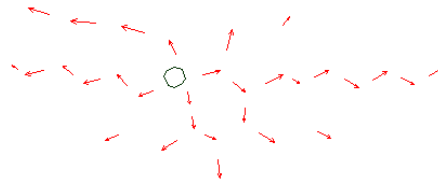
EFFECT OF STRESS RATIO ON PORE PRESSURE DISTRIBUTION

The next analysis is to evaluate the effect of the stress ratio on flow into the joints by changing the differences between the principal compressive stresses. The maximum principal stress ($\sigma_{xx}=30\text{ MPa}$) is kept constant and different values have been selected for the minimum stress. Figure 4.20 shows the flow direction from the pressurized injection point in the jointed rock mass subjected to an isotropic and a differential stress. Given the difference in in-situ stresses, the dominant flow is in the horizontal direction for most stress ratios and under the

induced pressures joints reopen dominantly parallel with the maximum principal stress. However, in approaching the isotropic stress condition, the propagation pattern starts to appear more isotropic as well. In the isotropic condition, no explicitly favored path exists for hydraulically induced Mode I fractures to propagate. Consequently, the fluid pressure has a similar effect all around the injection point, excluding the local small-scale fabric effects (locally, the Voronoi fabric may not be isotropic in nature). Similar results are seen for pressure diffusion effects, such that greater anisotropy is seen for pore pressure distributions under stronger differential stress. Interestingly, branching occurs shortly beyond the injection point after one or two segments if the in-situ stresses are close to each other, but much farther away if the stresses are strongly deviatoric. Although branching is restrained (suppressed) in most cases with larger deviatoric stress, some branching can develop even at smaller stress ratios. Branching reaches its highest level in the isotropic stress state, while its propagation distance is the smallest.



$$\sigma_{xx}/\sigma_{yy} = 30/27 = 1.1$$



$$\sigma_{xx}/\sigma_{yy} = 30/30 = 1$$

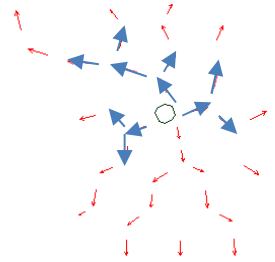


Figure 4.20. Flow direction in joints during fluid injection from the injection point in various anisotropic stress fields in the Voronoi tessellated rock fabric.

Figure 4.21 shows fluid pressures for three different stress ratios for the same observation points around an injection point during injection at the same rate. It can be seen that the maximum fluid pressure is in the isotropic stress state and drops sharply under stronger differential stress. This can be explained not only from the deviatoric stress view, but also from the magnitude of the principal stress. Note that the magnitude of σ_3 is also the highest at 30 MPa as the isotropic state is approached, thus more fluid pressure is needed to open joints. Given the difference in stresses, some favorably oriented joints require lower energy levels and can deform at a lower fluid pressure (less work).

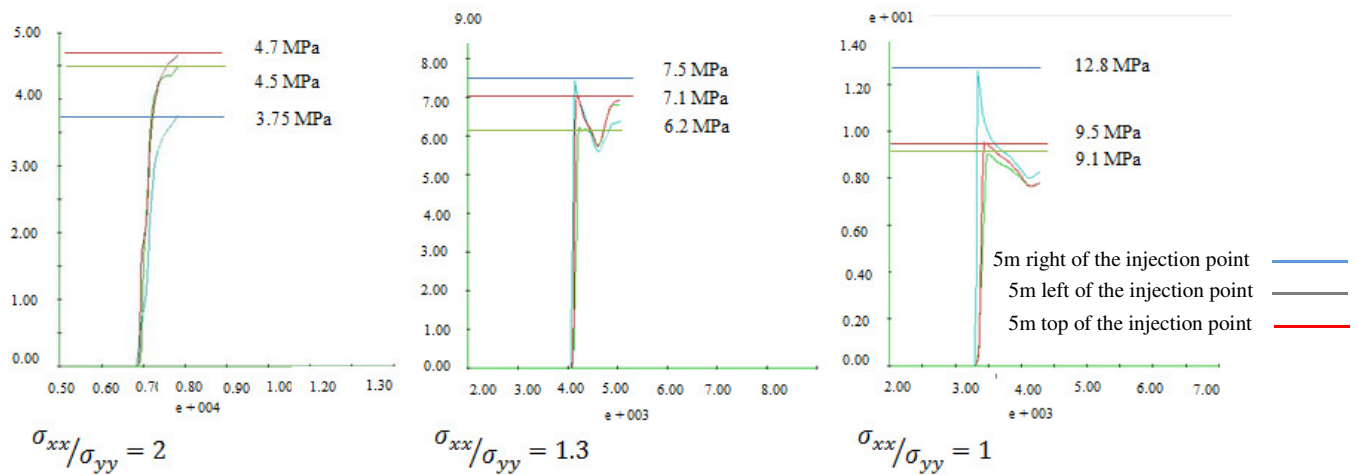


Figure 4.21. Fluid pressure histories versus number of cycles in the Voronoi tessellated rock fabric.

Therefore, in order to generate an open fracture network that is approximately isotropic with branches in many directions, a much higher pressure is needed. However, when opening a

fracture only in one direction in a more strongly deviatoric stress field, a lower pressure is required - a pressure that is very close to σ_3 as the deviatoric ratio gets larger.

EFFECT OF STRESS RATIO ON JOINT SHEARING AND OPENING

Figure 4.22 highlights those joints that have experienced normal and shear displacements (above a set threshold) during hydraulic injection in an anisotropic stress field. As always, the sequence of parallel lines indicates the magnitude of the variable: more lines indicate larger values. As shown in this figure, the aperture increase from the normal stress effect is larger than the aperture increase from the shear dilation effect. In the figure, normal opening dominantly occurs in the plane normal to σ_3 , whereas in the quadrants, there is a large shear effect. There is a continuous line of hydraulically opened joints near the injection point followed by single slipped or opened natural fractures. Interestingly, fractures that are not opened (Mode I) can undergo slip (Mode II). It seems that the orientation of joints with respect to the principal stresses mostly controls the deformation mechanism.

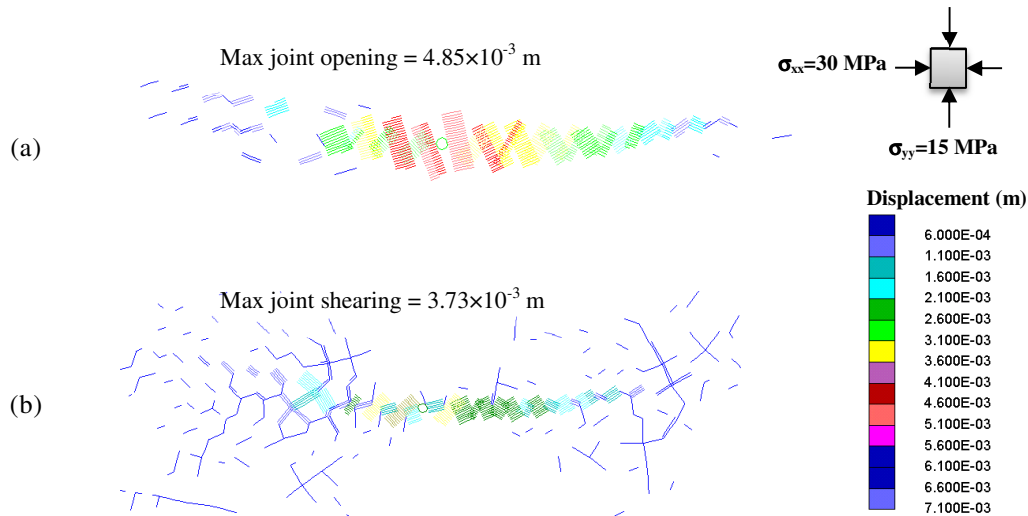


Figure 4.22. a) Normal and b) shear displacements on joints around a pressurized injection point in the Voronoi tessellated rock fabric in an anisotropic stress field (30, 15 MPa).

Figure 4.23 shows maximum joint shear and normal movements under differential stress states. It is concluded that there is some critical stress ratio that alters the dominant mechanism, here occurring at a stress ratio of about 1.25 (30, ~25 MPa). This is likely to be different depending on the fabric of the system and perhaps it is unscalable to a real rock mass. For isotropic or close to isotropic stress states, normal displacements are low, however some joints nevertheless undergo slippage. Under stronger stress differences, although both shearing and opening show an increasing trend, opening seems to be the main deformation mode.

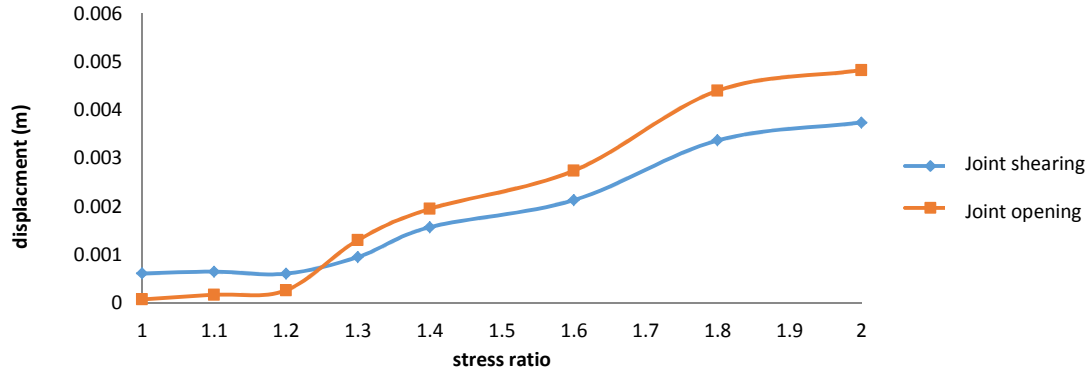


Figure 4.23. Maximum value of shear and normal displacements for different stress ratios in the Voronoi tessellated rock fabric.

4.3.1.2 EFFECT OF JOINT DENSITY

To explore the effect of strong fabric on propagation of hydraulic fractures in a naturally fractured rock, different types of fabric models have been studied. In a Voronoi tessellated rock fabric, the effect of joint density has been studied by adding persistent and non-persistent discontinuities to the system. A fault has been added to the model as a persistent discontinuity, which plays the role of a through-going plane, with the same properties as the other limited length joints. In another model, the presence of another dominant joint set oriented at an angle to the direction of the principal stresses is used to represent non-persistent but oriented discontinuities superposed on the randomly oriented Voronoi joints. Figure 4.24 shows schematic views of these models, and each of them is 40m × 40m in size. The medium is initially dry. Fluid was injected at a constant flow rate of $10^{-4} \text{ m}^3/\text{s}/\text{m}$ at the same injection point. The same properties as those listed in Table 4.2 were used for these different fabric models.

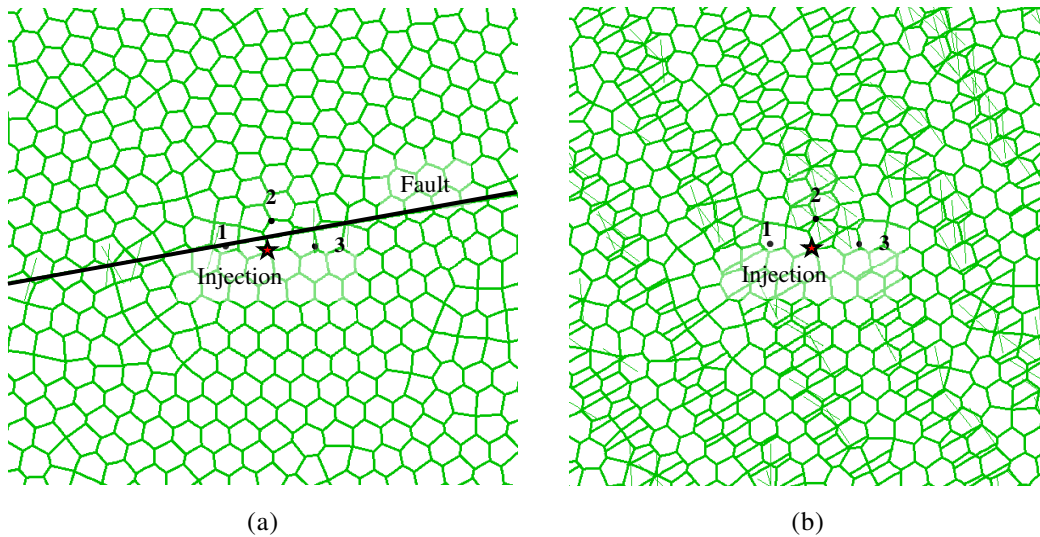


Figure 4.24. UDEC™ model of an injection point in a rock mass containing a Voronoi tessellation with a) persistent and b) non-persistent discontinuities.

These models were subjected to steady-state flow at which domain volume alterations have a negligible influence on pressure change, so the effect of fluid stiffness in the mechanical steps is eliminated and the bulk modulus of the water (k_w) is not required.

EFFECTS OF JOINT DENSITY AND STRESS RATIO ON MECHANICAL DEFORMATION

Pressurized fluid injection causes a combination of tensile opening and shear dilation in the vicinity of the wellbore. Shearing induces slippage on pre-existing joints and creates permanent flow channels through the process of dilation. For a better demonstration of this mechanism, Figure 4.25 was created. It shows joint shear and normal displacements around the pressurized injection point near the fault (above a set threshold) (see Figure 4.24a).

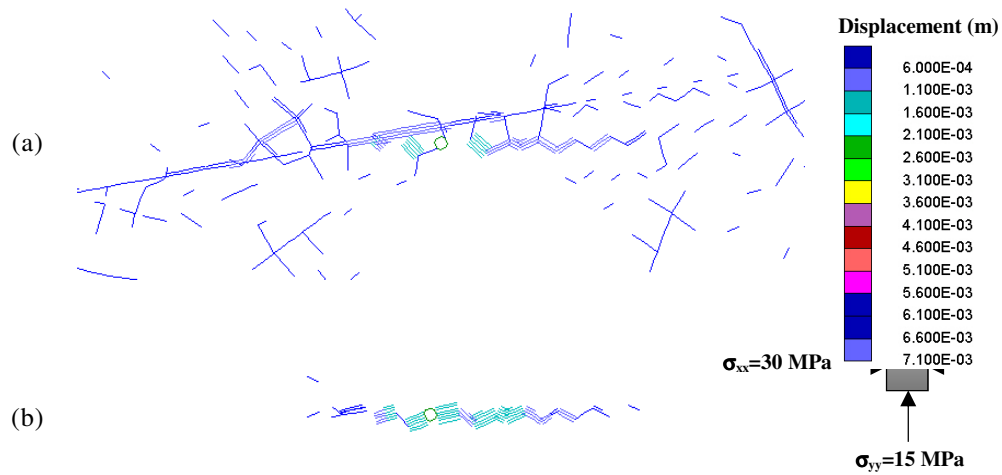


Figure 4.25. a) Shear and b) normal displacements on joints around a pressurized injection point in the Voronoi tessellated rock fabric with a nearby fault plane.

It is obvious that a large amount of slip is focused on the fault plane and the greatest shear displacement is near the injection point which is a reasonable and expected result. In this simulation, slip occurred before the opening of the hydraulic fracture and the slight rotation of natural fractures away from the plane is because of stress field modifications associated with the fault slip. There is a continuous line of hydraulic fractures near the injection point followed by single slipped or opened natural fractures. Interestingly, joints that are not opened can undergo slip. It seems that the orientation of joints with the principal stresses mostly controls the deformation mechanism, since fluid pressure is almost the same for the corresponding area.

Figure 4.26 shows maximum values of normal and shear displacements in the Voronoi tessellated rock fabric with a nearby fault plane. An increasing trend to joint opening is seen with an increase in the stress difference. In the isotropic stress condition, shearing and opening have an almost equal share of deformation. Given the stress difference, shear displacement remains almost constant though larger than the normal displacement, because of a large amount of slip along the fault (which has a constant dilation angle with deformation). After a “critical” stress

ratio under higher deviatoric stresses, here about 1.4 (30, 21 MPa), aperture generation due to normal stress effects is larger than the aperture generation due to shear stress effects, though the differences are modest (~10%).

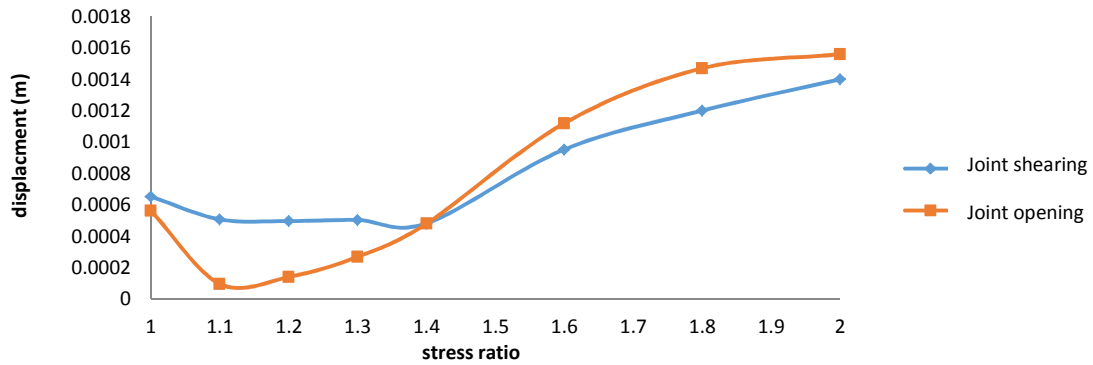


Figure 4.26. Maximum value of joint shearing and opening vs stress ratio for different Voronoi tessellated rock fabric with a nearby fault plane.

Figure 4.27 shows opened and slipped joints in a medium with non-persistent but strongly oriented discontinuities. The strongest shear movement occurs in the discontinuity that cuts the injection point, which also undergoes opening. Although the zone of Mode I opening still follows an approximately horizontal path, shearing occurs in most of the favorably oriented non-persistent discontinuities.

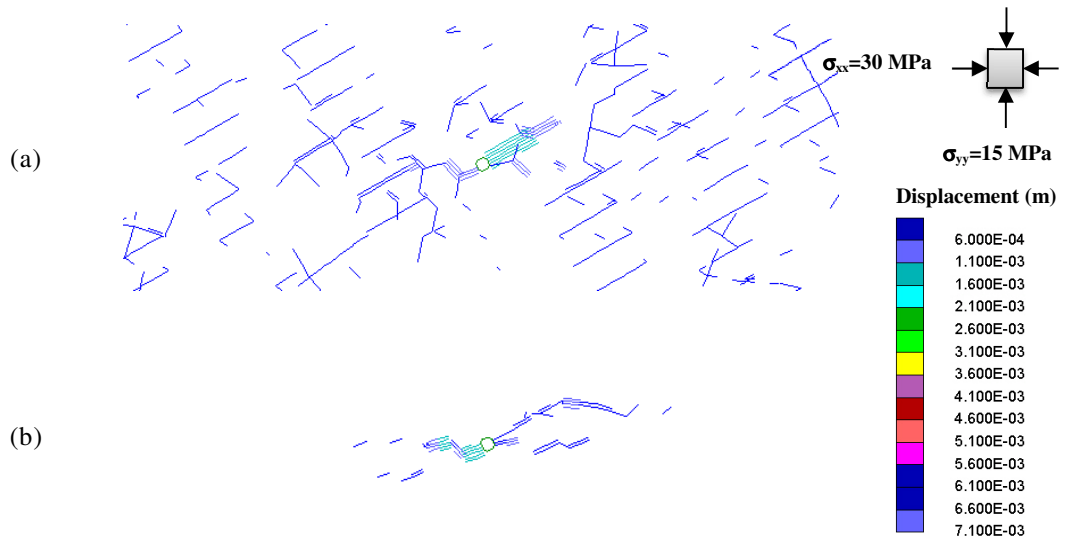


Figure 4.27. a) Shear and b) normal displacements on joints around a pressurized injection point in the Voronoi tessellated rock fabric with non-persistent discontinuities.

Figure 4.28 shows maximum values of normal and shear displacements in a Voronoi tessellated rock fabric with non-persistent discontinuities. The presence of the dominant joint sets oriented at a favourable angle to the direction of the principal stresses for slip to occur makes shearing the

dominant deformation mechanism. Additionally, both normal and shear displacements increase by increasing the stress ratio.

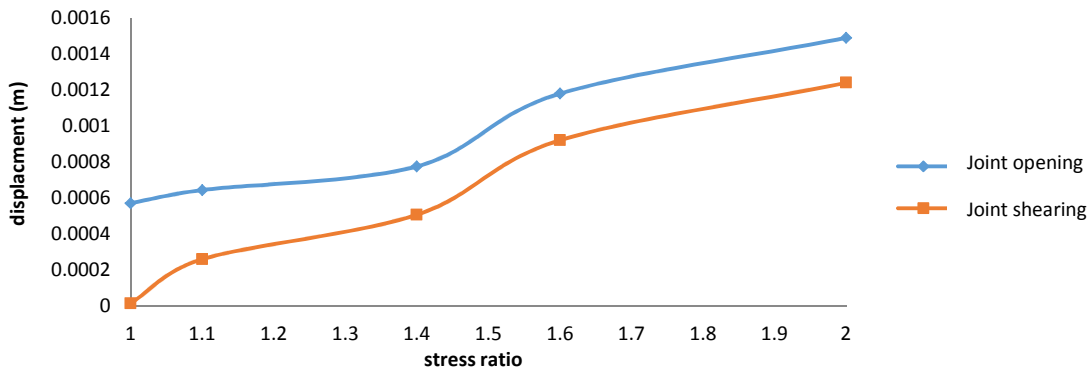


Figure 4.28. Maximum value of joint shearing and opening vs stress ratio for different Voronoi tessellated rock fabric with non-persistent discontinuities.

EFFECTS OF JOINT DENSITY AND STRESS RATIO ON PORE PRESSURE

Figure 4.29 depicts pore pressure distribution around the pressurized injection point. It is clear that the model containing non-persistent discontinuities has a smaller stimulated area than the one with a fault. It is concluded from several realizations that fluid flow and pore pressure distributions have similar patterns in most of the anisotropic stress states as in the simple Voronoi tessellated rock fabric and propagate normal to the direction of σ_3 .

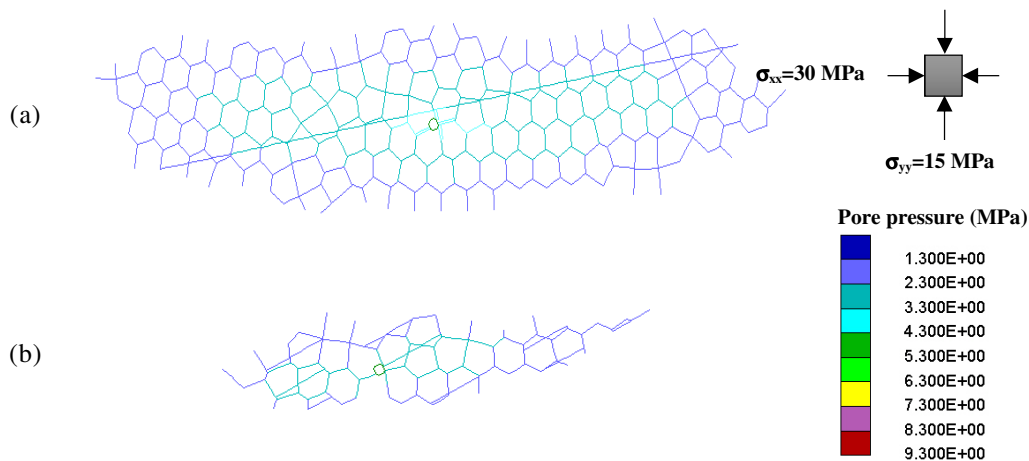


Figure 4.29. Pore pressure progression around a pressurized injection point in the Voronoi tessellated rock fabric with a) persistent and b) non-persistent discontinuities.

Figure 4.30 indicates maximum pore pressure values for a Voronoi tessellated rock fabric with persistent and non-persistent discontinuities under different bi-axial stress states. Although both curves have a decreasing trend, higher values are obtained in the non-persistent geometry model. This may arise from changes in joint hydraulic aperture. Relatively small changes in hydraulic aperture lead to large variations in conductivity and hence also in fluid pressure. Some

observation points both close to and far from the injection point have been tracked (Figure 4.31 and Figure 4.32, respectively) to see whether this is a regional effect. Based on these two figures, despite the fact that fluid pressure is decreasing with distance from the injection point, the same relative behavior is maintained with larger stress differences.

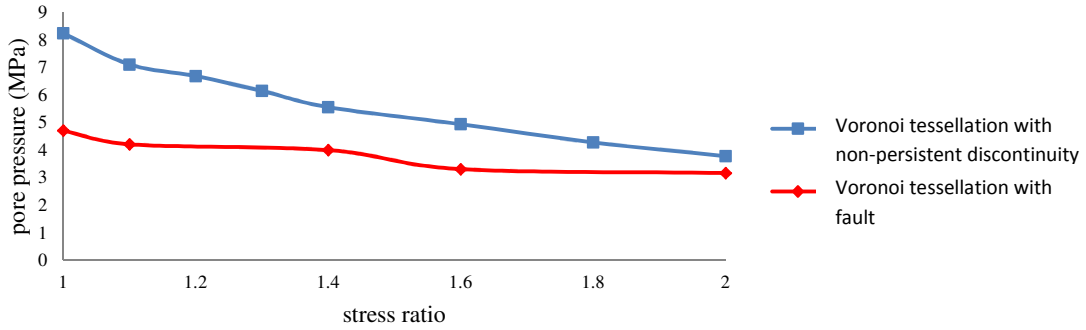


Figure 4.30. Maximum pore pressure values around a pressurized injection point in the Voronoi tessellated rock fabric with a) persistent and b) non-persistent discontinuities.

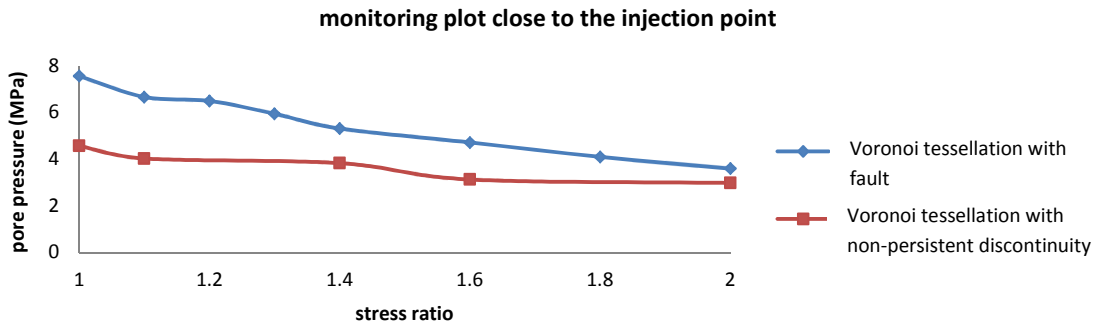


Figure 4.31. Values of pore pressure for a monitoring plot close to the pressurized injection point in the Voronoi tessellated rock fabric with a) persistent and b) non-persistent discontinuities.

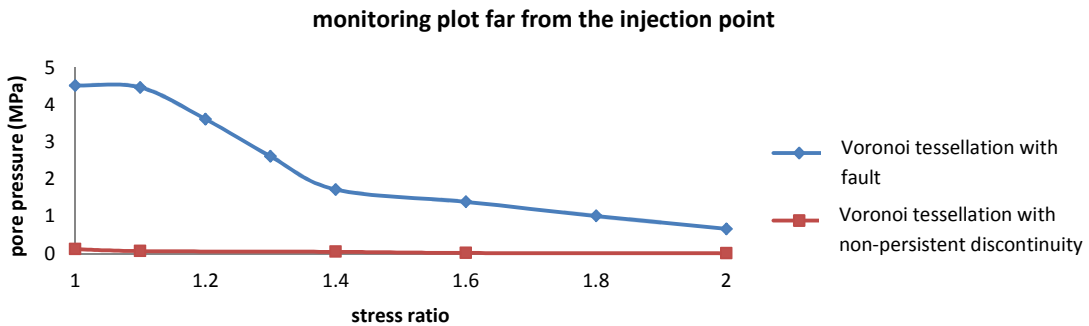


Figure 4.32. Values of pore pressure for a monitoring plot far from the pressurized injection point in the Voronoi tessellated rock fabric with a) persistent and b) non-persistent discontinuities.

4.3.1.3 EFFECTS OF FABRIC ON MECHANICAL AND HYDRAULIC DEFORMATION OF JOINTS

The purpose of the next set of analyses is to evaluate the effect of fabric on flow into the joints and on deformation patterns while changing the differential principal compressive stresses. Figure 4.33 and Figure 4.34 show normal and shear displacement plots for the region around the pressurized injection point in the different Voronoi tessellated rock fabrics subjected to isotropic and differential stresses. Both shearing and opening modes show an increasing trend with stress differences, while the opening mode has higher values and therefore contributes more to joint conductivity enhancement. For isotropic or close-to-isotropic stress states, normal and shear displacements are approximately zero though some joints undergo slippage. Overall mechanical deformation increases with higher stress differences in all fabrics, however it is more noticeable for a fabric with simple Voronoi tessellation.

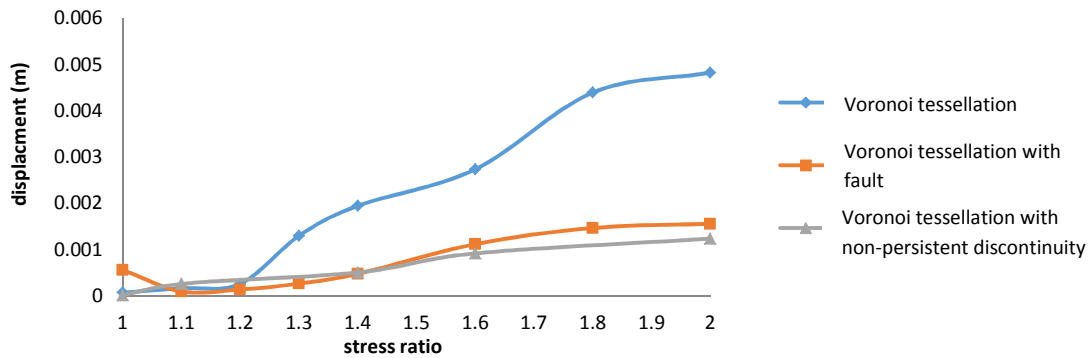


Figure 4.33. Maximum value of normal displacements vs stress ratio for different Voronoi tessellated rock fabrics.

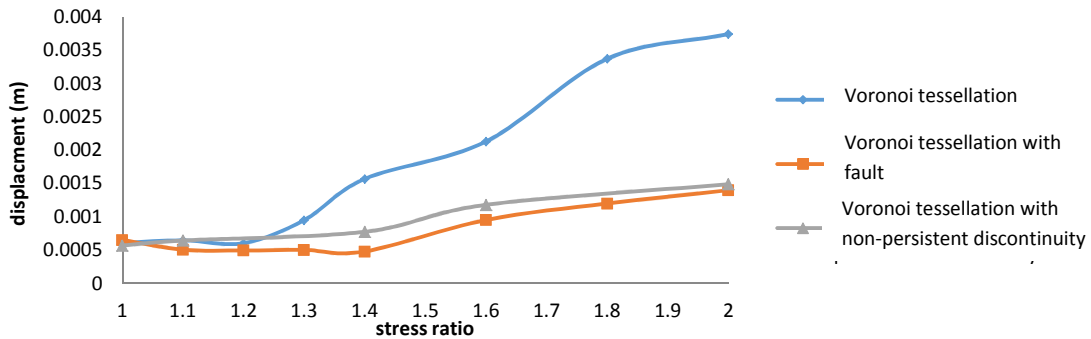


Figure 4.34. Maximum value of shear displacements vs stress ratio for different Voronoi tessellated rock fabrics.

Figure 4.35 shows the stress ratio impact on pore pressure for a jointed system with different geometries. Pore pressure has a decreasing trend under higher differential stress for all geometries. In addition, it has its maximum value in the simple Voronoi tessellation. Increasing the number of discontinuities leads to lower fluid pressure because the same amount of fluid is distributed into more spaces and each space would thus have a lower pressure. In other words,

the number of discontinuities inversely affects fluid pressure in these DEM models because more volume is provided by dilation for the fluid to flow into.

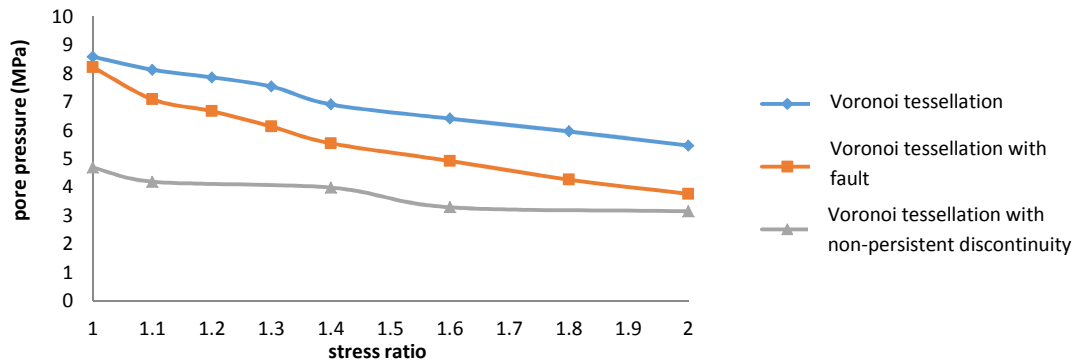


Figure 4.35. Maximum value of pore pressure vs stress ratio for different Voronoi tessellated rock fabrics.

4.3.2 FLOW FROM AN INJECTION POINT IN A BIAXIAL STRESS FIELD IN A ROCK MASS WITH ORIENTED JOINT SETS

Effects of oriented joint sets in a strong fabric and differential stress fields are studied in this section. Hard rocks with dominant joint sets oriented at some angle to the directions of the principal stresses are simulated. All simulations are performed in an anisotropic stress field of (30, 23 MPa) by keeping one joint set vertical and by changing the inclination of the other. Mostly, shear displacements are larger along the joint sets and normal displacements are negligible in these simulations so that joint conductivity only increases because of the shearing mechanism. Figure 4.36 shows maximum values of shear and normal displacements for different realizations. Except for normal (orthogonal) joint sets, in all others shearing is the main mode of aperture increase and the major reason for increases in the hydraulic conductivity of the jointed network.

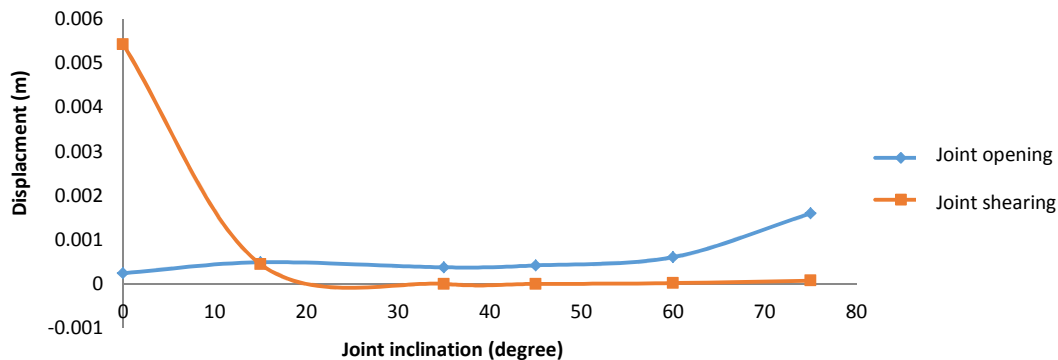


Figure 4.36. Maximum values of shear and normal displacements for different oriented joint sets in an anisotropic stress field (30, 23 MPa).

Orientation of joint sets greatly affects fracture propagation paths. In the case of orthogonal joint sets (Figure 4.37), fracturing Mode I is the main deformation mechanism. However, by reducing

the angle between joint sets, the dominant mechanism switches to Mode II (and Mode III in the real world) (Figure 4.38). In these realizations, fractures mostly propagate through the vertical joint set. It is to be noted that all values of normal and shear displacements are similarly scaled in the range of 1E-4 to 7E-3 m.

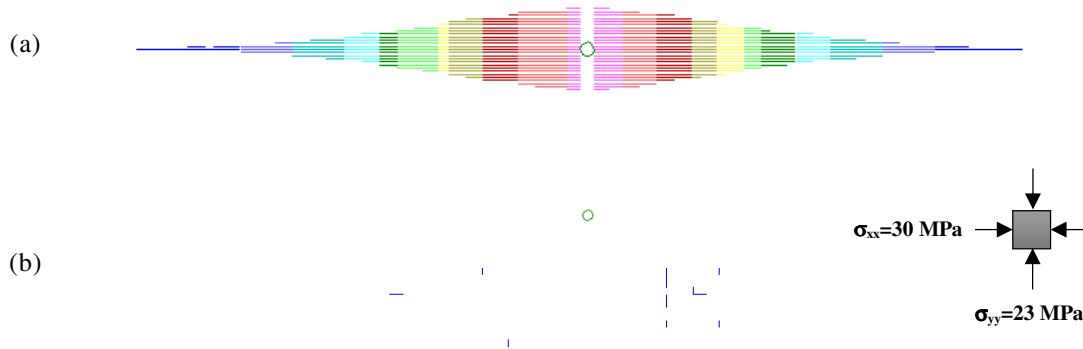


Figure 4.37. a) Normal and b) shear displacements around a pressurized injection point in orthogonal joint sets.

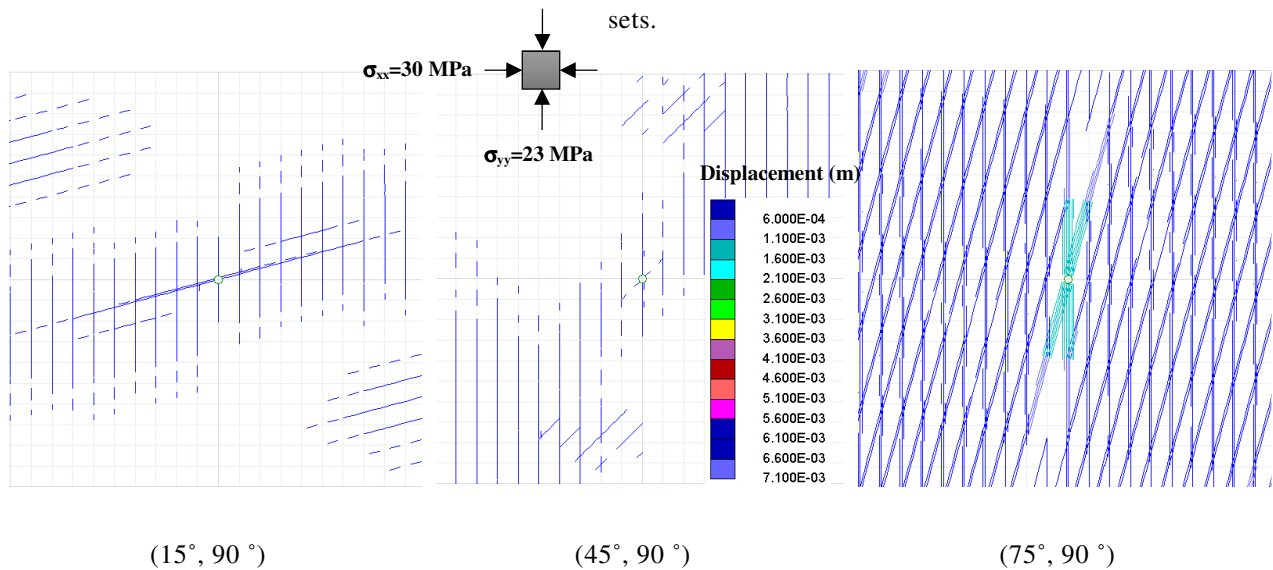


Figure 4.38. Shear displacement around a pressurized injection point for different orientations of joint sets.

4.3.3 FLOW FROM AN INJECTION POINT IN A BIAxIAL STRESS FIELD IN A ROCK MASS WITH COMPLEX FABRIC

More complicated geometries have been generated to study the effect of joint density in hydraulically pressurizing a rock mass with strong matrix blocks. Figure 4.39 shows several UDECTM models for this problem.

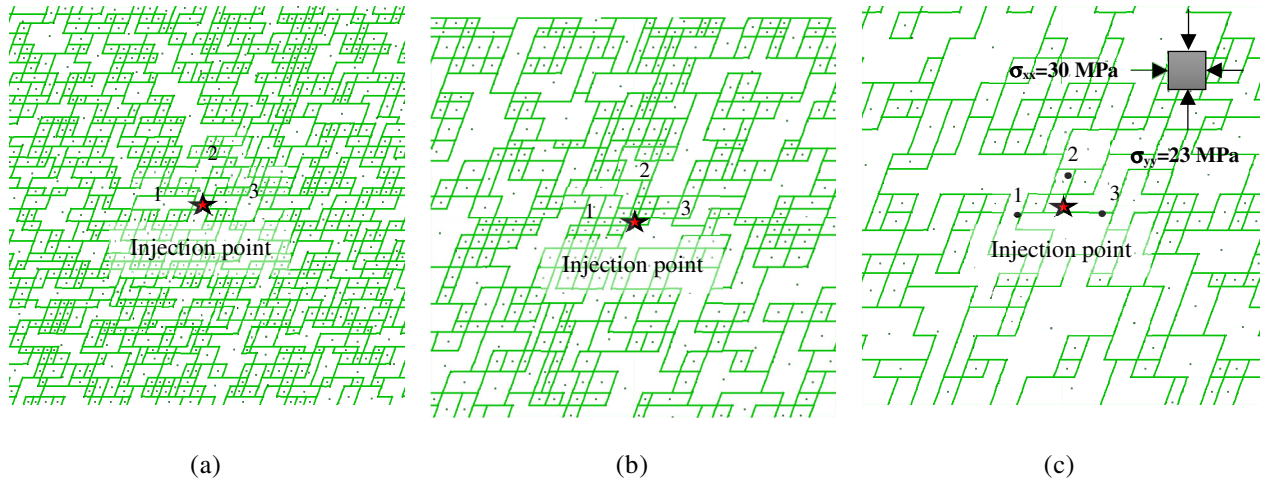


Figure 4.39. UDECTM models for different geometries representing various levels of a) high, b) medium and c) low joint density.

Figure 4.40 indicates that as the joint density of the jointed rock mass increases, pore pressure is distributed in a smaller portion of the model. Since injection pressure is the same for all simulations, increasing the number of discontinuities leads to a more rapid reduction in pressure outward. This is an expected result because more volume is made available for the fluid to flow into (constant injection rate).

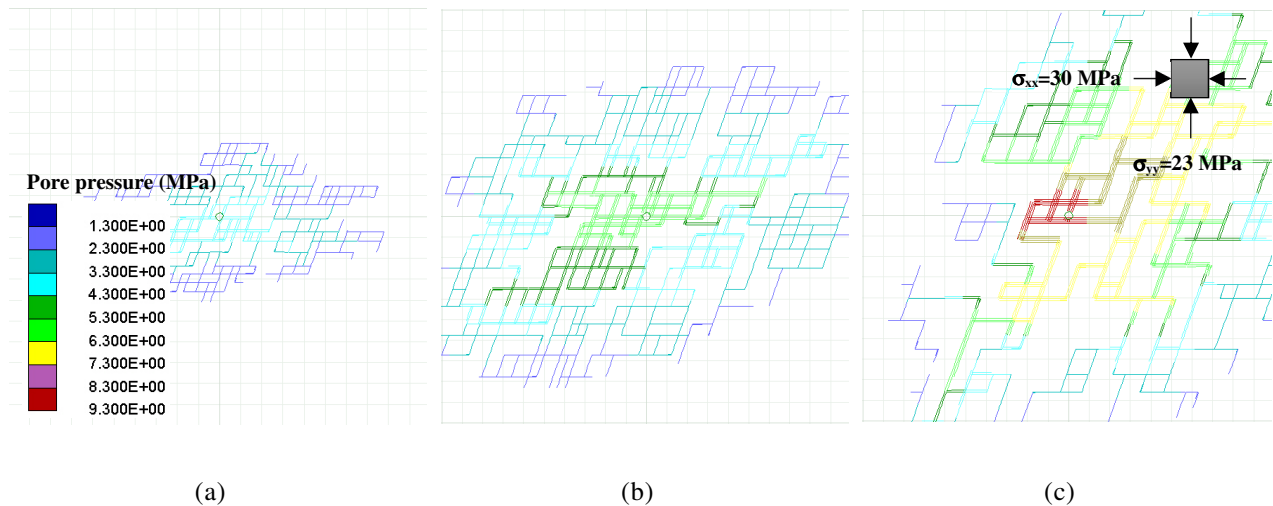


Figure 4.40. Pore pressure distribution in a fully connected geometry with various levels of a) high, b) medium and c) low joint density.

Figure 4.41 and Figure 4.42 demonstrate joint shearing and opening, respectively; mostly inclined joints undergo slip whereas tensile opening only occurs in horizontal joints.

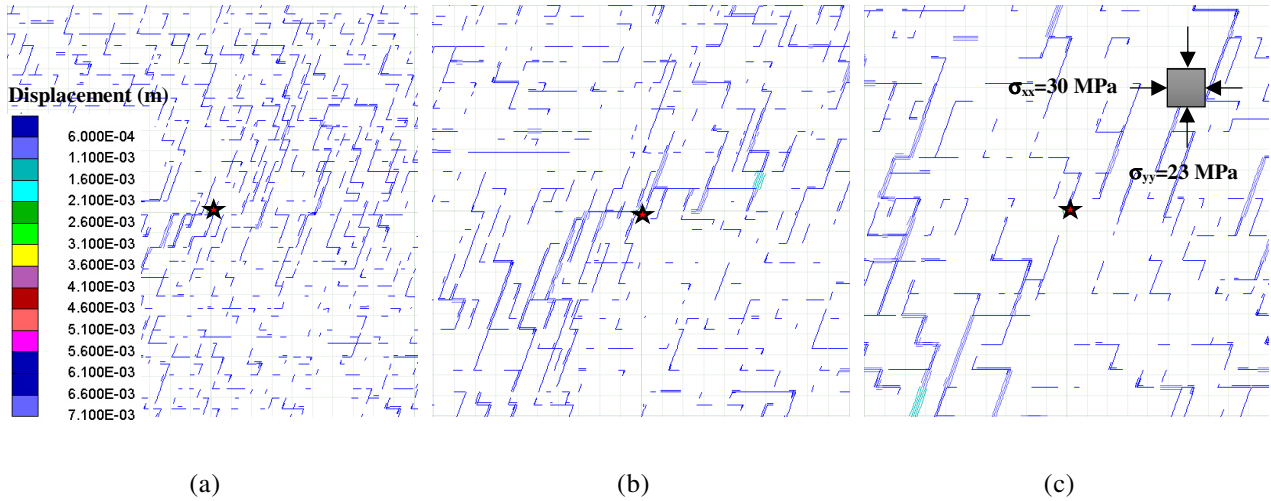


Figure 4.41. Joint shear displacement around a pressurized injection point in a fully connected geometry with various levels of a) high, b) medium and c) low joint density.

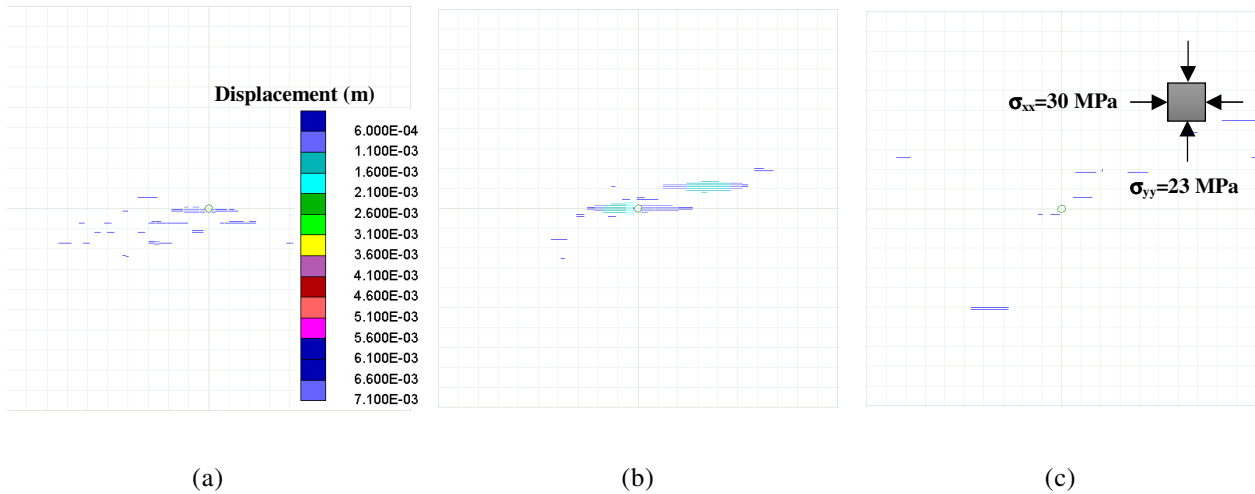


Figure 4.42. Joint normal displacement around a pressurized injection point in a fully connected geometry with various levels of a) high, b) medium and c) low joint density.

Figure 4.43 shows maximum values of joint normal and shear displacements in joint networks with different joint densities. It is clear that joint shear and normal displacement decreases by increasing the number of discontinuities; however normal displacements are larger than shear displacements. Far from the injection point, normal opening mode does not occur but a favorably oriented joint can shear. Thus, the slipped area (stimulated area) should be larger than the area affected by the opening mode.

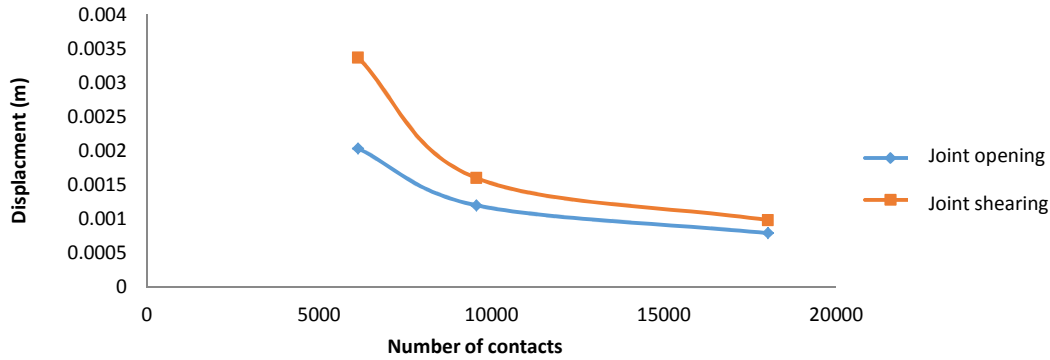


Figure 4.43. Maximum values of joint normal and shear displacements vs number of contacts in joint networks with different joint density.

4.4 SUMMARY

These preliminary simulation studies were performed mostly for simple cases to help understand the various processes involved. Different simplified basic components of a complex naturally fractured rock mass were subjected to hydraulic gradients in two different directions in a stress field having different anisotropy values. The following conclusions were obtained:

- The variations of flow-rate patterns are related to changes in hydraulic aperture and also the direction of pressure gradients. A rock mass with strong fabric responds differently if the flow gradients are oriented differently.
- Based on the simulations and comparing displacements and flow-rate results, joint displacement and fluid flow (aperture) are shown to be highly sensitive to joint stiffness. More closure of aperture in less stiff fractures leads to a strong reduction of fluid flow. A rock mass with compliant joints will show a greater change in flow rate than a rock mass with stiff fractures when subjected to a pressure gradient change.
- Changing stress conditions has an insignificant effect on displacement but has a strong impact on fluid pressure redistribution or flow-rates. This occurs because relatively small changes in hydraulic aperture lead to large variations in conductivity, and hence also in flow rates.
- NFR possesses a number of sources of strong non-linearity, and discrete block hydromechanically coupled simulations are needed to understand the effects; even then, this understanding is more than likely to remain qualitative because of the various sources of parameter and fabric uncertainty.

The Universal Distinct Element Code (UDECTM) is used to analyze fluid injection with steady-state flow through the joints in a jointed rock mass. Mechanical behavior of a jointed rock mass is studied at different values of stress field anisotropy and based on these simulations, it is understood that:

- Local natural fracture fabric affects hydraulically induced fracture direction, but the global orientation of induced fracture growth remains normal to the minimum principal stress;
- Pore pressure increases in a uniform pattern all around the injection point in the isotropic stress state; however it tends to focus sharply in one orientation under stronger differential stress, parallel to σ_{\max} ;
- Branching occurs a short distance from the injection point. It is usually suppressed under a higher stress ratio and is more highly developed in the isotropic stress state;
- It seems that there is a critical stress ratio that controls the dominant deformation mechanism.

In general, natural fractures that can be reactivated (Mode I or Mode II motion) by stress changes will also have alterable mechanical properties, which will lead to different behaviors in shearing, opening, sliding or closing in reaction to stress redistributions. Based on the current study, results can be compared for different fabrics to better understand the influence of both intensity of discontinuities and stress ratio.

- Both joint normal and shear displacements drop with an increasing number of discontinuities; however, this effect is smaller in models with persistent versus non-persistent discontinuities.
- Joint shearing and opening frequency have similar values for models with persistent and non-persistent discontinuities. In isotropic or close-to-isotropic conditions, they are almost zero in all fabrics and they increase with higher stress difference. However, this is more noticeable for a fabric based on a simple Voronoi tessellation.
- The combined effect of Mode I and II mechanisms causes conductivity enhancements in Voronoi tessellated media with persistent and non-persistent discontinuities.
- The number of discontinuities inversely affects fluid pressure; in other words, the area in which injection fluid flows through fractures decreases by increasing the number of discontinuities that can accept flow.
- Lower fluid pressure is obtained under higher differential stress, such that it has the maximum value in the isotropic stress state.

The results of this study should lead to a better understanding of hydraulic fracturing in naturally fractured rocks with major effects of the intensity of fractures (number of fractures per volume, or area in the case of this two-dimensional DEM), in the geometric nature of the natural fractures, in the distribution of fractures with respect to the deviatoric stress field, the magnitude of normal and deviatoric stresses and the presence of a single (or several) large through-going discontinuities. For example, the presence of a single large through-going discontinuity (section 4.3.1.2), clearly showed a focus of shear displacement on the major feature and this can be taken as indicative of the possibility of fault re-activation in a real case.

These results indicate the importance of natural rock fabric delineation in practical cases, and such results will have to be formulated with and calibrated against real data in order to achieve engineering utility. A real challenge in the short-term is performing three-dimensional simulations and understanding how to interpret them.

An important point in a practical sense is that in a deviatoric stress condition in a naturally fractured rock, even if the fabric itself is isotropic, injection with an increased pressure will induce anisotropy in the flow patterns because of the anisotropic dilation and shear of the joints. This has implications on well test analyses, especially if Δp is large enough to start changing the apertures of the jointed rock mass.

Another critical point is that in hydraulic fracturing, it seems likely that different strategies are needed for optimizing results and generating a genuine fracture network with high connectivity in cases of different rock fabric and different absolute and relative principal stress values.

CHAPTER 5 STIMULATED ZONE ASSOCIATED WITH HYDRAULIC FRACTURING IN LOW-PERMEABILITY NATURALLY FRACTURED ROCKS

This chapter presents results based on seeking to investigate how fabric patterns and stress redistribution affect the nature of the stimulated zone associated with hydraulic fracturing.

OVERVIEW

When a Naturally Fractured Rock (NFR) is subjected to hydraulic fracturing (HF) stimulation, a volume that is affected by the HF treatment is generated. This volume is referred to as the stimulated zone and is characterized by an increase in overall permeability. When performing HF stimulations in NFR, understanding the factors that control the size and shape of the stimulated zone can aid in optimizing the HF process.

This research uses the two-dimensional Distinct Element Method (DEM) to investigate the effect of rock fabric, in-situ stress state, and injection parameters on the size and shape of a stimulated zone. A parametric study of hydro-mechanically coupled HF simulations was conducted using UDEC™ software. To determine parameter effects on the stimulated zone, a new method was developed to quantitatively assess the stimulated zone using relative displacements. In addition, this chapter is focused on understanding the mechanisms leading to the differences in various stimulated zone simulations.

This investigation shows that rock fabric and in-situ stress state are key factors affecting the stimulated zone and the pathways of HF propagation. The injection rate does not have a substantial effect on the stimulated zone though it does affect the type of deformation that occurs within the zone. Joint deformation is affected more by stress ratio under lower injection rates. Higher injection rates cause higher fluid pressures and stimulate more joints because the fluid has enough pressure to overcome the normal stress, even in unfavorable directions; hence, the effect of stress ratio on zone development is reduced at higher injection rates. In the presence of one or more persistent joint sets, there are pre-existing preferential directions for fluid to travel, making the stimulated zone pattern and extent more complicated. If a dominant joint set is not co-axial with the principal stress orientations, zone extension and shape are substantially affected by the angle between the joint set and the principal stresses, especially at lower stress ratios.

5.1 INTRODUCTION

In hydraulic fracture (HF) stimulation, a fluid is injected under high pressure into the rock mass to intentionally fracture it, usually in order to enhance the hydraulic conductivity of the general region around the injection point. As hydraulic conductivity enhancement in a dense, low-porosity, naturally fractured rock (NFR) mass arises from mechanical deformation of naturally existing discontinuities; it is of interest to study their mechanical deformation during injection. These deformations include normal and shear displacements of pre-existing

discontinuities (i.e. joints), usually leading to long-term or permanent hydraulic conductivity enhancement.

Note: In an attempt to be clear, the term “joint” will replace “natural fractures” or “planar discontinuities”, to avoid confusion with the term “hydraulic fractures”. The term “permeability” is reserved for a bulk rock mass effect, and the term hydraulic conductivity is used for an individual joint or for a subset of the rock mass (an assemblage of joints not sufficient to be volume averaged).

In HF operations, especially in the presence of high deviatoric stresses, the contribution of joint shearing (Mode II displacement) to hydraulic conductivity enhancement may be as important as direct joint opening (Mode I displacement). This is indirectly supported by the numerous Mode II microseismic events resulting from frictional slippage associated with HF (Cipolla et al. 2013). Bagheri and Settari studied the effects of Mode I displacement of a single joint on the hydraulic conductivity of a naturally fractured rock using coupled geomechanical modeling (Bagheri and Settari 2006). Ji et al. developed their study by coupling fracture propagation with hydro-mechanical simulation (Ji et al. 2009). In the research performed by Nassir, the effect of shearing on mechanical and flow properties of rock has been studied (Nassir 2013), and he also investigated the critical pore pressure at which shear failure occurs, the orientation of induced fractures within the rock formation and the effect of transition from non-HF conditions to HF conditions on geomechanics and flow problems. However, the effect of rock fabric on the mechanical response of a NFR to HF remains poorly understood in the discipline of geomechanics. In this chapter, three different joint patterns are generated to represent different NFR macrofabrics, and to explore the effects of these geometries on mechanical deformation and fluid flow. The main objective of this work is to study the size and shape of the stimulated zone associated with HF under different stress states and NFR fabric conditions.

5.1.1 NATURALLY FRACTURED ROCK

Most rocks possess different mechanical discontinuities of various origins referred to as joints, fractures, faults, shear zones, bedding planes, schistosity, foliation, cleavage and other geological terms (Singhal and Gupta 2010). These different mechanical discontinuities may be considered “macrofabric” elements in contrast to “microfabric” elements such as preferred mineral alignment, grain/pore assemblages and microfissures. Joints are perhaps the most common and most important type of macrofabric element in igneous and sedimentary rocks and are usually found in sets (i.e. different groups of parallel or sub-parallel joints). The properties of these discontinuities almost always control the deformation and permeability of a NFR (Zhang 2005) where the matrix block shear strength is far larger than the shear strength of the discontinuities themselves. In other words, a NFR is viewed as a medium in which naturally occurring discontinuities have a dominant influence on the system’s deformability and permeability (Pirayehgar and Dusseault 2014). Discontinuities provide potential flow channels in a NFR, as well as potential slip planes (Singhal and Gupta 2010). Deformation is controlled by

the geometrical characteristics of the macrofabric elements (joints), the mechanical and hydraulic properties of the joints and the in-situ stress conditions. As a result, fluid flow in a jointed system is related to the deformation of both the planar discontinuities and rock blocks, through the processes of hydro-mechanical coupling (Zhang and Sanderson 2002).

Joints are planes of weakness with shear and normal strength usually far lower than intact rock blocks. Joints and other macrofabric elements are created by deformation and physico-chemical diagenesis of different types (Singhal and Gupta 2010). Natural fractures (including joints) are categorized into systematic and non-systematic systems; systematic natural fractures are planar with approximately regularly spaced distribution and generally in sets comprised of many parallel or subparallel surfaces while non-systematic natural fractures have an irregular distribution - they may be curved and there are no significant sets. Systematic discontinuities can be further divided into three categories based on the kinematics of their origin: shear (Mode II) fractures, tensile (Mode I) fractures and hybrid fractures (Singhal and Gupta 2010). To be more exact, three modes of deformation, including opening (Mode I), sliding (Mode II) and tearing modes (Mode III), can be recognized in natural fractures. These are associated with their formation processes and interactions with other discontinuities leading to segmentation, arrest and other factors related to their genesis in a natural stress field at depth.

Creating new induced fractures in NFRs using conventional small-scale HF usually results in limited extent induced fractures, limited new surface area generated and thus a limited enhancement of flow properties. Large-scale HF with proppants, high injection rates and various types of fluids have been developed to achieve greater drainage efficiency within a rock mass (Smith and Montgomery 2015). When a HF intersects a natural fracture, it may initially arrest. Yet with continued pumping, the HF may cross or open the natural fracture. Fluid diversion into the natural fracture system can result in higher propagation pressures, greater fluid leak-off, less efficient proppant transport and eventually may decrease the fracture length (or stimulated volume) that can be generated (Rahman et al. 2002). Warpinski indicated that conventional HF is relatively less efficient in regions with high deviatoric stresses and natural fractures and therefore recommended investigation of other stimulation techniques (Warpinski 1991). Hossain et al. found that the presence of natural fractures that were misaligned with the direction of fracture propagation lead to a tortuous flow path which ultimately caused the treatment to fail the intended goals. This was mostly due to the proppant “screen-out” that takes place prematurely in tortuous flow path conditions, inhibiting deep penetration of the granular proppant that maintains aperture after the HF pressures are allowed to decay. The large-scale natural fabric in a NFR is thus potentially both an advantage and a natural peril to the treatment’s efficiency in terms of its effect on meeting its rock mass permeability enhancement goals (Hossain et al. 2000).

An approach to HF has been presented by Hossain et al. (Hossain et al. 2002) for hydraulic stimulation that is known by various names such as no-proppant and proppant-free. However, recently it has been called the “shear dilation” treatment. Hossain et al. found that under specific stimulation pressures, a natural fracture can slip by shear and dilate (known as “shear dilation”),

thereby enhancing its conductivity. This enhancement is based on the preservation of remnant conductivity from shear displacement occurring because of the mismatch of natural asperities that is caused by small shear displacements across a planar surface (Hossain et al. 2002).

5.1.2 PARAMETERS AFFECTING THE STIMULATED ZONE

It is useful to predict, at least semi-quantitatively, the nature of stimulated zone generated from HF in a NFR for well layouts or treatment designs. Knowing the shape and size of the potential stimulated zone can aid in choosing well spacings and perforation cluster placement, as well as the volume and rate of the HF treatment (Dusseault 2013).

Natural stress fields are not isotropic ($\sigma_1 \neq \sigma_2 \neq \sigma_3$). This means that there are always differences between the principal stresses, so that shear stresses exist throughout the medium. Fluid injection raises pore pressures and creates a drop in normal effective stress which can lead to slip of appropriately oriented joint surfaces. These joint surfaces are rough and therefore slip generates joint aperture through irreversible dilation (normal opening accompanying shear displacement). Since the shear stress has been partly relieved by slip, both the slip and the dilation are largely irrecoverable, therefore the aperture increase through dilation is permanent. In other words, shear displacement of appropriately oriented joints in a NFR mass causes permanent dilated aperture known as shear dilation (Rahman et al. 2002). This dilation region may be viewed as a zone of enhanced percolation (connectivity plus conductivity).

Johri and Zoback suggest that three factors control the magnitude of the enhanced percolation zone: hydraulic fractures, pre-existing fractures and new fractures (Johri and Zoback 2013). Based on their study, the contribution of hydraulic fractures and newly-formed or connected fractures is insignificant; hence, stimulating the pre-existing fractures plays a key role in the enhancement of conductivity and connectivity around a well.

5.2 HYDRAULIC FRACTURE SIMULATIONS

A series of numerical HF simulations are performed using UDECTM, a code based on the Distinct Element Method (DEM). When using UDECTM, one assumes that pre-existing joints are reinitiated and reopened while no new fractures are created. In other words, the matrix blocks remain intact - a robust assumption for HF in a NFR mass with strong blocks and weak joints (igneous rocks, low-porosity shale gas and shale oil reservoirs).

Although blocks are strong and will not fracture, they are treated as deformable bodies. The constitutive model for shearing used for the joint in this study was the Coulomb-slip criterion. The UDECTM models are considered to be two-dimensional sections 300m × 300m in size and subjected to a biaxial in-situ stress state (Figure 5.1). The medium is initially dry, then water is injected at a constant flow rate at the center point of the model.

Table 5.1 shows fluid and material properties assumed, including the mechanical properties of the joints. These properties have been selected from the software database, which is collected from a wide range of real data (ITASCA Consulting Group Inc. 2010). It is possible to stipulate different properties for each joint (or each set of a group of joint sets) such that the resultant fracture network is probabilistic in nature, which perhaps more closely emulates a real rock mass, but because it remains unclear what distributions of properties would be most appropriate, joint properties have been assumed to be constant for all joints. Also, in this same manner, it is easier to assess the direct influence of joint stiffness and cohesion.

Table 5.1. Rock, joints and fluid properties (UDEC™ database).

Rock properties			Joint mechanical properties		
Density	2700	kg/m ³	Normal stiffness	10	GPa/m
Bulk modulus	27	GPa	Shear stiffness	4	GPa/m
Shear modulus	7	GPa	Friction angle	30	Degree
Friction angle	30	Degree	Cohesion	0.1	MPa
Cohesion	27.2	MPa	Dilation angle	5	Degree
Tensile strength	1.17	MPa			
Joint hydraulic properties			Fluid properties		
Permeability factor	0.83×10^8	MPa ⁻¹ s ⁻¹	Density	1000	kg/m ³
Residual hydraulic aperture	1×10^{-4}	m	Dynamic viscosity	10^{-3}	Pa·s
Aperture at zero normal stress	5×10^{-4}	m			

Stress ratio is defined as the ratio of maximum to minimum principal stress. Minimum principal stress is set to 15 MPa, while maximum principal stress varies in the range of 15 to 30 MPa. A stress ratio of 2 is expressed as $\sigma'_{xx}/\sigma'_{yy} = 30/15 = 2$ and so on. Understanding the impact of the

stress ratio was the main intention of this study rather than the magnitudes of the stresses. Similar simulations run with higher stress magnitudes confirmed that the general behavior of the system at higher stresses with similar ratios is comparable; however, results are different in terms of the magnitudes of the deformations of the joints (higher stresses lead to smaller aperture increases).

Since rock fabric plays a prominent role in the characteristics of the resultant stimulated zone, three different geometries of a NFR mass were comparatively investigated. A major challenge when modelling NFRs is determining how best to represent the jointed rock mass. Zhang and Sanderson (Zhang and Sanderson 2002) introduced three main types of rock fabric to represent a range of common geometries:

- a. A network of randomly oriented polygonal joints (such as cooling joints in columnar basalt). This geometry is called Voronoi tessellation (Figure 5.1a).

- b. Two sets of joints which are generally long, straight and sub-parallel with different spacings and which cross-cut one another. This geometry is called cross-joints (Figure 5.1b). In Figure 5.1b, one set is inclined at about 120° and the other one is oriented at about 25° .
- c. A set of long persistent joints between which are shorter non-persistent joints roughly orthogonal to them (often found in flat-lying shales in anisotropic stress fields, no tectonics). This geometry is called cross-cuts. Figure 5.1c shows this geometry in which one set is inclined at about 120° and intersects with some non-persistent joints at different angles.

The implementation of these three types of rock fabric can be seen in Figure 5.1.

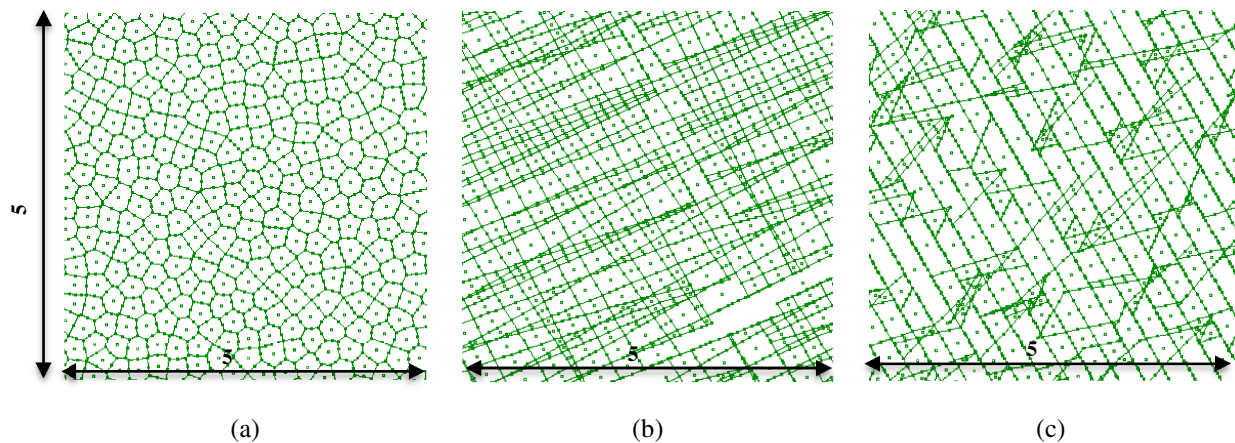


Figure 5.1. Representative geometries of natural fracture (joint) networks: a) Voronoi tessellation, b) Cross-joints; c) Cross-cuts.

Figure 5.2 shows results plotted as contact force vectors applied on grid points after injection under the in-situ stresses of 30 MPa and 15 MPa for all three geometries. The model is large enough to ensure that the boundary effects are small. The in-situ stress field is defined by two orthogonal principal stresses stipulated in the central figure.

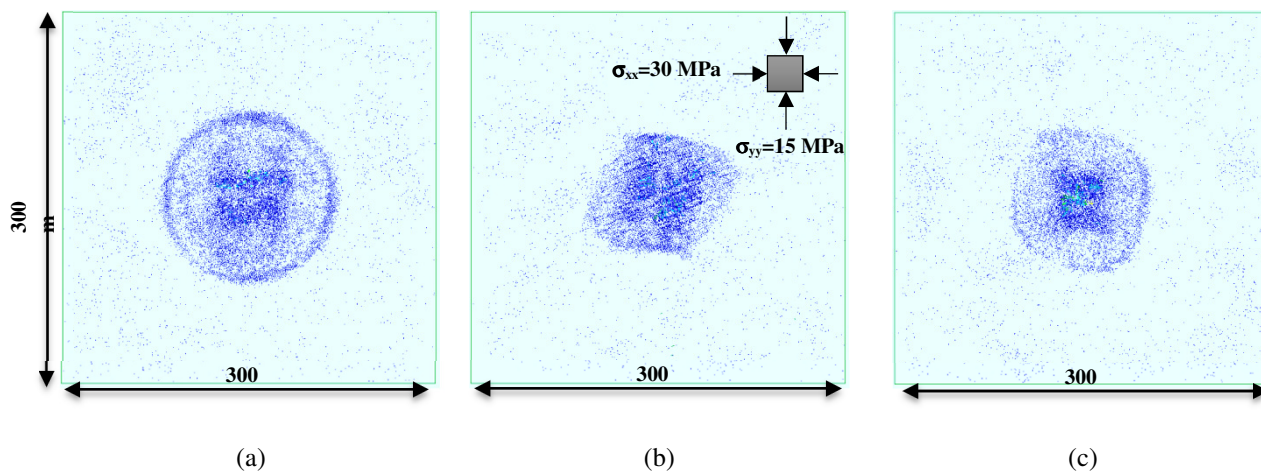


Figure 5.2. Gridpoint force vectors for different geometries: a) Voronoi tessellation, b) Cross-joints; c) Cross-cuts.

5.3 ASSESSING THE STIMULATED ZONE

Assessment of the stimulated zone was conducted based on the resultant normal and shear displacements of the block contacts during HF in the DEM (Discrete Element Method) model simulations. It is also possible to use joint rupture as an alternative criterion for assessing the stimulated zone; however, the binary nature of the metric was inadequate to describe partial opening of the joints. The joints have the capacity to yield and experience some displacement without completely failing. This displacement is important to capture when discussing stimulated zone and permeability enhancement along joints that have not experienced full strain-weakening failure (resulting in a shear-slip event), yet may have experienced some yield.

The stimulated zone in the context of this investigation was taken to be the minimum geometric area within which all displacement events exceeded a specified threshold. Two different stimulated zone geometries were considered for this investigation: elliptical and polygonal, as shown in Figure 5.3. The method to characterize the joint geometry area as an idealized ellipse was conducted by calculating the minimum bounding ellipse for the set of contacts which exceeded the displacement thresholds. In addition, the convex polygonal hull of the same set of points was also calculated as it is arguably a more rigorous, but less convenient metric (Fomin et al., 2006).

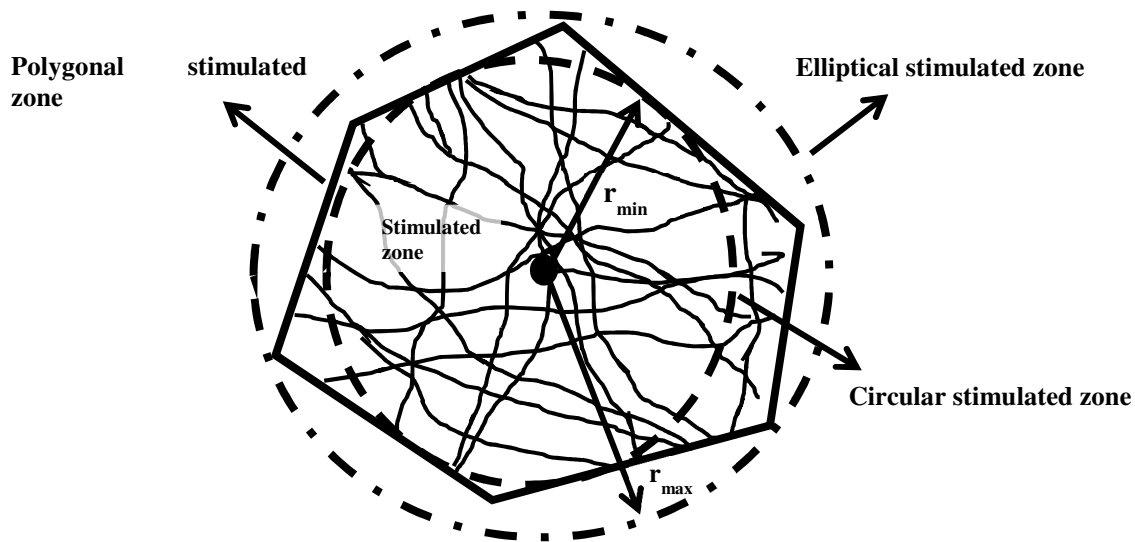


Figure 5.3. Schematic of the stimulated zone outlining the difference between an idealized circular shape and the actual polygonal shape. (Fomin et al. 2006)

The need to specify a displacement threshold when calculating the stimulated zone arises from the nature of a NFR. When the stress state of the model changes due to the injection of the fracturing fluid, the resultant stress change (generally diminution in normal effective stress) in areas not directly penetrated by the fracturing fluid can nonetheless lead to shear displacements along the joints and consequent shear dilation behavior. These displacements are often small and not necessarily hydraulically connected to the area directly stimulated by the HF fluid. As such, a

means to eliminate these peripheral displacement events from the stimulated zone can be accomplished by assuming that these displacements are appreciably less than the displacements directly associated with the HF process, such that there exists a threshold under which these displacement events should not be considered. The determination of this threshold was conducted by testing different thresholds over a specified range to see at which point the stimulated zone became relatively constant, consequently indicating the peripheral displacements as negligible and thus having potential to be excluded in the calculation of the stimulated zone. For example, Figure 5.4 and Figure 5.5 show a change in stimulated zone based on normal and shear displacements respectively as the displacement thresholds were varied for the Voronoi tessellated rock fabric with a stress ratio of 2. When the displacement threshold is increased from zero, the stimulated zone decreases rapidly until a threshold is reached at which point the stimulated zone remains relatively constant. It was decided that this was a convenient and empirical definition of the desired threshold that would eliminate small peripheral displacement events from the stimulated zone calculations. Additionally, there is an almost constant stimulated zone for the very small magnitude of displacements. However, a common dilation threshold was needed for this study for both shear and normal displacement. The use of a common dilation threshold also made it is possible to find the dominant deformation mechanism.

In Figure 5.4, the ideal normal threshold differs based on different simulation parameters. The two sets of simulations with the small meshes and small blocks (SM and SB) appear to have the same threshold; however, the simulations with the large blocks (LB) appear to require a larger threshold. This behavior indicates that the rock mass fabric scale with respect to the scale of the induced HF zone has a significant influence on the determination of the required displacement thresholds. Similar behavior can be seen in Figure 5.5 when considering shear displacement thresholds.

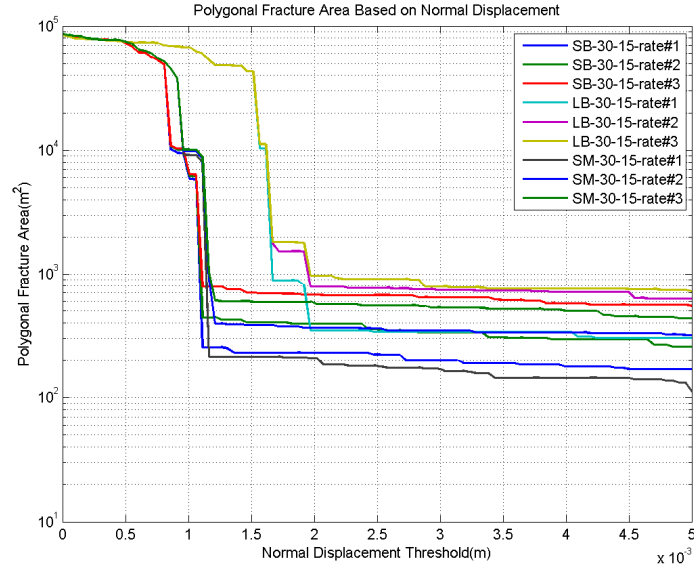


Figure 5.4. Polygonal stimulated zone based on normal displacement for various model simulations and flow rates and a stress ratio of 2 with Voronoi tessellated rock fabric. SB = Small Block size, LB = Large Block size, SM = Small Mesh size.

Furthermore, from Figure 5.4 and Figure 5.5 one can see that the difference between the refined mesh (SM) and the coarsely-discretized mesh (SB) is significant in terms of the resultant stimulated zone, despite the similarity in the required thresholds. The implication of this discrepancy is that the mesh in DEM modelling needs to be refined sufficiently to allow for mesh convergence and representativeness (a scaling issue). As such, the refined SM models are used for the remainder of the analysis.

For the case of the refined mesh for the small block Voronoi tessellated rock fabric, it can be seen that a normal displacement threshold of 1.5 mm and a shear displacement threshold of 2.5 mm would be sufficient for the stimulated zone calculations. (Note that these displacements do not necessarily correspond to “real” displacements because the choice of model parameters was not made on the basis of “establishing the best fit” to what are considered “realistic” values. These are challenging issues to address in future studies.)

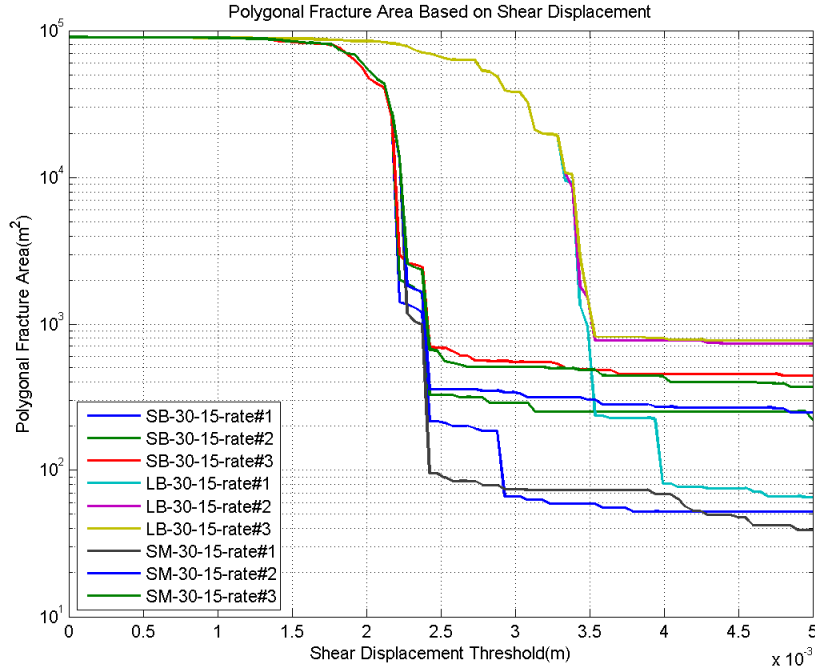


Figure 5.5. Polygonal stimulated zone based on shear displacement for various model simulations and flow rates and a stress ratio of 2. SB = Small Block size, LB = Large Block size, SM = Small Mesh size.

As the stress ratio increases, one would expect the required aperture threshold to also increase as the increased differential stress will facilitate peripheral shear in the non-stimulated zone. Consequently, for all stress ratios less than 2 that were investigated, the displacement thresholds were marginally less, allowing for the displacement thresholds determined at a large stress ratio to be used for all cases with lower stress ratios.

It is worth noting that the injection flow rates did not appreciably affect the displacement thresholds, indicating that the rock fabric has a dominant effect on the required displacement thresholds for the calculation of the stimulated zone.

When considering the stimulated zone assessment, it is convenient to idealize it as an ellipse spatially bounding all displacement events. In this study, the Khachiyan algorithm (Todd and Yildirim 2007) was implemented to calculate the minimum bounding ellipse for the set of spatially distributed contacts in which the displacement thresholds were exceeded. This algorithm iteratively generates a series of ellipses which contain all the specified points and are uniformly decreasing in area. The resultant minimum bounding ellipse was chosen once the relative difference between two successive iterations was identified to be below a specified tolerance. In this investigation the tolerance was specified to be 0.1% of the ellipse area as the variance due to other parameters was noted to be appreciably larger.

The use of an elliptical approximation, though useful, tends to overestimate the stimulated zone in a non-uniform jointed medium simulation as the shape of the stimulated zone is often irregular

and non-elliptical (Fomin et al. 2006), largely because of the fabric geometry. One may also approximate the stimulated zone as a convex polygon enclosing the threshold displacement events. On average the elliptical enclosure is 44% larger than the polygonal enclosure for the Voronoi tessellated rock fabric (Figure 5.6). This relationship between the polygonal and elliptical areas is dependent primarily on the rock mass fabric. In addition, when considering an idealized elliptical stimulated zone quantitatively, it is prudent to correct for this discrepancy.

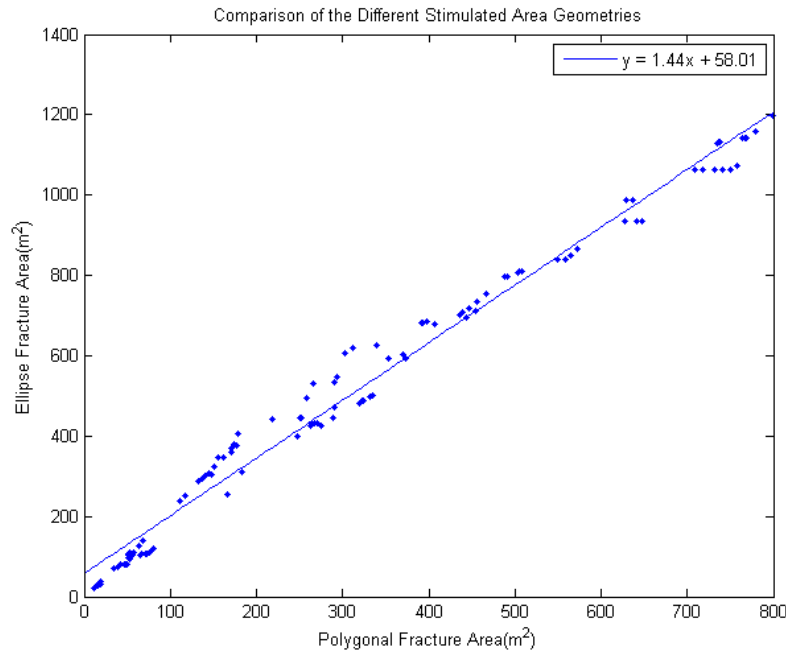


Figure 5.6. Comparison of the different stimulated zone geometries for the case of the Voronoi tessellated rock fabric. The stimulated zone based on an ellipse is approximately 44% larger than that based on the convex polygon hull.

A series of sensitivity analyses was carried out to study the effect of block size, mesh size and model size for the Voronoi tessellation. The results of these analyses show that numerical parameters have the capacity to affect the stimulated zone calculations if not considered appropriately. Here, the main finding is that it becomes important to have a sufficiently converged solution in terms of mesh refinement. Details of this study have been published elsewhere (Pirayehgar et al. 2016).

5.4 PARAMETRIC STUDY

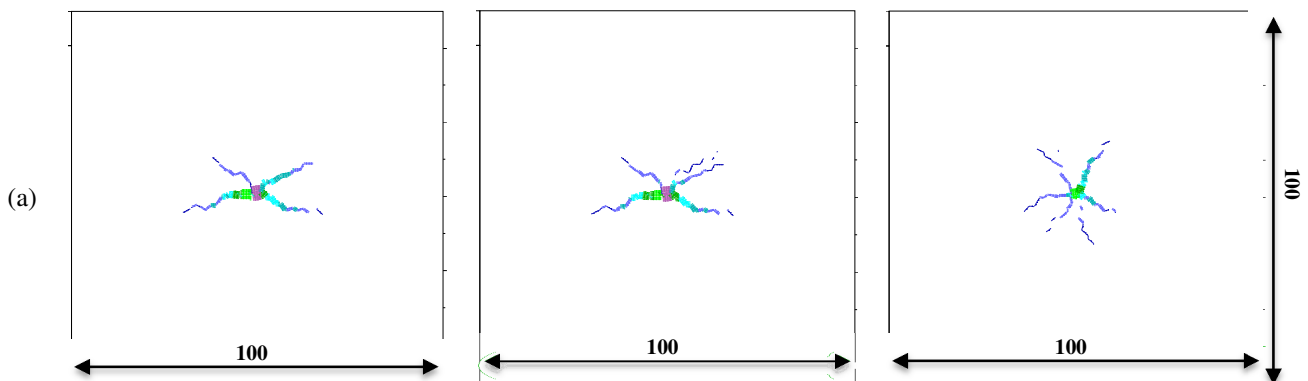
In order to investigate the influence of parameters that affect the stimulated zone due to HF, a parametric study was conducted. Here, the three specified rock fabrics (Voronoi tessellation, cross-cuts, and cross-joints) are subject to HF simulations under different stress ratios and injection rates. Stress ratios between 0.5 and 2 are considered along with fluid injection rates between 5L/s and 15L/s.

5.4.1 EFFECT OF ROCK FABRIC

Positive normal displacement of joints (joint opening) under different stress states can be seen in Figure 5.7. For the Voronoi tessellation, isotropic stress causes the induced HF zone to propagate radially from the injection point in all directions, while under differential stresses, a direction normal to the minimum principal stress is preferred. Figure 5.7b and Figure 5.7c indicate that in the presence of strongly oriented fabric, displacements typically occur along the joints and joint sets that are inclined to the principle stresses. In the case of strong differential stresses, the HF zone will propagate normal to σ_{\min} even if the joint sets are not oriented in that direction. Therefore, if the joints and the major principle stresses are not similarly oriented, the stimulated zone will be more radial or more directional under weaker or stronger deviatoric stress states, respectively. In general, an isotropic stress state grants a similar probability of growth to all directions, so in the case of the Voronoi tessellation with no preferential orientation, the stimulated zone would be radial and in case of cross-joints or cross-cuts, it would be directional. However, the HF zone tends to propagate mostly normal to the σ_{\min} direction under stronger deviatoric stresses. Therefore, for the Voronoi tessellated rock fabric, the more one departs from the isotropic stress state, the more directional the stimulated zone becomes. For the other fabrics, if there is no dominant joint set parallel to the direction of the maximum principal stress, the resultant stimulated zone would form in a more radial manner (Figure 5.10).

Pressurized fluid injection causes a combination of tensile openings and shear dilations in the neighboring zone which induce slippage on pre-existing joints, creating more or larger flow channels. Most of the joints around the injection point undergo both normal and shear displacements such that mixed mode is the dominant deformation mechanism. However, the joints undergo larger openings than shearing for all geometries, which can be observed in Figure 5.7 and Figure 5.8.

Based on Figure 5.7, the cross-joints geometry with two joint sets has the largest joint openings under all stress ratios followed by the cross-cuts geometry and then the Voronoi tessellation with no dominant jointing orientation. Therefore, the presence of joint set(s) often leads to larger normal displacements.



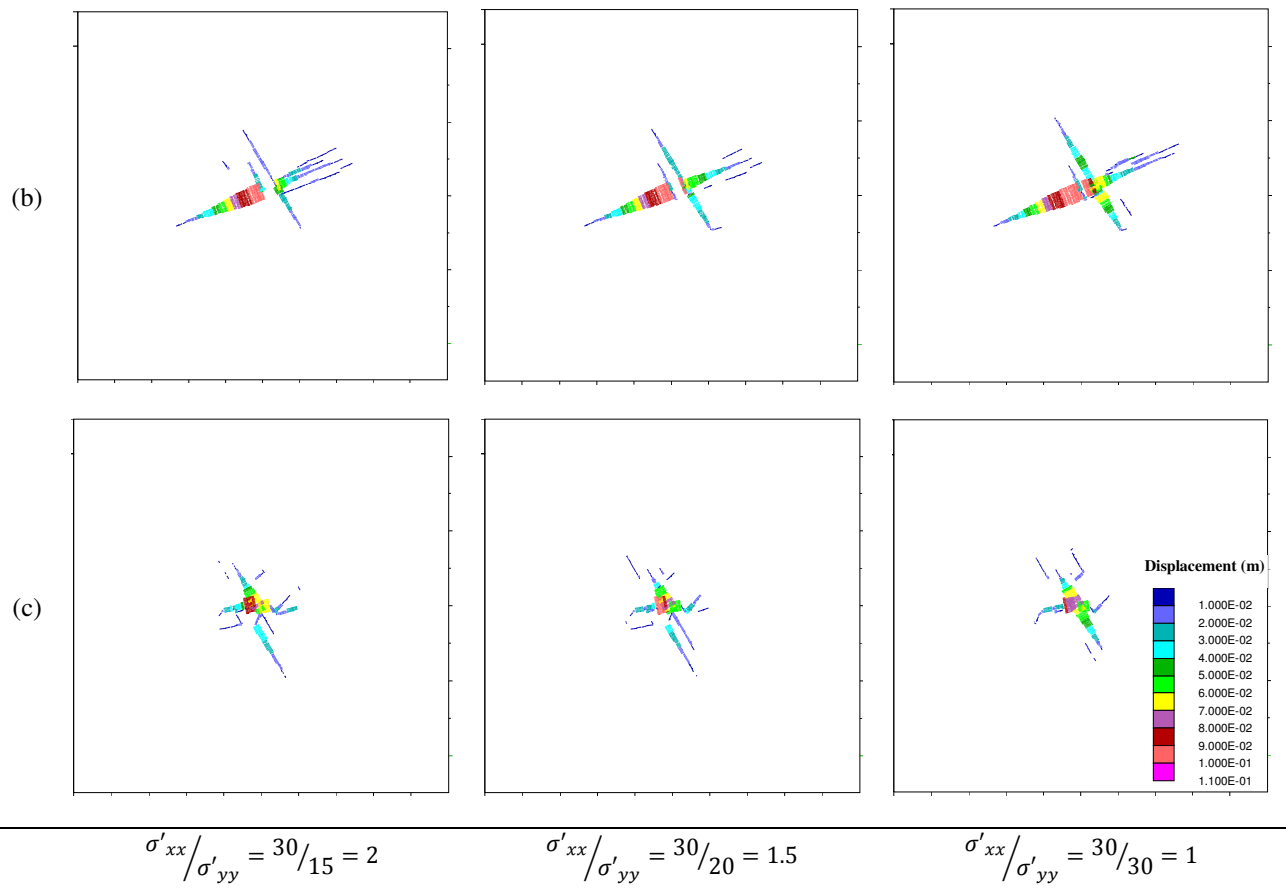
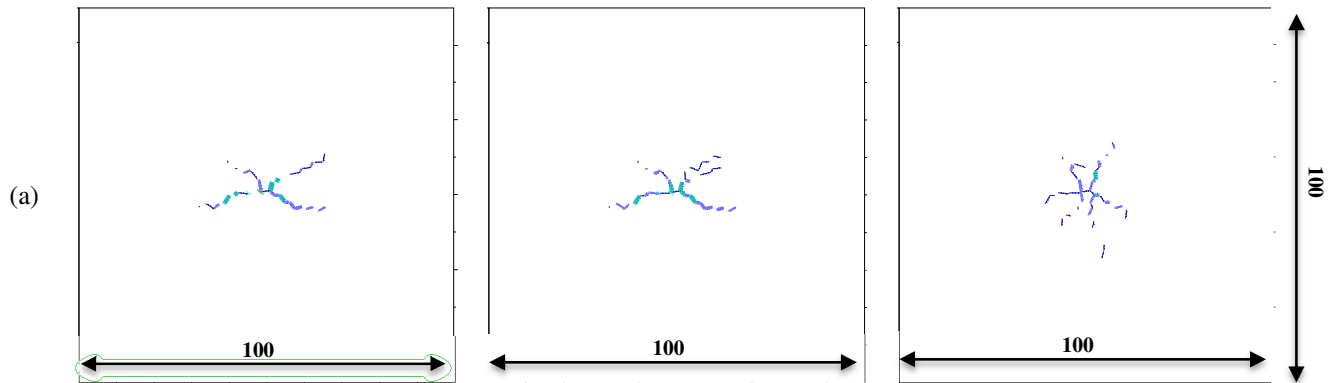


Figure 5.7. Opening under different stress states for: a) Voronoi tessellation, b) Cross-joints; c) Cross-cuts.



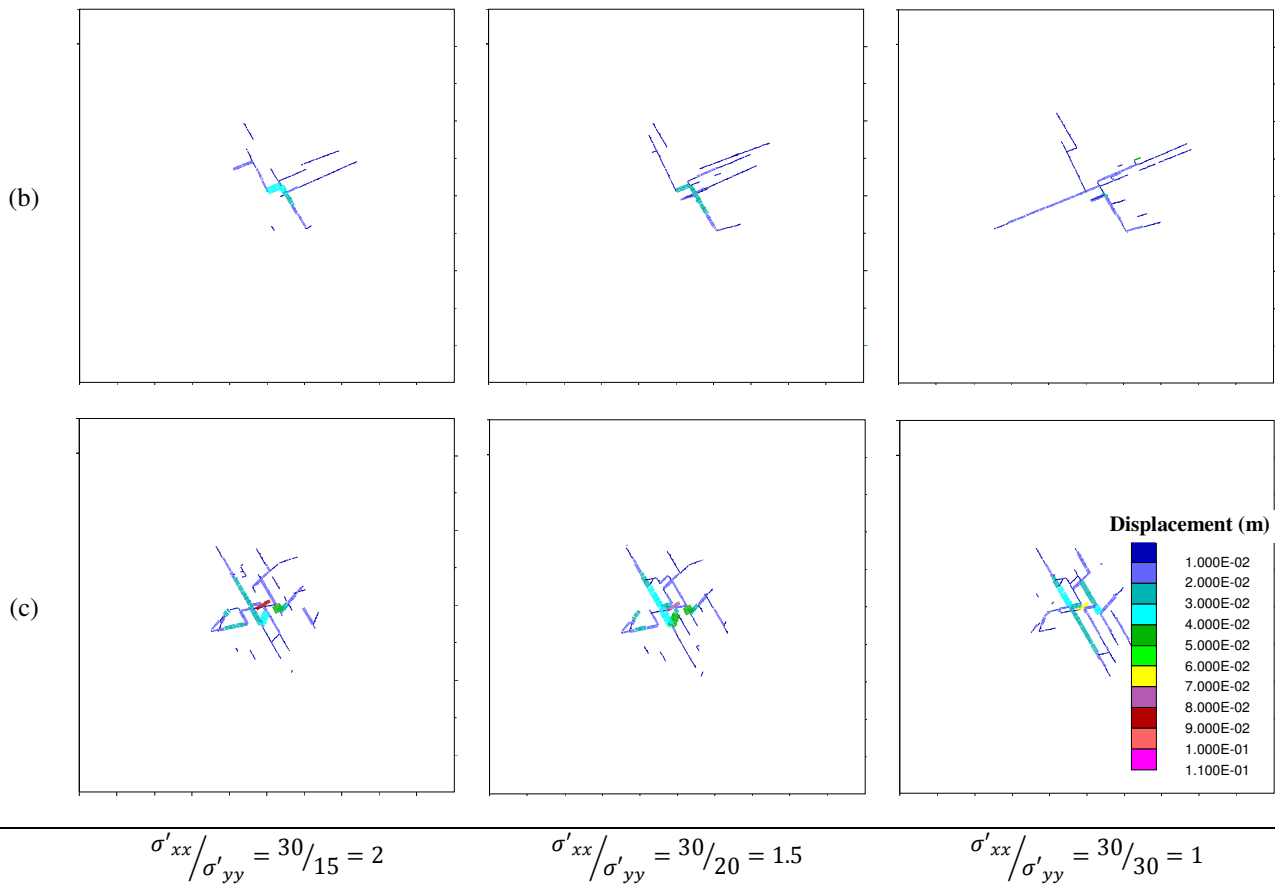
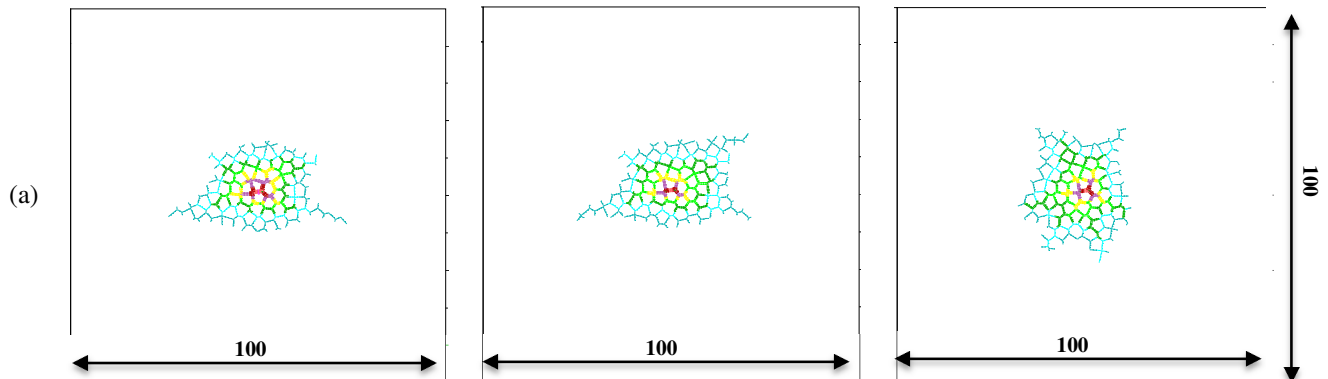


Figure 5.8. Shearing under different stress states: a) Voronoi tessellation, b) Cross-joints; c) Cross-cuts.

Pore pressure distributions for different rock fabrics under various stress ratios are shown in Figure 5.9. Here, it can be seen that pore pressure increases in a uniform pattern around the injection point, given an isotropic stress state. However, the pore pressure distribution tends to focus sharply in one orientation under stronger differential stress, normal to σ_{\min} . This pressure distribution shows that differential stress fields can lead to induced flow anisotropy for any set of joints, but particularly noticeable for the isotropic models.



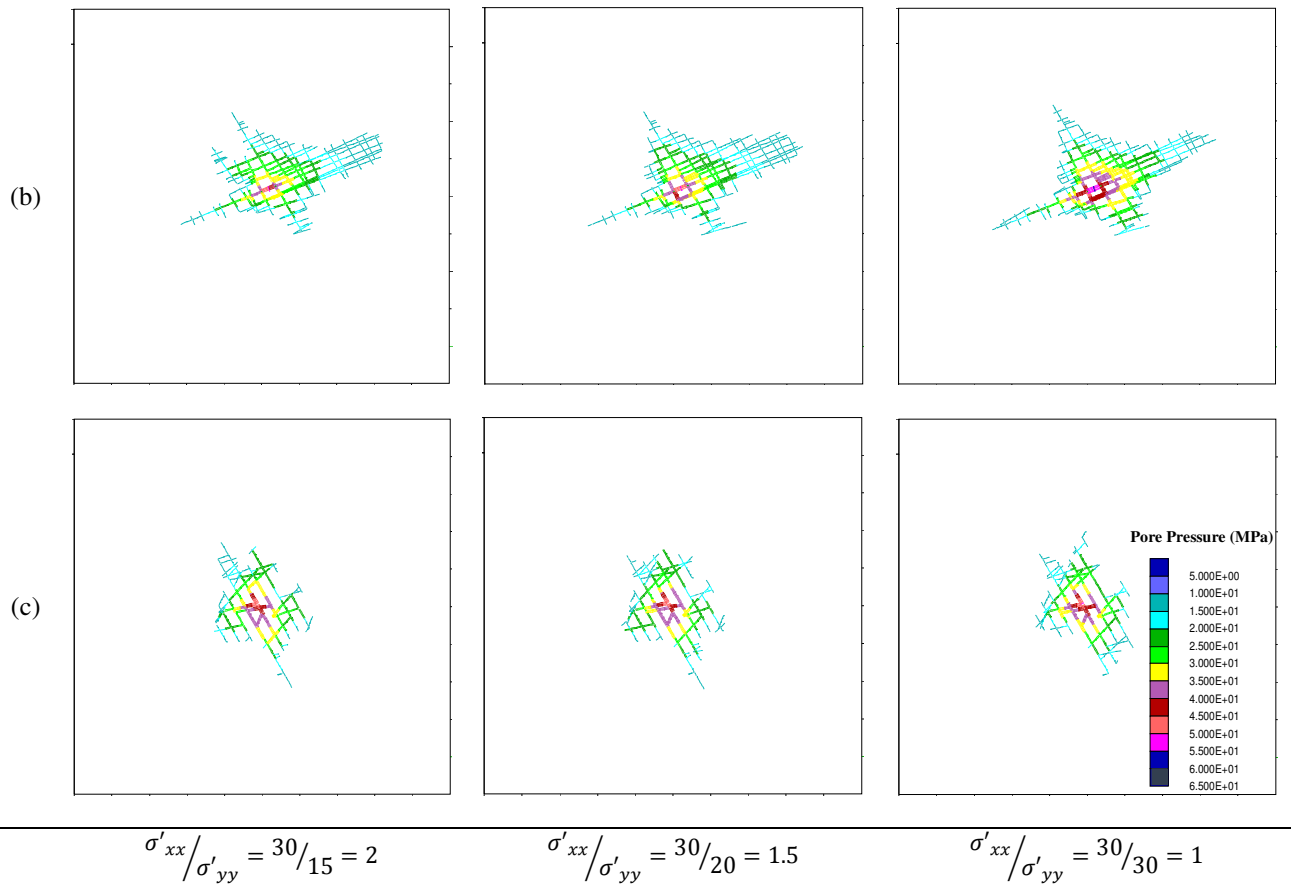


Figure 5.9. Pore pressure under different stress states for the representative geometries of natural fracture networks: a) Voronoi tessellation, b) Cross-joints; c) Cross-cuts.

5.4.2 EFFECT OF IN-SITU STRESS

In-situ stresses are also investigated to study effects that the stress ratio has on a stimulated zone. Stress ratios of 1, 1.5 and 2 are considered and subjected to HF simulations. Figure 5.10 shows flow directions in joints around the injection point in various stress fields in the Voronoi tessellated rock fabric. Arrows with a circle on one end indicate the new opened joints; new paths are pressurized as the stress state gets close to the isotropic condition and the pattern becomes more radial. Fluid travels farther and flow channels are more laterally developed through channels under higher differential stresses.

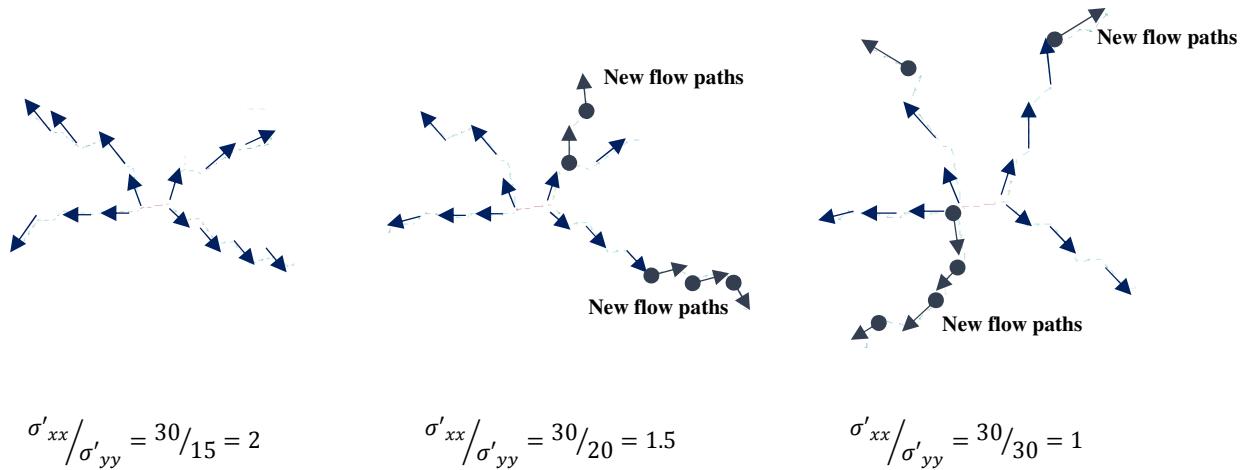


Figure 5.10. Flow direction in joints during fluid injection from the borehole in various anisotropic stress fields in the Voronoi tessellated rock fabric.

Figure 5.11 shows fluid pressure profiles along the center of the model in the σ_{MAX} direction for all geometries under different stress conditions and selected injection rates (rate^{#3} ≈ 15 L/s). Arrows indicate how far the fluid pressure is distributed laterally and where it starts branching until $\Delta p \rightarrow 0$. Additionally, the pressure at which a transition from opened joints to lower conductivity “closed” joints starts can be obtained. Figure 5.11(a) shows that in the Voronoi tessellation at higher deviatoric stresses, fluid travels farther from the injection point before dissipation to formation pressure conditions (zero in this study). In identical geometries but with an isotropic stress state, the lateral extent and fluid branching are suppressed, and the injection fluid pressure is much higher.

The abrupt transition point along the pressure profile curves where the slope changes abruptly (Figure 5.11) may be viewed as the “hydraulic fracture front” within which HF stimulation has occurred and beyond which normal fluid flow through the joints is occurring. The pressure at which this sharp slope change occurs is not consistent among simulations. In an isotropic stress regime, the pressure at the fracture front is large because of the lack of preferential HF propagation direction; a greater hydraulic pressure is required to HF. Conversely, in the case of a strongly deviatoric stress, the preferential fracture propagation direction allows the joints to initiate at a lower pressure. The size of the lateral pressurization zone in different fabrics is cross-joints, Voronoi tessellation and then cross-cuts (from high to low).

The stimulated zone is now assessed for each simulation using a displacement threshold of 2.5mm arising from the HF, as discussed above. Also, both polygonal and bounding ellipse area estimates were considered.

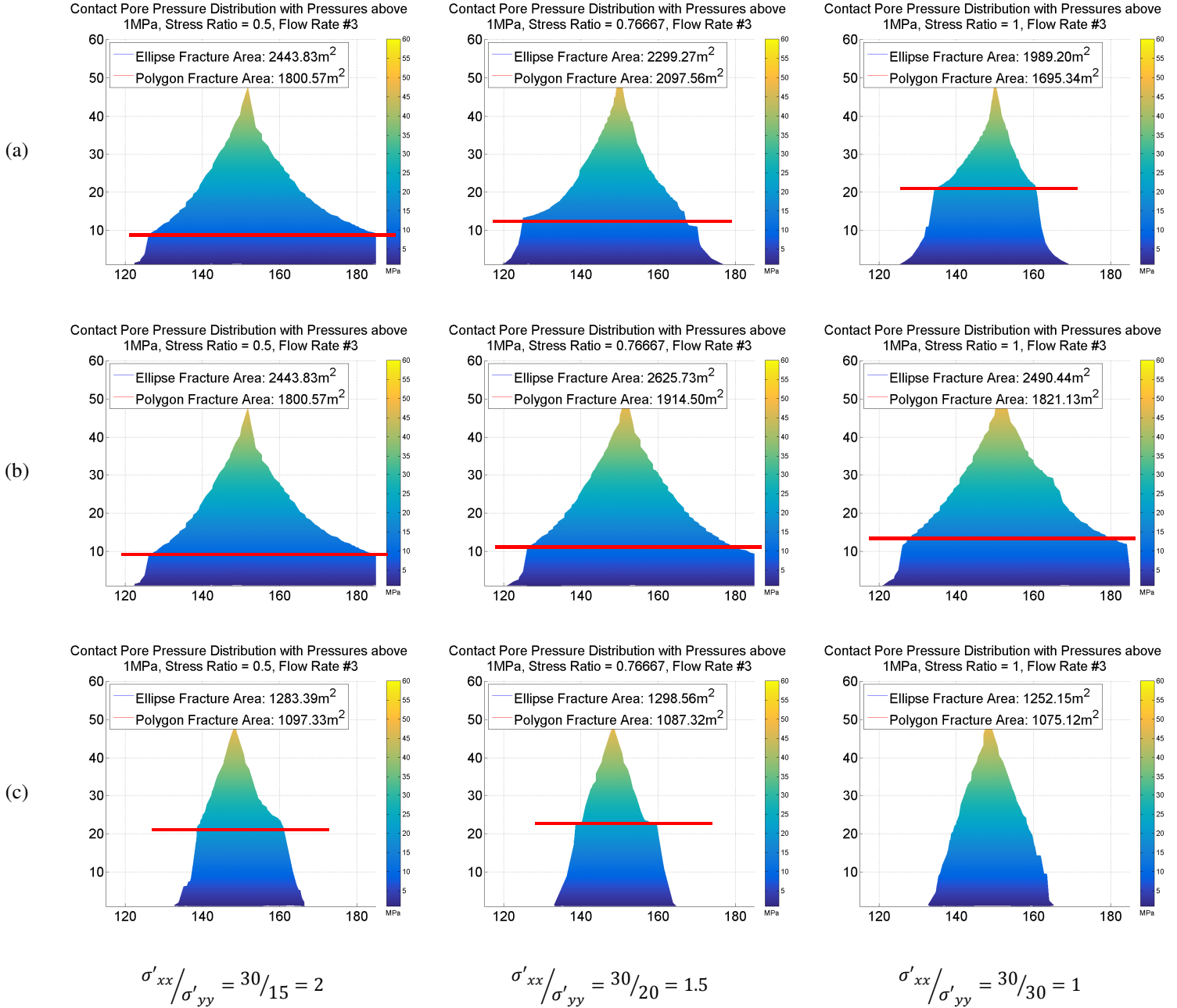


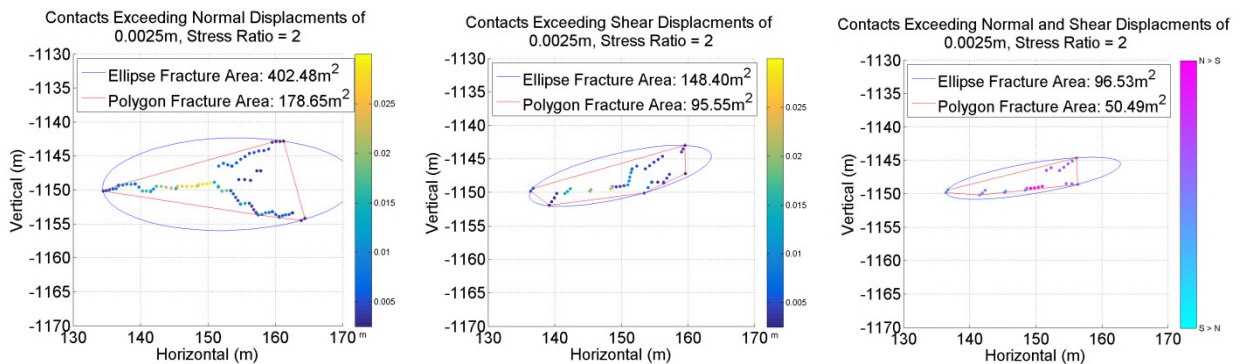
Figure 5.11. Fluid pressure profiles along the horizontal axis under different stress ratios and flow rate #3: a) Voronoi tessellation, b) Cross-joints; c) Cross-cuts.

For the Voronoi fabric at injection rate #1 (5 L/s) and three different stress ratios, the stimulated zones are shown in Figure 5.12. Here, the stress ratio appears to have an effect on the stimulated zone and as the in-situ stress state becomes more deviatoric, the eccentricity of the ellipse increases. In the ideal random geometry and a perfectly isotropic stress state, a circular stimulated zone is expected, whereas the strongly oriented joint fabric does lead to stimulated zones that are mildly eccentric.

The ellipse eccentricity increases as the differential stress increases whereas the area of the stimulated zone decreases as the stress ratio becomes closer to 1.0. This suggests that an optimal stress regime may exist which will yield a maximum area stimulated zone. In the isotropic state, there does not exist a preferential HF propagation direction, but the zone radius is suppressed; in highly deviatoric stress fields, the stimulated zone becomes relatively narrow (eccentric) so that the stimulated zone is reduced in area.

Figure 5.12 provides a description of the primary fracture mechanisms contributing to flow enhancement. In all cases, the stimulated zone based on normal displacements is the largest of the three - this is because joint opening is generally larger than the aperture increase for joint shear dilation. Ultimately it is this metric that is most useful as it relates more directly to the flow enhancement since permeability (as an averaged quantity) can be directly related to the residual apertures, which increase individual joint conductivity. It is likely that most of the shear displacements were induced subsequent to the normal displacements, as the normal openings facilitated pore pressure penetration to reduce the frictional resistance along the joint interface, allowing slip to occur more easily.

The stimulated zones based on both normal and shear displacements are marginally smaller than the stimulated zones based on shear displacement alone. This behavior implies that there are some sheared joints near the peripheries of the stimulated zone that were not directly caused by extensional opening. Of course, if a smaller threshold aperture had been assumed as more appropriate for the joint dilation, the intensity and area of shear stimulation would have been accordingly larger. Microseismic data suggests shear stimulation occurs at substantial distances beyond the supposed limit of the opened joints, and in a real case, it is likely that these small shear displacements could lead to additional flow enhancement beyond the limit of the opened joint network. If these results are to be interpreted in the context of real well behavior, it would be useful to further investigate this issue.



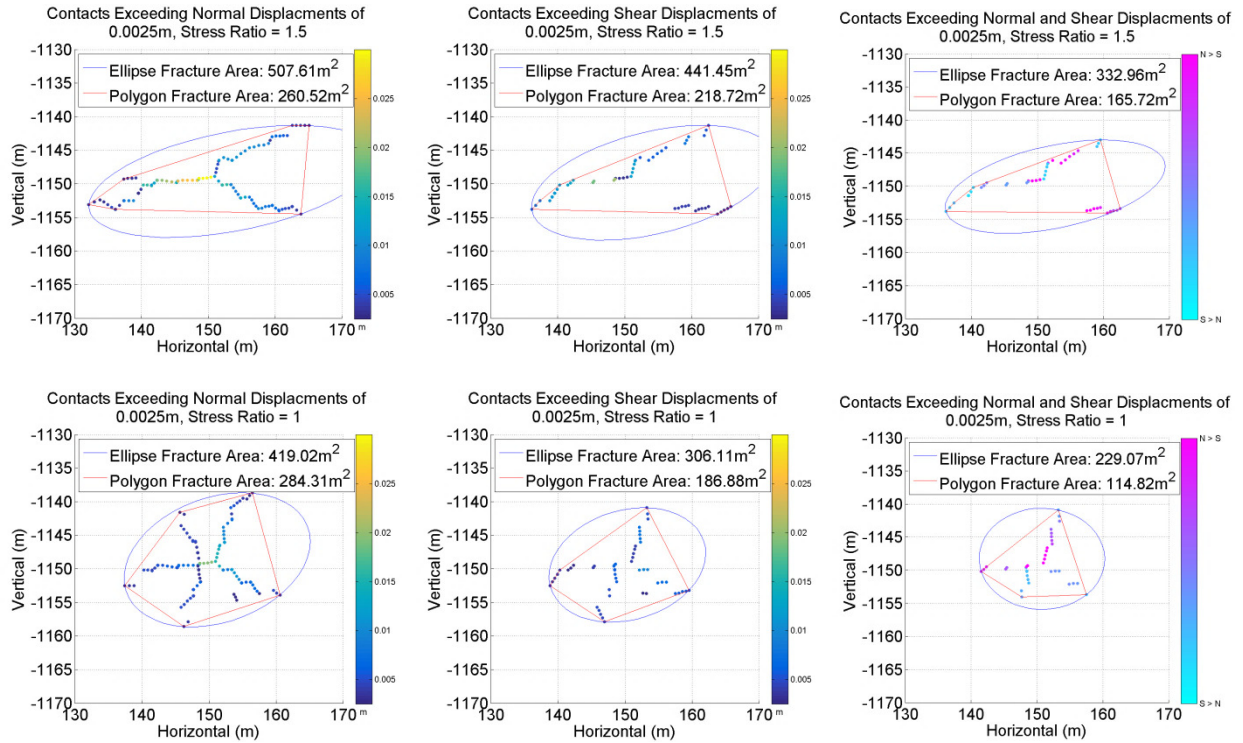
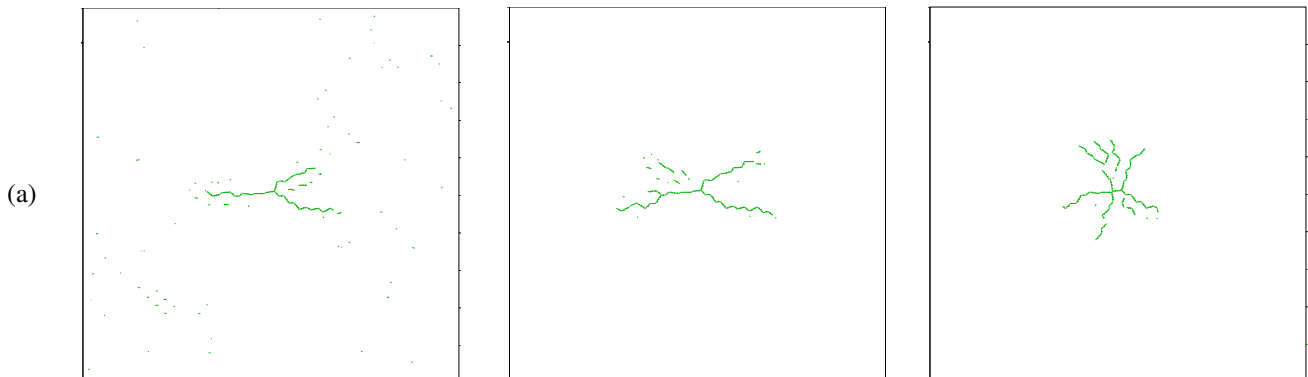


Figure 5.12. Associated stimulated zones with a determined threshold of 2.5mm for the Voronoi tessellated rock fabric, injection rate #1, and various stress ratios. Stimulated zones calculated based on both ellipse and convex hull geometries.

5.4.3 EFFECT OF INJECTION RATE

The effect of injection rate has been studied for the three representative geometries under the three chosen stress ratios. The initial injection rate (rate^{#1}) has been doubled (rate^{#2}) and tripled (rate^{#3}), for the same injection time. The injection rates increase by 5L/s intervals: rate^{#1} equals 5 L/s, rate^{#2} equals 10L/s and rate^{#3} equals 15 L/s. Effects of injection rate on normal and shear displacements for the same cases (Voronoi tessellated rock fabric at injection rate #1 and #3 different stress ratios) were analyzed and are shown in Figure 5.13 and Figure 5.14. The general pattern of normal displacement remains the same as the deformation pattern is globally controlled by in-situ stress and the injection rate has local effects on joint behavior.



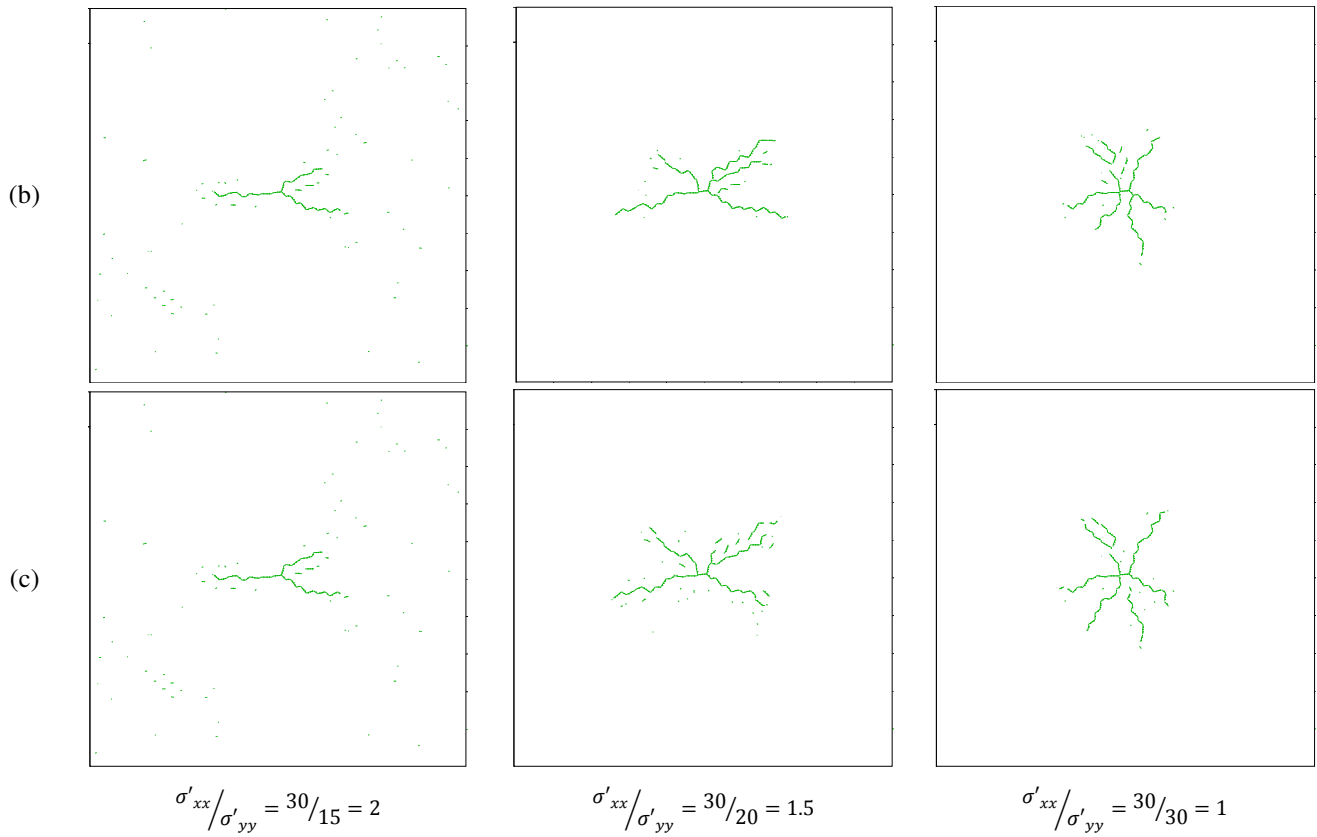
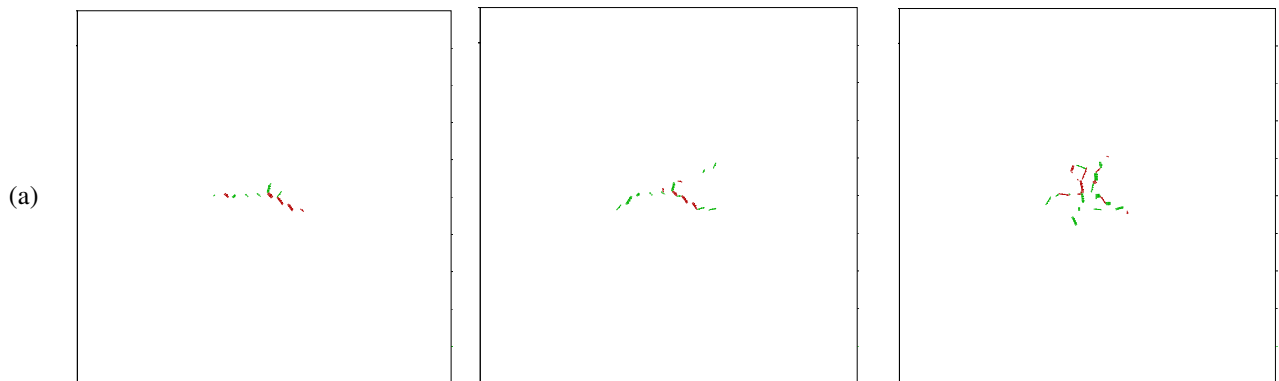


Figure 5.13. Effects of injection rate on normal displacement for the Voronoi tessellated rock fabric and various stress ratios: a) rate#1, b) rate#2 and c) rate#3.

Figure 5.14 shows that, most frequently, joints oriented in the NE-SW direction underwent right-lateral slip whereas the joints oriented in the NW-SE direction underwent left-lateral slip. Locally more joints underwent slip under higher injection rates and generated a larger stimulated zone.



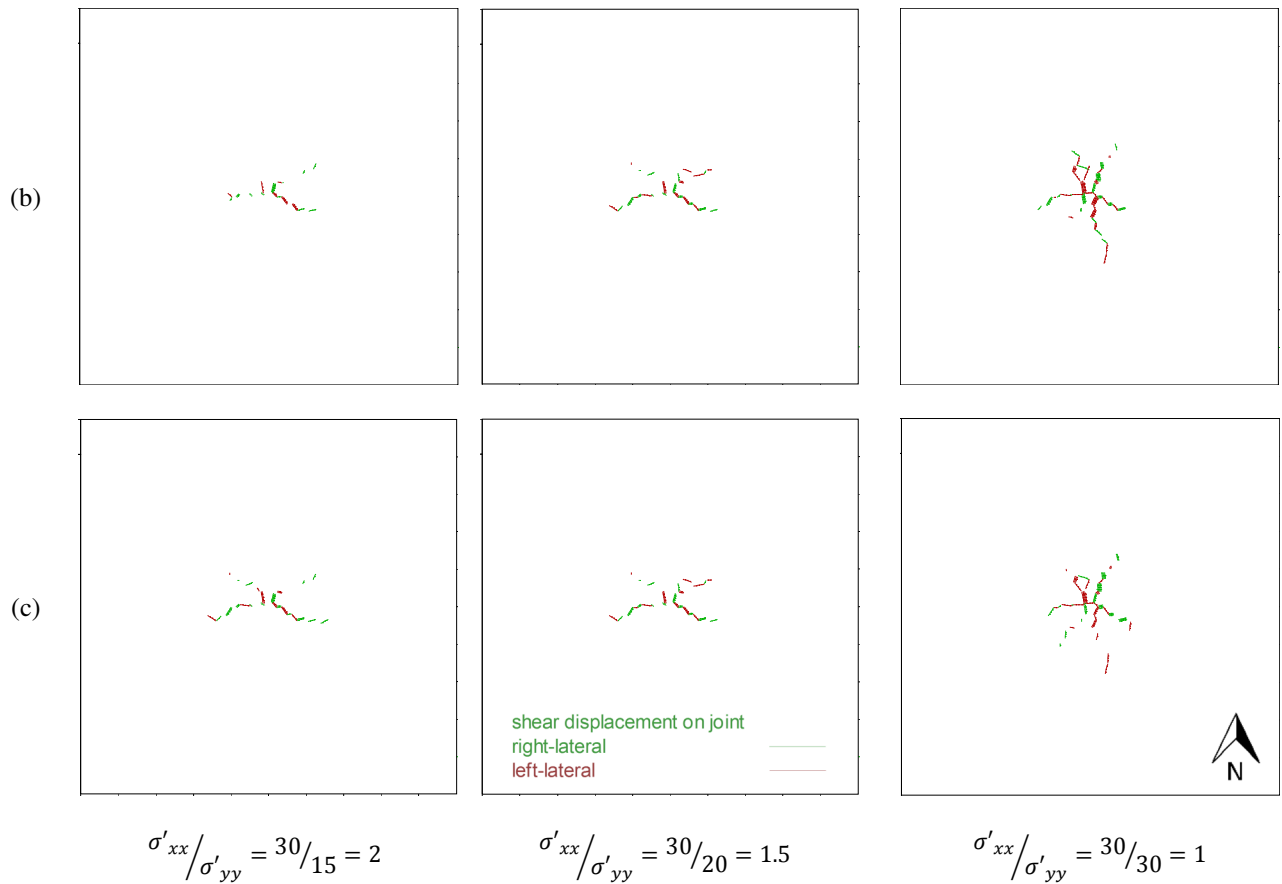


Figure 5.14. Effects of injection rate on shear displacement for the Voronoi tessellated rock fabric and various stress ratios: a) rate#1, b) rate#2 and c) rate#3.

The cross-sectional pressure profile along the horizontal axis was plotted (Figure 5.15); the top of the pyramids are the maximum pore pressure. As expected, the largest pressure occurs with the highest injection rate. The steep falling curves show the magnitude of pore pressure around the injection point while the pressurized area is almost the same size for all injection rates.

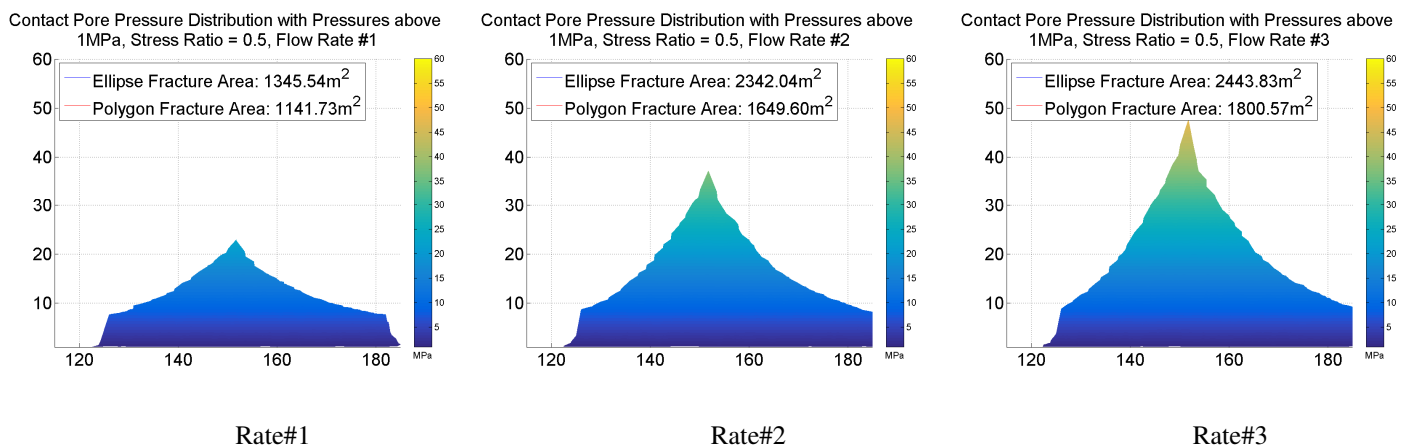


Figure 5.15. Effects of injection rates on shear displacement for the Voronoi tessellated rock fabric and various stress ratios: a) rate#1 (5 L/s), b) rate#2 (10 L/s) and c) rate#3 (15 L/s).

Similar simulations on the other geometries are reported in Figure 5.16 and Figure 5.17. Higher injection rates lead to more normal displacements along the joint set that is oriented closer to the direction of σ_{MAX} . Joint deformation is affected more by stress ratio under lower injection rates than higher ones. Higher injection rates cause higher fluid pressure and stimulated more joints because the fluid had enough pressure to counteract the increased confining stresses (see Figure 5.1) even in less favorable directions. Injection rates changes in these DEM simulations may also act as a proxy for changes in viscosity and future work will address the issue of changes in viscosity at constant injection rates.

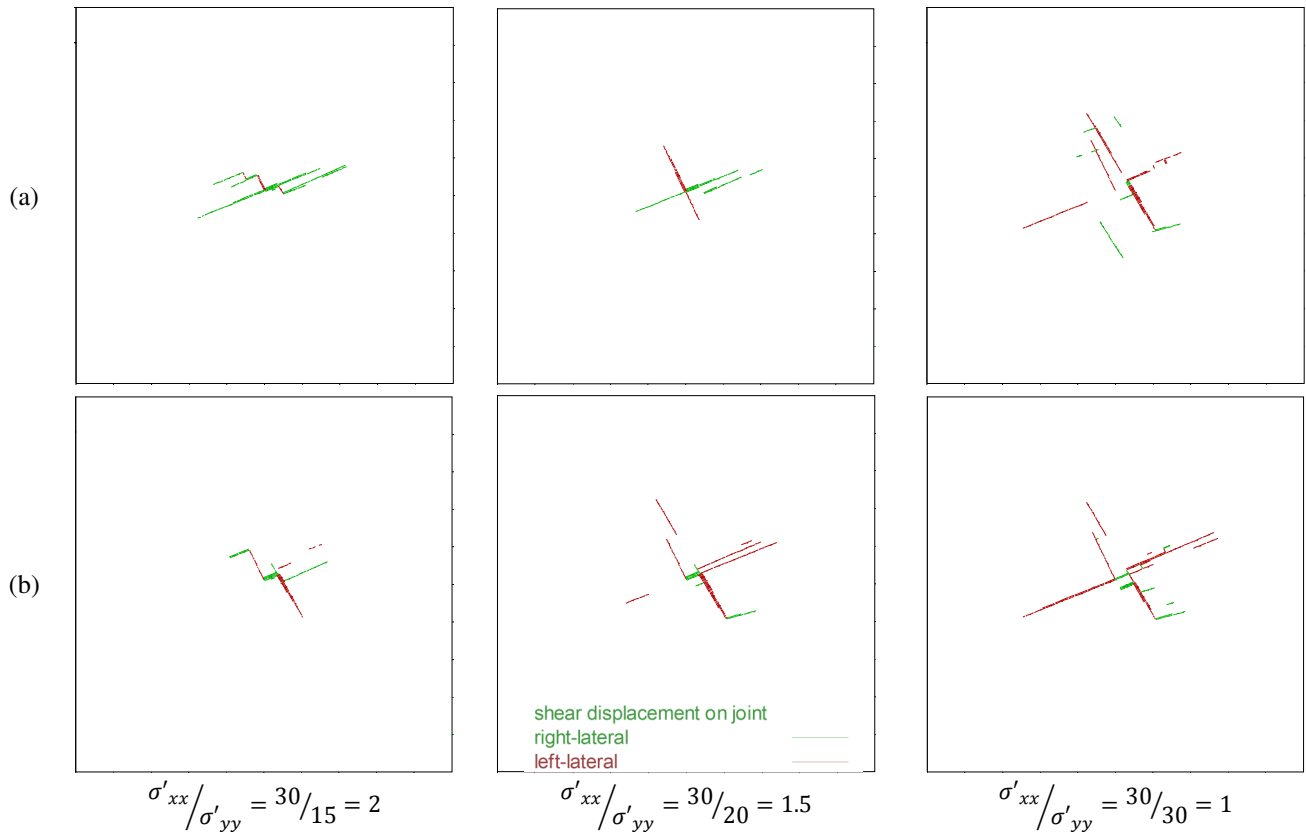
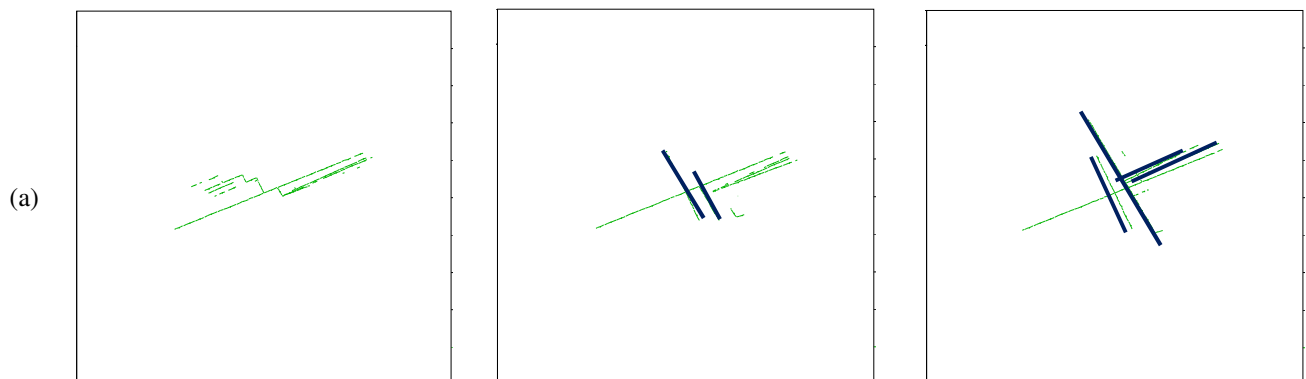


Figure 5.16. Effects of injection rates on shear displacement for the Cross-joints rock fabric and various stress ratios: a) rate#1 (5 L/s), b) rate#3(15 L/s).



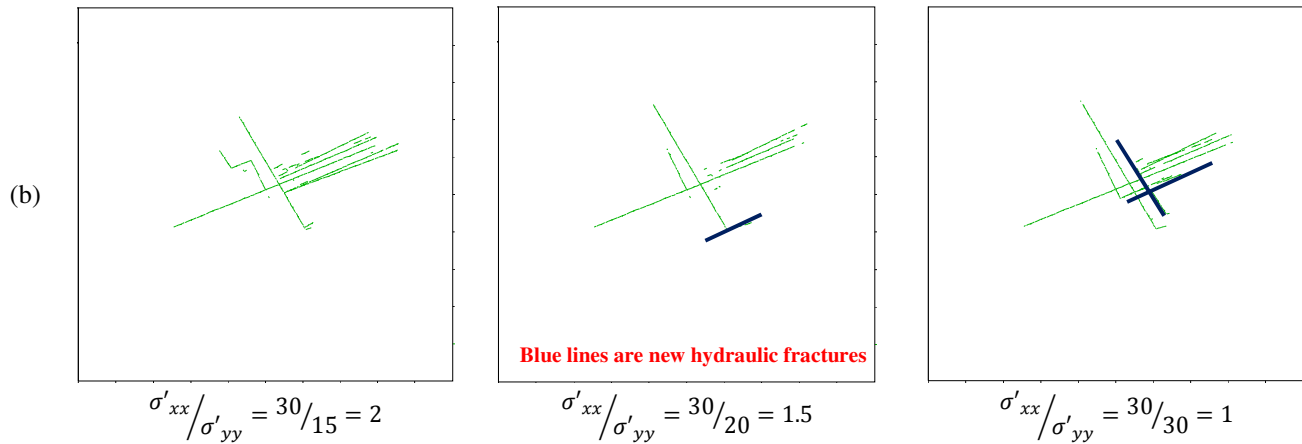


Figure 5.17. Effects of injection rate on normal displacement for the Cross-joints rock fabric and various stress ratios: a) rate#1 (5 L/s), b) rate#3 (15 L/s).

5.5 SUMMARY

In this chapter, a study investigating parameters that affect the stimulated zone associated with HF is presented. A means to quantify the stimulated zone area for a simulated HF treatment is developed using normal joint displacement as a threshold to specify the zone bounds. Results show that rock fabric and in-situ stresses are the primary controls on stimulated zone shape and size. Increasing flow rate under the modelling conditions has only a small effect on the resultant stimulated zone area at the same stipulated displacement threshold. Based on this study, more insight into the response of NFRs to hydraulic stimulations was achieved:

- Pore pressure distributions show preferential directions under higher differential stresses and become more uniformly radial as isotropic stress conditions are approached, except when a strongly anisotropic rock fabric dominates the HF propagation paths.
- Opening pre-existing joints in NFRs by HF also leads to shear slip and dilation affecting the flow path, implying that in a real case shear dilation is a mechanism of increasing the global permeability in a NFR.
- Branching may occur a short distance from the injection point; it is usually suppressed under a higher stress ratio and is more highly developed in the isotropic stress state, and particularly in an isotropic rock fabric.
- If the orientation of a joint set does not align normal to σ_{\min} , the fractures will propagate in a complex manner, generally globally normal to σ_{\min} , but with directions modified by the strong fabric.
- In general, with cross-joints and cross-cuts rock fabric, larger average displacements were noted than for the isotropic Voronoi tessellation, affecting both the magnitude of the deformations and size of the stimulated zone. This is logical because of the much longer joint length in the models with strong fabric.

- Injection rates do not appreciably affect the stimulated zone area or the general trend of fracture propagation, but they locally affect rock mass deformation (aperture). Higher injection rates cause higher fluid pressure and larger normal displacements within the joints.

CHAPTER 6 NUMERICAL INVESTIGATION OF SHEAR/SLIP EVENTS ASSOCIATED WITH HYDRAULIC FRACTURING

A major geomechanical question arising in mining engineering is: Can shear stresses be relieved in a deviatoric stress field through the process of injection? This chapter is focused on the magnitude of the shear/slip events associated with hydraulic fracturing in a naturally fractured rock mass because such events are evidence of local shear stress release.

OVERVIEW

There is concern that hydraulic fracturing (HF) near an existing critically stressed fault could trigger slip and generate a seismic event of significance (Zoback and Gorelick 2012). To examine this scenario, a mathematical discontinuum model representing a naturally fractured rock (NFR) mass containing a fault was created and fault slip response to fluid injection was studied. UDECTM is used as a Discrete Element Method (DEM) approach to define the seismic moment and also to assess the influence of injection and slip on further shear slip propagation. In most of the simulations, slip and dilation take place along a number of well-oriented joints surfaces, so it appears reasonable to assume that in a real case, microseismic emissions would accompany each **slip event**. A moment magnitude scale (M_w) was used to measure the size of the shear event in terms of the energy released. **Seismic moment** is a measure of the total energy (work) released during a shear event and is used to measure its magnitude. The injection energy is calculated as the total energy required for achieving the hydraulic fracturing; this is viewed as energy to open joints against the ambient stress field and much of it is potential stored energy that can be released and create discontinuities (work of fracture), deformations ($W = F \cdot d$) and heat and radiated seismic energy. A small amount of the total released energy is transformed to radiated seismic energy and another small amount results in tensile fractures. Fracture energy is used to calculate the work required to create fracture surfaces. Comparing the energy release by fracturing or shear events indicates their contribution to the total amount of released energy or total work. The amount of energy associated with the shear-slip event is small compared with the overall work done to generate the distortions (i.e. increases in aperture by forcing them open against the confining stresses) in the rock mass and in reality much of the energy in slip may be lost as heat from the plastic deformation rather than as radiated seismic energy.

Microseismic monitoring shows the spatial distribution and magnitude of seismicity associated with slip of bedding planes and natural and incipient fractures. Work calculations have been undertaken to analyze the various sources of energy storage (elastic strain energy) or dissipation (slip) and the energy losses from viscous dissipation, all to aid in clarifying HF processes in NFRs.

6.1 INTRODUCTION

Due to an increasing demand for energy, low-permeability hydrocarbon-bearing rocks such as tight sandstones and shales are regularly stimulated using hydraulic fracturing technology (Curtis 2002). Most stiff rocks are naturally fractured, affecting hydraulically induced fracture direction locally, but the global orientation of induced fracture growth remains normal to the minimum principal stress as a work minimization process. Shearing takes place along joint surfaces and may cause shear events along with weakening and softening of the joints in stiff rock mass (Pirayehgar and Dusseault 2014).

There are many studies of earthquakes induced by different processes such as mining, oil recovery, waste disposal, geothermal operations, in-situ combustion operations (Nyland and Dusseault 1983), water flooding and hydraulic fracturing. (Warpinski et al. 2012). Davies et al. carried out a comprehensive review of all published examples of seismic events ≥ 1 since the year 1929 (Davies et al. 2013), as shown in Figure 6.1. According to this study, the potential causes of induced earthquakes > 1 that have occurred since the year 1929 are as follows:

- Mine subsidence (M 1.6 - 5.6)
- Oil and gas field depletion (M 1 - 7.3)
- Fluid injection for secondary oil recovery (M 1.9 - 5.1)
- Waste-water disposal (M 2 - 5.3)
- Solution mining (M 1 - 5.2)
- Enhanced Geothermal Systems (EGS) operations (M 1 – 4.6)
- Reservoir impoundment (M 2 – 7.9)
- Groundwater extraction (M 1 – 5.1)
- Hydraulic fracturing in low-permeability rocks (M 1 - 4)

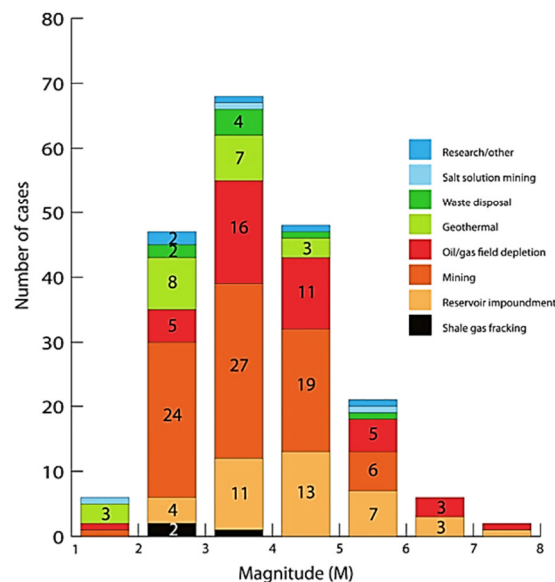


Figure 6.1. Frequency vs magnitude for 198 published examples of induced seismicity (Davies et al, 2013).

Among all mentioned reasons, hydraulic fracturing generally seems to induce relatively small seismic events, usually with negative Richter magnitudes that are hard to detect on surface (Baan et al. 2013). Nevertheless, Western Canada has of late been marked with significant HF induced seismicity. Recent analyses of long-term seismicity in the Horn River Basin in Northeastern British Columbia (BC), a shale gas development area, indicate an increase in the maximum seismic magnitude of events from 2.9 to 3.6 M_L over a five-year period (Farahbod et al. 2015). Hydraulic fracturing operations started in Fall 2013 in Western Alberta (Fox Creek area) induced seismic events greater than 4 M_L . During the last two years, more than 900 seismic events with a magnitude range of 1-4 M_L have occurred in BC and Alberta (Novakovic and Atkinson 2015). The largest reported seismic events to date have occurred in Western Alberta and in Northeastern BC; however, the maximum magnitude of the events that could potentially be triggered is not yet known (Atkinson et al. 2015).

Hydraulic fracturing may reactivate pre-existing fractures or faults and can therefore cause induced seismicity (Warpinski 2014; Rutqvist et al. 2013; Cipolla et al. 2012). When the shear stress along the surface of an extensive weak plane such as a fault exceeds its shear strength, it will undergo slip. This may be caused by fluid pressure increase during injection in a region with high deviatoric stresses, or perhaps during the flow-back period after shut-in. The occurrence of slip depends on geometric factors such as length and orientations of planes, stress directions, stress magnitudes, the roughness, cohesion and mechanical behavior of the planar features, and the poroelastic stress path and shape of the volume affected (e.g. in cases of permeability, anisotropy and heterogeneity). In a simple Mohr-Coulomb model, reduction of effective normal stress across a weak plane during injection pressure increase leads to a displacement to relieve the excess shear stress. Because this displacement is almost always a “stick-slip” process in real geomaterials, slip leads to a burst of seismic energy, called an earthquake (Warpinski et al. 2012).

Seismic events caused by anthropogenic fault reactivation such as water flooding or even the filling of a hydroelectric power reservoir, are cases of unintentional “triggered seismicity”. It is now relatively well-understood that, because all hydraulic fracturing activity will induce seismic activity, this constitutes intentional “induced seismicity”. These terms may be used interchangeably in the discipline and, as mentioned previously, hydraulic fracturing can be associated with fault activation (Maxwell 2013) and not only slip along natural fractures that have not experienced slip before stimulation. Davies et al. believe that three mechanisms may control fault reactivation (Davies et al. 2013):

1. Direct injection into the fault or direct connection between hydraulic fractures and the fault;
2. Transmission of fluid through pre-existing fractures or stimulated hydraulic fractures into the fault;
3. Transmission of fluid through a permeable stratum into the region of the fault.

Although the majority of seismic events resulting from hydraulic fracturing are very small, there appear to be some unequivocal examples of felt earthquakes in the USA (Oklahoma, $M_d = 2.8$) (Holland 2011), the UK (Preese Hall, $M_L = 2.3$) (Pater and Baisch 2011), Canada (Horn River Basin, $M_L = 3.8$) (BC Oil and Gas Commission (BCOGC) 2012) and (Fox Creek, $M_L = 4$) (Novakovic and Atkinson 2015). Among hundreds of thousands of hydraulic fracturing treatments, only a few events have been reported to have significantly been felt, with no physical damage or injury. Nevertheless, under conditions of high in-situ deviatoric stresses and reactivation of critically stressed pre-existing faults (see the aforementioned three mechanisms), the expressed magnitude may indeed be as high as 2 to perhaps 4 (Maxwell 2013).

A microseismic event transfers the potential energy to radiated and non-radiated energy (frictional energy loss, E_F , and fracture energy, E_G) (Kanamori 2001). The shear stress on a fault plane decreases from the initial value, τ_0 , to the final value, τ_1 , when a seismic event happens and this is called static stress drop. Static stress drop is one of the most widely used parameters in the interpretation of seismic events (Aki 1967); (Scholz 2002). Dynamic stress drop occurs during slippage and equals to the frictional stress (Kanamori 2001). Stress drop ranges between 0.1 to 10 MPa (Ruff 1999). Stress drop is considered to be constant for a plane fault and it appears to be about 3 MPa for most events (Kanamori and Anderson 1975). This is a very small value.

Based on the literature, small and large seismic events are similar in terms of their rupture physics; and as a result, stress drop should be independent of event size (Aki 1967); (Kanamori and Anderson 1975); (Hanks 1977); (Abercrombie 1995); (Ide et al. 2003); (Kanamori and Brodsky 2004); (Prieto et al. 2004); (Abercrombie and Rice 2005); (Shearer et al. 2006); (Candela et al. 2011).

A question about stress drop is its dependence upon the seismic moment, M_0 (Candela et al. 2011). Stress drop is usually defined by seismic moment and fault dimensions in the presence of complicating parameters such as a non-planar geometry (Madariaga 1979). Seismic moment is estimated primarily from the observed amplitude of seismic waves (Kanamori 2001) from a number of observation points, and then stress drop is obtained from the given seismic moment Calculations. However, in this study, the seismic moment needs to be calculated from numerical outputs, which may cause some uncertainties in the actual stress drop. In addition, stress drop in reality is not constant for the entire fault slip areas, and it should be averaged along the fault. However, averaging causes some concerns about the accuracy of the value of stress drop, particularly because there are dynamic effects such as a propagating shear stress concentration at the tip of the slip plane. So, simplified models are generated to determine seismic moment and seismic magnitude and these are to be used quantitatively with a degree of caution. Based on the constitutive model and model configuration chosen in this chapter, there is not a strong stress drop (frictional stress) during slippage. Small stress drops produce small seismic moments for a given sheared area that in turn leads to small moment magnitude or shear events.

In this chapter, a numerical method is used to study possible hydraulically induced seismicity (including size and strength of potential earthquakes), by varying parameters that may affect fault reactivation and joint slip. For example, to explore strong fabric effects on hydraulic fracture propagation in a naturally fractured rock, different types of fabric are used in simulations under various stress states. Two common geometries of natural fracture networks have been studied: first, a network of randomly oriented polygonal joints (Voronoi tessellation), and second, two sets of joints (cross-joints) which are long, straight and sub-parallel with different inclinations to the maximum principal stresses. Numerical simulations were carried out using UDEC™, a two-dimensional numerical DEM code. Coupled hydro-mechanical analysis was applied to simulate the mechanical behavior of discontinuities (a fault along with natural fractures and induced hydraulic fractures) in the HF/NFR system and to study the potential occurrence of shear/slip events.

6.2 METHODOLOGY

6.2.1 MOMENT MAGNITUDE SCALE, SEISMIC MOMENT

Earthquakes result from ground ruptures; the magnitude of an earthquake depends on the size of the rupture and the stress drop. The most well-known metric for earthquake magnitude is the Richter magnitude scale (Local Magnitude M_L). However, this method underestimates large earthquake energy releases and is most suitable for small shallow events with $M_L < 6.5$ (saturation magnitude) (Mccalpin 2009). The Moment Magnitude scale (M_w) has been introduced for large events and it corresponds with Richter magnitude for events $M_w < 6.5$ (Figure 6.2).

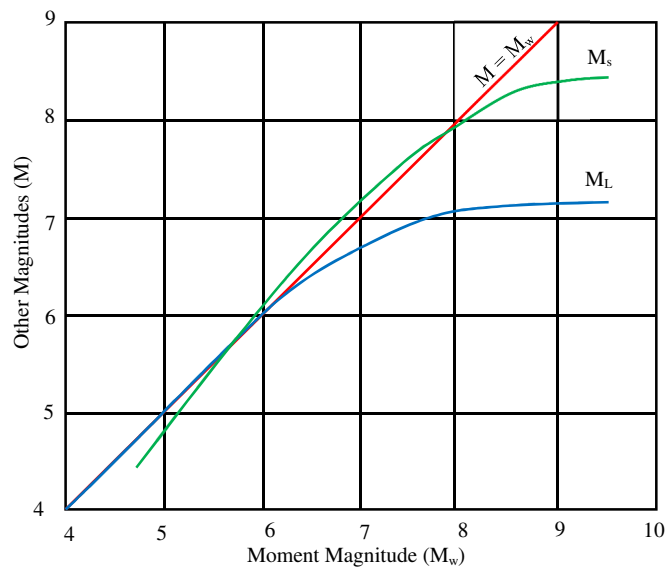


Figure 6.2. Comparison of different magnitude scales (Kanamori 1983).

The Moment Magnitude (M_w) is a dimensionless number and the subscript “w” stands for mechanical work (Hanks and Kanamori 1979). A log scale is used, given as:

$$M_w = \frac{2}{3} \log M_0 - 6 \quad (6-1)$$

Here, M_0 denotes seismic moment with dimensions of energy ($N \cdot m$) (Hanks and Kanamori 1979). Seismic moment (M_0) is the total strain energy released during an earthquake (e.g. Zangeneh et al. 2013):

$$M_0 = \mu AD \quad (6-2)$$

Here, μ is the shear modulus of the faulted rock (shear stiffness of the joints in the current study), the A is the shear-stimulated area (area of the fault) and D is the average shear displacement on shear-stimulated area. Therefore M_0 has units of work ($W = F \cdot d = \mu \cdot A \cdot d$).

6.2.2 MOMENT MAGNITUDE SCALE, SEISMIC ENERGY

The size of an earthquake relates to the amount of radiated energy. The amount of radiated energy that takes the form of surface waves is a measure of the potential for man-made structure damage. The moment magnitude in terms of the seismic energy radiated by an earthquake is given by an empirical relationship developed by Gutenberg and Richter (Warpinski et al. 2012). Using the following estimate and replacing it in equation (6-1) gives the magnitude-energy relationship, equation (6-4) (Choy et al. 1995)

$$E_s = 1.6 \times 10^{-5} M_0 \quad (6-3)$$

$$M_e = \frac{2}{3} \log E_s - 2.9 \quad (6-4)$$

where E_s is in $N \cdot m$ and M_e is unitless.

M_w and M_e are both magnitudes, yet they may not have the same numerical values for the same earthquake. M_w and M_e are computed from low and high frequency seismic data respectively, and they define different physical properties of an earthquake. M_w , is a static measure of the total mechanical work and M_e is more of a measure of seismic potential for damage which is mostly controlled by the dynamic nature of the rupture (rapid, slow, etc.). In other words, M_w estimates earthquake size and M_e indicates earthquake strength, therefore both are relevant for studying the potential hazardous damage of an earthquake (Bormann and Di 2011).

6.2.3 INTENSITY

Magnitude and intensity are commonly confused terms, both of which can be used to represent the severity of an earthquake. Magnitude and intensity are respectively a quantitative and subjective description of an earthquake size; however, magnitude is measured based on the released energy and seismic techniques while intensity does not have a mathematical basis. Intensity describes the effects of an earthquake and it is therefore dependent on factors such as distance from the epicenter and other geographical features, the nature and response of infrastructure including its sensitivity to excitation and soil and rock properties. Only one magnitude exists for an earthquake while many intensities are possible depending on the nature of the surface response. Finally, Roman symbols are used for stating intensity whereas Arabic numbers are used for magnitude (USGS 2013).

The most common scale for expressing intensity of an earthquake is the Modified Mercalli Intensity (MMI) scale introduced in 1931 by Harry Wood and Frank Neumann, shown in Table 6.1. It is based upon a qualitative description of earthquake intensity and empirically based on observed effects at the surface. There are 12 different levels ranging from an “unnoticeable event”, that is only detectable with instruments (geophones, seismometers, accelerometers), to an event with calamitous destruction. Table 6.2 gives a comparison of magnitude and intensity that occurs typically at locations near the epicenter of earthquakes (USGS 2013). The values in the table are all approximate as the two methods cannot be explicitly related.

Table 6.1. Modified Mercalli Intensity Scale (USGS 2013).

Potential hazard	Mercalli Intensity	Effects
Instrumental	I	Not felt except by very few people, under especially favorable conditions.
Weak	II	Felt by a few people, especially on upper floors.
Slight	III	Noticeable indoors and especially on upper floors, but may not be recognized as an earthquake.
Moderate	IV	Felt by many people indoors and a few outdoors. May feel like a heavy truck passing by.
Rather strong	V	Felt by almost everyone. Some people may be awakened from sleep. Small objects will be moved and trees and poles may shake.
Strong	VI	Felt by everyone. It will be difficult for people to remain standing. Some heavy furniture may be moved and some plaster from walls may have fallen. Chimneys may be slightly damaged.
Very strong	VII	Slight to moderate damage in well built, ordinary structures with considerable damage to poorly built structures. Some walls may fall.
Destructive	VIII	Little damage in specially built structures with considerable damage to ordinary buildings and severe damage to poorly built structures. Some walls collapse.
Violent	IX	Considerable damage to specially built structures with buildings shifted off foundations. Ground will noticeably be cracked. Wholesale destruction

		and landslides may also occur.
Intense	X	Most masonry and frame structures along with foundations will be destroyed. Ground will be extremely cracked. Landslides and wholesale destruction will occur.
Extreme	XI	Total damage. Few, if any, structures will remain standing. Bridges will be destroyed. Wide cracks in ground. Waves seen on ground.
Catastrophic	XII	Total damage. Waves seen on ground. Objects thrown up into the air.

Table 6.2. Comparing magnitude and intensity of earthquakes (USGS 2013).

Magnitude	Typical Maximum Modified Mercalli Intensity
1.0 - 3.0	I
3.0 - 3.9	II - III
4.0 - 4.9	IV - V
5.0 - 5.9	VI - VII
6.0 - 6.9	VII - IX
7.0 and higher	VIII or higher

6.3 HYDRO-MECHANICAL SIMULATIONS USING UDECTM

The DEM approach can be used to define an equivalent to the seismic moment and to study influences on shear slip propagation. Work calculations were undertaken to look at the various sources of energy storage (elastic strain energy) or dissipation (slip), as well as the potential energy losses from viscous dissipation. This will help clarify HF processes in NFRs. Future developments could include energy calculations to find a relation between the slip that can be simulated in these realizations and the MS emissions in the field. Through the use of appropriate constitutive laws, it may be possible to monitor an evolving stress field through the MS emissions (Dusseault 2013). In this research, the moment for an energy release event is of interest, and this might be interpreted as a seismic event with the moment reflecting the maximum amount of radiated energy.

6.3.1 MODEL OPTIONS

In order to create an energy release event of substantial magnitude, a fault, by definition a plane along which displacement has already occurred and which is much larger than the other natural fabric elements such as joints and bedding, must be subjected to a sufficient effective stress field to generate yield and accompanying slip displacements along the fault. Numerical simulations of this displacement are carried out with UDECTM to study the size and strength of energy release which might be linked to potential induced shear events. Since mechanical deformation and fluid flow are interdependent, hydro-mechanical coupling has been implemented to improve predictions of the rock mass hydraulic response to mechanical changes. UDECTM is used to study the effects of two different fabric patterns (Voronoi tessellation and

cross-joints) on the distribution of slip and opening of joints at different stress field anisotropies. A two-dimensional plane-strain section is generated in UDECTM to represent a naturally fractured rock mass 40 m × 40 m in size, subjected to a biaxial in-situ stress state. The medium is initially dry and then fluid is injected into the borehole at a constant flow rate of 0.0004 m³/s/m. Table 6.3 includes all fluid and material properties assumed for the rock mass, joints and fault:

Table 6.3. Rock, joint and fluid properties.

Rock properties			Joint mechanical properties		
Density	2700	kg/m ³	Normal stiffness	10	GPa/m
Bulk modulus	40	GPa	Shear stiffness	4	GPa/m
Shear modulus	24	GPa	Friction angle	30	Degree
Friction angle	27	Degree	Cohesion	0.1	MPa
Cohesion	27	MPa	Dilation angle	5	Degree
Tensile strength	1	MPa			
Joint hydraulic properties			Fluid properties		
Permeability factor	0.83×10^8	MPa ⁻¹ s ⁻¹	Density	1000	kg/m ³
Residual hydraulic aperture	1×10^{-4}	m	Dynamic viscosity	10^{-3}	Pa·s
Aperture at zero normal stress	5×10^{-4}	m			

Figure 6.3(a) and 2(b) respectively represent a network of randomly oriented polygonal joints (Voronoi tessellation) and two sets of perpendicular joints (cross-joints) which are long, straight and sub-parallel with different inclinations to the maximum principal stresses. Geometrical parameters (joint length, spacing, gap, density, etc.), and most of all joint density, significantly affect the deformation of NFRs (Xing & Sanderson, 2002).

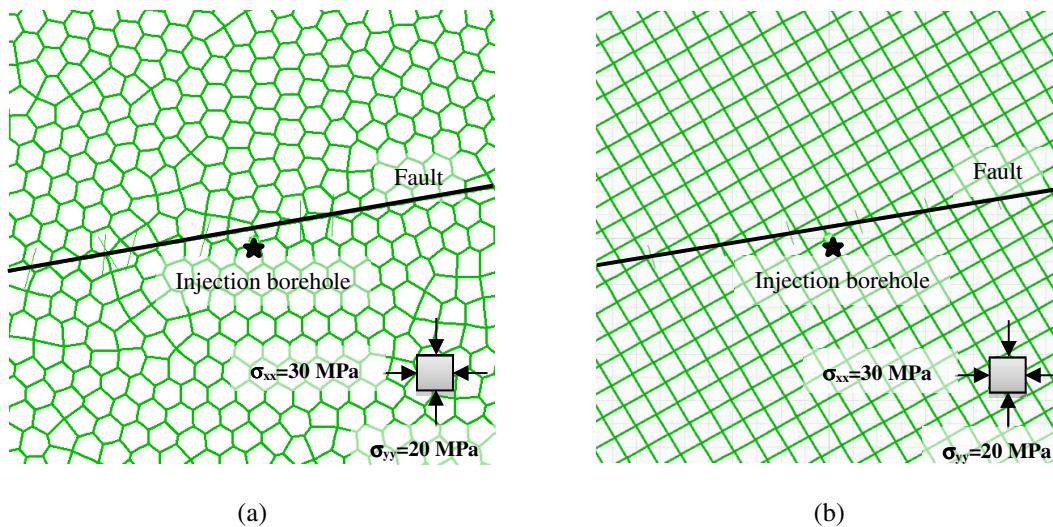


Figure 6.3. UDECTM model in a rock mass containing a) Voronoi tessellation and b) cross-joint sets.

The two fabric patterns have approximately the same joint density and almost the same block size to minimize the influence of different scale of joint patterns on the results (although such scale effects may be worthy of study in themselves). The injection starts with a rate of 0.4 L/s followed by a zero rate to study the after shut-in behavior. Results for two different fabrics under bi-axial anisotropic stress states were generated.

6.3.2 EFFECTS OF STRESS RATIO ON ENERGY RELEASE MAGNITUDE IN THE VORONOI TESSELLATED ROCK FABRIC

Joints and intact rock are sensitive to pressure and their failure criteria are functions of the effective confining stress; hence, to perform a meaningful numerical modeling representing a roughly realistic condition, a reasonable Poisson behavior of a naturally fractured rock mass is needed. The Poisson's ratio of the intact rock has a significant influence on the Poisson's ratio of the whole jointed system, depending on the relative frequency and aperture of the joints. For an isotropic elastic rock mass, the ratio of horizontal-to-vertical stress change when a uniform load is applied in a plane strain condition is a function of Poisson's ratio, ν (Pirayehgar and Dusseault 2014):

$$\frac{\Delta\sigma'_{xx}}{\Delta\sigma'_{yy}} = \frac{\nu}{1 - \nu} \quad (6-5)$$

The effect of stress ratio (horizontal over vertical stress) on the magnitude of the energy release events has been studied and results are shown on Figure 6.4. The maximum principal stress (horizontal stress, $\sigma'_{xx} = 30 \text{ MPa}$) was kept constant while the minimum principal stress was altered to obtain different stress ratios. For larger deviatoric stresses, larger events are created, easily explained by larger consequent displacements under higher differential stresses (Figure 6.5). As discussed, M_w and M_e (the size and strength of an earthquake or in our case the energy release event in the DEM model) may be dissimilar for the same event because they represent different properties of an earthquake. In these simulations, they are in fact very close; the difference is only about 3%.

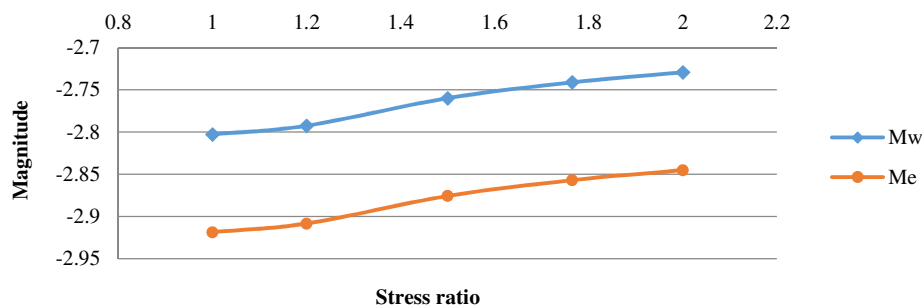


Figure 6.4. Magnitude of events vs stress ratio in the Voronoi tessellated rock fabric.

Figure 6.5 indicates the absolute values of average normal and shear displacements over the whole model after injection under different stress conditions. After injection, the main deformation mechanism is closure. Normal displacement has a decreasing trend for higher differential stresses and this is fitting as to generate the different stress states, only the vertical stress (σ_{\min}) is decreased while the horizontal stress (σ_{\max}) is held constant. This would lead to smaller applied normal components of stress and therefore smaller normal displacements. In contrast, the shear stress is increasing, leading to larger shear displacements.

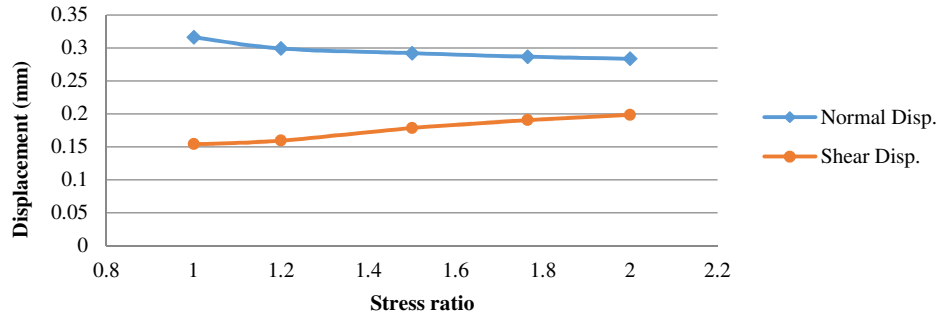


Figure 6.5. Values of shear and normal displacements vs stress ratio in the Voronoi tessellated rock fabric.

From the aspect of energy release (work), the estimated magnitude of the earthquake is about -2.8 (negative values are permitted in quantitative magnitude scales), which, if it were a kilometer deep, would be challenging to detect with sensors on the surface, let alone be felt (see Table 6.1). The scale of these numerical models is tens of meters in a two-dimensional framework. Events in reality might be triggered slip along faults that are hundreds of meters in length and width, so the work emissions would be several orders of magnitude larger. To carry out more explicitly realistic simulations using DEM models will require addressing the issues of fault scale, more distant boundary conditions and the three-dimensionality effects, perhaps by using 3DEC™, the three-dimensional version of UDEC™.

Figure 6.6 shows relationships among earthquake size, joint/fault size, amount of slip and seismic moment. According to this figure, joints less than 10 m long generate negligible magnitude earthquakes and larger joints are associated with larger stress release ($\Delta\sigma$ - stress drop), larger slip and thus larger earthquakes. Events greater than $M_0 = 6$ result from huge faults that are tens of kilometers long (Zangeneh et al. 2013) and tens of square kilometers in slip area. The fault size here refers to the size of the fault segment that undergoes slip, which is less than the size of the fault on which the earthquake occurs. For the current simulations with a fault size of around 40 m, the slipped segments are somewhat smaller and the events invariably have negative moments and are associated with < 0.1 mm slip (Zoback and Gorelick 2012). In Figure 6.4, the average shear displacements ranged from 0.15 to 0.2 mm.

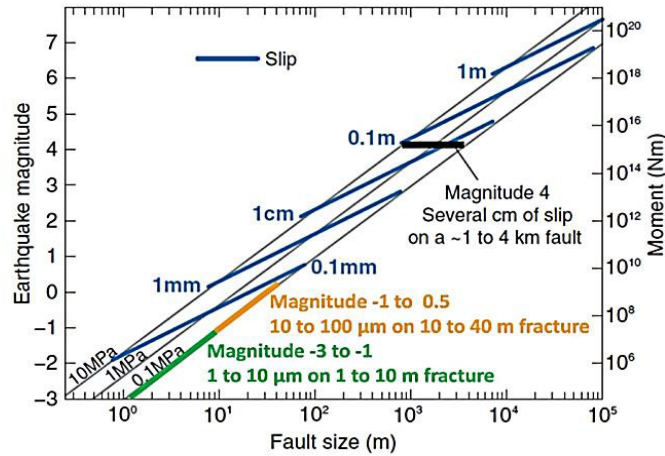
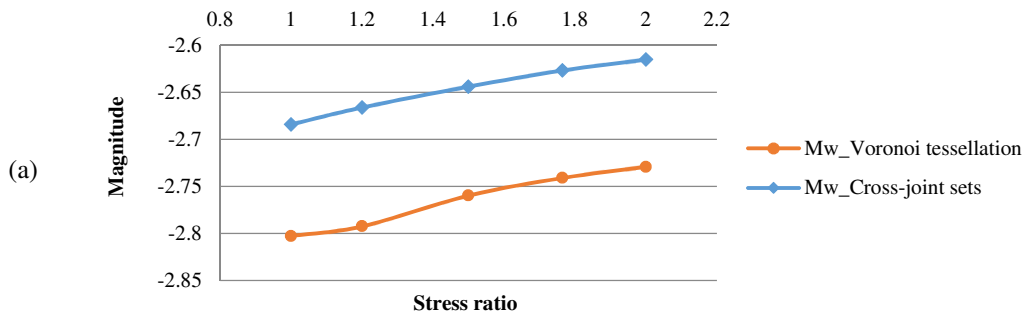


Figure 6.6. Relations among earthquake scaling parameters (Maxwell 2013).

6.3.3 EFFECTS OF STRESS RATIO ON SLIP IN CROSS-JOINT ROCK FABRIC

Effects of fabric and differential stress fields are studied in this section. In order to minimize the effect of geometrical parameters, the generated fabric has the same joint density and block size as the Voronoi tessellated rock fabric. Also, the joint sets in this model are oriented in the dominant average orientations of joints in the tessellated model; in this case, cross-joint sets oriented 30 and 120° to the direction of maximum principal stress (Figure 6.3b). Figure 6.7 shows the energy release magnitude for both fabrics. Although these plots have almost the same trend, cross-joint sets lead to a relatively larger amount of fault rupture and accompanying joint slip (M_w) and greater energy release (M_e). Interestingly, based on these initial results, in a large-scale case the presence of a strongly oriented fabric (e.g. stiff sedimentary strata) may lead to larger slip potential than the case of a rock mass with more random joints (e.g. a granitic rock mass).



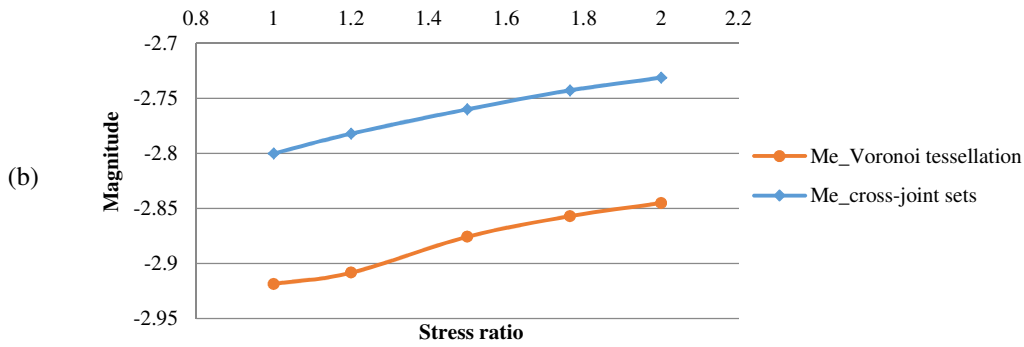


Figure 6.7. Magnitude of a) M_w and b) M_e vs stress ratio for different rock fabrics.

Figure 6.8 shows normal and shear displacements for different fabrics. The Voronoi tessellated rock fabric mostly has larger amounts of normal displacement, whereas in the strongly oriented fabric, shearing is about 0.1 mm higher (this is not negligible in the scale of our model). It seems that the cross-joint rock fabric has more preferentially oriented joints that can slip over longer distances compared to the Voronoi tessellated rock fabric which contains randomly oriented joints that terminate after a relatively small distance. The cross-joint rock fabric may also have more joints favorably aligned with the stress orientations than in the Voronoi tessellated rock fabric.

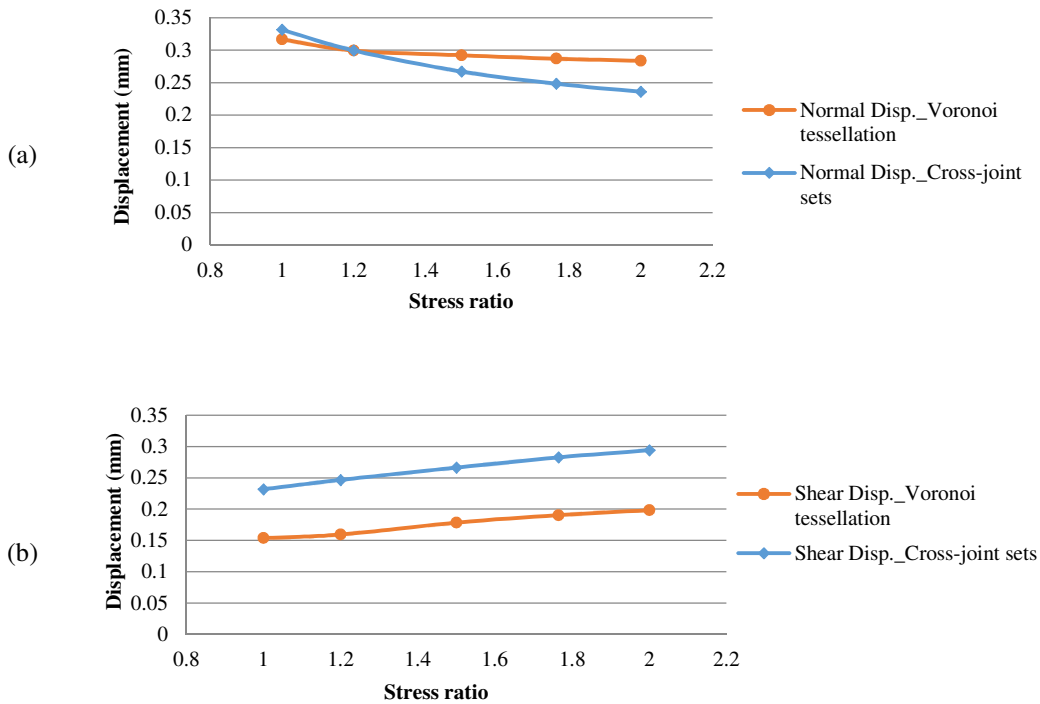


Figure 6.8. Average a) normal and b) shear displacements vs stress ratio for different rock fabrics.

6.3.4 EFFECTS OF FAULT INCLINATION ON SLIP IN THE VORONOI TESSELLATED ROCK FABRIC

Faults with different inclinations to the direction of σ_{MAX} are simulated. Figure 6.9 indicates the magnitude of energy release as a function of the fault inclination. It seems that there is a critical fault orientation with regard to the direction of in-situ stress that affects the size of the fault rupture as well as the radiated seismic energy. When the fault is inclined with a lower angle to the maximum principal stress, it undergoes larger displacements and creates larger events. Increasing the fault inclination degree reduces this effect, such that at some point the influence of the natural fracture displacement is more significant than the influence of the fault slip. Based on Figure 6.9, after 15°, the effect of fault reactivation is subsumed and the natural fracture slip dominates the size and strength of the energy release.

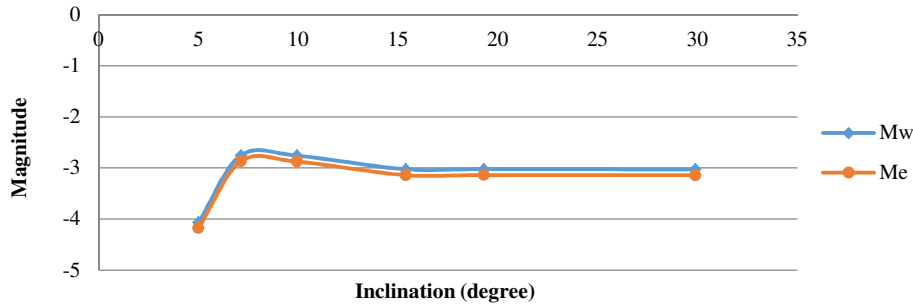


Figure 6.9. Magnitude of shear events vs fault inclinations in the Voronoi tessellated rock fabric.

Based on these preliminary results, the magnitude of the energy release grows substantially for the first three inclinations and then decreases somewhat to a constant value. The Magnitude scale on these figures is logarithmic, so going from -4.2 to -2.7 represents a large change in energy release; according to equation 6 (reformed shape of equation 4), seismic radiated energy is proportional to $10^{1.5M}$. As shown in equation (7), for one unit increase of magnitude, the radiated energy increases by a factor of 32 (Warpinski et al. 2012). In the same way, it would be increased by a factor of 1000 for two units' increase of magnitude. So, a -4.2 to -2.7 change in magnitude is approximately a 100-fold increase in the amount of energy released.

$$\log E_s = 1.5 M_e + 4.8 \rightarrow E_s \propto 10^{1.5 M_e} \quad (6-6)$$

$$\frac{E_2}{E_1} = \frac{10^{1.5(M+1)}}{10^{1.5M}} = 10^{1.5} = 32 \quad (6-7)$$

6.3.5 EFFECTS OF JOINT INCLINATION ON SLIP IN A CROSS-JOINT ROCK FABRIC

Cross-joint rock fabric with different inclinations to the σ_{MAX} orientation are generated to study how this strongly oriented fabric might affect the magnitude of energy release. Simulations

are carried out in an anisotropic stress field of (30, 20 MPa) by rotating the perpendicular cross-joint sets from 0° to σ_{MAX} in 15° increments from the previous inclination. Figure 6.10 shows magnitudes of energy release events for these simulations. The direction at which fault and joint sets are oriented and the angle they make with the principal stresses affect the applied normal and shear forces and stresses on the planar structures. Based on the principal of minimum work, fractures tend to propagate normal to the minimum principal stress (to minimize $W = \sigma \cdot A \cdot d$). Therefore, the more discontinuities that exist in this direction, the more displacements will occur, leading to larger events. It can be observed from Figure 6.10 that the moment magnitude is increasing until the 45°-135° cross-joint sets orientations. After this inclination, fault slip induction is the dominant reason for the energy release, which is why constant values for the earthquake size are noted thereafter. As suggested previously, these small models cannot generate any substantial energy release event; all magnitudes are several orders of magnitude less that any event that could possibly be “felt”. Any attempt to scale such results to a real case will require a much broader set of analyses, but these preliminary results seem to be useful.

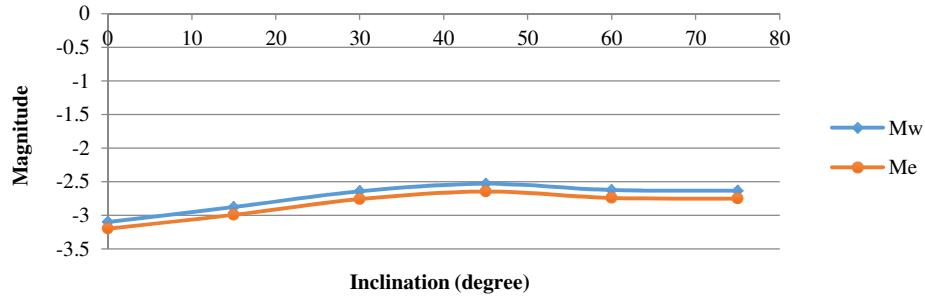


Figure 6.10. Magnitude of shear events vs angle of cross-joint sets to the orientation of the σ_{MAX} .

6.4 INJECTION ENERGY

From another aspect, the injection energy which is considered as the total energy required for hydraulic fracturing can be calculated as (Boroumand and Eaton 2012):

$$E_I = \int_{t_1}^{t_2} P Q dt \approx P(t) Q(t) \Delta t \quad (6-8)$$

where $P(t)$ is the injection pressure, $Q(t)$ is the injection rate, and Δt is the total injection time.

Injection energy is the potential stored energy that can be released and cause discontinuities to slip and deform, heat generation from frictional factors, and radiated seismic energy. Only a small amount of the total released energy is transformed into radiated seismic energy (E_s) and it can be estimated in units of Joules as (Boroumand and Eaton 2012):

$$\log_{10}(E_s) = 1.5M_0 + 4.8 \quad (6-9)$$

Another amount of the total released energy results in the opening of tensile fractures. Fracture energy is used to calculate the work required to create fracture surfaces. The following equation has been introduced to calculate the amount of energy needed for joint opening (Dusseault 2013)

$$E_F = F \times d \approx (P_f - \sigma_{hmin}) A_F w \quad (6-10)$$

Here, P_f is the pressure in the fracture and σ_{hmin} is the minimum principal stress, A_F is area of the fracture, and w is the mean fracture aperture. Since the hydraulic fracture is very thin and planar, the term $A_F \times w$ is negligible and only the net stress needs to be considered.

Therefore, comparing the amount of the energy release by fracturing or energy release slip events indicates their contribution to the total amount of released energy or total work. They express the same work concept, albeit for shear versus normal displacement. Figure 6.11 indicates the amount of energy associated with fracturing and energy release events in the Voronoi tessellated rock fabric. Values are normalized by the total amount of energy and the unit is percentage (%). It can be seen that a small amount of the total released energy is transformed into slip energy (which could potentially lead to radiated seismic energy) and another small amount results in tensile fractures. The amount of energy associated with the stick-slip process is small in comparison with the overall work performed to generate the aperture distortions (i.e. increases in aperture by forcing them open) in the rock mass. Much of the energy in slip is lost as heat from the plastic deformation rather than as radiated seismic energy (although these calculations cannot account for heat). According to Figure 6.11, about 8% of the total injection energy transforms to fracture energy and less than 1% is released as the seismic energy. Since these are hydro-mechanical models and not thermo-hydro-mechanical models, heat is not considered and it is believed that the rest of the energy is consumed for damping the DEM model (strong damping is used to stabilize the DEM model, which is actually an inertial model with forced damping to generate a quasi-static solution).

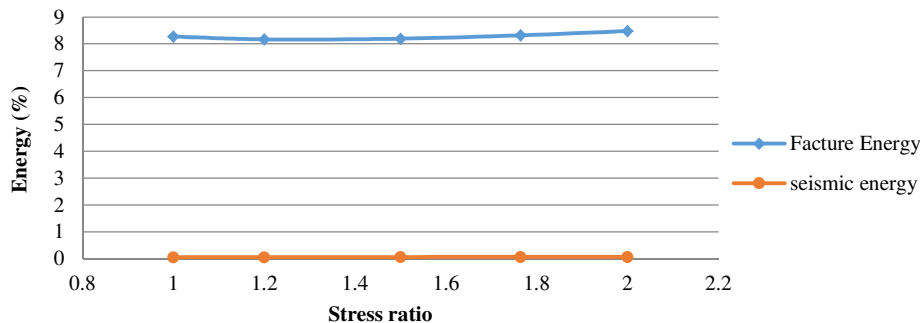


Figure 6.11. The amount of energy associated with fracturing and shear events in the Voronoi tessellated rock fabric.

Figure 6.12 shows plots corresponding to the amount of energy used for fracturing and potentially released as seismic energy for a Voronoi tessellation and for cross-joint sets. As discussed before, the role of displacement is negligible regarding the net stress magnitude and that is why higher amounts of normal displacement in the Voronoi tessellated model (Figure 6.8) do not affect the earthquake size and fracturing energy. However, it may affect the trend of the fracture energy as radiated seismic energy directly relates to the seismic moment (work), which is a function of the shear displacement. Thus, having an increasing trend and more percentage of energy for the cross-joint model is expected and it corresponds with the shear displacement behavior of the sets (Figure 6.8).

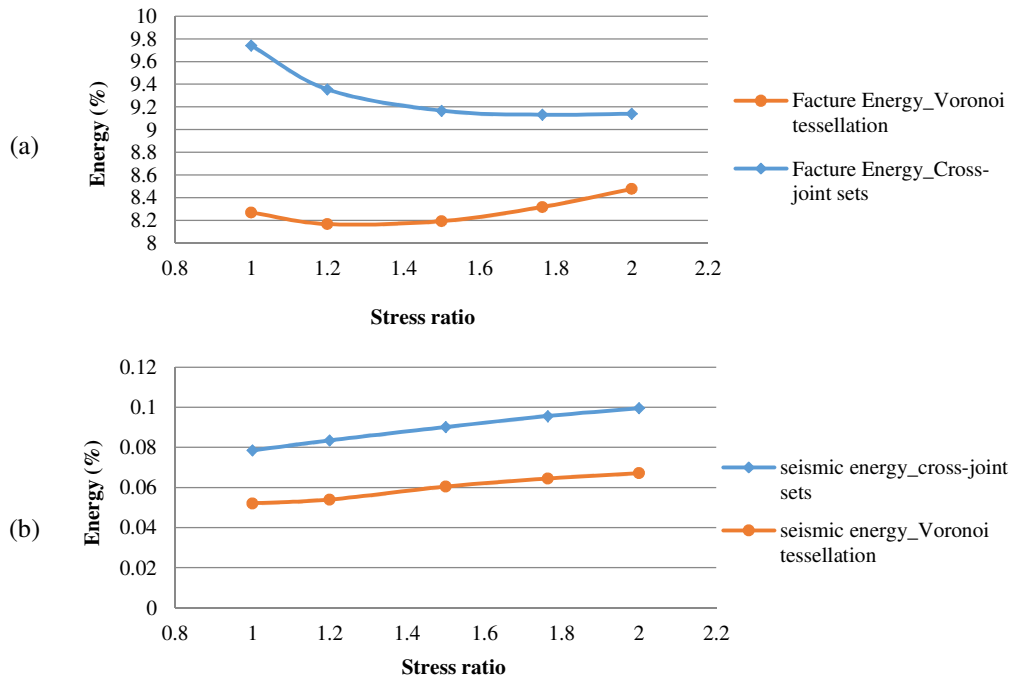


Figure 6.12. The amount of energy associated with a) fracturing and b) slip events in the Voronoi tessellated and cross-joint rock fabrics.

6.5 SUMMARY

Moment magnitude can be calculated in terms of energy (M_e) and seismic moment (M_w), which represent different physical characteristics of a shear event. For the size of model used in this study, the energy release magnitudes are in the range -4 to -2, far below any measure of intensity such as the Mercalli Intensity scale. Larger simulation models will be required to approach the scale of real cases, but in fact, the energy released by hydraulic fracturing is rarely large enough to create a shear event that could be felt on the surface by the local population. Only in the case of hydraulic fracture activity triggering a critically stressed near-by fault could one invoke any possible risk from the hydraulic fracturing operation itself. (Note that this is not necessarily the case for large-scale water injection operations which not only affect volumes 2 to

3 orders of magnitude greater, but also involve injection of massive amounts of cold water, giving a large thermoelastic effect as well and potentially leading to larger induced slip events.)

Energy release events resulting from stress and pressure changes induced by the fracturing treatment and the shear displacement can be used to calculate moment magnitude, considered equivalent to a seismic moment. The increased pressure from the fracturing reduces the normal stress along planes of weakness until slip occurs and a fault may reactivate. The size and strength of these energy release events can be calculated from seismic moment considerations and this provides indications about the total mechanical work and the amount of released “seismic” energy. In addition, knowing the seismic moment can help with geological estimates such as fault size and accompanying slip. The following are some preliminary observations from the simulations of this research:

- Hydraulic fracturing normally creates small magnitude events that have magnitudes less than zero.
- The size of the shear/slip event depends on the in-situ stress conditions, such that under higher differential stresses, larger events are more likely.
- The amount of seismic energy is small in comparison with the overall work done to generate the distortions in the rock mass.
- Although normal displacement is the main deformation mechanism in all simulations, it is mostly shearing that controls the magnitude of the energy release and thus the energy dissipation fraction.

CHAPTER 7 A DISCRETE ELEMENT METHOD APPROACH TO MODEL WASTE INJECTION OPERATIONS

This chapter presents an attempt to answer the question as to whether DEM numerical models could simulate or emulate fracture network creation during solid waste injection, followed by pressure falloff from the complex induced fracture network. To this end, two different cases were studied to empirically calibrate a jointed rock mass model to emulate pressure-time response.

OVERVIEW

A feasibility study for numerically modeling deep well slurried solids disposal processes to assess the ability of emulating empirical results from such operations was undertaken to potentially develop process control aids for field operations management. Two case studies with different locations, geologies, injection strategies, etc. have been analyzed. UDECTM, a two-dimensional Discrete Element Method software approach, is used to perform emulations of pressure-time data. Finding a suitable assumed macro-fabric (geometrical properties of the geological system of lithology and discontinuities in the model) for each case was the first goal; then, implementing appropriate rock, fracture and flow properties for each case to try and achieve a reasonable pressure profile match was tried. Different strategies were adopted to get the best match and assess if the fabric and rock parameter assumptions were reasonable. The second case study confirmed that the methodology may be applied to a difference fabric system, with a different type of rock mass and different type of injection strategies. This chapter outlines the challenges and lessons learned from numerical modeling of slurried solid waste disposal using injection under hydraulic fracture conditions in complex formations composed of relatively ductile shale, siltstone and sandstone strata. For this complex problem, the objective of this DEM model approach is to assess if such a method has merit for the simulation of such permeable formations, by emulating the pressure-time responses associated with the slurry injection and the post-injection pressure fall-off phases. If such an emulation can be developed and shown to be reasonable, then using a properly calibrated model consistently can help in analyzing data and understanding the large-scale formation response to many cycles of slurried solid waste injection. Such a capacity does not currently exist in any known history-matching flow software that is available.

7.1 INTRODUCTION

“Zero discharge” strategies have been embraced by many companies and regulatory agencies, both off-shore and on-shore, recommending or requiring that all produced solid waste from oil and gas upstream operations should be disposed properly with minimum risk. Conventionally, wastes were stockpiled on site (e.g. on a platform, or in a lined pit) for later treatment or burial (e.g. in the case of permitted non-hazardous solids), often shipped to a

treatment and disposal depot at some distance from the waste generation site. Storage and transshipment means multiple re-handling and conveyance episodes, increasing environmental risks and operating costs. Off-shore Cuttings Re-Injection (CRI) has been introduced as an environmentally safe and cost-effective waste management strategy. This slurried solids injection technology offers permanent disposal by injecting a slurry comprising a mixture of cuttings and seawater under hydraulic fracture conditions into a suitable deep formation, which is usually several hundred meters to a thousand meters below the surface (Bartko et al. 2009). On-shore, the method has been used to dispose of a wider range of materials (tank bottoms, emulsions, produced sand, NORMs, etc.), but generally limited to non-hazardous waste streams (Hailey et al. 1999; (Arfie et al. 2005).

CRI technology is now widely used in the offshore industry. On-shore, large volume disposal of various granular upstream oil industry wastes in Indonesia (Marika et al. 2009), Long Beach, California (Sipple-Srinivasan et al. 1997), and Alaska (Nadeem et al. 2005) deserve mention. Despite cost and environmental advantages, uncertainties remain that present challenges to design and operations. Having an engineered process to identify and mitigate potential risks and increase operational assurance is important (Guo and Geehan 2004), and because of the complexity and evolution of conditions, such a process requires continuous measurements and interpretation because of the changing conditions at depth during the many cycles of injection.

This work is an attempt to assess if the Discrete Element Method has merit for the simulation of such complex process of cyclic hydraulic fracturing through emulating pressure-time responses associated with injection and post-injection phases in CRI operations. Because solids are always being injected over many cycles, large permanent volume changes lead to stress changes at depth, and the injectivity of the formation may be altered by the solid particles in the slurry (Keck 2002). In early times, processes are dominantly near-wellbore (<30 m), but over years of injection cycles, the directly affected zone (the “wastepod”) can become quite large, on the order of several hundred meters (Xia 2007). The processes of injection, fracture propagation, filtration of solids, permeability evolution and stress changes interact in complex ways, and the injection/fall-off cycles have not proven to be amenable to direct physical understanding and mathematical simulation (Xia et al. 2014). Hence, empirical analysis of data is undertaken through a distinct element model as an extended feasibility study to provide insights into the evolution of the subsurface experiencing the mechanics of waste injection processes. More specifically, for operations management, insight into the stress-permeability-injectivity evolution of the injection zone at depth with continued injection episodes is needed, so that decisions (rates, total volumes, solids content, decay period, etc.) can be made for the next cycles, or for the entire project.

In-situ conditions and real data are used throughout the emulations to empirically analyze the process, although the specific physical mechanisms taking place at depth may or may not be correctly or fully represented. Hence, the word “emulate” is chosen to describe the procedure,

rather than the more widely used word “simulate”. This is to avoid any implication that the model used is physically correct in the sense that it represents correctly the physical mechanisms taking place during the slurried waste injection process. There is so much uncertainty associated with the processes taking place at depth (joint opening, shearing, changes in permeability, compressibility, etc.) that a true physics-based simulation is beyond current capabilities; the best that can be achieved is thought to be a reasonable “emulation” of an exceedingly complex process, and using the results to track, in a comparative and empirical manner, the evolution of the injection zone at depth over many injection episodes.

The first step is generating a model with the most appropriate geometry and applied stresses; then, fluid is injected according to the injection scenario. Two different CRI projects have been studied: a “Middle East” field and a “North Sea” field. The physical processes are affected by the high conductivity of joints which are further opened (dilated) by deformations induced by slurry injection under fracture conditions, affecting fluid leak-off rates in ways that remain ill-understood. Calibration of discrete element models (DEM) to field data of pressure-time response curves may provide insight to the changes taking place in the jointed rock mass.

Thus, numerical emulations of field behavior were carried out to help better understand the behavior of the system during and after injection episodes. The geomechanics stress-strain relations are solved by coupling with changes in fluid pressure in the joints of the discrete element model with the two-dimensional Universal Distinct Element Code (UDECTM). The use of DEM treats the rock mass in a more realistic manner than a purely continuum approach as it can account in part for the presence of discontinuities that represent planes of weakness and may be flow channels already, induced (complex) fracture planes that accommodate the slurry and provide flow channels, and opening and dilating joints and bedding planes that represent additional fluid pathways that respond in a non-linear manner to fluid pressures and stresses. To represent this complexity, fluid flow through a jointed rock mass under a biaxial (deviatoric) stress state is studied.

Although the process of hydraulic fracturing is considered to be strongly three-dimensional in nature, two-dimensional emulations may help to generate better understanding because flow is dominantly in two directions (both at 90° to the minimum principal stress direction). So, models of reduced dimensionality may nonetheless reflect some of the deformation and flow patterns arising because of fluid injection and withdrawal during the process.

7.2 CASE STUDY A: MIDDLE EAST FIELD

7.2.1 MODEL GENERATION – CASE A

The first case study is located in the Middle East and the candidate injection zone is sandstone. Based on available information, it was deemed appropriate to assume that the upper and lower boundaries are both impermeable. The initial pore pressure for the target zone is 20

MPa. The design of the CRI well is shown in Figure 7.1a, and Figure 7.1b shows the schematic of the geomodel.

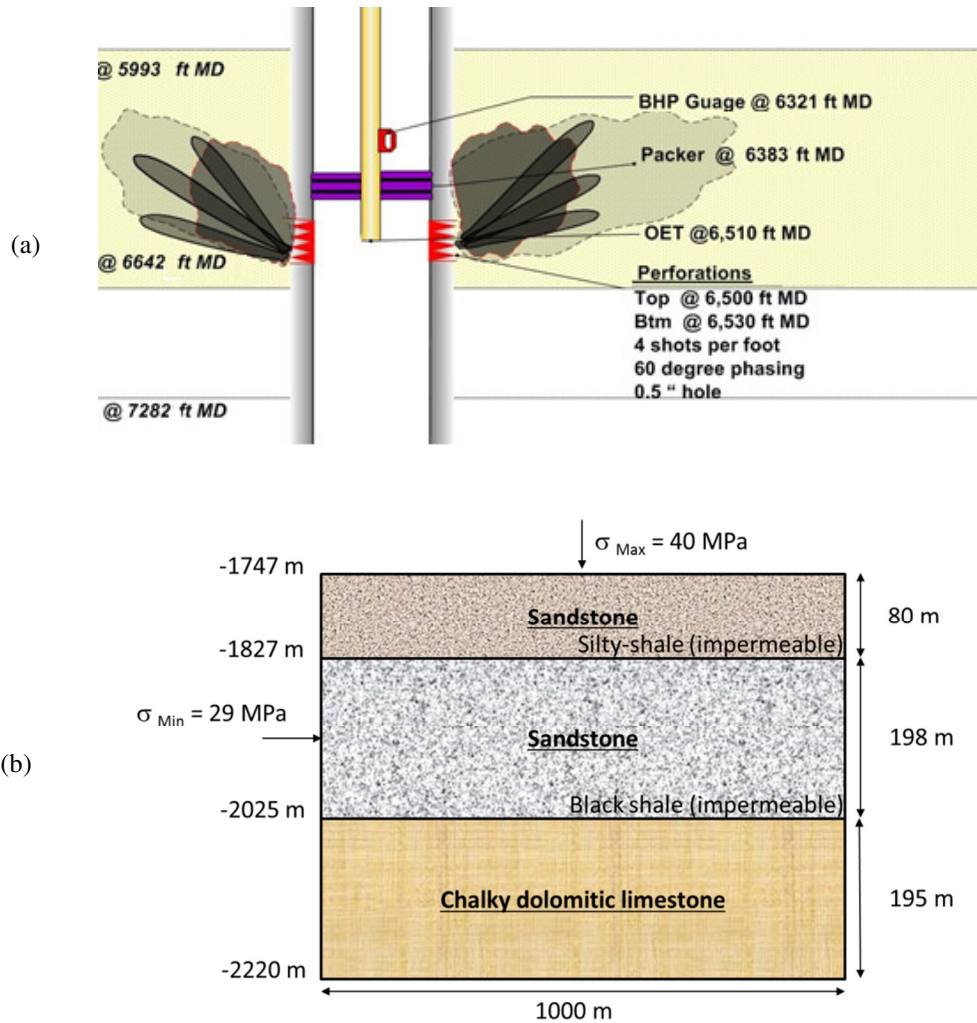


Figure 7.1. CRI operation #1; a) well schematic and b) geology information.

Hydraulic fracture geometry is characterized by its length, width and height (Figure 7.2). The relationship between these three dimensions and fracturing design has been a subject of debate among fracturing experts for many years. According to Daneshy (2010):

- Fracture length is a function of injection volume and it also affects fracture width directly, which means greater length leads necessarily to a wider fracture.
- Fracture length affects slurry volume such that creating greater length needs more volume of slurry (if height is constant in a constrained zone and length is doubled, volume increases by a factor of four if the rock is impermeable).

- Fracture width varies depending on mechanical properties of the formation, fluid properties and other fracture dimensions. For instance, wider and shorter fractures are created through using higher-viscosity fluids (and higher injection rates).
- Fracture height is related to the formation thickness and is often considered to be constant to simplify the modeling challenges. (This assumption of constant height is not met in practice for large-scale CRI operations.)

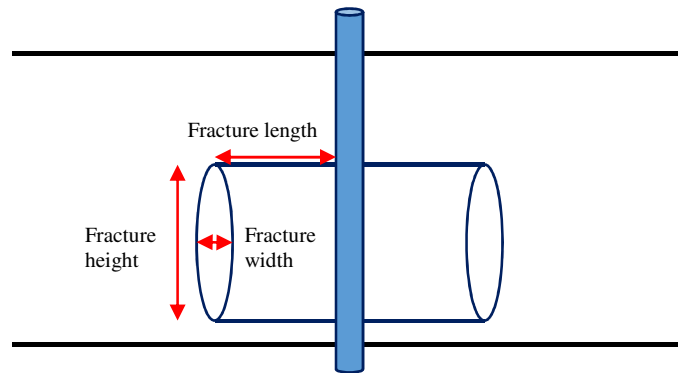


Figure 7.2. Geometry of a hydraulic fracture.

For these analyses, it was important to see how far fractures propagate laterally and vertically. In other words, estimating height and length of the hydraulic fractures was the primary purpose of the study. Known values of in-situ stresses were minimum horizontal stress and vertical stress, and a two-dimensional model under this biaxial stress state was developed. A three-dimensional model would likely give more realistic results and is highly recommended for future studies, but such an approach carries a huge computational burden if similar scales of discretization are desired and parametric studies needed.

Fracture growth is a function of pressure, fluid properties, and injection rate and volume. Hydraulically induced fracture orientation is dominantly controlled by principal stresses. In the absence of stress gradients and strong joint fabric, a fracture will propagate as a plane normal to the direction of least stress and grow equally in all directions until it reaches some heterogeneities in mechanical or flow properties that will suppress or promote growth rate in that direction. Under typical slurry injection conditions for ground cuttings, it is usually assumed that one cycle of injection results in a single vertical fracture plane that grows both vertically and horizontally as long as injection continues. This assumption is used in the modeling.

Shut-in periods between injection cycles give the target formation time to dissipate pressures and allow the solid waste to be compressed as the effective stresses rise. The larger zone affected by the pressures is the disposal domain which contains the smaller compressed waste pod that has a complicated shape because induced fracture patterns change as injection cycles continue. The differences in pressure response and dissipation behavior after shut-in are proof that the

formation response to waste injection is changing as the result of the increased extent and changing shape of the waste pod and associated pressure and stress effects.

Given that $\sigma_{min} = \sigma_h$, and based on experience, literature and inference in the absence of direct proof, successive injection cycles would be expected to generate an array of dominantly vertical fractures of similar size that are scattered with slightly different angles around the wellbore (Moschovidis et al. 2000). Also, solid disposal will increasingly lead to horizontal fracture growth over time because the increasing volumetric strains induced by the planes of compressed solids will increase the lateral stresses until, locally in the vicinity of the waste pod, $\sigma_h > \sigma_v$ (Veil and Dusseault 2003). Of course, regionally, at a scale much larger than the disposal domain, the original stress condition obtains, so fractures should retain a large vertical component even as they develop more horizontal components.

During the period of shut-in, the induced fractures may be viewed as gradually closing, and because fluid is no longer being injected, the flow pattern may be considered to be approaching linear flow conditions. This is a feature that helps justify the use of a two-dimensional emulation for a complex three-dimensional condition in the ground during pressure leak off in a CRI cycle.

The Voronoi tessellation generator is a UDECTM feature and it is used to simulate a random rock mass fabric of natural existing and incipient fractures by subdividing the rock mass into polygonal blocks with an overall (global) isotropic fabric (Figure 7.3). Existing and incipient fractures are defined as closed planes of weakness with low tensile strength that can be opened (Mode I) or reasonably easily sheared (Mode II) by stress changes. The Voronoi tessellated geometry consists of polygonal blocks with a limited area. It is possible to stipulate different properties for each joint (or each set of a group of joint sets) such that a probabilistic input is achieved, perhaps more closely emulating a real rock mass, but it remains unclear what distributions of properties would be most appropriate, so in this work the properties are assumed to be the same for all joints (Table 7.1).

Figure 7.3 shows a two-dimensional vertical section. A stiffness model for contact and a Mohr-Coulomb constitutive law are applied to represent the block and joint slip and deformation behaviour. The contact and Coulomb slip model needs six parameters: normal and shear stiffness, friction angle, cohesion, tensile strength and dilation angle. Part of the data required for emulations were available (such as large-scale geological information, geophysical borehole logs, and injection parameters) and the rest are assumptions made based on the literature and experience (such as geometrical and geomechanical properties). Table 7.1 includes material properties assumed for the target formation.

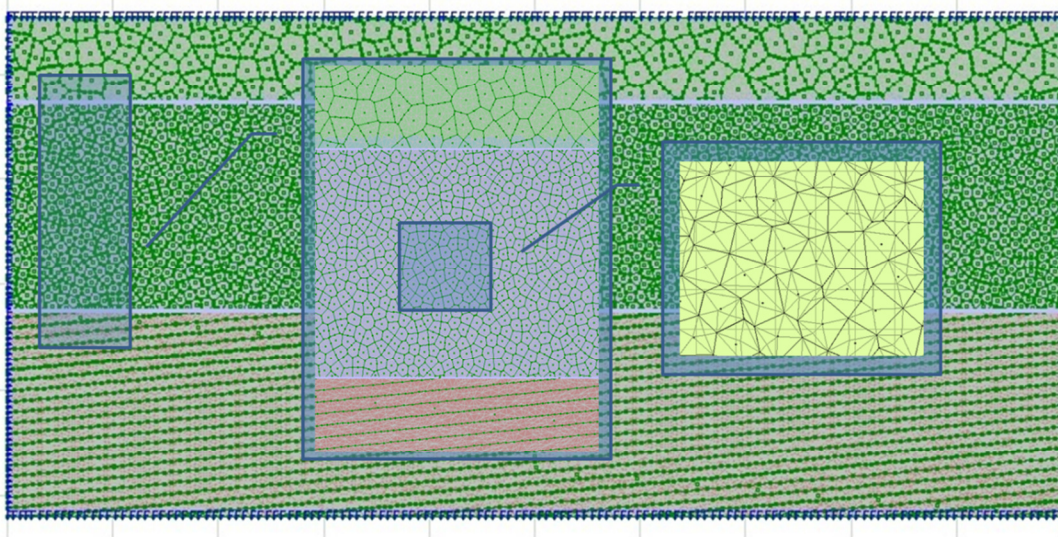


Figure 7.3. Generated geometries, case A.

Table 7.1. Rock, joint and fluid properties, case A.

Rock properties			Joint mechanical properties		
Density	2700	kg/m ³	Normal stiffness	10	GPa/m
Bulk modulus	38	GPa	Shear stiffness	4	GPa/m
Shear modulus	41	GPa	Friction angle	30	Degree
Friction angle	30	Degree	Cohesion	0.1	MPa
Cohesion	0	MPa	Dilation angle	5	Degree
Tensile strength	0	MPa			
Joint hydraulic properties			Fluid properties		
Permeability factor	0.83×10^8	MPa ⁻¹ s ⁻¹	SW Density	1.03	Mg/m ³
Residual hydraulic aperture	5×10^{-5}	m	SL Density	1.17	Mg/m ³
Aperture at zero normal stress	3×10^{-4}	m	Dynamic viscosity	10^{-3}	Pa·s

Flow in the DEM model is generated by the pressure difference between adjacent domains. In a steady-state flow analysis, domain volume alterations have negligible influence on pressure change, so the effect of fluid stiffness in the mechanical steps is eliminated and the bulk modulus of the water (k_w) is not required. Because of small values of pressure change in each hydraulic step, many fluid steps can be performed for each mechanical step while preserving the accuracy of the solution. For transient flow analysis, the numerical stability requirements may be rather severe, and may make some analyses time-consuming so as to be impractical for parametric comparisons, especially if large contact apertures and very small domain areas are present. Furthermore, the fluid filling a joint also increases the apparent joint stiffness by k_w/a , thus possibly requiring a reduction of the time-step size used in the mechanical equilibrium calculations (ITASCA Consulting Group Inc. 2010).

At each time step in the mechanical calculation in UDECTM, the geometry of the system is updated, giving new values of apertures for all contacts and new volumes of all domains. Flow rates are calculated, domain pressures are updated taking into account net flow into each domain and changes in domain volume arising from the incremental motion of surrounding blocks (ITASCA Consulting Group Inc. 2010).

Forces are summed at each contact and equilibrium is approximated when the forces F_i are equilibrated within acceptable accuracy for all j-nodes - $(\Sigma F_i)_j \approx 0$. Unbalanced forces are calculated continuously during time-stepping and the maximum unbalanced force is plotted so that equilibrium can be confirmed. Low values of the ratio of maximum unbalanced force show that forces balance at all gridpoints but steady-state plastic flow may still be happening, so convergence of displacement values to zero at the end of the iterative solution indicates equilibrium (ITASCA Consulting Group Inc. 2010).

7.2.2 INJECTION STRATEGY – CASE A

The injection strategy for the Middle East field is a single “batch” injection and consists of a sea-water pre-flush stage, slurried cutting injection, and a sea-water post-flush stage. Optimum cuttings slurry properties for injection are 1.04 – 1.30 SG, while the specific gravity of sea-water equals 1.03. The entire volume of slurry is being continuously injected during batch pumping (i.e. no shut down of the pumps or decrease in rate during this stage of pumping). Generally, these “switches” from pre-flush stage, slurry/slop stage, and into post-flush stage are “on the ‘fly’”, with no stopping of the pumps, so that momentum is maintained and solids settlement or blockages can be avoided.

Figure 7.4 shows the injection rates for the chosen date of CRI injection. The first two phases of injection are considered as steady-state flow, under which pressure or pressure gradient is constant over time. The third phase is considered as transient flow with a somewhat varying pressure gradient.

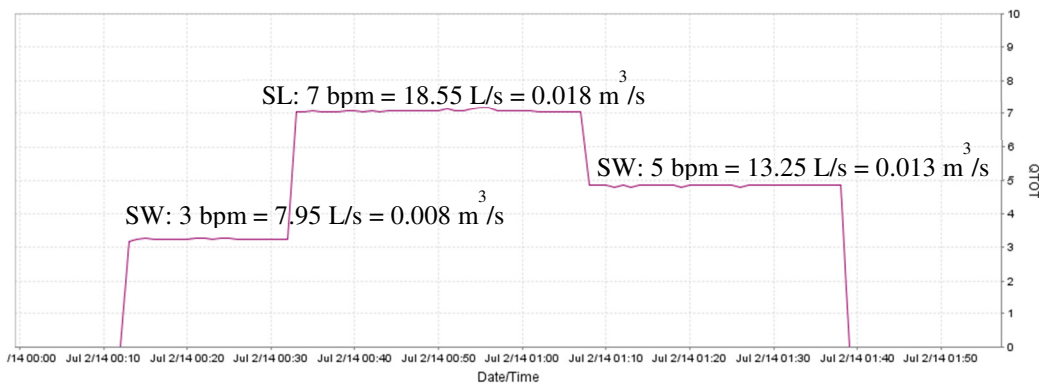


Figure 7.4. Injection actual data of the first case study, case A.

7.2.3 JOINT MODEL PRESSURE MATCHING – CASE A

Pressure matching includes two phases: injection and shut-in pressure matching. The first step is generating the model with the most appropriate geometry and applied stresses. Then fluid is injected according to the injection scenario with three phases of injection (seawater, slurry then seawater) with three different rates. Different challenges in this part of the study included the problem that injection rates should be adjusted for the two-dimensional model effects, as well as the issue of the flow regime changing from steady state (constant rate and conditions) to transient flow (pressure changes with all associated volumetric and rate effects). Importantly, the area near the injection point undergoes plastic deformations and becomes damaged over time; this zone is the waste pod which includes compressed waste and damaged formation, and it has different characteristics from the virgin formation or from zones that have not experienced recent injection. Although it is important to estimate the extent of the waste pod, it is initially more important to be able to generate such a zone in the model, by changing the geometry of the waste pod or changing its physical characteristics (or both). One may also choose to model a very early injection pressure history in which the formation is more likely virgin and no large waste pod is yet created that would dominate system response. In the current study, data from early injection cycles were not available, so the waste pod was already of substantial volume (area in the model) and this undoubtedly has affected the results.

To deal with the challenge of converting injection rate to an appropriate value in a two-dimensional framework, the injection rate should be divided by the missing (constant) dimension of the model. Having this in mind, Figure 7.5 shows the best pressure match achieved between the real data and numerical results. There is a negligible offset at the first phase of the injection when the pressure is rising. This offset reflects the effect of the waste pod. In the case of a virgin formation, pressure would increase more abruptly to reach the fracture point of the formation because the virgin formation is observed to be much “stiffer” in its response than a formation that has been subjected to extensive waste pod growth through numerous injection cycles. This is because the compacted solid waste is much softer than the virgin rock, which also may have been softened by shearing and dilation.

It is assumed that pre-existing fractures are open with a uniform initial aperture of 5×10^{-5} m. The aperture of each joint is calculated as a function of its orientation relative to the in-situ principal stresses. Although the fluid density is changing from seawater to slurry, the real effects of the two phases of fluid flow have not been modeled in the current emulations. Because the joint conductivity factor ($K_j = 1/12\mu$) can be applied only once in the system, it is necessary to decide which fluid viscosity is dominant in the whole system. In the current case, seawater has been injected twice and for a longer time, so it was assumed that seawater is the major fluid in the system.

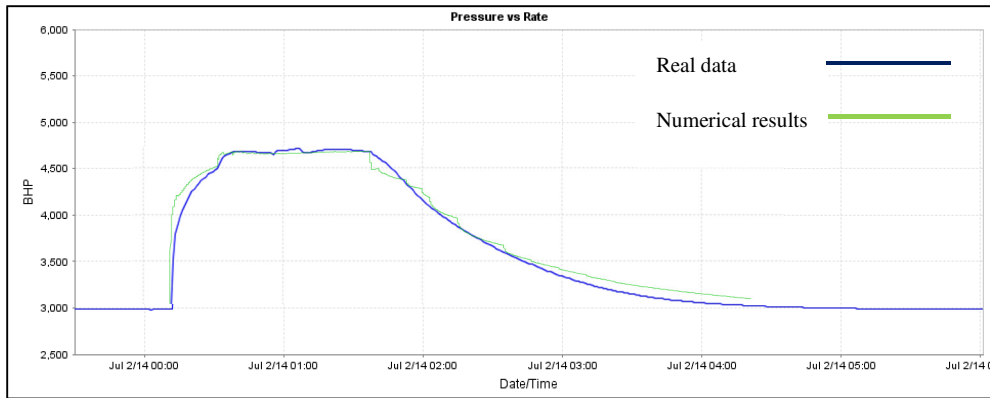


Figure 7.5. Matching numerical and real pressure curves, case A.

The next step was emulating the shut-in condition and matching the fall-off pressure “realistically”. The software is not capable of directly modeling the shut-in condition therefore a new simulation was developed for the shut-in time response, and it provided a better match for the pressure-time curves. Figure 7.5 shows matching numerical results with real data. Note that the pressure drop in the numerical results comes from removal of frictional losses, fluid loss to the formation and further growth (extension) of the fracture.

7.2.4 PHYSICAL UNDERSTANDINGS OF THE CRI OPERATION # 1

The same emulations were carried out for subsequent cycles of injection; here the results for three cycles of injection will be discussed. Four square zones with different length of edges were assumed around the injection points (Figure 7.6); these are referred to as effective zones, and joint displacements are calculated in these effective zones to see how they change with distance from the injection point.

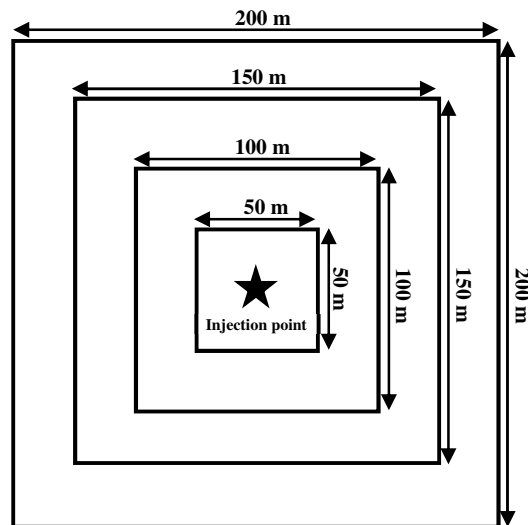
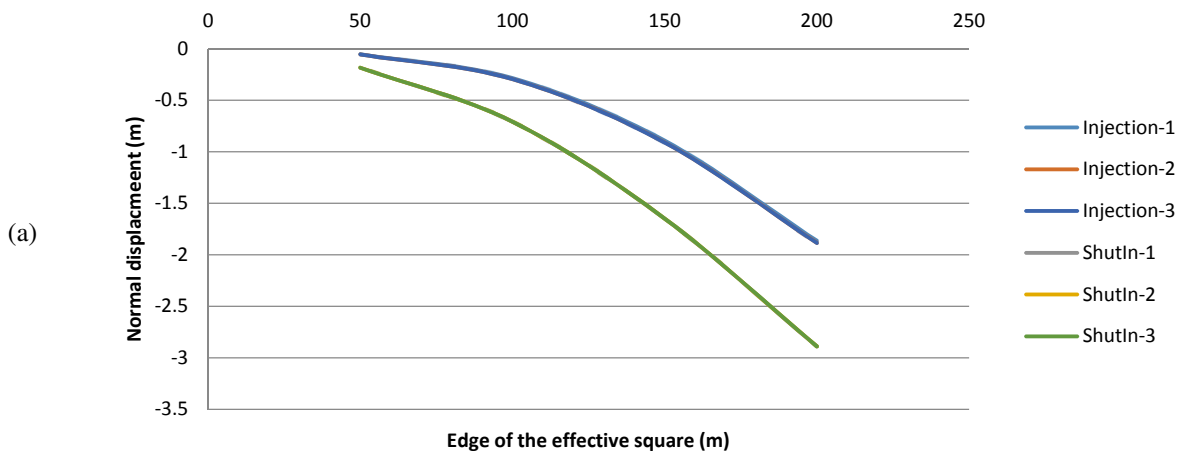


Figure 7.6. Effective zones around the injection point, case A.

Figure 7.7 shows cumulative amounts of normal and shear displacements inside each effective zone plotted against the edge length of the squares for three subsequent cycles of injection and shut-in. Cumulative normal displacement has negative values because more closure than opening is happening in the corresponding zones. According to this figure:

- The cumulative normal displacement is increased by increasing the effective zone size. However, higher fluid pressure around the injection point would induce more joints opening and in turn more distant joints will undergo closure because the total stress increases but the pore pressure at a distance does not, hence the effective stress increases. On the other hand, shear displacement is increasing farther from the injection point and would affect a larger area as the result of induced additional shear stress from the volumetric distortions near the injection well caused by the increase in joint aperture by normal opening and shear dilation.
- Shear displacements of joints are not reversed during the shut-in pressure decline, and these irreversible dilational shear displacements likely form persistent flow channels of higher fluid conductivity (Figure 7.8). (This feature of a DEM is considered to be one of the major reasons why conventional continuum well-test models fail to achieve realistic history matching, whereas the DEM approach seems to give better matches.)
- Within the same effective square, there is more joint closure during shut-in than during injection, which means that the normal joint displacements in the UDEC™ model formulation are largely reversible, and opened joints can get back to their original apertures after injection and with pressure dissipation.



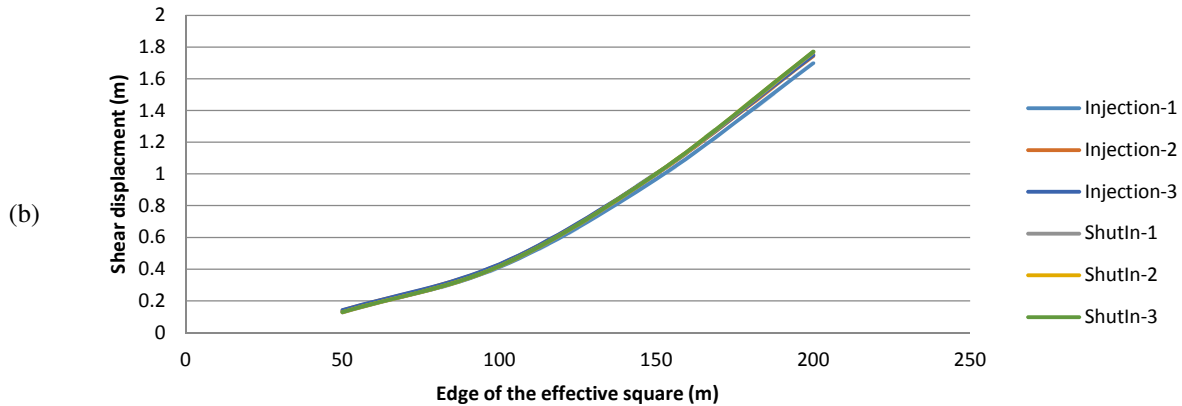


Figure 7.7. Cumulative a) normal and b) shear displacements vs edge of the effective zones for three cycles of injection and Shut-in, case A.

Figure 7.8 shows right and left lateral displacements during injection and shut-in. It also indicates how hydraulic fracturing affects the “overburden”, although there is an impermeable layer between formations and no fluid gets into the upper formation in these analyses. It can be seen that shear displacement is essentially irreversible and the induced shear-dilation flow channels remain connected after shut-in. The direction of right- or left-lateral displacement is a function of initial far-field stress orientations, induced stress changes and joint orientations. Since in a Voronoi tessellated rock fabric there are joints oriented in all directions, joint shear is mostly a function of stress directions, and right- and left-lateral shear movements are respectively mostly aligned NW-SE and NE-SW in this emulation. Such information may be important for seismic risk studies. For example, if there is a known fault through the process zone, and if the original stresses are well-understood, this information could allow prediction of the direction of movement, and the magnitude of movement extracted from such emulations might even be scaled to possible ranges of magnitude as stick-slip processes develop (Rutqvist et al. 2013b).

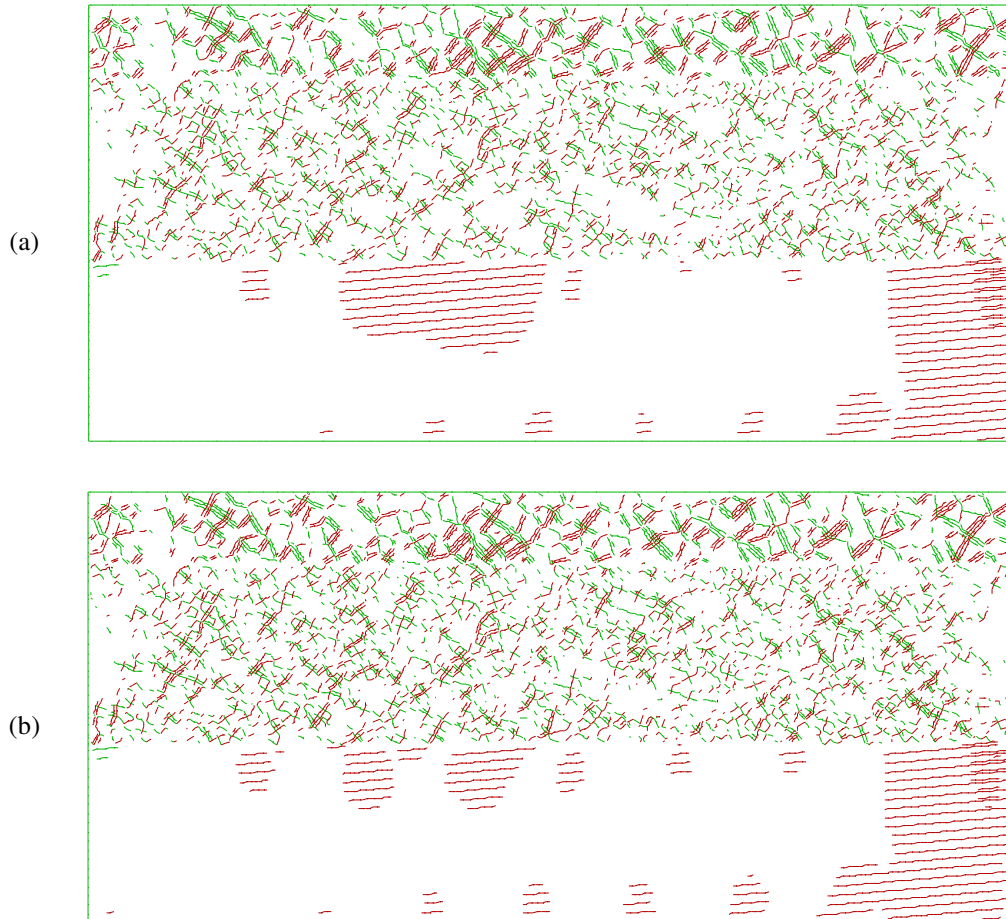


Figure 7.8. Right and left lateral shear displacements during a) injection and b) shut-in, case A.

Figure 7.9 shows cumulative opening and closure for three cycles of injection. Here instead of the general term “normal displacement”, “opening” and “closure” are used to differentiate between deformation types during injection and shut-in. Not surprisingly, opening is much larger during injection, and more joints undergo closure during shut-in than during injection. However, results could be interpreted based on the size of the effective area as well; joint openings inside the two smallest effective zones disappear during the shut-in, and by increasing the size of the studied zone, part of the opening remains. So, farther from the injection point, joints undergo both normal and shear displacement and appear to stay open somewhat more even after stopping injection. This partially irreversible normal deformation must be also linked to the amount of irrecoverable shear deformation taking place in those regions. So, importantly, not only do fluid pressure and joint compressibility effects have impact on overall evolving system compressibility and flow potential, the irreversible shear displacements and the resulting incomplete normal closure leave an appreciable increase in system fluid conductivity and mechanical compliance. The figures showing pore pressure distribution indicate how far the pressure is traveling through the formation.

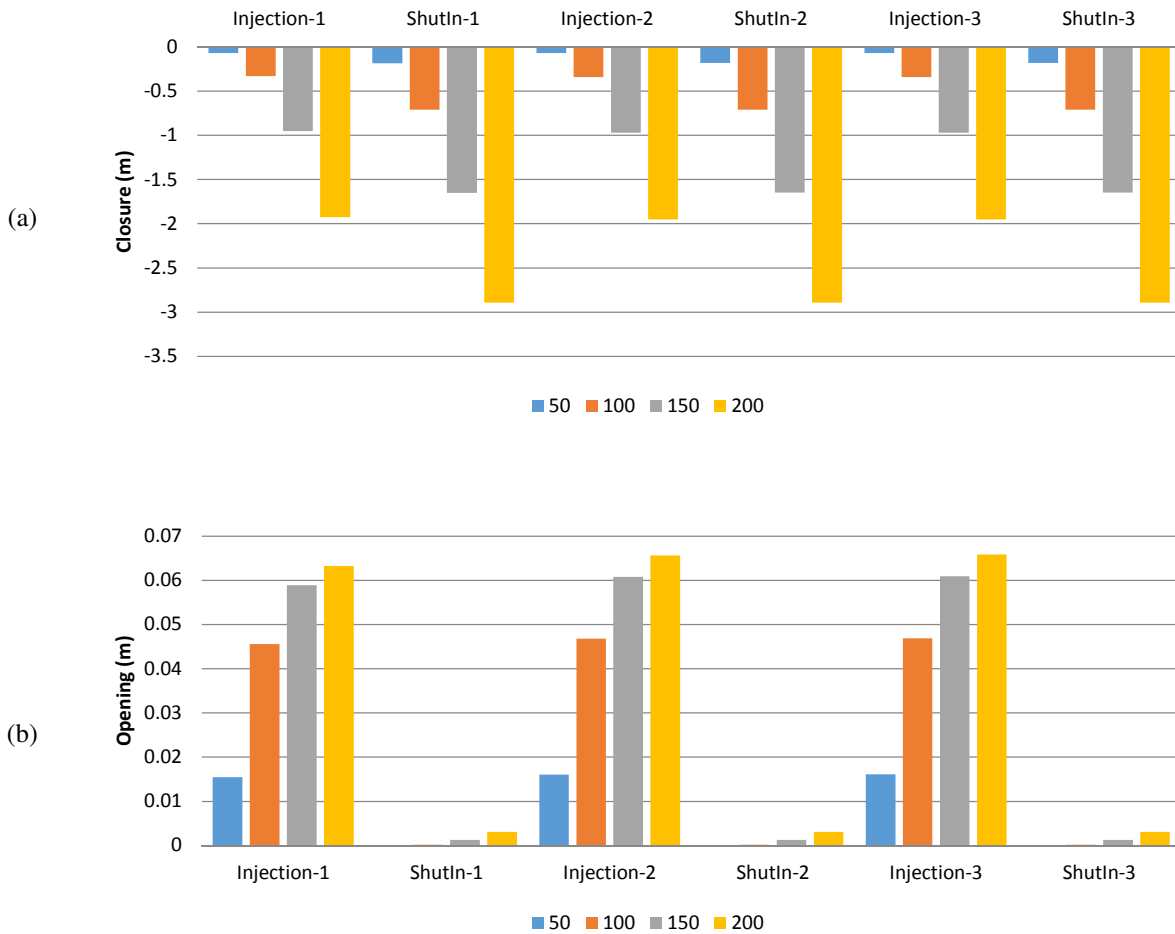


Figure 7.9. Cumulative a) closure and b) opening vs edge of effective zones for three cycles of injection and shut-in, case A.

With simulated impermeable boundaries on top and bottom of the formation, the vertical fracture extension would be no larger than the thickness of the formation (198m), so lateral growth of the hydraulic fractures is favored. Figure 7.10 shows x-displacement contours of the model during and after injection; the negative sign on the legend is due to the central axis location and the displacement relative to that axis. The left side of the injection point undergoes larger displacements during both injection and shut-in, likely as the result of local fabric differences (although the Voronoi tessellation is globally isotropic, there are appreciable sub-regions with non-isotropic fabric). After stopping injection, locations further from the injection point show almost the same amount of displacement as during the injection, which means joints in more distant regions remain deformed because of the shear displacement mechanisms mentioned above.

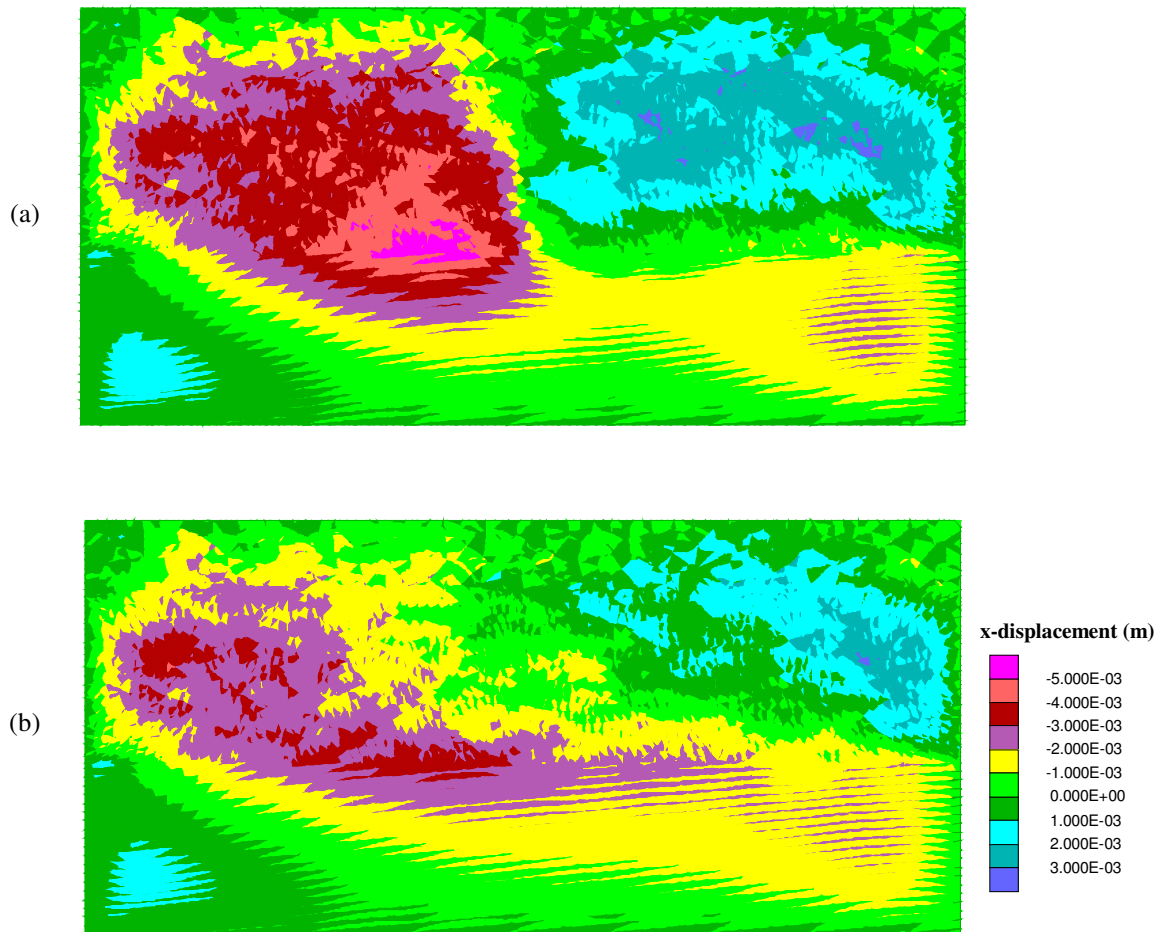


Figure 7.10. X-displacement contour during a) injection and b) shut-in, case A.

Figure 7.11 shows pore pressure distribution along the x-axis during the injection and the shut-in. Asymmetry of left and right lateral growth is from local fabric effects. However, this figure gives an idea about the length of lateral growth. The trend of the pressure curve is different during injection from shut-in because flow channels are already opened and flow-back would allow reaching the formation pressure quickly.

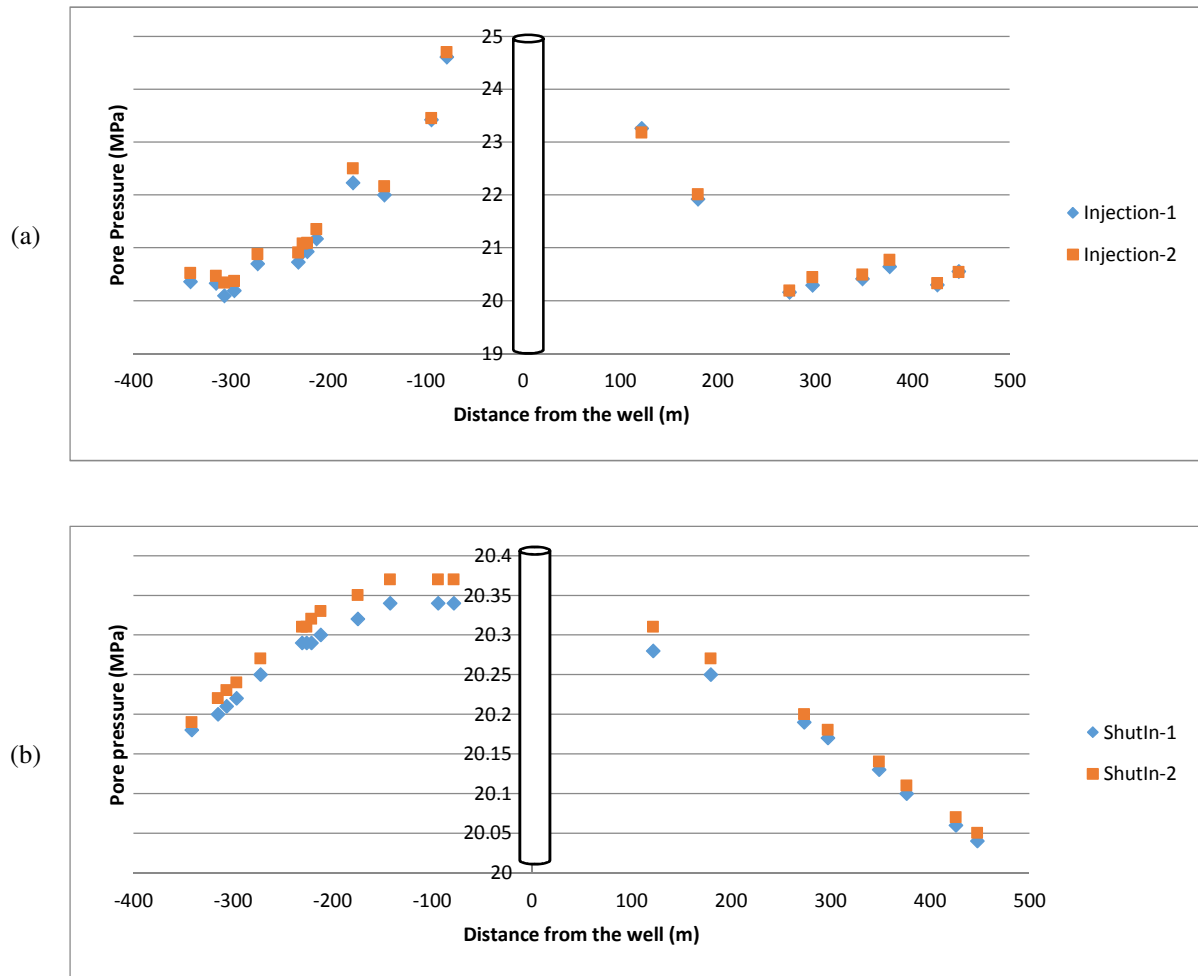


Figure 7.11. Pore pressure profile along x-axis during a) injection and b) shut-in, case A.

7.3 CASE STUDY B: NORTH SEA FIELD

In order to help in establishing the utility of this approach to simulating slurry injection and shut-in, another case study in a different location with different geology was chosen and the same type of studies repeated.

7.3.1 MODEL GENERATION – CASE B

The second case is an offshore field located in the North Sea. The injection region lithostratigraphy consists of horizontal layers of sandstone, shale and mudstone in a sequence called the Hordaland Formation. Hydraulic CRI injection was performed in the mudstone formation. This geology is much more complicated to model and analysis might help indicate whether DEM can be used for a granular material that appears not to be inherently fractured

initially (before the induced fracturing occurs during CRI). Figure 7.12 shows a schematic of the formations.

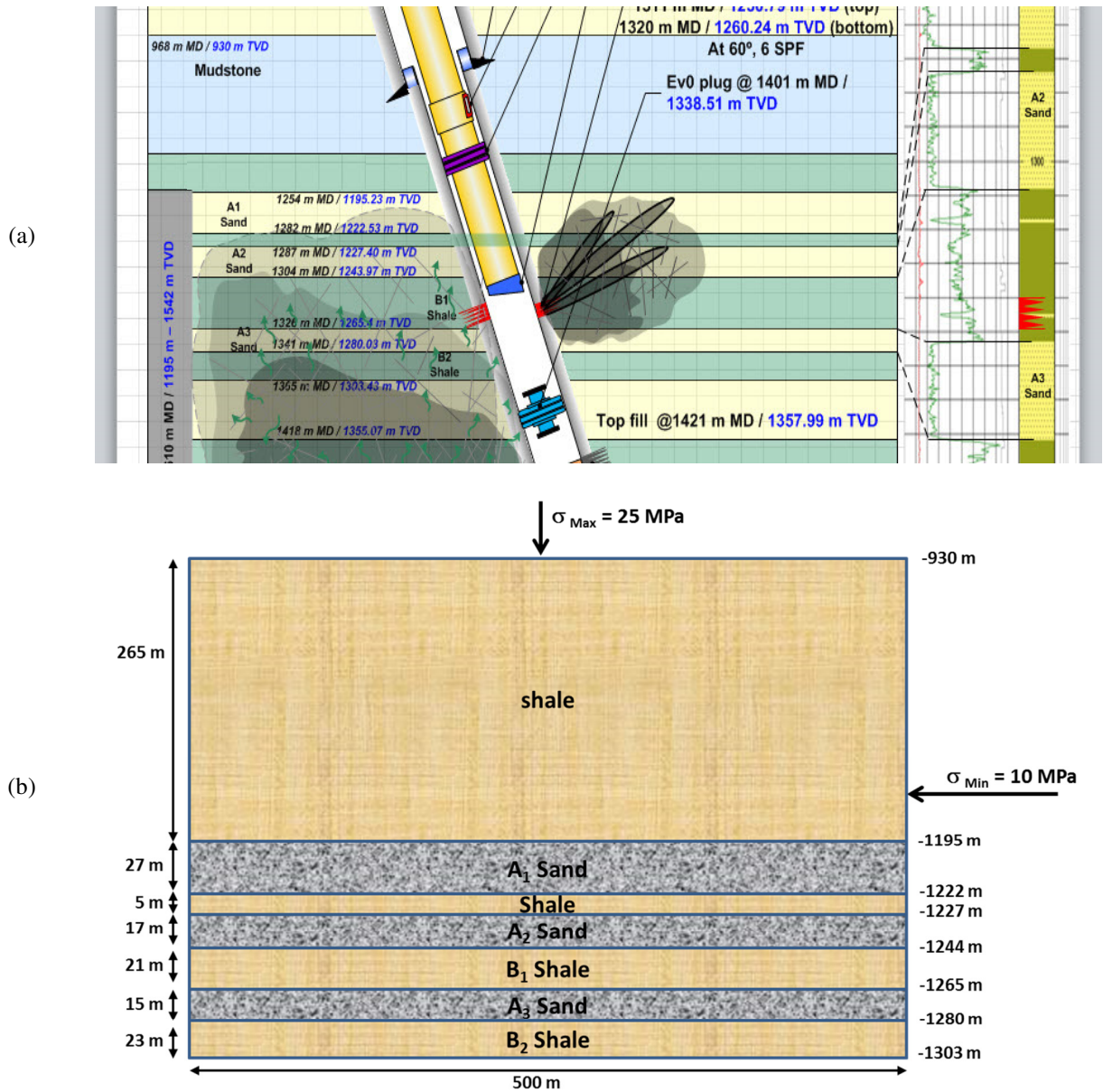


Figure 7.12. CRI operation #2; a) well schematic and b) geology information, case B.

As before, UDECTM is used to perform coupled hydro-mechanical emulations using a seven-layer model representing the Hordaland Formation, so the generated geometry is quite different from the previous case. Figure 7.13 shows the schematic of the model; each layer has its real thickness and 0.5 km length, so the model size is 160m × 500m.

Table 7.2 shows material properties assumed for the formations.

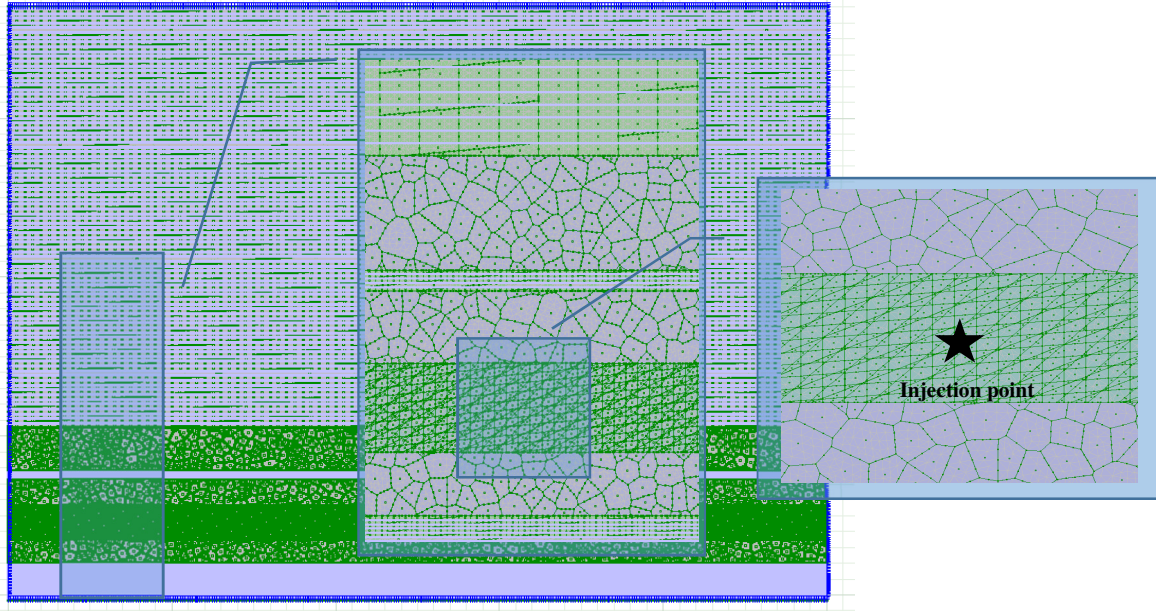


Figure 7.13. Geometries generated by UDEC™, case B.

Table 7.2. Rock, joint and fluid properties, case B.

Rock properties			Joint mechanical properties		
Density	2700	kg/m ³	Normal stiffness	10	GPa/m
Bulk modulus	14	GPa	Shear stiffness	4	GPa/m
Shear modulus	10	GPa	Friction angle	30	Degree
Friction angle	25	Degree	Cohesion	0.1	MPa
Cohesion	25	MPa	Dilation angle	10	Degree
Tensile strength	1	MPa			
Joint hydraulic properties			Fluid properties		
Permeability factor	0.83×10^8	MPa ⁻¹ s ⁻¹	SW density	1.03	Mg/m ³
Residual hydraulic aperture	3×10^{-5}	m	Slop density	1.03	Mg/m ³
Aperture at zero normal stress	1×10^{-4}	m	Dynamic viscosity	10^{-3}	Pa·s

7.3.2 INJECTION STRATEGY – CASE B

This case study has three phases of injection in each cycle: seawater, slurried cutting or slop injection, seawater. Since all three phases of injection have same injection rate and density, they can be assumed as one injection in the numerical modeling with steady-state flow. Injection rate is 0.0192 m³/s and considering the assumed thickness of 350 m for the missing dimension of the formation, the applied injection rate would be 5.3×10^{-5} m³/s/m. Figure 7.14 shows the injection rate and bottom-hole pressure for the corresponding calendar date.

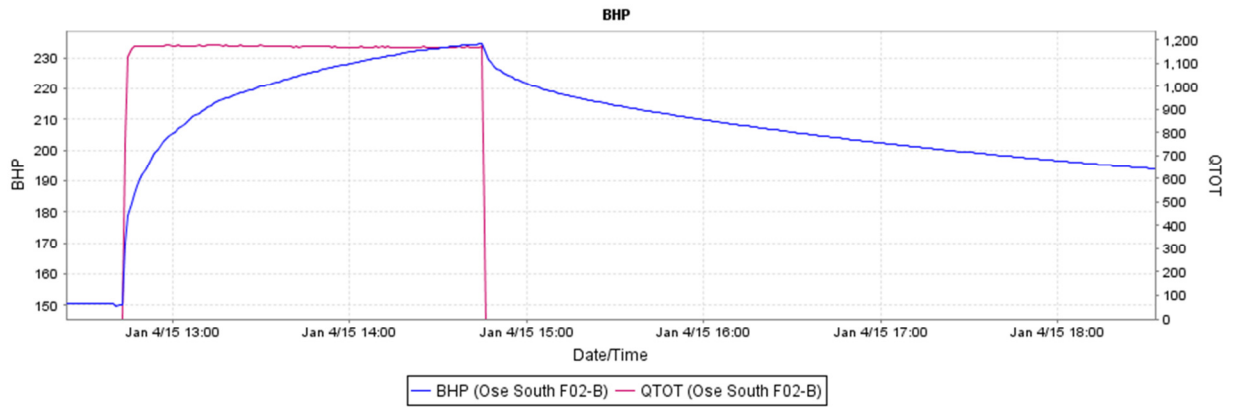


Figure 7.14. Injection actual data of the second case study, case B.

7.3.3 JOINT MODEL PRESSURE MATCHING – CASE B

The same procedure for modeling was applied: the first step is generating an appropriate geometry which gives the best match for the injection phase. After a number of trials, the geometry shown in Figure 7.13 was observed to give a good match with the real data for the injection stage. Remember that conventional flow models give much poorer fits (see next section).

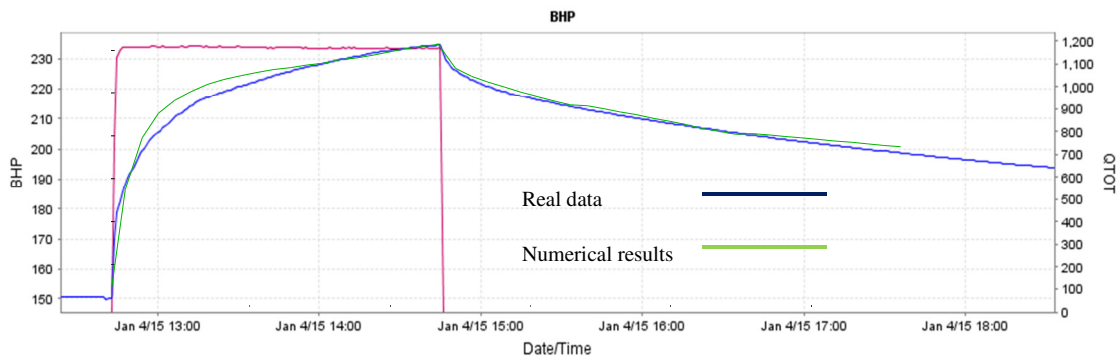


Figure 7.15. Matching numerical and real pressure curves, case B.

Figure 7.16 indicates how the fluid pressure changes over time for the injection point and four monitoring points around it. They all show similar trends, but are somewhat different in terms of magnitude. The monitoring point on the right hand side of the injection point has the lowest pressure values, which means fluid did not travel much in this direction.

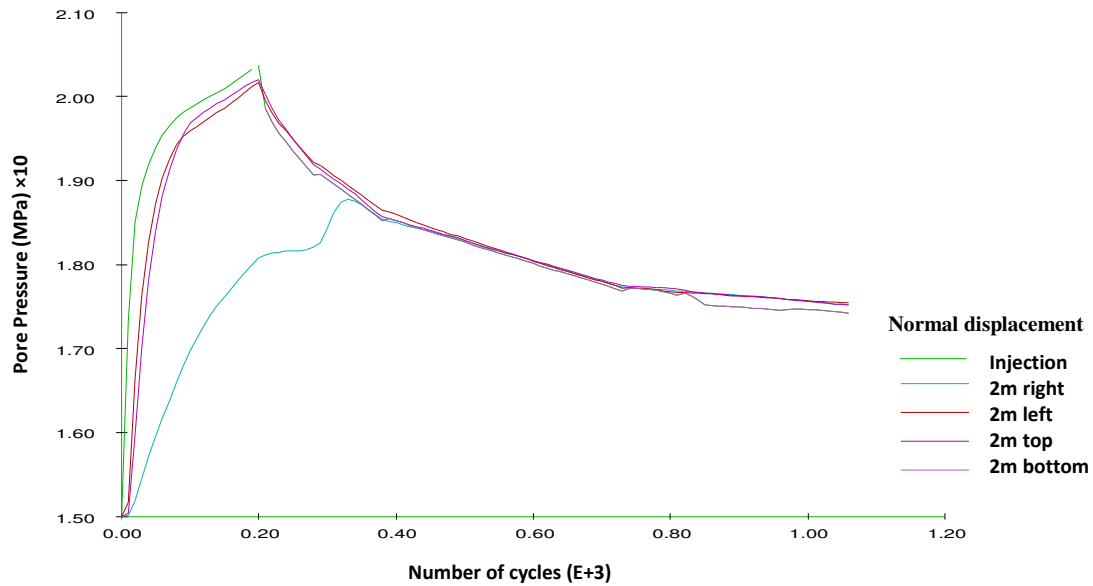


Figure 7.16. Fluid pressure trends over one cycle operation for five monitoring points, case B.

7.3.4 INTERPRETATION OF CRI OPERATION # 2 RESULTS

Before further discussion, key differences between these two cases are noted:

- Differential stresses in case B are much larger than in case A. The Middle East field has in-situ stresses of (29, 40) MPa, while field stresses in the North Sea field are (10, 25) MPa.
- Lithology and thus material properties of these two case studies are different: sandstone vs mudstone.
- Thickness of the injection zone in case B and case A is respectively 20m and 200m.
- The neighboring layers in the Middle East field are acting as barriers; however, the target zone in the North Sea is surrounded by permeable boundaries.

Hence, it is reasonable to expect different behaviors of fluid flow and deformation in these two case studies.

Figure 7.17 indicates displacement vectors for one cycle of injection. Deformation migrates from the injection zone to neighboring layers and then gets suppressed as it contacts more distant mudstone layers. Since the target zone is too thin to accommodate the volumes being injected by pure lateral fracture growth, it is reasonable to observe such fracture transport out-of-zone. Also, the neighboring layers of the target zone consist in part of sandstone and therefore they offer some accommodation for fluid flow, which is clearly coupled with mechanical deformations.

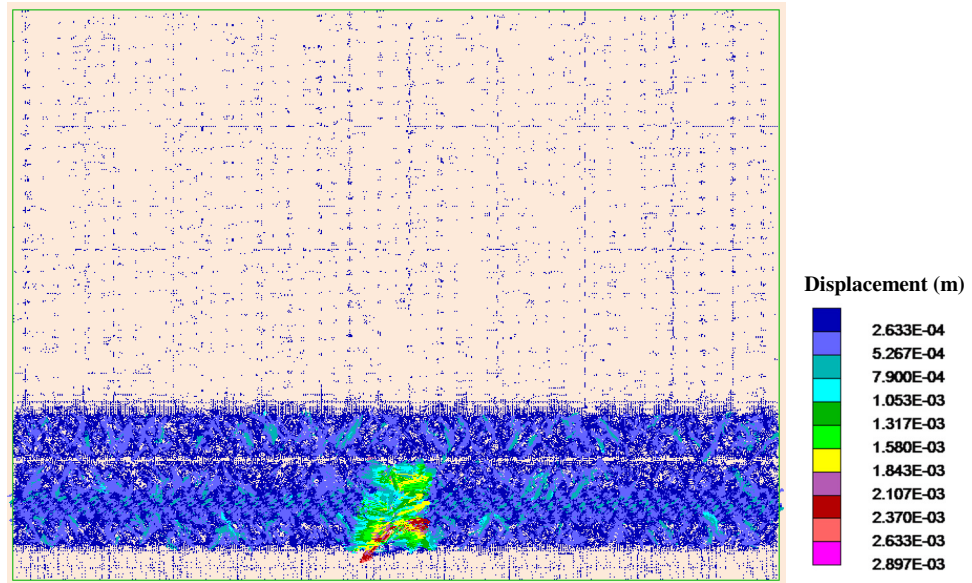
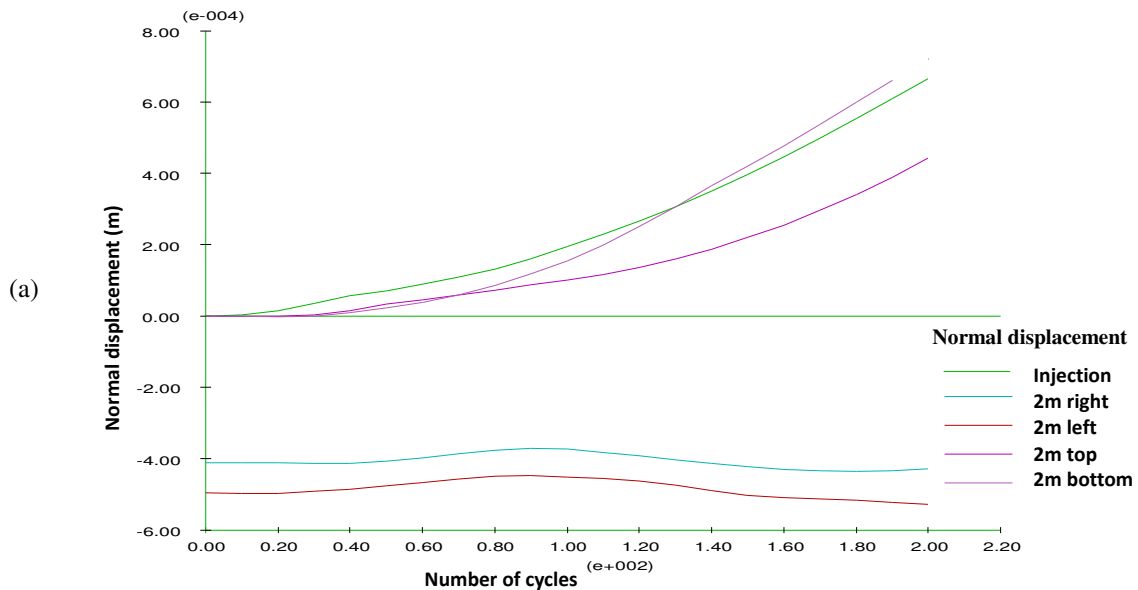


Figure 7.17. Displacement vectors after one cycle of injection.

Figure 7.18 shows a history of normal and shear displacements over time for the injection point and four observation points. It shows that points located on the right and left hand sides of the injection point do not undergo large displacements during the cycle. This means that fluid flows more vertically than laterally, which would be the expected effect with $\sigma_{min} = \sigma_h$ and a low effective stress ratio (10:25 MPa).



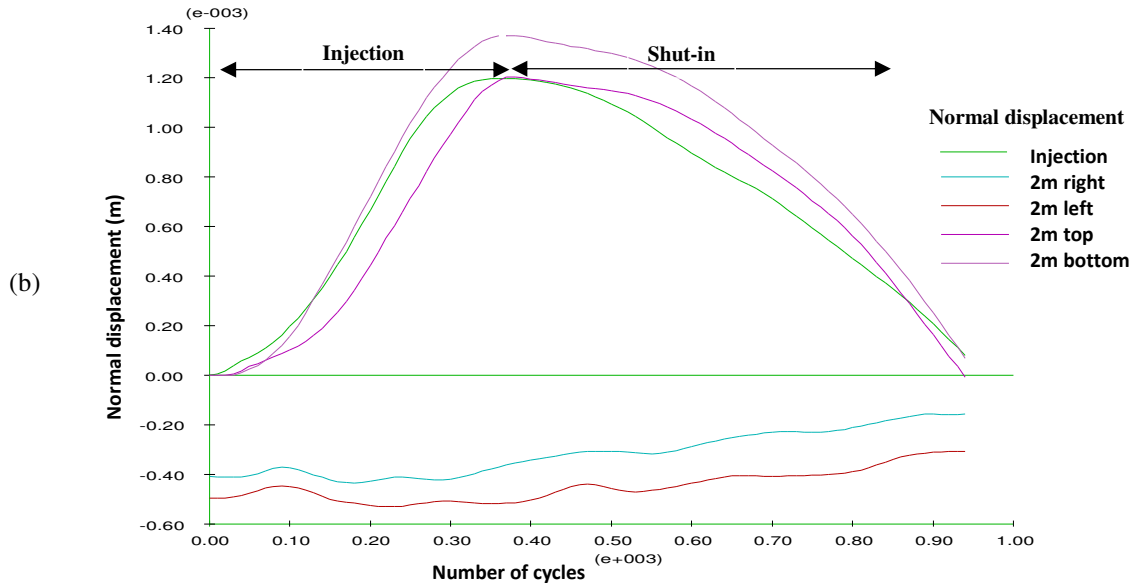
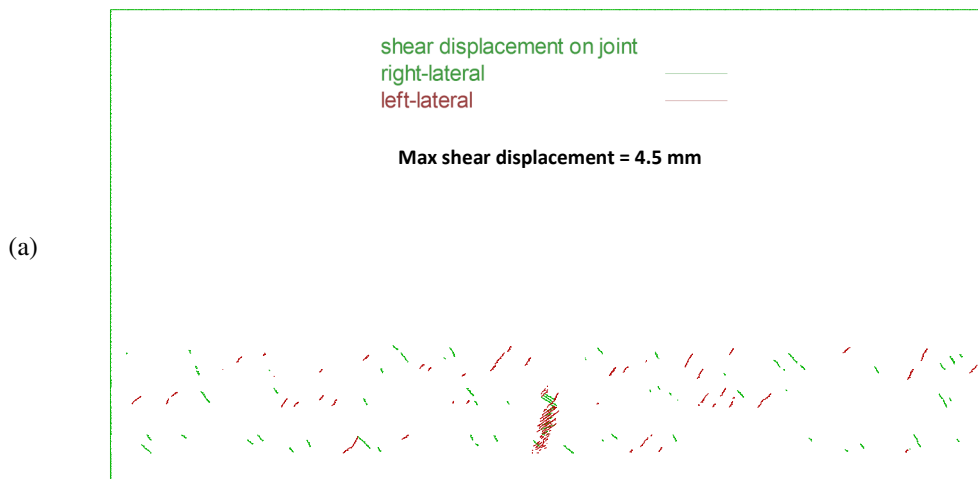


Figure 7.18. Normal displacement for five monitoring points during a) injection and b) shut-in, case B.

Figure 7.19 displays shear displacement during one cycle of operation. Shearing is dominantly growing vertically, which reflects the controlling role of principal stresses. More joints undergo shear displacement during shut-in both in the injection zone and surrounding layers. Fluid leak-off after injection seems to be increasing because fluid can more easily enter the surrounding sandstone layers, which are more permeable.



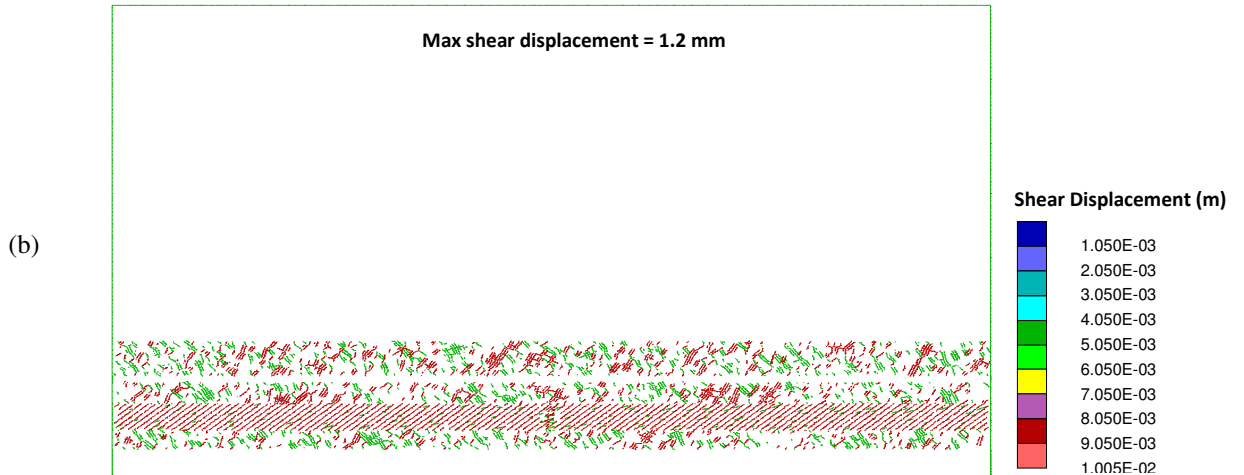


Figure 7.19. Joints undergo shear displacement during a) injection and b) shut-in, case B.

Results for three selected cycles of injection, among dozens analyzed, will be discussed. Figure 7.20 delineates defined effective zones around the injection point. Total joint displacements are calculated in these zones to see how they change with distance from the injection point. Figure 7.21a shows cumulative shear displacement. Total amount of shearing during shut-in is larger than during the injection phase, which is discussed in the previous section. Figure 7.21b shows cumulative magnitude of normal displacement. There is not much difference but this does not necessarily mean that all joints remained open. Joints located around the injection point tend to lose their aperture after injection; however, more distant joints undergo more permanent normal displacement. Hence, the total amount of normal displacement remained almost the same, but the spatial distribution changed.

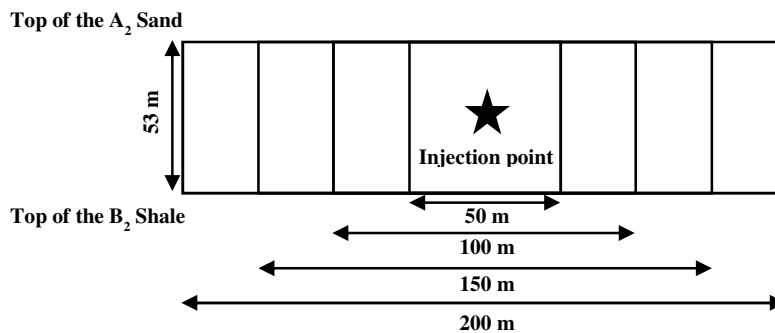


Figure 7.20. Effective zones around the injection point, case B.

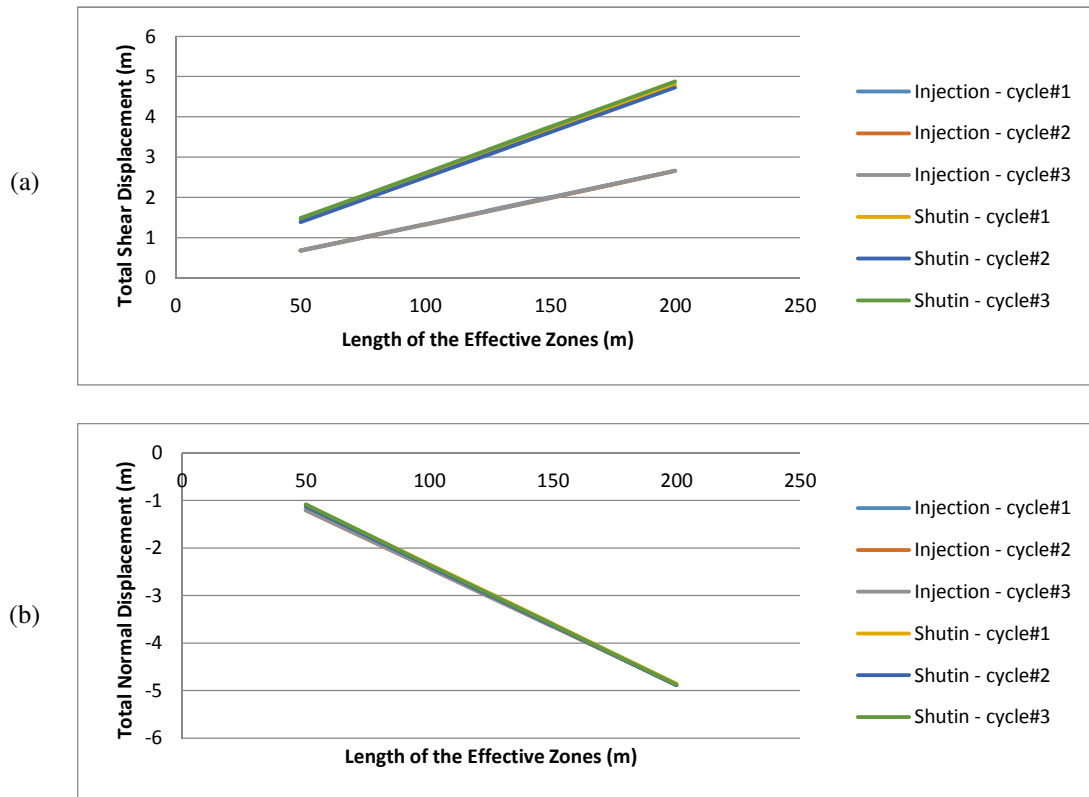


Figure 7.21. Cumulative a) closure and b) opening vs edge of effective zones for three cycles of injection and shut-in, case B.

7.4 UPGRADED MODELING APPROACH – CASE A

A new approach is introduced to find the best match between the numerical results and real data. The same fabric with similar model size as previously were generated for both methods (Figure 7.1 and Figure 7.3). The symmetry of the problem allows modelling of only one quarter of the space, permitting a scaling up the size of model by four times and giving information about a larger area around the injection point, which is always a benefit. Figure 7.22 shows the schematic of the generated model and injection points.

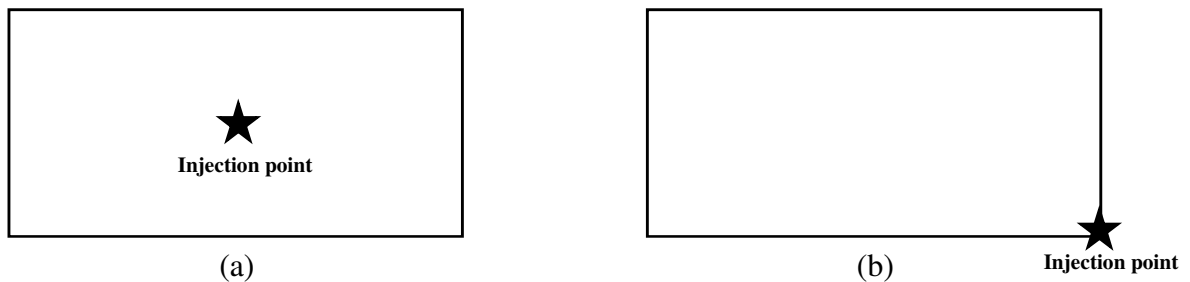


Figure 7.22. Schematic of the model and injection points.

It is understood that the case of symmetrical fracture behavior is approached only in homogeneous formations with constant physical parameters and in-situ stress. Here, the generated fabric is relatively homogenous in an attempt to maintain the simplicity of the work and therefore using symmetry is a robust assumption.

Transient flow is applied in the upgraded approach, which makes it possible to assign a real injection time to the system as opposed to a “scaled” time. Also, the transient flow is computationally no more demanding than a series of steady-state approximations. Comparing to the first approach, this method has the advantage that it leads to more realistic modeling scenarios as a real rate of injection is applied to the system (albeit adjusted for the 3rd dimension).

In UDECTM, injection rates are added up in the case of having multiple rates. Here there are three injection phases and injection rates which are determined, so that the first and last injection rates are known and the difference will give the injection rate for the second phase. However, in the case of having more than three injection phases, it would be challenging to find the right value of injection rate for each phase. From another aspect, these simulations are performed in a 2D framework and applying real values may not be very realistic, since one dimension is missing.

There are three main categories of properties that control results: Fluid properties and injection strategy, mechanical properties of joints and rock, and the geometry or natural fracture network. Changing any of these parameters will affect stress redistribution, which in turn leads to change in fracture aperture, and consequent changes in fluid pressure, which is the essence of hydro-mechanical coupling in a jointed system. An effect of fabric was discussed in the first attempt to emulate CRI operations. Effects of geomechanical properties are studied in this upgraded method and give more realistic realizations. Having constant fabric, fluid and rock properties leaves only changing the joint properties to achieve a better match. The properties of the new modeling configuration are listed in Table 7.3.

Table 7.3. Joint properties for the initial and upgraded models, case A.

Joint mechanical properties, initial model			Joint mechanical properties, upgraded model		
Normal stiffness	10	GPa/m	Normal stiffness	10	GPa/m
Shear stiffness	4	GPa/m	Shear stiffness	4	GPa/m
Friction angle	30	Degree	Friction angle	15	Degree
Cohesion	0.1	MPa	Cohesion	0.1	MPa
Dilation angle	10	Degree	Dilation angle	15	Degree

Figure 7.23 shows joints undergoing opening for one cycle of injection. Joints closer to the injection point undergo larger amount of displacement than those at farther distances. Figure 7.23b indicates that some joints remain open after shut-in and may slip as well, representing mix-mode fracturing (normal plus shear opening – or Mode I and Mode II).

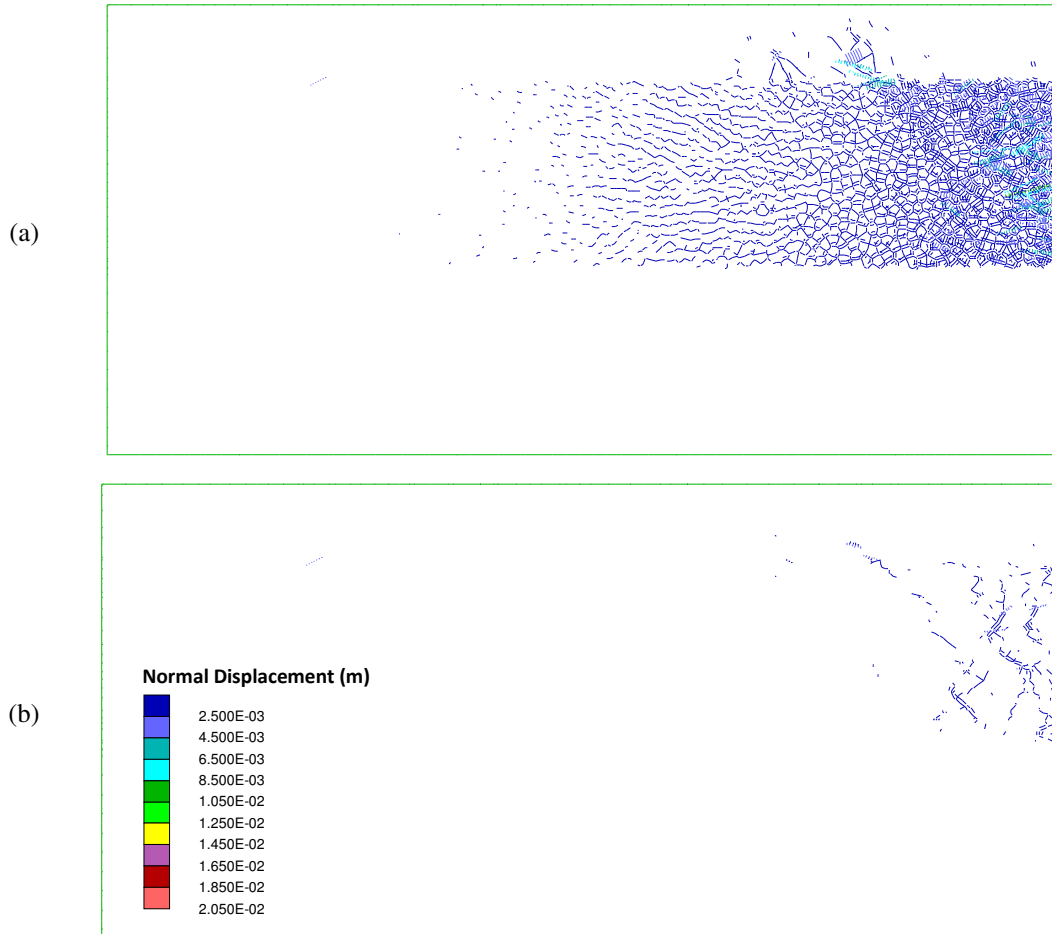
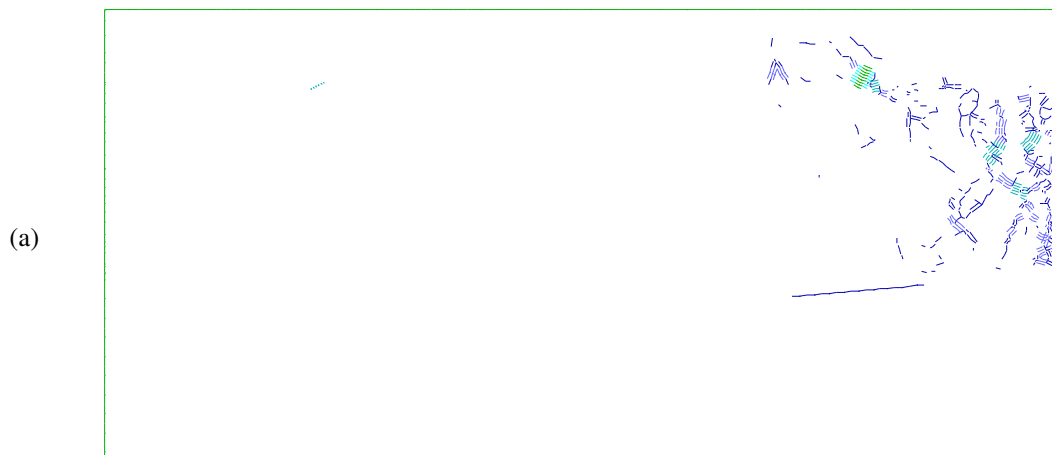


Figure 7.23. Joints undergo opening during a) injection and b) shut-in, case A.

Figure 7.24 shows joints that experience shear displacement during injection and shut-in for one cycle of operation. Although the magnitude of shear displacement is less than the normal displacement, the number of joints remaining sheared and dilated after shut-in is larger.



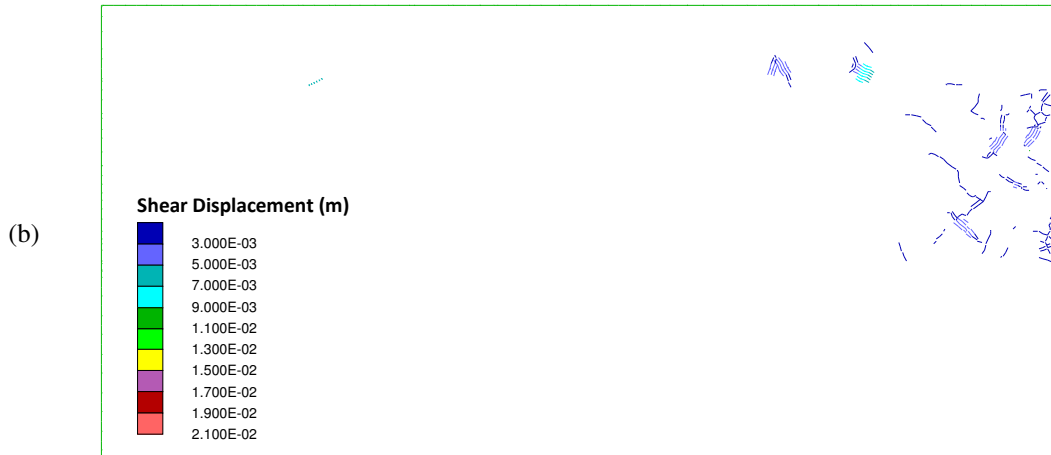


Figure 7.24. Joints undergo shearing during a) injection and b) shut-in, case A.

Figure 7.25 shows pore pressure distribution around the injection point during injection. It indicates pressure decreasing over distance from the injection point in a regular manner for a 2-D case.



Figure 7.25. Pore pressure distribution around the injection point, case A.

Figure 7.26 is one of the best realizations obtained from this approach for case A. It does not give a good match for the first phase of injection, which is probably because of the presence of the waste pod with different compressibility and permeability characteristics. Generally the pressure trend corresponds well with the real data for the later phases of injection and during shut-in.

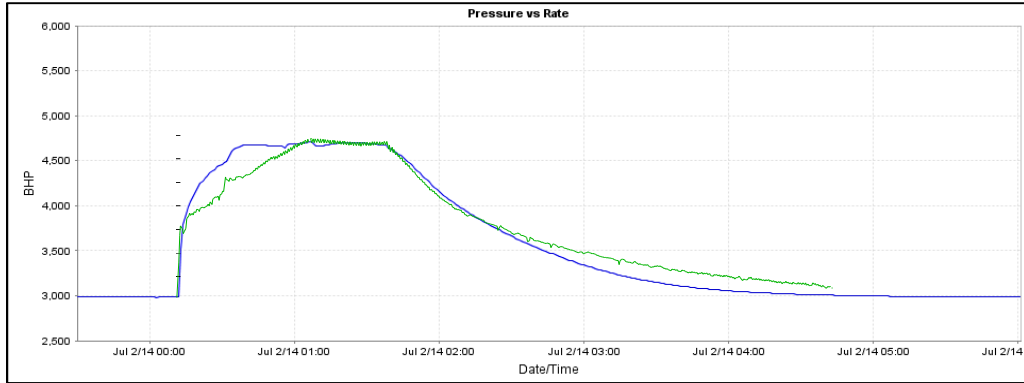


Figure 7.26. Matching numerical and real pressure curves using the upgraded approach, case A.

The waste pod is created over time in the nearwell zone and as it develops, there are changes in rock and joint properties within and around the waste pod. The waste pod development and growth is only one of the physical reasons for changes in the behavior of the system. Changes take place in the total and effective stresses (particularly in σ_{hmin}) associated with the volume changes, and stress changes take place at a substantially larger scale than the waste pod itself. Similarly, alterations in stiffness parameters and conductivity from joint dilation are partially permanent. It is too ambitious to attempt to emulate a time history for a process with an unstable set of parameters by defining only one initial condition to the model, even though the model is fully coupled. It is therefore suggested that in future analyses, redefinition of the model configuration should be done during the modeling to implement the changes in the system. This approach leads to a type of modeling called “interactive modeling” in this study.

There are different ideas of how to deal with evolving parameters to find a more realistic model and that is why this type of modeling is called “interactive modeling” in this study, as different approaches may be tried, all the while being guided by physics and reasonable expectations (experience). For example, another idea for upgrading this modeling approach is to apply changes of fluid flow capacity in the system by changing fracture apertures within the modeling process, between injection phases, which in turn changes the fluid pressure distribution. Changing boundary conditions or having a moving boundary conditions is also worth trying. Hydraulic fracturing for solid waste emplacement is a long-term and complex injection process and no parameter stays constant, so redefining what the model is facing in subsequent steps, guided all the time by the real data, is a reasonable strategy.

7.5 DISCUSSION

Understanding the response of rock masses to slurried solid waste injection has helped in interpreting data and optimizing processes in the field, despite the fact that the emulations shown here remain semi-quantitative in nature. For example, there is no real data about the large-scale fabric of natural fractures in the injection formations, and there is an absence of data other than the pressure-time-volume responses that are used. If other data would become available, such as

deformations (Dusseault and Rothenburg 2002), microseismic behavior and evolution (House et al. 1996) (Keck and Withers 1994) over many cycles, or even pressures in several offset wells, the emulations would be more rigorous and physically reasonable. But in general, companies tend to keep costs of waste disposal operations as low as possible because these activities do not generate revenue, so, other than p-Q-t, detailed monitoring data are unavailable.

The cases herein deal with clastic strata using a randomly jointed medium in a DEM formulation. However, technical management of slurried solid waste injection operations in fractured carbonate strata, currently occurring in the Middle East, is apparently quite different. The response of clastic sequence sediments such as the mudstones, siltstones and poorly consolidated fine-grained sandstones in the cases analyzed here, have proven difficult to extrapolate to naturally fractured carbonates with strong and stiff matrix blocks (personal communication, Bilak 2015). There is nevertheless a strong incentive to develop procedures that can consistently and reasonably reliably analyze injection and fall-off in such systems to avoid unexpected formation impairment and asset loss during waste disposal. Below, a comparison to standard well analysis software results is presented to show that the DEM approach seems to give far better results, but more work is needed. Prediction of the life-span of the rock mass around an injection well in terms of its ultimate capacity to accept solid and liquid waste safely is a largely unknown factor in fractured carbonates. DEM modeling, combined with a history of monitoring data and comparison to injection process modeling results in other cases, may help in making decisions about well life span and ultimate solids input capacity.

A conventional flow modeling package (PANTM) was used to provide comparative pressure matches for injection and shut-in periods. Figure 7.27 and Figure 7.28 show PANTM-generated and real data pressure matching respectively for the Middle East and North Sea fields. The injection approach used for each case study is different. In the Middle East field, injection is applied with a so-called “Direct Sand” injection approach (into a high-permeability zone) and for the North Sea field, the well is completed with a “bottom shale” injection approach (into a low-permeability zone). As shown in these figures, even with careful calibration, pressure matches are not particularly close to the original field pressure curves; although in the Middle East field the late time matches well with the shut-in curve. Standard well-test interpretation programs have some value as interpretive tools but they must be used consistently and with a great deal of caution, interpreted in a relative (comparative) manner rather than in an “absolute” manner. UDECTM software provides an additional tool to help understand processes and track the evolution of the properties of the process zone and waste pod. In these examples, reasonable matches were achieved for most of the injection periods and for the early shut-in period, which is a time of particular interest because of the development of the waste pods and their effects on formation behavior.

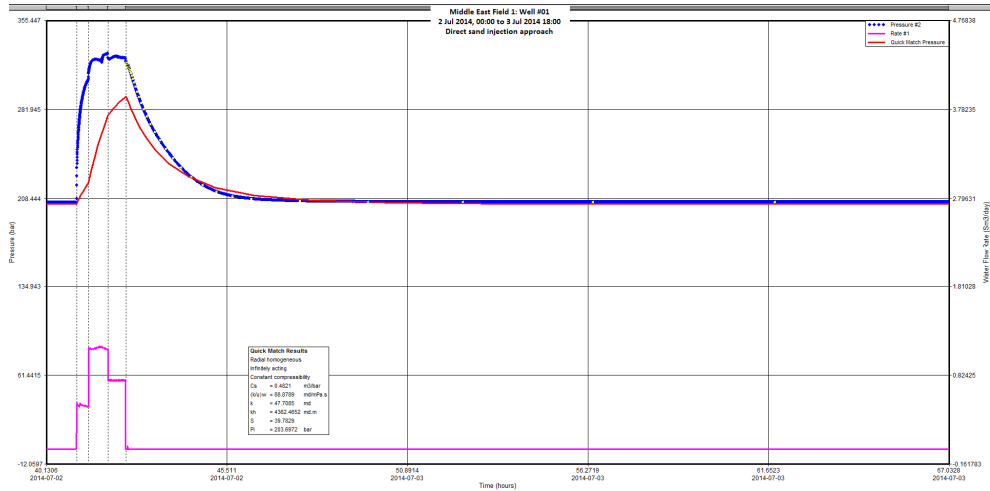


Figure 7.27. PAN pressure match during injection and shut-in for Middle East field.

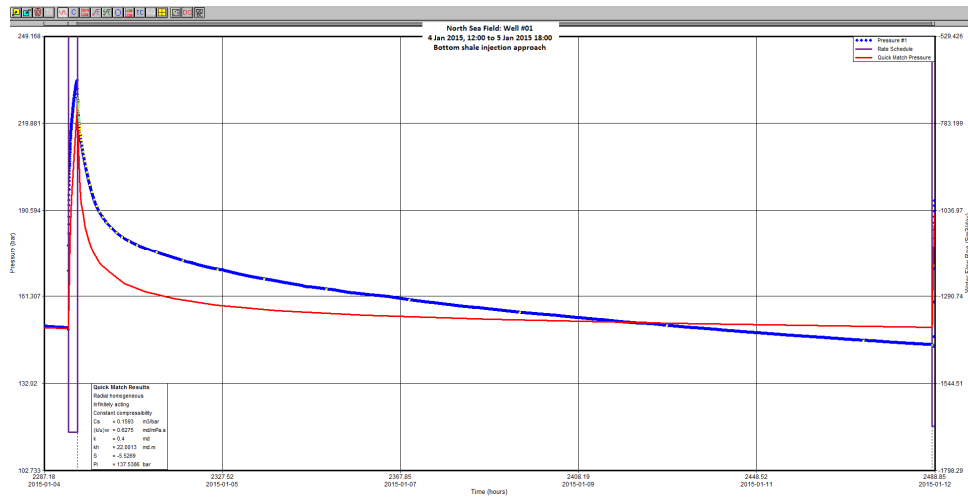


Figure 7.28. PAN pressure match during injection and shut-in for North Sea field.

7.6 SUMMARY

The analysis of pressure data from many cycles of two slurried solid waste injection operations has led to some observations. Caution is to be applied to the generalization of some of these, as it is recognized that the modeling and curve-fitting are highly empirical in nature, such that the term “emulation” is preferred to the term “simulation”.

- Induced fracture geometry is a function of pressure, fluid properties, volume of injected fluid, and injection time; also, it is a function of local lithostratigraphy and in-situ stresses; most importantly, local stresses and formation response (e.g. stiffness, leak-off response) will change with time and the number of injection cycles.

- At typical injection depths (generally 500-2000 m) and conditions, using a number of cycles of injection with a pressure dissipation period between each injection cycle, a waste pod of emplaced and compacted granular solid waste forms, grows, and makes the well response more complicated and difficult to predict because of changes in properties and in-situ conditions in a growing region.
- Fracture growth in the emulations presented for case A is constrained by impermeable boundaries with upper and lower formations in order to study mainly lateral fracture growth; reduction of such constraints is feasible if this would be deemed to be more representative of actual conditions in the ground.
- The lateral fracture growth can be estimated using the Discrete Element Method software modeling shown here, which gives some approximate information about the extent of the waste pod and the region of altered properties around the injection well.
- Both normal and shear displacements are responsible for joint deformations. Near the injection point, joints experience larger normal displacements, much of which is reversible after shut-in and pressure decay. More distant from the injection point, mostly shear displacement happens, and this leads to permanent flow channels (shear is irreversible, shear dilation only partly reversible), albeit on smaller effective aperture than the normal displacement mode fractures generated during injection.
- In the DEM model used here, fracture propagation may be asymmetrical due to fabric effects. In nature, asymmetrical effects would also be expected to arise because of natural and induced heterogeneities, but these cannot be specified at this stage of modeling.
- Conventional well-test software analysis has proven to be a difficult and somewhat unreliable way to assess pressure data and assess evolution of the waste pod and process zone; it must be used with caution and careful consistency. Such software has little capacity to simulate (or emulate) fracture-dominated and k-evolution behavior (included local redistribution of stresses), but the DEM software UDECTM seems to handle these effects more easily and to allow a better match to the real data.
- In particular, these emulations, although limited and without other corroborative data available, are considered more realistic than conventional well test approaches because of two factors: the explicit inclusion of stresses (hydro-mechanical coupling) and the assumption that the system response is dominated by the behavior of a network of natural fractures that are planes of weakness and channels for flow compared to the matrix blocks.

- Because DEM approaches appear more realistic and seem to give substantially better matches in these cases, they are likely to lead to a better interpretive tool for the evolutionary tracking of slurry injection operations.
- Although the upgraded method is more realistic at some levels than the first attempt, it does not necessarily provide the best approach. In other words, it may always be challenging to find the best approach and it changes from problem to problem. It also depends on the identified objectives and the required information.

Different geometries have been created and studied, but the presented geometries were those that obtained the best results. Also, a parametric study was carried out on the effects of joint conductivity factors, initial and residual aperture and joint stiffnesses. Results presented herein are those providing the best match and the rest omitted because of size constraints.

It is clear that there are no highly appropriate models in this process as the mechanics of fracturing is complex both in terms of fluid flow and mechanical deformation; there is no effective model that can handle the evolving conditions realistically. Therefore, the question is what models are best suited to model soft rock waste injection fracturing? DEM from a coupling stand point makes sense, and that is a spark. It is worth introducing UDECTM as a systematic analysis program that is able to allow intervention with the system parameters (and perhaps boundary conditions, initial lithostratigraphic disposition, and waste pod growth). As parameters are changing continuously in a way that we do not understand or are able to measure, we need a model that is as rigorous as possible to show compliance with the mechanics that we think are happening. This approach is called “interactive modeling” and it involves recalibrating (adjusting) a model to implement changes of the system or reasonable introversion to readjust the model based on new conditions of the system. It is a reasonable and feasible approach to redefine evolving parameters during modeling because the slurry injection episodes alter all properties and the initial conditions in a growing zone.

CHAPTER 8 DISCUSSION AND CONCLUSIONS

In analyzing flow and displacement in naturally fractured rocks, there are a number of sources of strong non-linearity, but hydro-mechanically coupled discrete block simulations can address some of these, and are helpful to understand NFR behavior. However, this understanding will likely remain semi-quantitative because of the various sources of parameters and fabric uncertainty. Some of the factors playing important roles in controlling the behaviour of natural fractures and NFRs include intensity of joints (number of joints per area in the case of this two-dimensional DEM model), geometric nature of the natural fractures, distribution of natural fractures with respect to the deviatoric stress field, the mechanical properties of these fractures, the magnitude of normal and differential stresses, and the presence of a single (or several) large through-going discontinuities such as a significant fault. For example, the presence of a fault, explored in Chapter 6, clearly showed a focus of shear displacement on this major feature. This can at once be seen as related to the possibility of fault re-activation and perhaps as less satisfactory to the implementation of hydraulic fracture stimulation in practice. These results indicate the importance of natural rock fabric delineation in practical cases. As such, results will have to be formulated and calibrated against real data in order to achieve engineering utility as predictive models.

An important point in a practical sense is that in a deviatoric stress field in a naturally fractured rock, even if the fabric itself is isotropic, injection with an increased pressure will induce anisotropy in the flow patterns because of the anisotropic dilation and shear of the joints in the differential stress field. This has implications on well test analyses, especially if Δp is large enough to start changing the apertures of the jointed rock mass. This clearly identifies a challenge for conventional well test interpretation in jointed rock masses.

Another important practical point is that in hydraulic fracturing for oil and gas well stimulation, it seems likely that different strategies are needed for optimizing results and generating a genuine geometry with high connectivity in cases of different rock fabrics and different absolute and relative principal stress values.

Using DEM-based modeling may contribute, among other areas, to the following:

- **Well design:** Well direction can be improved with regard to the critical orientation of the joints and their orientations with respect to the principal stresses.
- **Hydraulic conductivity of the rock mass:** Differential stresses and rock fabrics are two of the factors controlling the size of the stimulated zone. Part of the wider range of goals of this research on DEM modeling is to study if it is possible to simulate (or emulate) a network of hydraulic fractures that can link wells together. This may have particular importance, for example, in the case of vertical or inclined geothermal wells that must be explicitly linked together along their lengths.

- **Post-injection properties:** Investigating the effects of remnant displacements after shut-in on pressure distribution decay can help interpret stimulation interpretation, as well as help provide information relevant to jointed rock mass behavior and to solid waste injection operations.
- **Microseismic activity:** shear/slip events associated with hydraulic fracturing can be explored qualitatively by linking the slip locations to MS emissions.

8.1 CHAPTER SUMMARIES

8.1.1 PARAMETRIC STUDIES

One of the main objectives of the current research is to investigate how in-situ stresses affect the behaviour of hydraulically stimulated natural fractures. This objective has been addressed in chapters 4, 5 and 6, and based on these studies:

- Local natural fracture fabric affects hydraulically induced fracture direction, although the global orientation of hydraulic fracture growth remains normal to the minimum principal stress;
- Pore pressure distributes laterally under higher differential stresses and it becomes more radial closer to isotropic stress conditions. This is more obvious in the case of a more subdivided mesh (Voronoi tessellated rock fabric), and it even occurs under pressure increase without explicitly opening an hydraulic fracture in a jointed rock mass.
- Branching occurs at a short distance from the injection point. It is usually suppressed under a higher stress ratio and is more highly developed in the isotropic stress state;
- It is likely that there is a critical stress ratio that controls the dominant deformation mechanism.

In order to evaluate the effects of rock mass fabric on fluid flow and deformation, different geometries were generated and following are the understandings based on this work:

- Both joint normal and shear displacements drop with increasing intensity of discontinuities; however, this effect is smaller in models with persistent versus non-persistent discontinuities.
- The number of discontinuities inversely affects fluid pressure; in other words, the area in which injection fluid flows through joints decreases by increasing the number of discontinuities that can accept flow.

In general, natural fractures that can be reactivated (Mode I or Mode II) by stress changes will also have alterable mechanical properties that will lead to different behaviour in shearing, opening, sliding or closing in reaction to stress redistributions and injection cycles. In order to evaluate the effects of rock mass fabric on fluid flow and deformation, different geometries were

generated. Based on this study, results can be compared for different fabrics in terms of intensity and persistency:

- Both joint normal and shear displacements drop with increasing intensity of discontinuities; however, this effect is smaller in models with persistent versus non-persistent discontinuities.
- The number of discontinuities inversely affects fluid pressure; in other words, the area in which injection fluid flows through joints decreases by increasing the number of discontinuities that can accept flow.

8.1.2 STIMULATED ZONE ASSOCIATED WITH HYDRAULIC FRACTURING IN LOW-PERMEABILITY ROCKS

Chapter 5 addresses another objective of this study, which is evaluating the size of the stimulated zone associated with hydraulic fracturing. Opening pre-existing joints in NFRs by hydraulic fracturing will also lead to shear slip and dilation, affecting the flow behavior. This implies that in a real case, shear dilatation is a mechanism of increasing permeability in a NFR. A means to determine the stimulated area of a HF treatment from UDECTM was developed in this study and more insight into the response of NFRs to hydraulic stimulations was achieved:

- In the presence of one or more persistent joint sets, there would be a preferential direction(s) for fluid to travel, making the stimulation pattern and extent more complicated.
- If a dominant inclination of joints does not match with σ_{min} orientation, they will grow along all directions. Under isotropic stress conditions, there does not exist a preferential fracture propagation direction. However, in the presence of naturally existing joint sets, the hydraulic fractures will orient preferentially along the existing joint set(s), altering the shape of the stimulated zone.
- Joints undergo larger opening than shearing for all geometries. In the case of cross-joints and cross-cuts rock fabrics, larger displacements occur than for a Voronoi tessellated rock fabric. Thus strongly oriented joints affect both magnitude of the deformations and size of the stimulated area.
- Injection rate does not change the general trend of fracture propagation but locally affects the stimulation. Joint deformation is affected more by stress ratio under lower injection rates. Higher injection rates cause higher fluid pressure and stimulate more joints because the fluid has enough pressure to overcome the normal stress even in unfavorable directions. Therefore, the effect of stress ratio would be less noticeable at high rates than at low rates.

8.1.3 NUMERICAL INVESTIGATION OF SHEAR/SLIP EVENTS ASSOCIATED WITH HYDRAULIC FRACTURING

Energy release events result from stress and pressure changes induced by the fracturing treatment and shear displacements are used to calculate moment magnitude, considered equivalent to a seismic moment. The size and strength of these energy release events can be calculated from seismic moment considerations and this provides indications about the total mechanical work and the amount of released “seismic” energy. Evaluating energy release from deviatorically stressed rock masses may provide some insight into the magnitude and distribution of induced seismicity during HF and potentially help to develop strategies to manage the seismicity. This objective of the thesis is studied in chapter 6 and the following are some preliminary observations from these calculations:

- Hydraulic fracturing normally creates small magnitude slip events that have magnitudes less than zero (from the literature).
- The size of the shear event depends on the in-situ stress conditions, such that under higher differential stresses, larger events are more likely.
- The amount of seismic energy is small relative to the overall work done to generate the opening and dilatant distortions in the rock mass.
- Although normal displacement is the main deformation mechanism in all simulations, it is mostly shear displacement that controls the magnitude of the energy release and thus the energy dissipation fraction.

8.1.4 A DISCRETE ELEMENT METHOD APPROACH TO MODEL WASTE INJECTION OPERATIONS

An empirical calibration of numerical results is another objective of the current study, which is performed by the modelling and analysis of waste injection operations, as reported in chapter 7. Better insight into the changes taking place in a naturally fractured rock mass is acquired by the calibration of discrete element models to pressure-time curve field data. This study provides the following understandings:

- Hydraulic fracture geometry is a function of pressure, fluid properties, volume of injected fluid and injection time; also, it is a function of local lithostratigraphy and in-situ stresses. Most importantly, local stresses and formation response change with time and the number of injection cycles.
- At typical injection depths (generally 500-2000 m) and conditions, subsequent cycles of injection with a pressure dissipation time between each cycle allow the waste pod to form, grow and this makes the joint responses more complicated to predict.
- The occurrence of different fall-off rates also indicates the presence of zones with different aperture and permeabilities; i.e. multiple flow systems are evident and evolving.

- Normal and shear displacements are both responsible for joint deformations; however, the magnitude and size of the stimulated zone are also important. Near the injection point, joints experience larger normal displacements, much of which is reversible after shut-in and pressure decay. Shear displacement occurs most often farther from the injection point and this leads to permanent flow channels (shear is irreversible, shear dilation only partly reversible).
- Fracture propagation may be asymmetric due to fabric effects.
- Conventional well-test software is a difficult and somewhat unreliable way to assess or match data and thereby assess the evolution of the waste pod and process zone and must be used with caution and careful consistency. Such software has little capacity to simulate (or emulate) fracture-dominated and k-evolution behavior (which includes the local redistribution of stresses), but UDECTM appears to model these effects somewhat more easily and better matches to the real data can be achieved.
- As DEM approaches become more realistic and give better matches as time moves on, they are likely to lead to the development of a better interpretive tool.

8.2 FURTHER RESEARCH

8.2.1 THREE-DIMENSIONAL MODELING

3DECTM is a more sophisticated analysis tool that can model three-dimensional operations in a discrete element mode. It possesses some ability to simulate fluid flow in joints with a degree of thermal and mechanical coupling that makes it an appropriate software to cover certain parts of this study. However, 3DECTM is computationally laborious and requires significantly more running time than UDECTM for large problems, and therefore was not used in this study.

8.2.2 THERMO-HYDRO-MECHANICAL COUPLING

Since cold water may be injected during the hydraulic fracturing treatment process and circulated for long durations after interconnected joint networks are generated, stress redistribution effects on joint aperture should be modeled, and in some cases it may be important to include aspects of rock weakening through thermoelastic stress transfer and compressive yielding. This may especially be the case in geothermal energy development and massive waste water injection operations.

8.2.3 EVALUATING THE ROCK STIFFNESS (BULK ELASTIC PROPERTIES)

Hydraulic fracturing (HF) is a strong candidate technology to implement stress management in several ways. First, rock mass stiffness modification can be achieved by introducing more compliant flaws; second, by using HF one may create a permeable network that can be used to heat, cool, or change the pore pressure in the affected rock region; third,

judicious use of HF in one well within an array of wells may lead to a relief of shear stress at a defined scale, reducing the risk of a larger-magnitude stick-slip event; fourth, given an array of wells (for geothermal development for example), it may be feasible to operate the wells in such a manner as to redistribute or relieve stress deliberately through cyclic injection or deliberate rotations among wells in the array. In order to develop a stress management program in a jointed rock mass, such as in the fractured rock mass around a mine in igneous rock, stiffness changes arising from more compliant flaws should be evaluated as a means of reducing the amount of strain energy that can be stored as mining progresses.

8.2.4 JOINT CONDUCTIVITY

Connectivity of joints plays a prominent role in the deformability and permeability of naturally fractured rock masses. Joint connectivity is mostly controlled by joint density and therefore so are deformation and permeability. Connectivity may be described by a fractal dimension and a power law may be used to characterize the relationship between the connectivity and joint density which also describes its relationship with deformation and permeability. Note that joint density should be considered above a critical value known as the percolation threshold for simple flow problems (though this may be affected by hydraulic fracture). According to the study by Zhang and Sanderson (1994), the fractal dimension of a critical joint cluster is dominated by joint density and is largely independent of other geometrical parameters. Therefore, the use of fractal dimensions to make the model less sensitive to geometric parameters (orientation and size of joints) is an important area of study. In addition, these models could be scale-invariant and provide some ability to generalize results and find more universal property behaviors of joints (Zhang and Sanderson 1994). This is a version of up-scaling, which seems to be an important area to pursue in understanding NFRs.

BIBLIOGRAPHY

- Abercrombie, R.E. 1995. Earthquake Source Scaling Relationships from -1 to 5 ML using Seismograms Recorded at 2.5 km Depth. *Journal of Geophysics Research*, **100**(B12).
- Abercrombie, R.E., and Rice, J.R. 2005. Can Observations of Earthquake Scaling Constrain Slip Weakening? *Geophysical Journal International*, **162**. doi:10.1111/j.1365-246X.2005.02579.x.
- Adachi, J., Siebrits, E., Peirce, A., and Desroches, J. 2007. Computer Simulation of Hydraulic Fractures. *International Journal of Rock Mechanics and Mining Sciences*, **44**(5). doi:10.1016/j.ijrmms.2006.11.006.
- Aki, K. 1967. Scaling Law of Seismic Spectrum. *Journal of Geophysical Research*, **72**(4): 1217–1231. doi:10.1029/JZ072i004p01217.
- Arfie, M., Marika, E., Elwin, S., and W.A., H. 2005. Implementation of Slurry Fracture Injection Technology for E & P Wastes at Duri Oilfield. *In* SPE Asia Pacific Health, Safety and Environment Conference and Exhibit. Kuala Lumpur, Malaysia. pp. 1–14.
- Asgian, M. 1989. A numerical model of fluid-flow in deformable naturally fractured rock masses. *International Journal of Rock Mechanics and Mining Sciences & Geomechanics Abstracts*, **26**(3–4): 317–328. doi:http://dx.doi.org/10.1016/0148-9062(89)91980-3.
- Atkinson, G.M., Ghofrani, H., and Assatourians, K. 2015. Impact of Induced Seismicity on the Evaluation of Seismic Hazard: Some Preliminary Considerations. *Seismological Research Letters*, **86**(3): 1009–1021. doi:10.1785/0220140204.
- Baan, M. Van Der, Eaton, D., and Dusseault, M. 2013. Microseismic Monitoring Developments in Hydraulic Fracture Stimulation. *In* Effective and Sustainable Hydraulic Fracturing.
- Bagheri, M.A., and Settari, A. 2006. Modeling fluid flow in deformable fractured reservoirs using full tensor permeability. *Golden Rocks 2006, The 41st US Symposium on Rock Mechanics (USRMS)*,.
- Bandis, S.C., Lumsden, A.C., and Barton, N.R. 1983. Fundamentals of rock joint deformation. *International Journal of Rock Mechanics and Mining Sciences and*, **20**(6): 249–268. doi:10.1016/0148-9062(83)90595-8.
- Bartko, K., Al-shobaili, Y., Gagnard, P., Warlick, M., Im, A.B., and Aramco, S. 2009. Drill Cuttings Re-Injection (CRI) Assessment for the Manifa Field : An Environmentally Safe and Cost-Effective Drilling Waste Management Strategy. *In* SPE 126077.
- Batchelor, G.K. 1967. *An Introduction to Fluid Dynamics*. Cambridge University Press.
- BC Oil and Gas Commission (BCOGC). 2012. Investigation of Observed Seismicity in the Horn River Basin : British Columbia Oil and Gas Commission open report.
- Belytschko, T., Liu, W., Moran, B., and Elkhodary, K.I. 2000. Nonlinear Finite Elements for Continua and Structures. *In* Wiley. Wiley. doi:10.1016/S0065-230X(09)04001-9.

- Blanton, T. 1982. An Experimental Study of Interaction Between Hydraulically Induced and Pre-Existing Fractures. Proceedings of SPE Unconventional Gas Recovery Symposium, 559–571. doi:10.2118/10847-MS.
- Board, M. 1989. UDEC-Universal Distinct Element Code, Version ICG1.5, Software Summary. *In* ITASCA Consulting Group Inc.
- Bormann, P., and Di, D. 2011. The moment magnitude M_w and the energy magnitude M_e : common roots and differences. *Journal of Seismology*, **15**: 411–427. doi:10.1007/s10950-010-9219-2.
- Boroumand, N., and Eaton, D. 2012. Comparing energy calculations: Hydraulic fracturing and microseismic monitoring. *In* 74th EAGE Conference and Exhibition incorporating SPE EUROPEC 2012, Copenhagen, Denmark. pp. 1–4. doi:10.3997/2214-4609.20148187.
- Bui, T. 2010. Explicit and Implicit Methods In Solving Differential Equations. University of Connecticut.
- Candela, T., Renard, F., Bouchon, M., Schmittbuhl, J., and Brodsky, E.E. 2011. Stress Drop during Earthquakes: Effect of Fault Roughness Scaling. *Bulletin of the Seismological Society of America*, **101**(5): 2369–2387. doi:10.1785/0120100298.
- Carles, B.P. 2014. Discrete element simulations with LIGGGHTS. Swansea University.
- Cengel, A., and Cimbala, J. 2006. Fluid mechanics: Fundamentals And Applications. International Edition, McGraw Hill Publication, 1–2023.
- Chapra, S.C., and Canale, R.P. 2015. Numerical methods for engineers. *Mathematics and Computers in Simulation*, **33**(3): 260. doi:10.1016/0378-4754(91)90127-O.
- Choy, G.L., Boatwright, J.L., Survey, U.S.G., and Park, M. 1995. Global patterns of radiated seismic energy and apparent stress. *Journal of Geophysical research*, **100**(B9): 18205–18228.
- Cipolla, C., Maxwell, S., and Mack, M. 2012. Engineering Guide to the Application of Microseismic Interpretations. *In* SPE Hydraulic Fracturing Technology Conference, The Woodlands, Texas, USA. The Woodlands, Texas, USA. doi:http://dx.doi.org/10.2118/152165-MS.
- Cipolla, C.L., Warpinski, N.R., and Mayerhofer, M.J. 2013. Hydraulic Fracture Complexity: Diagnosis, Remediation, And Exploitation. SPE Asia Pacific Oil and Gas Conference and Exhibition, (October): 20–22. doi:10.2118/115771-MS.
- Cundall, P.A. 1971. A computer model for simulating progressive large-scale movements in blocky rock system. *In* Proceedings of International Symposium on Rock Mechanics (ISRM). Nancy, France. pp. 128–132.
- Curtis, J.B. 2002. Fractured shale-gas systems. *AAPG Bulletin*, **11**(11): 1921–1938.
- Damjanac, B., Gil, I., Pierce, M., and Sanchez, M. 2010. A New Approach to Hydraulic

- Fracturing Modeling in Naturally Fractured Reservoirs. 44th US Rock Mechanics Symposium,: 7.
- Daneshy, A. 2010. Hydraulic Fracturing To Improve Production. The way ahead, **6**(3): 14–17.
- Davies, R., Foulger, G., Bindley, A., and Styles, P. 2013. Induced seismicity and hydraulic fracturing for the recovery of hydrocarbons. *Marine and Petroleum Geology*, **45**: 171–185. Elsevier. doi:10.1016/j.marpetgeo.2013.03.016.
- Demirdzic, I., Ivankovic, A., and O’Dowd, N. 2005. Computational Continuum Mechanics (CCM). Lecture Note.
- Dusseault, M., and Jackson, R. 2013. Seepage pathway assessment for natural gas to shallow groundwater during well stimulation, production and after abandonment. CNC/IAH Conference, **3**(3): 8. doi:10.1306/eg.04231414004.
- Dusseault, M.B. 2011. Geomechanical challenges in petroleum reservoir exploitation. *KSCE Journal of Civil Engineering*, **15**(4): 669–678. doi:10.1007/s12205-011-0007-5.
- Dusseault, M.B. 2013. Geomechanical aspects of shale gas development. *In Rock Mechanics for Resources, Energy and Environment*. CRC Press, London. pp. 39–56.
- Dusseault, M.B. 2015. Geomechanics in Shale Gas Development. *In Geotechnical Synergy in Buenos Aires*. IOS Press.
- East, L., Soliman, M.Y., and Augustine, J. 2011. Methods for Enhancing Far-Field Complexity in Fracturing Operations. *In SPE Production & Operations*. Florence, Italy. doi:10.2118/133380-PA.
- Economides, M.J., and Nolte, K.G. 2013. Summary for Policymakers. *In Third*. Wiley New York, Cambridge.
- Farahbod, A.M., Kao, H., Walker, D.M., and Cassidy, J.F. 2015. Investigation of Regional Seismicity Before and After Hydraulic Fracturing in the Horn River Basin , Northeast British Columbia. *Canadian Journal of Earth Sciences*,. doi:10.1139/cjes-2014-0162.
- Favier, L., Daudon, D., Donzé, F.-V.F.-V., and Mazars, J. 2009. Predicting the drag coefficient of a granular flow using the discrete element method. *Journal of Statistical Mechanics: Theory and Experiment*,. doi:10.1088/1742-5468/2009/06/P06012.
- Fish, J., and Belytschko, T. 2007. A First Course in Finite Elements. *In Wiley*. Wiley. doi:10.1002/9780470510858.
- Fjaer, E., Holt, R.M., Horsrud, P., Raaen, A.M., and Risnes, R. 2008. Petroleum Related Rock Mechanics. *In second*. Elsevier.
- Fomin, S., Chugunov, V., and Hashida, T. 2006. Assessment of Stimulated Area Growth During High-Pressure Hydraulic Stimulation of Fractured Subsurface Reservoir. *Transport in Porous Media*, **63**(1): 99–125. doi:10.1007/s11242-005-3326-5.
- Gale, J.F.W., Reed, R.M., and Holder, J. 2007. Natural fractures in the Barnett Shale and their

- importance for hydraulic fracture treatments. *AAPG Bulletin*, **91**(4): 603–622. doi:10.1306/11010606061.
- Geertsma, J., and De Klerk, F. 1969. A Rapid Method of Predicting Width and Extent of Hydraulically Induced Fractures. *Journal of Petroleum Technology*, **21**: 1571–1581. doi:10.2118/2458-PA.
- Ghazvinian, E., and Kalenchuk, K. 2016. Application of 3D Random Voronoi Tessellated Models for Simulation of Hydraulic Fracture Propagation within the Distinct Element Formulation. 50th US Rock Mechanics / Geomechanics Symposium held in Houston, Texas, USA, 26-29 June 2016,.
- Gil, I., Nagel, N., and Sanchez-nagel, M. 2011. The Effect of Operational Parameters on Hydraulic Fracture Propagation in Naturally Fractured Reservoirs – Getting Control of the Fracture Optimization Process. *In American Rock Mechanics Association (ARMA)*.
- Guo, Q., and Geehan, T. 2004. An Overview of Drill Cuttings Re-Injection – Lessons Learned and Recommendations. *In 11th International Petroleum Environmental Conference*.
- Hainey, B.W., Keck, R.G., Smith, M.B., Lynch, K.W., and Barth, J.W. 1999. On-site Fracturing Disposal of Oilfield- Waste Solids in Wilmington Field, California. *In SPE 56070, SPE Production and Facilities*. doi:10.2118/38255-MS.
- Hanks, T.C. 1977. Earthquake Stress Drops, Ambient Tectonic Stresses and Stresses that Drive Plate Motions. *Pure and Applied Geophysics PAGEOPH*, **115**(1-2): 441–458. doi:10.1007/BF01637120.
- Hanks, T.C., and Kanamori, H. 1979. A Moment Magnitude Scale. *Journal of Geophysical research*, **84**(9): 2348–2350.
- Hart, R.D. 1991. An Introduction to Distinct Element Modeling for Rock Engineering. *ISRM, 7th Congress*,. doi:10.1017/CBO9781107415324.004.
- Hofmann, H., Babadagli, T., and Zimmermann, G. 2014. Numerical Simulation of Complex Fracture Network Development by Hydraulic Fracturing in Naturally Fractured Ultratight Formations. *Journal of Energy Resources Technology*, **6**. doi:10.1115/OMAE2013-11084.
- Hofmann, H., Yoon, J.S., Zang, A., Blöcher, G., Zimmermann, G., and Babadagli, T. 2015. A New Hybrid Simulation Approach to Evaluate the Efficiency of Hydraulic Stimulation Treatments. *In World Geothermal Congress, Melbourne, Australia, 19-25 April 2015*. pp. 19–25.
- Holland, A. 2011. Examination of Possibly Induced Seismicity from Hydraulic Fracturing in the Eola Field , Garvin County, Oklahoma. *Oklahoma Geological Survey, Open-File Report*.
- Hossain, M.M., Rahman, M.K., and Rahman, S.S. 2000. Hydraulic Fracture Initiation and Propagation: Roles of Wellbore Trajectory, Perforation and Stress Regimes. *Journal of Petroleum Science and Engineering*, **27**(3-4): 129–149. doi:10.1016/S0920-4105(00)00056-5.

- Hossain, M.M., Rahman, M.K., and Rahman, S.S. 2002. A Shear Dilation Stimulation Model for Production Enhancement From Naturally Fractured Reservoirs. SPE 78355, (January): 1–4.
- Hudson, J.A., and Harrison, J.P. 1997. Engineering Rock Mechanics: An Introduction to the Principles. In E. Elsevier Ltd. doi:10.1016/B978-008043864-1/50021-5.
- Ide, S., Beroza, G.C., Prejean, S.G., and Ellsworth, W.L. 2003. Apparent break in earthquake scaling due to path and site effects on deep borehole recordings. Journal of Geophysics Research, **108**(B5). doi:10.1029/2001JB001617.
- ITASCA Consulting Group Inc. 2010. UDEC-Universal Distinct Element Code, Version 5.0, User's Manual. Minneapolis, MN: ICG. Itasca.
- Jaeger, J.C., Cook, N.G.W., and Zimmerman, R.W. 2007. Fundamentals of Rock Mechanics. Blackwell Publishing Ltd. doi:10.1017/CBO9781107415324.004.
- Jeffrey, R.G., Zhang, X., and Bunger, A.P. 2010a. HYDRAULIC FRACTURING OF NATURALLY FRACTURED RESERVOIRS.
- Jeffrey, R.G., Zhang, X., and Bunger, A.P. 2010b. Hydraulic Fracturing of Naturally Fractured Reservoirs. In Thirty-Fifth Workshop on Geothermal Reservoir Engineering. Stanford University, Stanford, California.
- Ji, L., Settari, A., and Sullivan, R.B. 2009. A Novel Hydraulic Fracturing Model Fully Coupled With Geomechanics and Reservoir Simulation. SPE Journal, **14**(03): 423 – 430. doi:10.2118/110845-PA.
- Jing, L. 2003. A Review of Techniques, Advances and Outstanding Issues in Numerical Modelling for Rock Mechanics and Rock Engineering. International Journal of Rock Mechanics and Mining Sciences, **40**(3): 283–353. doi:10.1016/S1365-1609(03)00013-3.
- Jing, L., and Hudson, J.A. 2002. Numerical methods in rock mechanics. International Journal of Rock Mechanics and Mining Sciences, **39**(4): 409–427. doi:10.1016/S1365-1609(02)00065-5.
- Jing, L., and Stephansson, O. 2007. Fundamentals of Discrete Element Methods for Rock Engineering: Theory and Applications. Elsevier Science. doi:10.1016/S0165-1250(07)85017-6.
- Johri, M., and Zoback, M.D. 2013. The Evolution of Stimulated Reservoir Volume during Hydraulic Stimulation of Shale Gas Formations. In Unconventional Resources Technology Conference, Denver, Colorado. Society of Exploration Geophysicists, American Association of Petroleum Geologists, Society of Petroleum Engineers. doi:10.1190/urtec2013-170.
- Kanamori, H. 1983. Magnitude Scale and Quantification of Earthquakes. Tectonophysics, **93**: 185–199.
- Kanamori, H. 2001. Energy Budget of Earthquakes and Seismic Efficiency. In Earthquake thermodynamics and phase transformations in the Earth's interior. Academic Press.

- Kanamori, H., and Anderson, D. 1975. Theoretical Basis of some Empirical Relations in Seismology. *Bulletin of the Seismological Society of America*, **65**(5): 1073–1095.
- Kanamori, H., and Brodsky, E.E. 2004. The Physics of Earthquakes. *In* Institute of Physics Publishing. doi:10.1088/0034-4885/67/8/R03.
- Kazerani, T., and Zhao, J. 2010. Micromechanical parameters in bonded particle method for modelling of brittle material failure. *International Journal for Numerical and Analytical Methods in Geomechanics*,. doi:10.1002/nag.
- Keck, R. 2002. Drill Cuttings Injection: A Review of Major Operations and Technical Issues. *Proceedings of SPE Annual Technical Conference and Exhibition*,: 1–12. doi:10.2523/77553-MS.
- Keilich, W. 2009. Numerical Modelling of Subsidence, Upsidence and Valley Closure Using UDEC. University of Wollongong.
- Khrstianovic, S.A., and Zheltov, Y.P. 1955. Formation of Vertical Fractures by Means of Highly Viscous Liquid. *In* 4th World Petroleum Congress. Rome, Italy.
- Koshelev, V.F., and Ghassemi, A. 2003. Hydraulic Fracture Propagation Near a Natural Discontinuity. *Twenty-Eight Workshop on Geothermal Reservoir Engineering*,: 8.
- Kulhawy, F.H. 1975. Stress Deformation Properties of Rock and Rock Discontinuities. *Engineering Geology*, **9**(4): 327–350. doi:10.1016/0013-7952(75)90014-9.
- Ladubec, C., Gracie, R., and Craig, J. 2015. Geometric Numerical Integration for Complex Dynamics of Tethered Spacecraft. *International Journal for Numerical Methods in Engineering*, **102**: 316–331. doi:10.1002/nme.
- Legarth, B., Huenges, E., and Zimmermann, G. 2005. Hydraulic fracturing in a sedimentary geothermal reservoir: Results and implications. *International Journal of Rock Mechanics and Mining Sciences*, **42**(7-8 SPEC. ISS.): 1028–1041. doi:10.1016/j.ijrmmms.2005.05.014.
- Lemos, J. V. 2012. Recent developments and future trends in distinct element methods— UDEC/3DEC and PFC codes. *In* *Advances in Discontinuous Numerical Methods and Applications in Geomechanics and Geoen지니어ing*.
- Lisjak, A., and Grasselli, G. 2014. A review of discrete modeling techniques for fracturing processes in discontinuous rock masses. *Journal of Rock Mechanics and Geotechnical Engineering*, **6**(4): 301–314. Elsevier Ltd. doi:10.1016/j.jrmge.2013.12.007.
- Luding, S. 2008. Introduction to Discrete Element Methods: Basic of Contact Force Models and How to Perform the Micro-macro Transition to Continuum Theory. *European Journal of Environmental and Civil Engineering*,. doi:10.3166/ejece.12.785-826.
- Madariaga, R. 1979. On the Relation Between Seismic Moment and Stress Drop in the Presence of Stress and Strength Heterogeneity. *Journal of Geophysical Research*, **84**(B5).
- Marika, E., Asa, S., and Bilak, R. 2009. Achieving Zero Discharge E & P Operations using Deep

Well Disposal. *In* World Heavy Oil Congress.

- Mase, G., and Mase, G. 2009. Continuum Mechanics for Engineers. *In* CRC Press, Third Edit. CRC Press LLC. doi:http://dx.doi.org/10.1016/0020-7683(79)90025-8.
- Maxwell, S. 2013. Unintentional Seismicity Induced by Hydraulic Fracturing. CSEG RECORDER, **38**(8): 40–49.
- Mccalpin, J.P. 2009. Earthquake Magnitude Scales. *In* Paleoseismology. Academic Press.
- Mcgarr, A. 2002. Case Histories of Induced and Triggered Seismicity. *In* International Handbook of Earthquake and Engineering Seismology. *Edited by* and C.K. W.H.K. Lee, H. Kanamori, P. Jennings. pp. 0–12.
- McLennan, J., Tran, D., Zhao, N., Thakur, S., Deo, M., Gil, I., and Damjanac, B. 2010. Modeling Fluid Invasion and Hydraulic Fracture Propagation in Naturally Fractured Rock : A Three-Dimensional Approach. 2010 SPE International Symposium and Exhibition on Formation Damage Control, Lafayette, Louisiana, USA, 10-12 February.,: 1–13.
- Min, K.-B., Rutqvist, J., Tsang, C.-F., and Jing, L. 2004. Stress-Dependent Permeability of Fractured Rock Masses : A Numerical Study. International Journal of Rock Mechanics & Mining Sciences,.
- Moschovidis, Z., Steiger, R., Peterson, R., Warpinski, N., Wright, C., Chesney, E., Hagan, J., Abou-Sayed, A., Keck, R., Frankl, M., Fleming, C., Wolhart, S., McDaniel, B., Sinor, A., Ottesen, S., Miller, L., Beecher, R., Dudley, J., Zinno, D., and Akhmedov, L. 2000. The Mounds Drill-Cuttings Injection Field Experiment: Final Results and Conclusions. *In* IADC/SPE Drilling Conference. New Orleans, Louisiana. doi:10.2118/59115-MS.
- Munjiza, A. 2004. The Combined Finite-discrete Element Method. Wiley: University of London.
- Munjiza, A.A., Knight, E.E., and Rougier, E. 2011. Computational Mechanics of Discontinua. *In* Computational Mechanics of Discontinua. WILEY. doi:10.1002/9781119971160.
- Nadeem, M., Dusseault, M.B., and Bilak, R.A. 2005. Assessment Criteria for Deep Waste Disposal Sites. *In* 40th American Rock Mechanics Association (ARMA). Anchorage, Alaska.
- Nagel, N. 2013. Critical Geomechanics Concepts for Hydraulic Fracturing and Well Completions in Shales. *In* AAPG Geoscience Technology Workshop, Geomechanics and Reservoir Characterization of Shales and Carbonates. doi:10.1007/s00603-013-0391-x.Nagel.
- Nagel, N.B., Sanchez-Nagel, M. a., Zhang, F., Garcia, X., and Lee, B. 2013. Coupled Numerical Evaluations of the Geomechanical Interactions Between a Hydraulic Fracture Stimulation and a Natural Fracture System in Shale Formations. Rock Mechanics and Rock Engineering, **46**(3): 581–609. doi:10.1007/s00603-013-0391-x.
- Nassir, M. 2013. Geomechanical Coupled Modeling of Shear Fracturing in Non-Conventional Reservoirs. University of Calgary.

- Nelson, R. 2001. Geologic Analysis of Naturally Fractured Reservoirs. *In* second. Gulf Professional Publishing, an imprint of Butterworth–Heinemann, United States of America.
- Nicol, A. 2013. A Multicomponent Seismic Investigation of Natural and Induced Fracturing,. University of Calgary. doi:10.1017/CBO9781107415324.004.
- Nordgren, R.R.P. 1972. Propagation of a Vertical Hydraulic Fracture. *In* Society of Petroleum Engineers Journal. pp. 306–314. doi:10.2118/3009-PA.
- Novakovic, M., and Atkinson, G.M. 2015. Preliminary Evaluation of Ground Motions from Earthquakes in Alberta. *Seismological Research Letters*, (August): 0220150059–. doi:10.1785/0220150059.
- Nyland, E., and Dusseault, M. 1983. Fireflood Microseismic Monitoring Results and Potential for Process Control. *Journal of Canadian Petroleum TEchnology*, **22**(2): 62–68. doi:http://dx.doi.org/10.2118/83-02-03.
- Pater, C.J., and Baisch, S. 2011. Geomechanical Study of Bowland Shale Seismicity. Cuadrilla Resources Ltd.
- Perkins, T.K., and Kern, L.R. 1961. Widths of Hydraulic Fractures. *Journal of Petroleum Technology*, (SPE 89). doi:10.2118/89-PA.
- Pirayehgar, A., and Dusseault, M.B. 2014. The Stress Ratio Effect on Hydraulic Fracturing in the Presence of Natural Fractures. *In* American Rock Mechanics Association. Minneapolis, MN, USA, 1-4 June 2014.
- Pirayehgar, A., Yetisir, M., and Dusseault, M.B. 2016. Fabric Pattern Effects on Deformation and Fluid Flow in Anisotropic Stress Fields. *In* 4th Itasca Symposium on Applied Numerical Modeling. Lima, Peru.
- Potluri, N., Zhu, D., Hill, A.D., and Texas, A. 2005. Effect of Natural Fractures on Hydraulic Fracture Propagation. *In* Society of Petroleum Engineers (SPE 94568).
- Preisig, G., Eberhardt, E., Hosseinian, A., and Bustin, M. 2015. Coupled Hydromechanical Modeling of Rock Mass Response to Hydraulic Fracturing: Outcomes Related to the Enhancement of Fracture Permeability. *In* 13th International Congress of Rock Mechanics.
- Prieto, G.A., Shearer, P.M., Vernon, F.L., and Kilb, D. 2004. Earthquake Source Scaling and Self-similarity Estimation from Stacking P and S Spectra. *Journal of Geophysical Research*, **109**(B08310). doi:10.1029/2004JB003084.
- Rahman, M.K., Hossain, M.M., and Rahman, S.S. 2000. An Analytical Method for Mixed-Mode Propagation of Pressurized Fractures in Remotely Compressed Rocks. *International Journal of Fracture*, **103**(3): 243–258. doi:10.1023/A:1007624315096.
- Rahman, M.K., Hossain, M.M., and Rahman, S.S. 2002. A Shear-Dilation-Based Model for Evaluation of Hydraulically Stimulated Naturally Fractured Reservoirs. *International Journal for Numerical and Analytical Methods in Geomechanics*, **26**(5): 469–497. doi:10.1002/nag.208.

- Riahi, A., and Damjanac, B. 2013. Numerical Study of Interaction Between Hydraulic Fracture and Discrete Fracture Network. INTECH,.
- Riahi, A., Hammah, E.R., and Curran, J.H. 2010. Limits of Applicability of the Finite Element Explicit Joint Model in the Analysis of Jointed Rock Problems. 44th US Rock Mechanics Symposium - 5th US/Canada Rock Mechanics Symposium,.
- Rosso, R.S. 1976. A comparison of joint stiffness measurements in direct shear, triaxial compression, and In Situ. *International Journal of Rock Mechanics, Mining Sciences and Geomechanics*,. doi:10.1016/0148-9062(76)91282-1.
- Ruff, L.J. 1999. Dynamic Stress Drop of Recent Earthquakes: Variations within Subduction Zones. *Pure and Applied Geophysics*, **154**: 409–431. doi:10.1007/s000240050237.
- Rutledge, J.T., and Phillips, W.S. 2001. Hydraulic Stimulation of Natural Fractures as Revealed by Induced Microearthquakes, Carthage Cotton Valley Gas Field, East Texas.
- Rutqvist, J., Rinaldi, A.P., Cappa, F., and Moridis, G.J. 2013a. Modeling of fault reactivation and induced seismicity during hydraulic fracturing of shale-gas reservoirs. *Journal of Petroleum Science and Engineering*, **107**: 31–44. Elsevier. doi:10.1016/j.petrol.2013.04.023.
- Rutqvist, J., Rinaldi, A.P., Cappa, F., and Moridis, G.J. 2013b. Modeling of fault reactivation and induced seismicity during hydraulic fracturing of shale-gas reservoirs. *Journal of Petroleum Science and Engineering*, **107**: 31–44. doi:10.1016/j.petrol.2013.04.023.
- Scholz, C.H. 2002. The Mechanics of Earthquakes and Faulting. *In Seismological Research Letters*, 2nd edition. Cambridge University Press. doi:10.1785/gssrl.74.3.333.
- Sesetty, V., and Ghassemi, A. 2012. Simulation of Hydraulic Fracture Propagation in a Naturally Fractured Reservoir. *In Thirty-Seventh Workshop on Geothermal Reservoir Engineering*. Stanford University, Stanford, California.
- Shearer, P.M., Prieto, A., and Hauksson, E. 2006. Comprehensive Analysis of Earthquake Source Spectra in Southern California. *Journal of Geophysical Research*, **111**(B06303). doi:10.1029/2005JB003979.
- Singhal, B.B.S., and Gupta, R.P. 2010. Applied Hydrogeology of Fractured Rocks. *In 2nd edition*. Springer Netherlands, Dordrecht. doi:10.1007/978-90-481-8799-7.
- Sipple-Srinivasan, M., Bruno, M.S., Bilak, R.A., and Danyluk, P.G. 1997. Field Experience with Oilfield Waste Disposal Through Slurry Fracture Injection. *In 67th Annual Western Regional Meeting of the SPE*.
- Smith, M.B., and Montgomery, C.T. 2015. Hydraulic fracturing. CRC Press.
- Sorkhabi, R. 2014. Fracture, Fracture everywhere - Part I. *GeoExPro*, **11**(3): 86–91.
- Thiercelin, M., and Makkhyu, E. 2007. Stress Field in the Vicinity of a Natural Fault Activated by the Propagation of an Induced Hydraulic Fracture. *In American Rock Mechanics Association*. pp. 1617–1624.

- Todd, M.J., and Yildirim, E.A. 2007. On Khachiyan's Algorithm for the Computation of Minimum-Volume Enclosing Ellipsoids. *Discrete Applied Mathematics*, **155**(13): 1731–1744. doi:10.1016/j.dam.2007.02.013.
- Twiss, R.J., and Moores, E.M. 1992. *Structural Geology*. W. H. Freeman and Company.
- USGS. 2013. The Severity of an Earthquake. Available from <http://pubs.usgs.gov/gip/earthq4/severitygip.html>.
- Vandamme, L., Jeffrey, R.G., and Curran, J.H. 1988. Pressure Distribution in Three-Dimensional Hydraulic Fractures. *SPE Production Engineering*, **3**(2): 181–186. doi:10.2118/15265-PA.
- Veil, J.A., and Dusseault, M.B. 2003. Evaluation of Slurry Injection Technology for Management of Drilling Wastes. U.S. Department of Energy, National Petroleum Technology Office.
- Wang, S. 1992. Fundamental Studies of the Deformability and Strength of Jointed Rock Masses at Three Dimensional Level. The University of Arizona.
- Warpinski, N. 1991. Hydraulic Fracturing in Tight, Fissured Media. *Journal of Petroleum Technology*, **43**(2). doi:10.2118/20154-PA.
- Warpinski, N.R. 2014. A Review of Hydraulic-Fracture Induced Microseismicity. *In* American Rock Mechanics Association. Minneapolis, MN, USA, 1-4 June 2014.
- Warpinski, N.R., Du, J., Zimmer, U., and Service, P.A.H. 2012. Measurements of Hydraulic-Fracture-Induced Seismicity in Gas Shales. *In* SPE Hydraulic Fracturing Technology Conference. Woodlands, Texas, USA. pp. 6–8.
- Warpinski, N.R., Mayerhofer, M.J., Vincent, M.C., Cipolla, C.L., and Lonon, E.R. 2009. Stimulating unconventional reservoirs: Maximizing network growth while optimizing fracture conductivity. *Journal of Canadian Petroleum Technology*, **48**(10): 39–51. doi:10.2118/114173-PA.
- Warpinski, N.R., and Teufel, L.W. 1987. Influence of Geologic Discontinuities on Hydraulic Fracture Propagation (includes associated papers 17011 and 17074). *Journal of Petroleum Technology*, **39**(2). doi:10.2118/13224-PA.
- Weng, X., Kresse, O., Cohen, C.-E., Wu, R., and Gu, H. 2011. Modeling of Hydraulic-Fracture-Network Propagation in a Naturally Fractured Formation. *SPE Production & Operations*, **26**(04): 368–380. doi:10.2118/140253-PA.
- Williams, J.R., Hocking, G., and Mustoe, G.G.W. 1985. The Theoretical Basis of the Discrete Element Method. *International Journal of Numerical Methods of Engineering*,.
- Williams-Stroud, S.C., Barker, W.B., and Smith, K.. 2012. Induced Hydraulic Fractures or Reactivated Natural Fractures ? Modeling the Response of Natural Fracture Networks to Stimulation Treatments. *In* 46th US Rock Mechanics/Geomechanics Symposium. Chicago, IL, USA. pp. 24–27.

- Wu, R., Germanovich, L.N., and Hurt, R.S. 2009. Experimental and Theoretical Study of Mixed-Mode I + III Crack Propagation and Segmentation. *In* American Rock Mechanics Association. pp. 1–13.
- Wu, Y.-S., Li, J., Ding, D., Wang, C., and Di, Y. 2013. A Generalized Framework Model for Simulation of Gas Production in Unconventional Gas Reservoirs. 2013 SPE Reservoir Simulation Symposium,. doi:10.2118/163609-MS.
- Xia, G. 2007. Volume Changes during Fracture Injection of Biosolids. University of Waterloo.
- Xia, G., Bilak, R., Marika, E., Al-Shehri, H.A., and Al-Qahtani, F.Y. 2014. Performance Assessment of Cuttings Re-Injection (CRI) Operations at the Manifa OilField, KSA. *In* Rock Mechanics for Natural Resources and Infrastructure.
- Zangeneh, N. 2013. Numerical Simulation of Hydraulic Fracture, Stress Shadow Effects and Induced Seismicity in Jointed Rock. The University of British Columbia.
- Zangeneh, N., Eberhardt, E., and Bustin, R.M. 2015. Investigation of the influence of natural fractures and in situ stress on hydraulic fracture propagation using a distinct-element approach. *Canadian Geotechnical Journal*, **52**(7): 926–946. doi:10.1139/cgj-2013-0366.
- Zangeneh, N., Eberhardt, E., Bustin, R.M., and Bustin, A. 2013. A Numerical Investigation of Fault Slip Triggered by Hydraulic Fracturing. *In* Effective and Sustainable Hydraulic Fracturing. doi:10.5772/56191.
- Zhang, L. 2005. Rock Discontinuities. *In* Engineering Properties of Rocks. Elsevier.
- Zhang, X., and Sanderson, D.J. 1994. Fractal Structure and Deformation of Fractured Rock Masses. *In* Fractals and Dynamic Systems in Geoscience. pp. 37–52.
- Zhang, X., and Sanderson, D.J. 1995. Anisotropic features of geometry and permeability in fractured rock masses. *Engineering Geology*, **40**.
- Zhang, X., and Sanderson, D.J. 2002. Numerical Modeling and Analysis of Fluid Flow and Deformation of Fractured Rock Masses. Elsevier Science Ltd.
- Zhou, J., Jin, Y., and Chen, M. 2010. Experimental Investigation of Hydraulic Fracturing in Random Naturally Fractured Blocks. *International Journal of Rock Mechanics and Mining Sciences*, **47**(7): 1193–1199. Elsevier. doi:10.1016/j.ijrmms.2010.07.005.
- Zhou, J., and Xue, C. 2013. Experimental Investigation of Fracture Interaction between Natural Fractures and Hydraulic Fracture in Naturally Fractured Reservoirs. SPE EUROPEC/EAGE Annual Conference and Exhibition,; 1–12. Society of Petroleum Engineers. doi:10.2118/142890-MS.
- Zoback, M.D., and Gorelick, S.M. 2012. Earthquake Triggering and Large-Scale Geologic Storage of Carbon Dioxide. *Proceedings of the National Academy of Sciences of the United States of America*, **109**(26). doi:10.1073/pnas.1202473109.